RAPID ASSESSMENT
OF
EATHQUAKE-INDUCED LANDSLIDES

HAKAN TANYAŞ

Graduation committee:

Chairman/Secretary

Prof.dr.ir. A. Veldkamp	University of Twente

Supervisor(s)

Dr. C.J. van Westen	University of Twente
Prof.dr. V.G. Jetten	University of Twente

Co-supervisor(s)

Dr. K.E. Allstadt	US Geological Survey

Members

Prof.dr. M. van der Meijde	University of Twente
Prof.dr. N. Kerle	University of Twente
Prof.dr. M.L. Süzen	Middle East Technical University
Prof.dr. H-B. Havenith	University of Liege
Prof.dr. X. Fan	State Key Laboratory of Geohazard Prevention and Geoenvironment Protection (Chengdu University of Technology)

ITC dissertation number 340
ITC, P.O. Box 217, 7500 AE Enschede, The Netherlands

ISBN 978-90-365-4705-5
DOI 10.3990/1.9789036547055

Cover image painting by Khrystyna Kozyuk
Cover designed by Ceren Gamze Yasar & Hakan Tanyas
Printed by ITC Printing Department
Copyright © 2019 by Hakan Tanyaş

UNIVERSITY OF TWENTE.
ITC
FACULTY OF GEO-INFORMATION SCIENCE AND EARTH OBSERVATION

RAPID ASSESSMENT
OF
EATHQUAKE-INDUCED LANDSLIDES

DISSERTATION

to obtain
the degree of doctor at the University of Twente,
on the authority of the rector magnificus,
prof.dr. T.T.M. Palstra,
on account of the decision of the graduation committee,
to be publicly defended
on Thursday January 17, 2019 at 16.45

by

Hakan Tanyaş

born on July 23, 1983

in Ankara, Turkey

This thesis has been approved by
Dr. Cees J. van Westen, promoter
Prof. dr. Victor G. Jetten, co-promoter
Dr. Kate E. Allstadt, co-supervisor

Table of Contents

1. Introduction 1
1.1.1. Phase-1: before the 1994 Northridge earthquake 1
1.1.2. Phase-2: ShakeMaps introduced 4
1.1.3. Phase-3: after the 2008 Wenchuan earthquake 5
1.1.4. Phase-4: after the 2015 Gorkha earthquake 6
1.2. Problem statement 8
1.3. Research objectives 9
1.4. Structure of the thesis 9
2. Presentation and Analysis of a Worldwide Database of Earthquake-Induced Landslide Inventories 11
2.3.1. Analysis of reported EQIL events 20
2.3.2. Analysis of reported EQIL characteristics 20
2.3.3. Analysis of digital EQIL inventories 24
2.4.1. Evaluation Criteria 30
2.4.2. Evaluating EQIL inventories using the criteria 34
3. An updated method for estimating landslide-event magnitude 39
3.3.1. Step 1: Test the validity of the power-law distribution 46
3.3.2. Step 2: Obtain the cutoff point and power-law exponent 46
3.3.3. Step 3: Calculate the normalization constant 46
3.3.4. Step 4: Plot the power-law fit with empirical lines to estimate mLS 47
3.3.5. Step 5: Identify the best approach of mLS estimation 48
3.3.6. Step 6: Assess the uncertainty 49
4. Factors controlling landslide frequency-area distributions 57
4.3.1. FADs of EQIL inventories 64
4.3.2. Rollover and cutoff sizes 64
4.3.3. Proposed hypotheses 69
4.3.4. Amalgamation due to lack of spatial resolution and mapping preferences 74
4.3.5. Subjectivity of mapping procedure 76
4.3.6. Effect of distinguishing between landslide sources and deposits on FAD shape 80
4.4.1. A proposed explanation for the divergence from the power-law: Successive slope failure 81
4.4.2. The interpretation of the proposed explanation 83
5. Rapid prediction of magnitude-scale of landslide events triggered by an earthquake 89
5.2.1. Available data 91
5.2.2. Selection of inventories 95

6. A global slope unit-based method for the near real-time prediction of earthquake-induced landslides..... 110
6.3.1. Selection of earthquake-induced landslide inventories and events 115
6.3.2. Slope Units 116
6.3.3. Statistical Approach 121
6.3.4. Dependent and independent variables 122
6.3.5. Categorization of the EQIL inventories 123
6.4.1. Selection of independent parameters..... 124
6.4.2. Defining the Optimum Training Set 128
6.4.3. Categorization..... 132
6.4.4. Model Results..... 134
7. Synthesis 143
Bibliography..... 147
Summary 155
Appendices 158
Biography..... 160
ITC Dissertation List..... 162

1. Introduction[1]

1.1. Background

An earthquake-induced landslide (EQIL) inventory is a primary data source showing the locations and characteristics of landslides triggered by a single earthquake. Creating an EQIL inventory is a time-consuming process (e.g., Wasowski *et al.*, 2011) despite advances in mapping techniques. For example, the EQIL inventory for the 2008 Wenchuan earthquake required more than one year of image interpretation work (Xu *et al.*, 2014b) and the one for the 2015 Gorkha, Nepal earthquake required about one month to create despite being part of one of the fastest global rapid hazard response campaigns ever undertaken (Kargel *et al.*, 2016; Robinson *et al.*, 2017). Thus, the time required to create an EQIL inventory is too long to be useful for search and rescue operations (Robinson *et al.*, 2017). Given these time constraints on producing an EQIL inventory, an alternative approach that predicts EQIL distributions in near real-time is needed to provide critical information regarding potential blockages of roads, streams and rivers, and other critical lifelines.

In the absence of a predictive model regarding the spatial distribution and the occurrence probability of EQIL, data on the boundary of the landslide-affected area, the total landslide area or total landslide volume could also valuable information soon after an earthquake to assess the extents of emergency operations. These predictions also can contribute to estimate casualties and economic losses (e.g., Wald, 2013).

Progress in EQIL modeling efforts can be divided into four phases that are punctuated by three milestone earthquakes that led to rapid advancement: 1994 Northridge, California; 2008 Wenchuan, China; and 2015 Gorkha, Nepal (Figure 1.1).

1.1.1. Phase-1: before the 1994 Northridge earthquake

The first phase includes the era prior to the 1994 Northridge earthquake and thus is defined by early conceptual studies of seismic slope stability that laid the foundation for later regional hazard modeling. One of the first pioneer attempts to capture the extent of landslide-affected areas in world-wide studies was to establish statistical relations between earthquake magnitude and the area affected by landslides or the maximum landslide distance, either from the epicenter or the rupture zone as proposed by Keefer (1984). Later, Jibson and Harp (2012) found that the proposed landslide distance limits of Keefer (1984) differ between plate-boundary earthquakes and intraplate earthquakes, where seismic-wave attenuation is generally much lower. Moreover, they can only provide a one-dimensional measure, which gives the distance from the epicenter / rupture zone to the furthest individual landslide. Therefore, it is not a suitable parameter to define the

[1] This chapter is based on the following paper: Fan X., Scaringi G., West A.J., Tanyas H., Hovius N., van Westen C.J., Hales T.C., Korup O., Jibson R.W., Zhang L., Allstadt K.E., Evans S.G., Xu C., Li G., Pei X., Xu Q., and Huang R. Earthquake-induced chains of geo-hazards: Pattern, mechanism and impacts, Reviews of Geophysics, under review, 2018.

landslide-affected area. As another alternative to this one-dimensional measures, the peak ground acceleration (PGA) levels, which show a correlation with landslide density (e.g. Meunier *et al.*, 2007), have also been used to identify the landslide-affected area. Wilson and Keefer (1985) were the first who proposed a minimum threshold of 0.05g to such a boundary based on the data from 40 earthquakes gathered by Keefer (1984). However, in that study, EQIL inventory maps were only available for a few of the 40 reported earthquakes (Tanyaş *et al.*, 2017) (Chapter 2), and thus the reported threshold were derived from limited observations. In the same study, Keefer (1984) also proposed an identification method for landslide-event magnitude scale, which quantifies the severity of the event, using the total number of landslides triggered by an earthquake.

In addition to these simplified relations, some modeling perspectives were established to better understand seismically-induced landslides. Terzaghi (1950) was perhaps the first to apply rigorous engineering principles to the seismic stability of slopes when he proposed what would come to be known as pseudostatic analysis, wherein the earthquake shaking is simply added as a permanent force to the existing driving (gravity) and resisting (material strength) forces within a slope, and any exceedance of the resisting forces is defined as failure. Newmark (1965) improved on this by modeling a landslide as a rigid block sliding on an inclined plane under the influence of seismic shaking; the cumulative displacement induced by a given increment of shaking is a measure of the seismic stability of the slope.

Wilson and Keefer (1983) used earthquake strong-motion records and field observations of a landslide triggered by the 1979 Coyote Creek, California earthquake to show that the Newmark (1965) sliding-block method can fairly accurately model the dynamic behavior of landslides on natural slopes. Wilson and Keefer (1985) proposed a framework for using Newmark's sliding-block model to produce regional-scale seismic slope stability maps, and Wieczorek *et al.* (1985) applied this to produce an experimental seismic slope stability map; these studies were primarily conceptual, however, and were not calibrated to actual EQIL inventories or to regional strong-motion models from actual earthquakes. Jibson (1993) developed a simplified version of the Newmark method that facilitates applying this approach to regional analysis by using a regression equation to predict Newmark displacement as a function of earthquake shaking intensity and seismic slope stability.

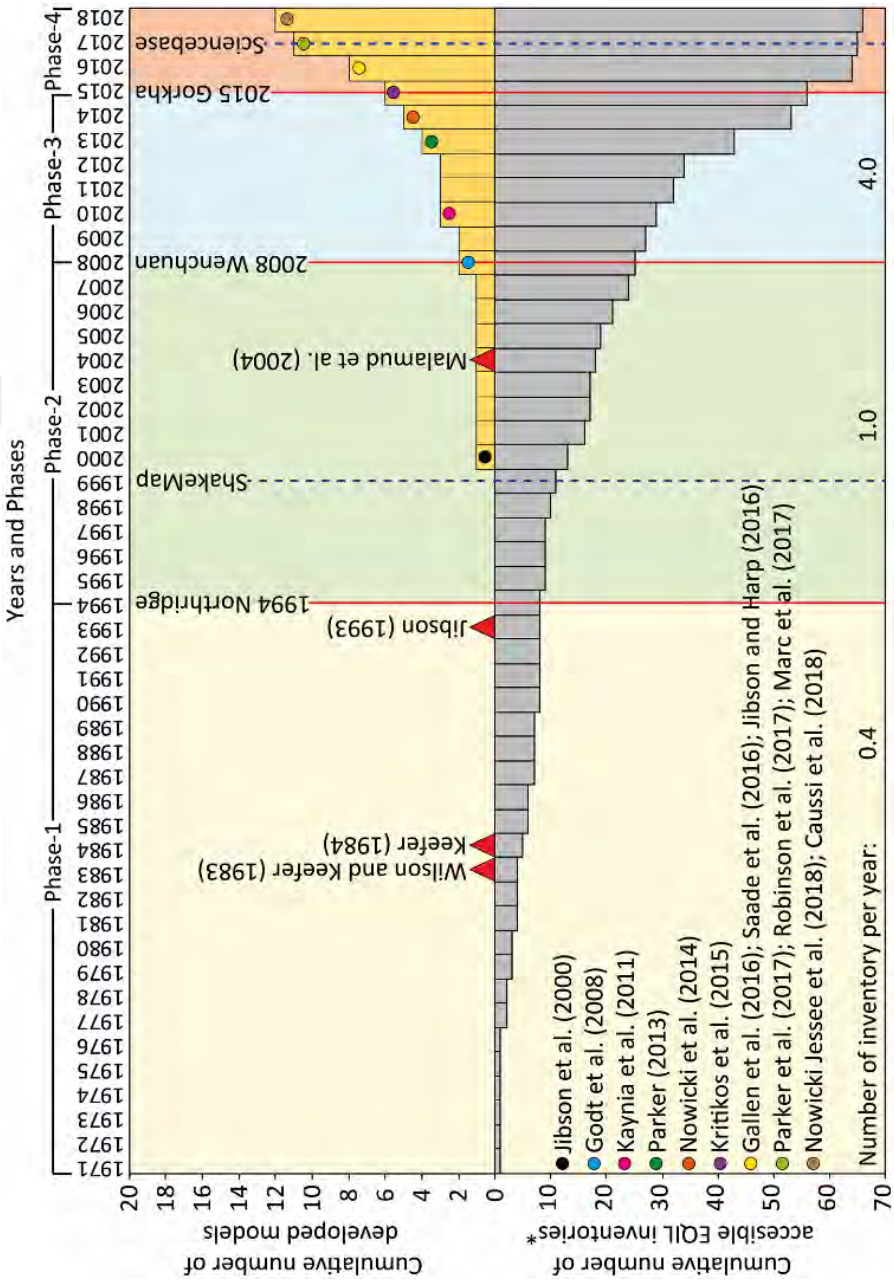

*Figure 1.1. Sketch showing the progress in EQIL modeling studies through time. *EQIL inventories from Tanyaş et al. (2017).*

1.1.2. Phase-2: ShakeMaps introduced

The second phase in EQIL modeling studies was marked by the 1994 Northridge earthquake (Figure 1.1), which was a 'watershed' event because it was the first earthquake for which extensive data on engineering properties of geologic units, ground shaking, and triggered landslides were available to permit detailed regional analysis. Jibson *et al.* (2000) used these data sets to conduct a regional-scale seismic slope stability analysis. They combined shear-strength data for each geologic unit in the area with slope steepness derived from a 10-m digital elevation model (DEM) to predict the threshold of ground-shaking acceleration required for the initiation of the sliding (referred to as the critical or yield acceleration). They then predicted the resulting displacement using an empirical displacement model based on Newmark's sliding-block method that used shaking levels recorded during the earthquake. Finally, they compared the predicted displacements to the EQIL inventory and showed that increasing predicted Newmark displacement does, in fact, correlate with increasing landslide frequency. The study provides a simple mathematical relation between predicted Newmark displacement and the probability of landsliding, and gives a basic quantitative framework for using a physical modeling approach to estimate seismic landslide hazards at regional scale. As with most physically based methods, this simplified approach has the advantage of more accurately reflecting the underlying processes, despite the uncertainties caused by those simplifications (Allstadt *et al.*, 2017). But the geotechnical and seismic data required to apply this model are not available everywhere and can be difficult to estimate.

After the 1994 Northridge earthquake, real-time, digital seismic networks were expanded in many areas (Wald *et al.*, 2003), and the U.S. Geological Survey ShakeMap system was developed (Wald *et al.*, 1999) to provide estimates of ground-motion parameters in near real time. This system provides estimates of ground-motion parameters worldwide and thus provides one of the data requirements of EQIL modeling studies. These ground-motion predictions are now commonly used in many EQIL susceptibility assessments (Allstadt *et al.*, 2017).

In addition to these modelling efforts, in the second phase, the statistical relation proposed by Keefer (1984) was updated (Rodriguez *et al.*, 1999), and similar statistics were also derived using national databases (Hancox *et al.*, 2002; Papadopoulos and Plessa, 2000; Prestininzi and Romeo, 2000). Additionally, Keefer (1994) established a linear regression relation between total landslide volume (V_{LT}) and seismic moment (M) (Equation 1.1).

$$logV_{LT} = 1.45M - 11.50 \quad \text{(Equation 1.1)}$$

Malamud *et al.* (2004) updated Keefer (1994) approach using size-statistics of landslides. To do that, Malamud *et al.* (2004) modelled the frequency-area distribution of three well-documented event inventories, each with a different triggering mechanism, including the 1994 Northridge earthquake-induced landslide inventory (Harp and Jibson, 1995, 1996). Malamud *et al.* (2004) argued that the frequency-size (area or volume) distributions of landslides are independent of the landslide trigger. Consequently, they proposed empirical curves which are assumed to be valid for the frequency-size distribution of any landslide inventory. They considered landslide areas as proxy and proposed an updated method of identification of landslide-event magnitude scale (mLS), which was first suggested by Keefer (1984). Malamud *et al.* (2004) suggested that completeness of landslide-event

inventories can be assessed by comparing the frequency-size distribution of a partial inventory and the proposed empirical curves. They noted that, based on this comparison, the number of missing small landslides, total number of landslides (N_{LT}) and a landslide-event magnitude scale of the examined inventory can be estimated (Equation 1.2).

$$mLS = logN_{LT} \qquad \text{(Equation 1.2)}$$

Malamud *et al.* (2004) estimated the total landslide area (A_T) (the sum of polygon areas) (Equation 1.3) and the area of the largest expected landslides using the estimated number of landslides (Equation 1.4).

$$A_T = 3.07x10^{-3}x10^{mLS} \qquad \text{(Equation 1.3)}$$

$$A_{Lmax} = 1.10x10^{-3}xN_{LT}^{0.714} \qquad \text{(Equation 1.4)}$$

Malamud *et al.* (2004) also proposed a relationship to estimate the total volume of landslides (V_{LT}) which depends on the largest landslide size (Equation 1.5) and established a relation between earthquake magnitude and landslide-event magnitude (Equation 1.6).

$$V_{LT} = 7.30x10^{-6}xN_{LT}^{1.1222} \qquad \text{(Equation 1.5)}$$

$$mLS = 1.29M - 5.65 \qquad \text{(Equation 1.6)}$$

1.1.3. Phase-3: after the 2008 Wenchuan earthquake

The third phase in EQIL modeling progress followed the 2008 Wenchuan, China earthquake (Figure 1.1), which triggered the largest number of landslides ever recorded (e.g., Tanyaş *et al.*, 2017). Hundreds of papers were published on various aspects of this earthquake, and the knowledge gained from analysis of the landslides triggered improved our understanding regarding EQIL (e.g., Fan *et al.*, 2018).

Godt *et al.* (2008a) developed a global model for the rapid assessment of EQIL that uses ground-motion parameters from ShakeMap and globally available data to estimate the critical acceleration of slopes at regional scale. They modified the approach of Jibson *et al.* (2000) by using a heuristic approach to make the model globally applicable. They used shear-strength parameters defined by Nadim *et al.* (2006), who uses the global geological map of Bouysse (2010) to assigned shear strengths to each geological unit based on age and lithology. To calculate displacements, Godt *et al.* (2008a) used the regression equation developed by Jibson (2007). They applied a failure threshold displacement of 5 cm to estimate the proportion of 1-km grid cells that would be affected by landslides. Godt *et al.* (2008a) compared their model outputs to three EQIL inventories from the 1994 Northridge, 1976 Guatemala, and 2008 Wenchuan earthquakes. They did not perform a quantitative validation of their results but indicated that their model gives a qualitatively successful result.

Many studies applying the Newmark sliding-block approach have been published that include a variety of proposed refinements or unique applications (e.g., Gallen *et al.*, 2015; Kaynia *et al.*, 2011; Saade *et al.*, 2016). The most challenging aspect of all of these physically based approaches to regional modeling is the availability of reliable data with which to characterize the strengths of the geologic units (Dreyfus *et al.*, 2013) as well as seismological data that allow accurate estimation of ground motion. The ground-motion

problem is particularly acute because of the difficulty in predicting topographic amplification in the steeply sloping areas in which most landslides occur.

An alternative to physically based models are statistical models, which use either logistic regression (Nowicki Jessee *et al.*, 2018; Nowicki *et al.*, 2014; Parker *et al.*, 2017) or fuzzy logic (Kritikos *et al.*, 2015) to predict the probability of landslide occurrence for a given grid.

Parker (2013) trained his model using two earthquakes (1929 Buller and 1968 Inangahua), for the calibration he included three other earthquakes (1994 Northridge, 1999 Chi-Chi, and 2008 Wenchuan). He ran this model for 30 m resolution grids and limited the model for the landslides larger than 11,000 m^2. Parker (2013) indicated that this model could be used in hazard assessment of future earthquakes, though the estimates are likely to be conservative. Nowicki *et al.* (2014) trained their model using four earthquakes (1976 Guatemala, 1994 Northridge, 1999 Chi-Chi, and 2008 Wenchuan) and tested the model using another earthquake (2004 Niigata-Chuetsu). They run the model for about 1 km resolution grids. Nowicki *et al.* (2014) stated a similar conclusion as Parker (2013) that their model is capable of capturing the pattern of observed landslides, yet overpredicts the landslide probability. Kritikos *et al.* (2015) used two earthquakes (1994 Northridge and 2008 Wenchuan) for training and another earthquake (1999 Chi-Chi) for validation of their model. They worked with 60-m grids. They noted that their model performs well and can be applied to future earthquakes for rapid assessment of EQIL.

What is apparent about the studies in phase 3 is that they all use the same EQIL inventories (1994 Northridge, 1999 Chi-Chi, or 2008 Wenchuan). Moreover, none of these models was initially tested in real-time applications.

1.1.4. Phase-4: after the 2015 Gorkha earthquake

The fourth (current) phase of EQIL modeling was initiated by the 2015 Gorkha earthquake (Figure 1.1), which provided the opportunity to test some of these models in real time. Immediately following the 2015 Gorkha earthquake three different landslide hazard maps, based on the methods developed by Kritikos *et al.* (2015), Parker (2013) (www.ewf.nerc.ac.uk/2015/04/25/nepal-earthquake-likely-areas-of-landsliding), and Gallen *et al.* (2015) (www.sites.google.com/a/umich.edu/nepalearthquake/landslide-maps) were created and posted online. No quantitative validation has been made of the first two of these models; visual comparisons between the available inventories and these products show that they are not yet sufficiently mature to apply in disaster response phase. Gallen *et al.* (2016) made a detail evaluation of their model including a quantitative validation using the landslide inventory created by Roback *et al.* (2017). Gallen *et al.* (2016) state that their model significantly overpredicted the area that would be affected by landslides; they mainly attributed this to limitations of the shaking estimates provided by ShakeMap, which had little instrumental control in this earthquake.

Following the Gorkha earthquake, a new discussion began regarding inventory maps as an input layer of modeling studies. Robinson *et al.* (2017) argued that the proposed models suffer from inadequate training data that are not representative of the site of prediction. They suggest using only a part of landslides mapped in first few hours or days immediately after an earthquake as the training set. Based on this approach, they modeled the landslide density distribution for 2015 Gorkha earthquake using fuzzy logic and argued

that the output is useful for the emergency response phase, though it is coarse in detail. However, even mapping just a representative sample of triggered landslides could take enough time to reduce the usefulness of the predictions in the time frame needed for emergency response. Parker *et al.* (2017), also in the fourth face, focus on the limitations of training data and suggest a critical approach to completeness of EQIL landslide inventories based on landslide size statistics (e.g., Malamud *et al.*, 2004). They use this completeness level to reflect the effect of missing small landslides in their hazard assessment.

So after the 2015 Gorkha earthquake, the focus of EQIL studies shifted from modeling method to inventory data. In fact, there is a steadily increasing number of EQIL inventories: Tanyaş *et al.* (2017) (Chapter 2) listed nine (accessible) inventories created before the 1994 Northridge earthquake; 14 more inventories were created between the Northridge and Wenchuan earthquakes Between Wenchuan and Gorkha, 33 more inventories were created (Figure 1.1). Access to those inventories was a challenging issue, however. Nowicki Jessee *et al.* (2018) updated the model proposed by Nowicki *et al.* (2014) using 23 EQIL inventories. Nowicki Jessee *et al.* (2018) increased the grid resolution to 250 m and developed a transfer function to convert the probability prediction of a given grid to areal coverage.

The U.S. Geological Survey's Prompt Assessment of Global Earthquakes for Response (PAGER) system (Earle *et al.*, 2009) provides rapid estimates of earthquake-specific economic losses and fatalities, but does not explicitly account for losses due to landslides. This has been a long-recognized problem and has initiated research toward the goal of explicitly including ground failure in PAGER's loss estimates (Wald, 2013). In a step toward that goal, the USGS has recently released a new near-real-time earthquake product, *Ground Failure*, which considers both landslides and liquefaction and provides an overall assessment of hazard and population exposure as well as geospatial maps of hazard. The system considers global earthquakes, therefore any models implemented currently must be applicable worldwide, and therefore, any input datasets of sufficient quality must also be available globally. The models also must produce geospatial maps of probability. As a result, only three relatively coarse models meet this criteria and are currently implemented for landslides, Godt *et al.* (2008a), Nowicki *et al.* (2014), and Nowicki Jessee *et al.* (2018), with the latter serving as the default for event alert level determination and for display on interactive web maps. As of July 2018, this system provides only qualitative descriptors of hazard and loss estimates. Full integration with PAGER necessitates quantitative estimates, but further research and development is required to reach that point.

Allstadt *et al.* (2018) used remote-sensing and field observations from the 2016 Kaikōura (New Zealand) earthquake to evaluate the three models that are currently implemented in the USGS Ground Failure earthquake product. They examined the model performances and how prediction maps changed as the ShakeMap ground motion estimates evolved through time. For this test case, Allstadt *et al.* (2018) concluded that any of the models could be used for rough prediction of coseismic landslide spatial distribution but that all models overpredict the hazard and that the temporal evolution of the ShakeMap models has a strong of effect on model output.

The Swiss Seismological Service (SED) is integrating the near-real-time shaking-based prediction to the Swiss ShakeMap (Cauzzi *et al.*, 2015). To reach this goal, Cauzzi *et al.*

(2018) implemented the model developed by Nowicki *et al.* (2014) to the Swiss ShakeMap system using the available datasets for Switzerland.

In the absence of a predictive model regarding the spatial distribution and the occurrence probability of EQIL, to predict the boundary of landslide-affected area, Jibson and Harp (2016) analyzed six EQIL events and explored the absolute minimum PGA value considering the very smallest failures (<1 m^3) triggered by the corresponding earthquakes. They examined four of those inventories by field studies and showed that PGA contour covering all landslides ranges from 0.02g to 0.08g. They investigated two other inventories using aerial-photographic interpretations and pointed out that the PGA range of 0.05-0.11g was an absolute outermost limit of triggered landslides. However, Jibson and Harp (2016) also stated that the proposed outermost limits of triggered landslides can only be valid where susceptible slopes are extensive. Yet the actual area that is affected by landslides depends on the local topographic, lithologic, climatic and land cover conditions. These conditions are different for each earthquake-affected area, and the interaction between these conditions and ground shaking results in the specific landslide distribution pattern that actually occurs. Thus, for some settings, such a common PGA limits could be considerably larger than the real landslide-affected area, for example, if the susceptible slopes are limited with a small region.

Marc *et al.* (2017) proposed an alternative analytical expression to estimate the landslide-affected area by gathering geophysical information and estimates of the landslide distribution area for 83 earthquakes. However, they noted that only for 10 of those 83 earthquakes they had detailed landslide inventories, whereas for the rest rough estimates regarding landslide affected areas were available. Marc *et al.* (2017)'s expression is based on scaling laws relating seismic moment, source depth, and focal mechanism with ground shaking and fault rupture length. They noted that their model significantly overpredicted for some earthquakes, whereas for some others the model does not capture an along-strike asymmetry in landslide-affected area.

1.2. Problem statement

Despite a large body of literature on the above mentioned aspects of earthquake-induced landslides, significant challenges remain in studies regarding frequency-size distribution of landslides and prediction of EQIL:

- Access to existing EQIL inventories is a problem in the absence of a centralized database. On the other hand, the available inventories have a varying level of quality and completeness.
- The factors controlling frequency-size distribution of EQIL have not been investigated in sufficient detail.
- The proposed method of Malamud *et al.* (2004) to determine landslide-event magnitude scale is highly subjective, particularly when curves are selected using visual comparison, as they propose.
- The proposed method to estimate the total volume and area of EQIL (Marc *et al.*, 2016) requires inputs such as the parameters describing rock strength,

earthquake asperity depth, and ground motion attenuation that are often not precisely known (Li *et al.*, 2017).

- Representativeness of training data has not been discussed in detail for the models developed to predict the probability of occurrence of EQIL.

1.3. Research objectives

The main objective of this study is to develop a method for the rapid assessment of earthquake-induced landslides (EQIL) immediately after an earthquake has happened. The method should provide reliable information for organizations involved in the disaster response phases regarding the intensity of the landslide-event and the spatial distribution of landslides. To achieve this goal, the following sub-objectives were defined:

i. Gathering a large number of EQIL inventories and evaluating them in terms of their quality and completeness levels and creating a centralized repository for sharing them (Chapter 2).

ii. Developing an objective and automated methodology to estimate landslide-event magnitudes, which we can be used to quantify the severity of a landslide-event (Chapter 3).

iii. Assessing the factors controlling the frequency-size distribution of EQIL to better understand the mechanism of triggered landslides (Chapter 4).

iv. Developing a method to predict landslide event-magnitude scale immediately after an earthquake without having an EQIL inventory (Chapter 5).

v. Developing a method for near real-time estimation of the probability of EQIL occurrence (Chapter 6).

1.4. Structure of the thesis

This thesis consists of seven chapters. The five core chapters, and the literature review part of the introduction, are under review, accepted or published as peer-reviewed journal papers. The main contents of chapters can be summarized as follows:

This chapter (Chapter 1) presented the general research framework of the thesis and the research objectives, and thesis structure.

Chapter 2 presents an EQIL database contains information on 363 landslide-triggering earthquakes including 66 digital landslide inventories. The general characteristics of EQIL inventories in term of morphologic and seismogenic features are summarized. Additionally, an evaluation system is presented to help users assess the suitability of the available inventories for different types of EQIL studies and model development.

Chapter 3 presents a method for estimating landslide-event magnitude and its uncertainty that better fits the observations and is more reproducible, robust, and consistent than existing methods. A relation is proposed to estimate the total area of landslides (the sum of polygon areas) using landslide-event magnitude scale.

Chapter 4 examines the frequency-size distributions of earthquake-induced landslides that show a power-law relation for medium and large landslides. The factors controlling the frequency-size distributions of landslides are analyzed and an explanation is proposed to understand the divergence from the power-law for small landslides.

Chapter 5 presents a method to estimate landslide-event magnitude scale using globally available morphologic and seismogenic variables.

Chapter 6 presents a comprehensive method for the near real-time landslide probability estimation using a logistic regression model based on slope units and incorporating 25 earthquake-induced landslide inventories.

Chapter 7 summarizes the results of the previous chapters 2 to 6, provides general conclusion and recommendations for future work.

2. Presentation and Analysis of a Worldwide Database of Earthquake-Induced Landslide Inventories[2]

2.1. Introduction

Losses due to earthquake-triggered landslides can be significant, and for some events they exceed losses directly due to shaking (Bird and Bommer, 2004; Harp *et al.*, 1984). Approximately 70% of all earthquake-related casualties not caused by ground shaking are caused by landslides (Marano *et al.*, 2010). From 2004 to 2010 a total of 47,736 earthquake-induced landslide (EQIL) casualties were reported (Kennedy *et al.*, 2015; Petley, 2012). In addition, EQIL commonly have considerable indirect and long-term effects on society and infrastructure that intensify their overall damage (e.g. Huang and Fan, 2013; Shafique *et al.*, 2016) such as blocked roads that hamper medical care (Marui and Nadim, 2009), floods from the failure of landslide dams, increased debris-flow activity (e.g. Shieh *et al.*, 2009; Tang *et al.*, 2016), downstream river aggradation and associated flooding (e.g. Korup, 2006).

Papers having both worldwide (Keefer, 1984; Rodriguez *et al.*, 1999) and national (Hancox *et al.*, 2002; Papadopoulos and Plessa, 2000; Prestininzi and Romeo, 2000) perspectives have established a baseline for understanding the relations between EQIL distributions, landslide types, and areas of coverage. However, several authors have demonstrated that these relationships have high uncertainty and they are not always valid (e.g. Barlow *et al.*, 2014; Gorum *et al.*, 2014; Hancox *et al.*, 2002; Jibson and Harp, 2012; Jibson *et al.*, 2004). A number of explanations have been given to explain this uncertainty. Hancox *et al.* (2002) stated that the data used to derive these relationships might be inadequate to characterize the whole world, as the work by Keefer (1984) was based predominantly on earthquakes in North America, and data sets belonging to different climatic, geologic and topographic conditions may give different results. Jibson and Harp (2012) found that landslide distance limits differ between plate-boundary earthquakes, which made up most of Keefer (1984)'s data set, and intraplate earthquakes, where seismic-wave attenuation is generally much lower. Furthermore, Gorum *et al.* (2014) concluded that estimating the number of coseismic landslides from earthquake magnitude alone remains highly problematic. It is well established that the ground shaking experienced at a given location depends on

[2] This chapter is based on the following paper: Tanyas, H., van Westen, C.J., Allstadt, K.E., Jessee (Nowicki), M.A., Gorum, T., Jibson, R.W., Godt, J.W., Sato, H.P., Schmidt, R.G., Marc, O., Hovius, N., 2017. Presentation and Analysis of a World-Wide Database of Earthquake-Induced Landslide Inventories. Journal of Geophysical Research: Earth Surface 122: 1991-2015. DOI: 10.1002/2017JF004236

numerous factors beyond just magnitude, such as local site conditions, source mechanism, region, depth, and rupture directivity. Therefore, the existence and the reliability of the input data such as digital elevation model, geologic map and ground shaking parameters are also essential for a comprehensive analysis.

A few authors have started to develop models that take a more complete view of the driving factors (e.g. Kritikos *et al.*, 2015; Marc *et al.*, 2016; Nowicki *et al.*, 2014). However, the literature is still relatively sparse, in part because it is challenging and time consuming to pull together input datasets (e.g. EQIL inventories) that cover the wide range of conditions under which EQIL occur. The importance of different tectonic, geomorphologic, and climatic settings to landslide distribution patterns and the internal relation between EQIL-related factors such as landslide number, size-frequency distribution, and total landslide-affected area still requires further investigation using EQIL inventories from many different environments.

Even though landslide susceptibility assessment using different statistical analyses has become a common approach, the use of seismic indicators in these analyses to estimate EQIL hazard is still rare (Budimir *et al.*, 2014; Carro *et al.*, 2003; Gallen *et al.*, 2016; Lee, 2014; Marzorati *et al.*, 2002; Nowicki *et al.*, 2014; Robinson *et al.*, 2017). The generation of EQIL hazard maps for new or scenario events is complicated as each earthquake has specific characteristics and existing EQIL inventories only reflect the characteristics of a single earthquake. For statistical EQIL hazard assessments, many more EQIL inventories are needed to represent the response to different amounts of ground shaking and regional differences in landslide susceptibility. Physically based methods are not prone to the same limitations, but the existing models are still rather simple and focus mainly on shallow landslides by applying the widely used Newmark method (Jibson *et al.*, 2000). Other models use weighted approaches that combine a number of factor maps but do not use information on frequency and expected landslide densities (e.g. Kritikos *et al.*, 2015), or utilize statistical approaches that assume a single relationship between landslide occurrence and susceptibility to landsliding across the globe (e.g. Nowicki *et al.*, 2014).

A limited number of preliminary studies have used EQIL inventories to produce globally applicable models for near real-time prediction of seismically induced landslides (Godt *et al.*, 2008a; Kritikos *et al.*, 2015; Marc *et al.*, 2016; Nowicki *et al.*, 2014). Though they are not yet sufficiently mature to operationally inform disaster response after earthquakes, the development of such models benefits greatly from the availability of past data for model development and testing. The more data available, the better the models can become.

Beyond its value for the hazard studies, having more EQIL data could also help us to improve our understanding in terms of some other natural processes such as erosion, sediment transportation, landscape evolution, and climatic and environmental change. For example, Malamud *et al.* (2004) relate the magnitude of earthquakes to erosion rates using EQIL inventories. Parker *et al.* (2011) analyze the relationships between coseismic slip, mass wasting and relief generation considering the landslides triggered by the Wenchuan earthquake. Marc *et al.* (2016) use EQIL inventories to derive total landslide volumes and area affected. Later, Marc *et al.* (2016) use this knowledge to assess seismic mass-balance over multiple earthquakes. Gallen *et al.* (2015) suggest the EQIL inventories can be a useful tool to probe the near-surface environment for spatial patterns of material strength. On the other hand, Schlögel *et al.* (2011) try to detect climatic and environmental

change analyzing landslide inventories. Although the authors do not use particularly the EQIL inventories in their studies, having a larger EQIL database could also provide opportunity to increase the quality in such studies.

These findings emphasize the importance of collecting EQIL inventories from as many past events as possible and making them easily accessible to the EQIL community. We can use them to better understand the causal factors of the landslide distribution under different conditions, which can help determine landslide susceptibility, hazard, vulnerability, and risk, and can provide rapid assessments of landslide densities after an earthquake (Guzzetti *et al.*, 2012). Though there are two national scale EQIL databases for Italy (Martino *et al.*, 2014) and New Zealand (Rosser *et al.*, 2017), currently no global-scale centralized database exists for recording these events and storing the available inventory maps.

In this work, we strive to overcome and account for some of these issues, which are mainly caused by the scarcity of data, in order to create an openly available EQIL database and promote progress in this field. We have compiled 66 digital EQIL inventories from numerous authors. We have created a centralized repository using the U.S. Geological Survey's ScienceBase platform for sharing the inventories that we have permission from the original authors to redistribute.

In the following sections, we present the results of our compilation. First, we summarize the EQIL data sources and define different data types to categorize them. Based on the available inventories, we analyze EQIL distributions for different years, continents, countries and mountain belts. Frequency distributions are presented for some of the reported EQIL parameters such as total area affected, total number of landslides, landslide area, maximum distance from fault rupture and epicenter location, slope angle, ruggedness, local relief, distance to stream, peak ground acceleration (PGA), peak ground velocity (PGV), and Modified Mercalli Intensity (MMI). We conclude by establishing a schema for evaluating EQIL inventories utilizing published standards for ideal inventories (Harp *et al.*, 2011; Xu, 2014), applying this to the EQIL inventories in our database, discussing implications for using EQIL inventories for a range of applications, and detailing the ScienceBase repository we created for openly sharing EQIL inventories with the community.

2.2. EQIL data types

Earthquake-induced landslide information is presented in the literature with large variability in detail and data format because they were generated by many different researchers with different methods, objectives, and priorities. For some earthquakes, there are comprehensive spatial landslide data available, whereas for other cases, we cannot even be sure whether a single landslide was triggered. For example, within one a week of the main shock of 15 April 2016 in Kumamoto earthquake (Mw=7), the Geospatial Information Authority of Japan provided a basic landslide inventory on their web site (http://www.gsi.go.jp/). This swift provision is attributed to efficient landslide interpretation and mapping using ortho-photos, produced by digital aerial photos, Global Navigation Satellite System- (GNSS) and Intertial Measurement Unit- (IMU) measured aerial triangulation, and semi-automated mosaic image producing. On the other hand, for the

earthquake of 7 December 2015 that occurred in mountainous region of Tajikistan (Mw=7.2), no information on landslide occurrence is available. Because of gaps such as this, there are an unknown number of undocumented events in addition to the known EQIL events presented here.

Figure 2.1 illustrates how we can evaluate information obtained from different sources. The first major division separates earthquakes with or without reported landslides. Depending on this division, we have defined five types of data sources ranging from Type-1 to Type-5.

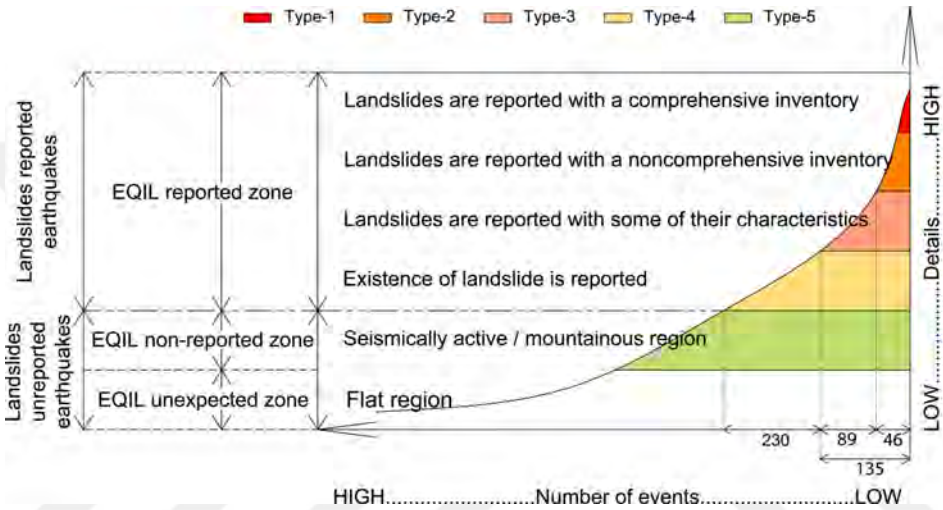

Figure 2.1. Schematic graph showing the different types of EQIL data sources. The numbers in the lower right corner refer to the number of EQIL events of each data type currently available to our knowledge.

Landslide inventory maps are the most useful EQIL data source. Ideally they contain records on the location, date of occurrence, and attribute information such as age, depth of failure, degree and style of activity, and landslide type for each mapped landslide (Guzzetti *et al.*, 2000; Guzzetti *et al.*, 2012; Hansen, 1984a; McCalpin, 1984; Pašek, 1975; Wieczorek, 1984). However, to our knowledge, no EQIL inventory satisfies all these ideal conditions. In reality, ancillary information such as landslide size and (or) type can be presented at best in high-detail EQIL inventories. In this study, we have named these high-detail inventories data source Type-1 (Figure 2.1). However, such inventories are compiled for few earthquakes that trigger landslides, and we observe that many of the available inventories lack the relevant attribute information. We have named these low-detail inventories data source Type-2 (Figure 2.1).

In this study, we have collected either the digital or hardcopy versions of the inventories after contacting the authors or organizations producing the inventories. We have converted the hardcopy inventory maps to shapefiles that can be used in a GIS. As a result of these efforts, we were able to collect EQIL digital inventory maps for 46 earthquakes (Figure 2.1 and Table 2.1). For some earthquakes, multiple inventories are available from different sources; therefore, we have 64 digital EQIL inventories that can be classified as

either Type 1 or 2 data. More EQIL inventories have been produced, but the originators of these data either did not respond, declined to share their inventories, or we did not know about them.

In several cases, the publications describing EQIL do not contain actual inventory maps, and only the general characteristics of the landslide distribution are given (Type-3 inventories). For example, Keefer (1984) used 40 EQIL inventories in his study. Although this is one of the few global-scale EQIL studies, only a limited number of inventory maps referred to in this study are accessible today. D.K. Keefer [written commun(s), 2016] indicated that EQIL inventory maps were only available for a few of the 40 reported earthquakes, and the general relations and conclusions reported were pieced together from various resources, listed in Keefer and Tannaci (1981). Information from the general characteristics of these events can still be significant, and thus we add the Type-3 events to our database. Because EQIL characteristics cannot be directly verified from an inventory, Type-3 events might introduce more uncertainty and outliers into the observations, and thus these data should be used with care. We carried out an extensive literature review of EQIL events and were able to find an additional 89 earthquakes having at least one reported EQIL inventory (Type-3 in Figure 2.1). We have extracted some landslide characteristics for these events, such as the approximate landslide-affected area, the total number of landslides, and the maximum landslide distance to the epicenter and rupture zone. Additionally, we listed fault types, earthquake magnitude, and focal depth for these events. The complete list is presented in Table S2.1 in the Appendix.

In addition to the above-mentioned EQIL data types, for some earthquakes we only know of the existence of triggered landslides without any other information. For these events, we do not have reliable qualitative, quantitative, or spatial information on the triggered landslides. We have named this data source Type-4 (Figure 2.1). Marano *et al.* (2010) compiled such events in their study; they used the catalogue of the U.S. Geological Survey's Prompt Assessment of Global Earthquakes for Response (PAGER) system, PAGERCAT (Allen *et al.*, 2009). This database was compiled from news reports and official sources available at the time of publishing. Based on this catalogue, 276 earthquakes from 1968 to 2008 had confirmed EQIL occurrences, of which 51 overlap with events classified as Type-3, Type-2, or Type-1. Therefore, the database from Marano *et al.* (2010) contributes 225 additional landslide-triggering earthquakes (Figure 2.2), giving a total of 363 reported EQIL events.

It is also useful to collect data on null events (earthquakes in mountainous environments that did not trigger landslides) in order to understand the causes and mechanisms of EQIL. If no landslides are reported for a particular earthquake, it may be that the earthquake did not cause any landslides, or that it did but the landslides were not documented. We classify these as Type-5 (Figure 2.1). However, no official recording procedure exists for earthquakes that do not trigger landslides. Therefore, identifying null events with certainty is not possible.

Table 2.1. List of the digitally available EQIL inventories (as of September 2016). Inventories having the same number (e.g. 6a and 6b) relate to the same earthquake

ID	Location	Date / Time	Epicenter Location	Data type	Magnitude	Depth (km)	Number of landslides	Total landslide area (km^2)	Fault type	Reference study
1	San Fernando, California (USA)*	1971-02-09 / 14:00:41 UTC	34.416°N 118.370°W	Pt	6.6 (Mw)	8.9	391	N/A	S	Morton, 1971
2	Guatemala	1976-02-04 / 09:01:43 UTC	15.324°N 89.101°W	Plg	7.5 (Mw)	5.0	6224	60.8	S	Harp et al., 1981
3	Friuli (Italy)	1976-05-06 / 20:00:11 UTC	46.356°N 13.275°E	Plg/Pt	6.5 (Ms)	9.0	1007	1.1	T	Govi, 1977
4	Izu Oshima Kinkai (Japan)	1978-01-14 / 03:24:39 UTC	34.809°N 139.259°E	Plg	6.6 (Ms)	14.0	659	1.5	S	Suziki, 1979
5	Mount Diablo, California (USA)	1980-01-24 / 19:00:09 UTC	37.852°N 121.815°W	Pt	5.8 (Mw)	11.0	105	N/A	S	Wilson et al., 1985
6	Mammoth Lakes, Calif. (USA)*	1980-05-25 / 19:44:50 UTC	37.696°N 118.750°W	Plg	6.5 (ML)	6.0	4027	33.8	ND	Harp et al., 1984
7	Coalinga, California (USA)	1983-05-02 / 23:42:37 UTC	36.240°N 120.300°W	Plg	6.7 (ML)	9.6	3980	4.8	T	Harp and Keefer, 1990
8	San Salvador (El Salvador)	1986-10-10 / 17:49:24 UTC	13.827°N 89.118°W	Pt	5.7 (Mw)	7.0	268	N/A	S	Rymer, 1987
9a	Loma Prieta, California (USA)	1989-10-18 / 00:04:15 UTC	37.036°N 121.880°W	Pt	6.9 (Mh)	17.2	1775	N/A	T	Keefer and Manson, 1998
9b	Loma Prieta, California (USA)			Plg			138	0.4	T	McCrink, 2001
10	Limon (Costa Rica)	1991-04-22 / 21:56:51 UTC	9.685°N 83.073°W	Plg	7.6 (Mw)	10.0	1643	8.2	T	Marc et al., 2016
11	Finisterre Mt./ (Papua N. G.)*	1993-10-13 / 02:06:00 UTC	5.889°S 146.020°E	Plg	6.9 (Mw)	25.3	4790	69.0	T	Meunier et al., 2008
12	Northridge, California (USA)	1994-01-17 / 12:30:55 UTC	34.213°N 118.537°W	Plg	6.7 (Mw)	18.2	11111	23.8	T	Harp and Jibson, 1995
13	Hyogo-ken Nanbu (Japan)	1995-01-16 / 20:46:52 UTC	34.583°N 135.018°E	Plg	6.9 (Mw)	21.9	2353	0.5	S	Uchida et al., 2004
14a	Umbria-Marche (Italy)*	1997-09-26 / 09:40:26 UTC	43.084°N 12.812°E	Pt	6.0 (Mw)	10.0	233	N/A	N	Esposito et al., 2000; Antonini et al., 2002
14b	Umbria-Marche (Italy)*			Plg			210	1.9		Marzorati et al., 2002
15	Jueili (Taiwan)	1998-07-17 / 04:51:14 UTC	23.407°N 120.736°E	Plg	5.7 (Mw)	12.6	847	4.8	T	Huang and Lee, 1999
16	Chi-chi (Taiwan)	1999-09-20 / 17:47:18 UTC	23.772°N 120.982°E	Plg	7.7 (Mw)	33.0	9272	127.5	T	Liao and Lee, 2000
17	Santa Tecla (El Salvador)	2001-01-13 / 17:33:32 UTC	13.049°N 88.660°W	Pt	7.7 (Mw)	60.0	139	N/A	N	Ministerio de Medio Ambiente y Recursos Naturales, El Salvador, 2001
18	Santa Tecla (El Salvador)	2001-02-13 / 14:22:05 UTC	13.671°N 88.938°W	Pt	6.6 (Mw)	10.0	62	N/A	S	
19	Avaj (Iran)	2002-06-22 / 02:58:21 UTC	35.626°N 49.047°E	Pt	6.5 (Mw)	10.0	50	N/A	T	Mahdavifar et al., 2006
20	Denali Alaska (USA)	2002-11-03 / 22:12:41 UTC	63.517°N 147.444°W	Plg	7.9 (Mw)	4.9	1579	121.2	S	Gorum et al., 2014
21	Lefkada Ionian Islands (Greece)	2003-08-14 / 05:14:54 UTC	39.160°N 20.605°E	Plg	6.3 (Mw)	10.0	274	2.9	S	Papathanassiou et al., 2013

Table 2.1. (Continued)

ID	Location	Date / Time	Epicenter Location	Data type	Magnitude	Depth (km)	Number of landslides	Total landslide area (km^2)	Fault type	Reference study
22a	Mid-Niigata (Japan)*	2004-10-23 / 08:56:00 UTC	37.226°N 138.779°E	Plg	6.6 (Mw)	16.0	10516	14.4	T	GSI of Japan, 2005
22b	Mid-Niigata (Japan)*			Plg			4615	12.6		Sekiguchi and Sato, 2006
22c	Mid-Niigata (Japan)*			Plg			3922	8.1		Yagi et al., 2007
23a	Kashmir (India-Pakistan)	2005-10-08 / 03:50:40 UTC	34.539°N 73.588°E	Plg	7.6 (Mw)	26.0	2424	10.4	T	Sato et al., 2007
23b	Kashmir (India-Pakistan)			Plg			1461	49.9		Basharat et al., 2014
23c	Kashmir (India-Pakistan)			Plg			2930	109.4		Basharat et al., 2016
24	Kiholo Bay (Hawaii)	2006-10-15 / 17:07:49 UTC	19.878°N 155.935°	Plg	6.7 (Mw)	38.9	383	2.8	N	Harp et al., 2014
25a	Aysen Fjord (Chile)*	2007-04-21 / 17:53:46 UTC	45.243°S 72.648°W	Plg	6.2 (Mw)	36.7	540	17.2	S	Sepúlveda et al., 2010
25b	Aysen Fjord (Chile)*			Plg			517	13.2	S	Gorum et al., 2014
26a	Niigata Chuetsu-Oki (Japan)	2007-07-16 / 01:13:22 UTC	37.535°N 138.446°E	Plg	6.6 (Mw)	12.0	312	0.4	T	Kokusai Kogyo, 2007
26b	Niigata Chuetsu-Oki (Japan)			Pt			70	N/A		Collins et al., 2012
27	Pisco / (Peru)	2007-08-15 / 23:40:57 UTC	13.386°S 76.603°W	Plg	8.0 (Mw)	39.0	271	1.1	T	Lacroix et al., 2013
28a	Wenchuan (China)	2008-05-12 / 06:28:01 UTC	31.002°N 103.322°E	Pt	7.9 (Mw)	19.0	13114	N/A	T	Qi et al., 2010
28b	Wenchuan (China)			Plg			59108	812.2		Dai et al., 2011
28c	Wenchuan (China)			Pt			60109	N/A		Gorum et al., 2011
28d	Wenchuan (China)			Plg			197481	1159.9		Xu et al., 2014b
28e	Wenchuan (China)			Plg			69605	530.3		Li et al., 2014
28f	Wenchuan (China)			Plg			6727	54.6		Tang et al., 2016
29	Iwate-Miyagi Nairiku (Japan)	2008-06-13 / 23:43:45 UTC	39.030°N 140.881°E	Plg	6.9 (Mw)	7.8	4211	14.4	T	Yagi et al., 2009
30a	L'Aquila/Abruzzo (Italy)*	2009-04-06 / 01:32:39 UTC	42.334°N 13.334°E	Pt	6.3 (Mw)	8.8	570	N/A	N	Guzzetti et al., 2009
30b	L'Aquila/Abruzzo (Italy)*			Pt			89	N/A		Piacentini et al. 2013
31	Sumatra (Indonesia)	2009-09-30 / 10:16:09 UTC	0.720°S 99.867°E	Pt	7.6 (Mw)	81.0	87	N/A	T	Umar et al., 2014

Table 2.1. (Continued)

ID	Location	Date / Time	Epicenter Location	Data type	Magnitude	Depth (km)	Number of landslides	Total landslide area (km2)	Fault type	Reference study
32a	Haiti	2010-01-12 / 21:53:10 UTC	18.443°N 72.571°W	Plg	7.0 (Mw)	13.0	4490	7.98	S	Gorum et al., 2013
32b	Haiti			Plg			23567	24.85		Harp et al., 2016
33	Sierra Cucapah (Mexico)	2010-04-04 / 22:40:42 UTC	32.286°N 115.295°	Plg	7.2 (Mw)	10.0	453	0.7	S	Barlow et al., 2014
34	Yushu (China)	2010-04-13 / 23:49:38 UTC	33.165°N 96.548°E	Plg	6.9 (Mw)	17.0	2036	1.2	S	Xu et al., 2013
35	Eastern Honshu (Japan)	2011-03-11 / 05:46:24 UTC	38.297°N 142.373°E	Plg	9.1 (Mw)	29.0	3475	4.35	T	Wartman et al., 2013
36	Lorca (Spain)	2011-05-11 / 16:47:25 UTC	37.699°N 1.672°W	Pt	5.1 (Mw)	1.0	270	N/A	S	Alfaro et al., 2012
37	Sikkim (India)	2011-09-18 / 12:40:51 UTC	27.730°N 88.155°E	Pt	6.9 (Mw)	50.0	164	N/A	S	Chakraborty et al., 2011
38a	Lushan (China)	2013-04-20 / 00:02:47 UTC	30.308°N 102.888°E	Plg	6.6 (Mw)	14.0	1289	5.2	T	Li et al., 2013
38b	Lushan (China)			Pt			15546	18.5		Xu et al., 2015
39	Minxian-Zhangxian (China)	2013-07-21 / 23:45:56 UTC	34.512°N 104.262°E	Plg	5.9 (Mw)	8.0	2330	0.8	T	Xu et al., 2014a
40	Cook Straight (New Zealand)	2013-07-21 / 05:09:31 UTC	41.704°S 174.337°E	Pt	6.5 (Mw)	17.0	35	N/A	S	Van Dissen et al., 2013
41	Lake Grassmere (New Zealand)	2013-08-16 / 02:31:05 UTC	41.734°S 174.152°E	Pt	6.5 (Mw)	8.2	501	N/A	S	Van Dissen et al., 2013
42	Eketahuna (New Zealand)	2014-01-20 / 02:52:44 UTC	40.660°S 175.814°E	Pt	6.1 (Mw)	28.0	176	N/A	N	Rosser et al., 2014
43	Ludian (China)	2014-08-03 / 08:30:13 UTC	27.189°N 103.409°E	Plg	6.2 (Mw)	12.0	1024	5.2	S	Ying-ying et al., 2015
44	Wilberforce (New Zealand)	2015-01-05 / 17:48:42 UTC	43.055°S 171.236°E	Pt	5.6 (Mw)	8.1	265	N/A	S	GNS Science, 2015
45a	Gorkha (Nepal)	2015-04-25 06:11:25 UTC	28.231°N 84.731°E	Pt	7.8 (Mw)	8.2	4312	N/A	T	Kargel et al., 2016
45b	Gorkha (Nepal)*			Plg			2654	15.6		Zhang et al., 2016
45c	Gorkha (Nepal)			Plg			2513	14.2		Tanyas, et al., 2018
45d	Gorkha (Nepal)			Plg			24903	86.5		Roback et al., 2017
46a	Kumamoto (Japan)	2016-04-15 / 16:25:06 UTC	32.791°N 130.754°E	Plg	7.0 (Mw)	10.0	336	1.8	S	DSPR-KU, 2016
46b	Kumamoto (Japan)			Plg			2742	8.2		NIED, 2016

*Landslides that can be attributed to more than one earthquake (Mw: Moment magnitude; Ms: Surface-wave magnitude; ML: Local magnitude; Plg: Polygon; Pt: Point; S: Strike-slip fault; T: Thrust fault; N: Normal fault; NDC: Non-Double-Couple earthquake).

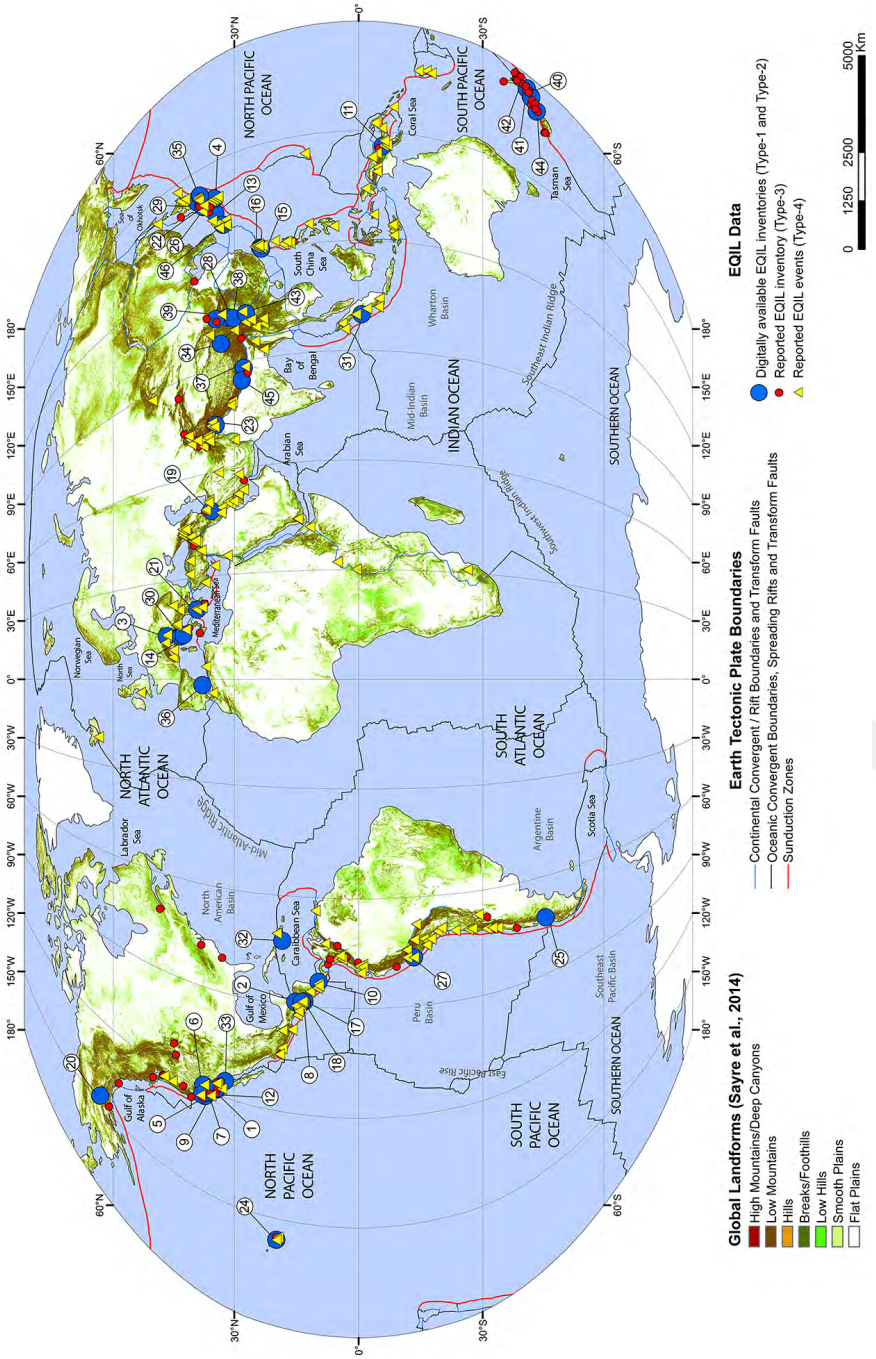

Figure 2.2. Location of EQIL reported events (with and without inventories; digitally available EQIL inventories are marked with same IDs listed in Table 2.1).

2.3. Analysis of EQIL Characteristics

In what follows, we review the characteristics of the EQIL events presented in this database, discussing general aspects of each inventory; important characteristics to consider before utilizing these data are discussed, including specific features of EQIL inventories of Type-1 and Type-2.

2.3.1. Analysis of reported EQIL events

Although our database of 363 reported EQIL events includes events as early as the 1840s, more than 85% of the known events were documented after 1975 (Figure 2.3a). Since that time, innovations in data-acquisition systems and remote sensing techniques have led to a sharp increase in the quantity of reported EQIL events and digitally available inventories. Because the data provided from the PAGER system only covers 1968-2008, and we divide the data into 10-year intervals, an artificial decrease is shown in the number of reported events occurring after 2005 (Figure 2.3a). Work is ongoing to continue the PAGER-related work for the period from 2008 until present.

Overall, only 10% of reported EQIL events have available digital inventories. About 90% of the reported EQIL events are from America, Oceania, and Asia. Only a few inventories are available for Europe, and none exist for Africa (Figure 2.3b and Table 2.2). About half of the inventories come from the USA, Japan, New Zealand, China, Iran, Taiwan, and Indonesia (Figure 2.3c and Table 2.2). For both Iran and Indonesia, only one digital inventory is available, although almost 20 EQIL events were reported for each.

From a morphological point of view, about 80% of all reported events and inventories belong to major mountain belts (Figure 2.3d and Table 2.2), such as the Andes, Himalayas, Sierra Madre, Japanese Alps, U.S. Coast Range, New Zealand Southern Alps, and Zagros Mountains.

2.3.2. Analysis of reported EQIL characteristics

Here, we examined the relation between documented characteristic features of Type-1, Type-2, and Type-3 EQIL events (Figure 2.1) and four parameters that are reported for the majority of the events (Table S2.1 – Appendix): the approximate area affected by landslides, the total number of landslides, the maximum distance from the fault-rupture zone, and the epicentral distance. To calculate the approximate area affected by landslides, we defined a polygon including the all landslides for the analyzed inventory and calculate the area of that polygon. For the maximum distance measures, we took the farthest landslide and calculated its perpendicular distance to the fault-rupture zone and earthquake epicenter. To identify the fault-rupture zone, we used the fault trace if there is no surface rupture. For Type-1 and Type-2 events, we obtained the available fault plane/surface rupture and epicenter location from the literature.

Figure 2.4 shows the frequency distribution of the EQIL events for these parameters, without taking into account different levels of completeness. However, the level of completeness influences the total area affected by landslides and the total number of landslides in a given inventory, so these numbers should be considered minimum values in most cases.

Although there is significant variability, more than 80% of the EQIL events affected areas (area containing all mapped landslides) less than 10,000 km^2; the maximum value is 120,000 km^2 for the Wenchuan event (Figure 2.4a). Likewise, for about 80% of the inventories, the total number of landslides is less than 4,000; however, about 200,000 landslides (Figure 2.4b) were triggered in the 2008 Wenchuan event (Xu *et al.*, 2014b). Additionally, for about 80% of the inventories, maximum distances to epicenter and fault-rupture zone are less than 150 km (Figure 2.4c) and 100 km (Figure 2.4d), respectively.

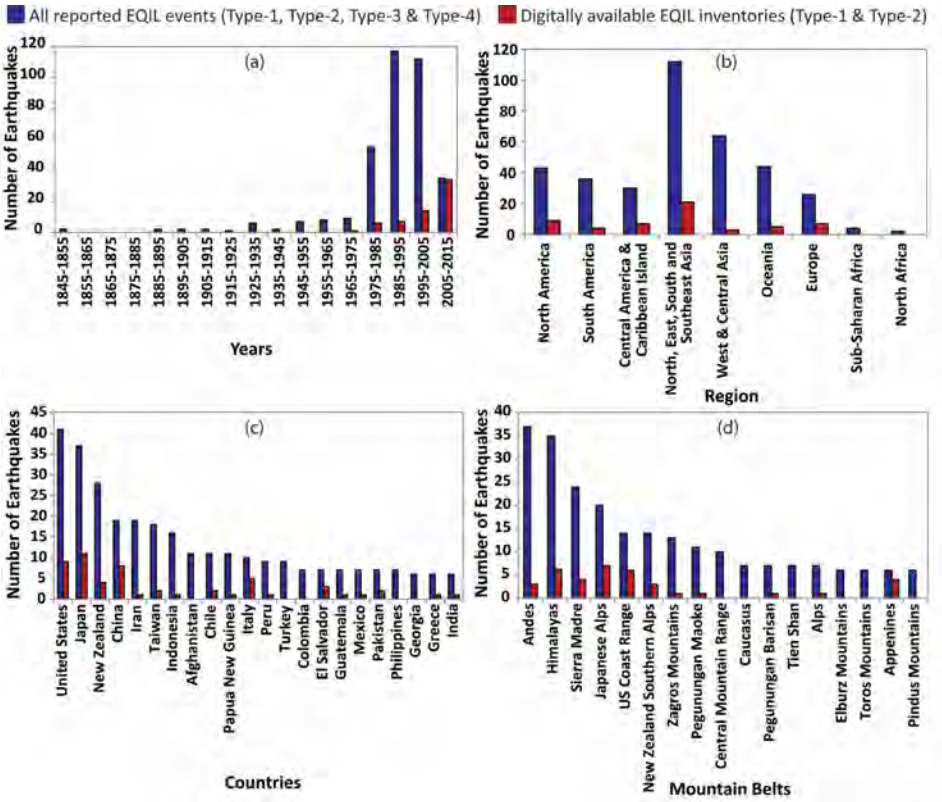

Figure 2.3. Number of reported EQIL events and digitally available EQIL inventories shown by (a) 10-year period, (b) region, (c) country and (d) mountain belt.

Table 2.2. Number of EQIL reported events by country, region, and mountain belt.

Country	# of Inv / # of Eqs*	Region (# of Inv/ # of Eqs*)	Mountain Belt	# of Inv / # of Eqs*
United States	9/42	North America (9/44)	Coast Range	6/15
			Cascade Range	0/5
			Alasaka Range	1/3
Canada	0/2		Appalachian Mountains	0/3
			Sierra Nevada	1/3
			Rocky Mountains	0/2
			Coastal Mountains	0/1
Chile	2/11	South America (3/36)	Andes	3/37
Peru	1/9			
Colombia	0/7			
Ecuador	0/5			
Argentina	0/2			
Bolivia	0/1			
Venezuela	0/1			
El Salvador	3/7	Central America & Caribbean Island (8/30)	Sierra Madre	4/24
Guatemala	1/7			
Mexico	1/7			
Costa Rica	1/5			
Nicaragua	0/1			
Panama	0/1			
Dominican Republic	0/1			
Haiti	2/1			
Japan	11/37	North, East, South and Southeast Asia (29/113)	Himalayas	7/35
China	10/19		Japanese Alps	7/20
			Central Mountain Range	0/10
Taiwan	2/18		Caucasus	0/7
Indonesia	1/16		Pegunungan Barisan	1/7
			Tien Shan	0/7
Philippines	0/7		Xueshan Range	0/5
India	1/6		Cordillera Central	0/4
			Dalou Mts.	3/3
Nepal	4/4		Qinling Mountains	1/3
Russia	0/3		Alishan Range	2/3
			Altay Mountains	0/3
Bangladesh	0/1		Kunlan Shan	0/2
Myanmar	0/1		Sierra Madre	0/1
Iran (Islamic Republic of)	1/19	West & Central Asia (3/64)	Zagros	1/13
Afghanistan	0/11			
Turkey	0/9		Elburz Mountains	0/6
Pakistan	2/7			
Georgia	0/6		Toros Mountains	0/6
Tajikistan	0/5			
Yemen	0/2		Eastern Black Sea Mountains	0/4
Armenia	0/1			
Cyprus	0/1		Tiamat Ash Shan	0/2
Kyrgyzstan	0/1			
Palestine	0/1		Sulaiman Range	0/1
Uzbekistan	0/1			

Table 2.2 (Continued)

Country	# of Inv / # of Eqs*	Region (# of Inv / # of Eqs*)	Mountain Belt	# of Inv / # of Eqs*
New Zealand	4/28	Oceania (5/44)	Southern Alps	3/14
Papua New Guinea	1/11			
Vanuatu	0/3		Central Range (Pegunungan Maoke)	1/11
Guam	0/1			
Solomon Island	0/1			
Italy	6/10	Europe (8/26)	Alps	1/7
Greece	1/6			
Slovenia	0/2		Appenines	4/6
Bosnia and Herzegovina	0/1		Pindus Mountains	0/6
Croatia	0/1			
France	0/1		Dinaric Alps	0/3
Iceland	0/1		Carpathian	0/1
Romania	0/1			
Serbia	0/1		Cambrian Mountains	0/1
Spain	1/1		Vatnajökull	0/1
United Kingdom	0/1			
Sudan	0/1	Sub-Saharan Africa (0/4)	Kenyan Highlands	0/2
Djibouti	0/1		Drakensberg	0/1
South Africa	0/1		Ethiopian Highlands	0/1
Uganda	0/1			
Algeria	0/1	North Africa (0/2)	Atlas Mountains	0/2
Morocco	0/1			

* Number of digitally available EQIL inventories / Number of reported EQIL events

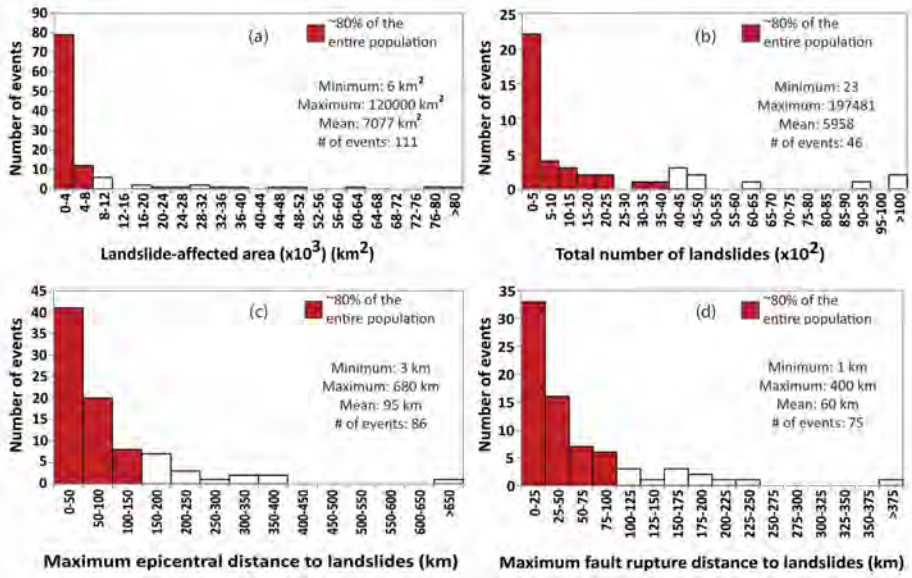

Figure 2.4. Frequency values and basic statistics for (a) the landslide-affected area, (b) the total number of landslides, (c) the maximum epicentral distance to landslides, and (d) the maximum fault-rupture distance to landslides. Red bars show the range of values for 80% of the total number of EQIL events in the database for which information was available. Since many inventories are not complete, in most cases, these refer to minimum values.

2.3.3. Analysis of digital EQIL inventories

Type-1 and Type-2 data provide a means for detailed EQIL characterization. These data sources include 66 EQIL inventories from 46 earthquakes and each has a varying level of quality and completeness. Landslides were delineated as polygon vector data for 44 of the available digital EQIL inventories; the other 22 were represented as points. To compare both types of inventories during this evaluation, we reduced each polygon to a single point by assigning a point at the highest elevation of each landslide polygon (as a proxy for the initial source point of the landslide). By doing so, we have 554,333 landslide-initiation points in this database; this landslide population is dominated by the Wenchuan earthquake because 406,144 of the landslides belong to six inventories for this event, which were made by five independent groups. The inventory of Xu *et al.* (2014b) can be considered as an updated version of the Dai *et al.* (2011) inventory. Even this single Wenchuan inventory (Xu *et al.*, 2014b) contains approximately 76,000 more landslides than the total of all other inventories. The Wenchuan event was an extraordinary EQIL event where a large magnitude earthquake occurred along the steepest boundary of the Tibetan Plateau (Fielding, 1996; Liu-Zeng *et al.*, 2011). The anomalously large number of landslides triggered by this event dominates the observations coming from different inventories. Joint evaluation of Wenchuan and other inventories can bias hazard upwards. Therefore, we decided to evaluate these five Wenchuan inventories separately, excluding the Dai *et al.* (2011) inventory to avoid duplications.

The landslide points were analyzed first in terms of topographic factors including slope, local relief, distance to streams and vector ruggedness measure (VRM). VRM is a terrain ruggedness measure that quantifies local variation in terrain more independently of slope than other methods such as land surface ruggedness index or terrain ruggedness index (Sappington *et al.*, 2007). It is derived by incorporating the heterogeneity of both slope and aspect. The Shuttle Radar Topography Mission digital elevation model (about 30 meters resolution) (NASA Jet Propulsion Laboratory, 2013) was used in the analyses. Frequency distributions for these parameters show that the highest landslide frequencies are concentrated in particular intervals for all of these parameters (Figure 2.5). Landslides related to the Wenchuan inventories show different distributions and mean values. When we look at the entire dataset (excluding Wenchuan inventories), the mean values for slope, VRM, local relief and the distance to streams are 27° (Figure 2.5a), 0.035 (Figure 2.5b), 524 m (Figure 2.5c) and 413 m (Figure 2.5d), respectively. However, for the Wenchuan inventories, the mean values for the same parameters are 35° (Figure 2.5e), 0.09 (Figure 2.5f), 916 m (Figure 2.5g), and 468 m (Figure 2.5h). Therefore, as explained earlier, we can have a better understanding of the general characteristics of EQIL if we exclude the Wenchuan event. By excluding Wenchuan, we can conclude that about 80% of the remaining population of EQIL occurs within the interval of 10-45° (Figure 2.5a), 0-0.05 (Figure 2.5b), 200-800 m (Figure 2.5c) and 0-700 m (Figure 2.5d) for slope, VRM, local relief, and distance to stream, respectively.

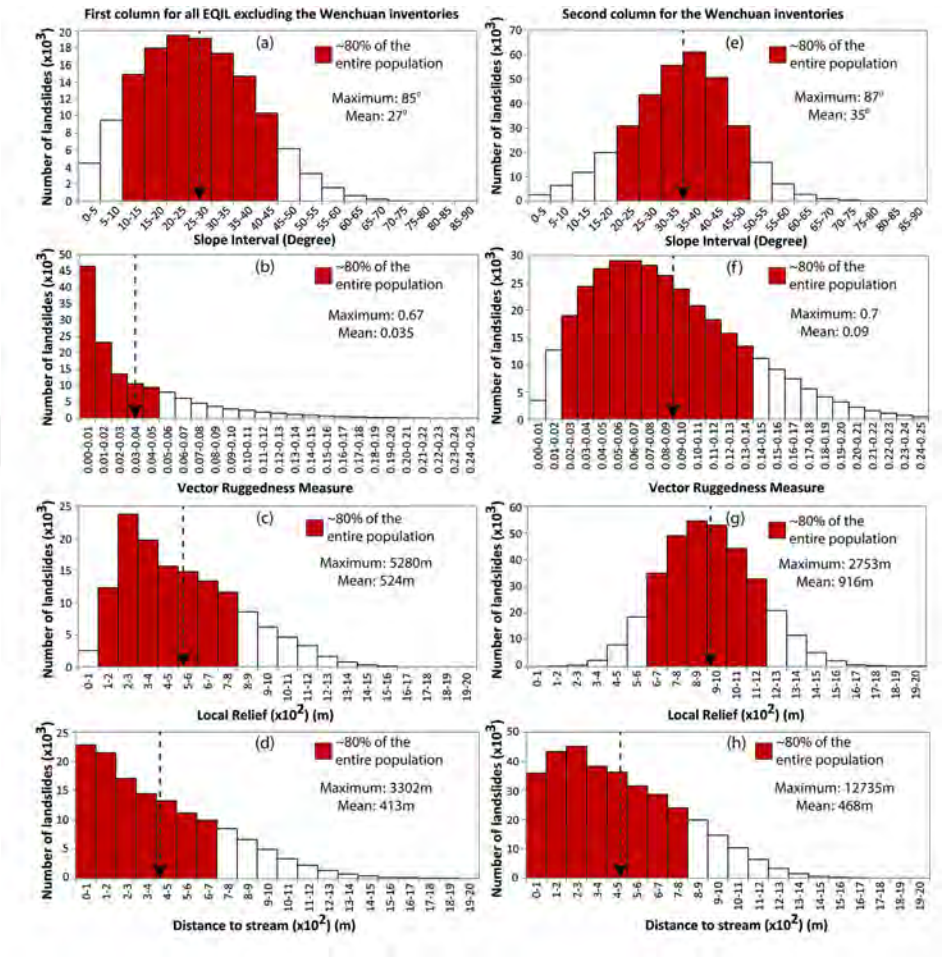

Figure 2.5. Frequency values of earthquake-induced landslides in intervals of (a) slope, (b) vector ruggedness measure (VRM), (c) local relief, and (d) distance to stream for all EQIL excluding the Wenchuan inventories (in first column), and for the Wenchuan inventories separately (e-h) (in second column). The arrows point out the mean values.

We investigated ground-shaking parameters in a similar manner. Estimated values of peak ground acceleration (PGA), peak ground velocity (PGV) and Modified Mercalli Intensity (MMI) were obtained at the location of each landslide from the U.S. Geological Survey (USGS) ShakeMap Atlas 2.0 (Garcia *et al.*, 2012). As in the previous analysis, we discussed the Wenchuan inventories separately (Figure 2.6).

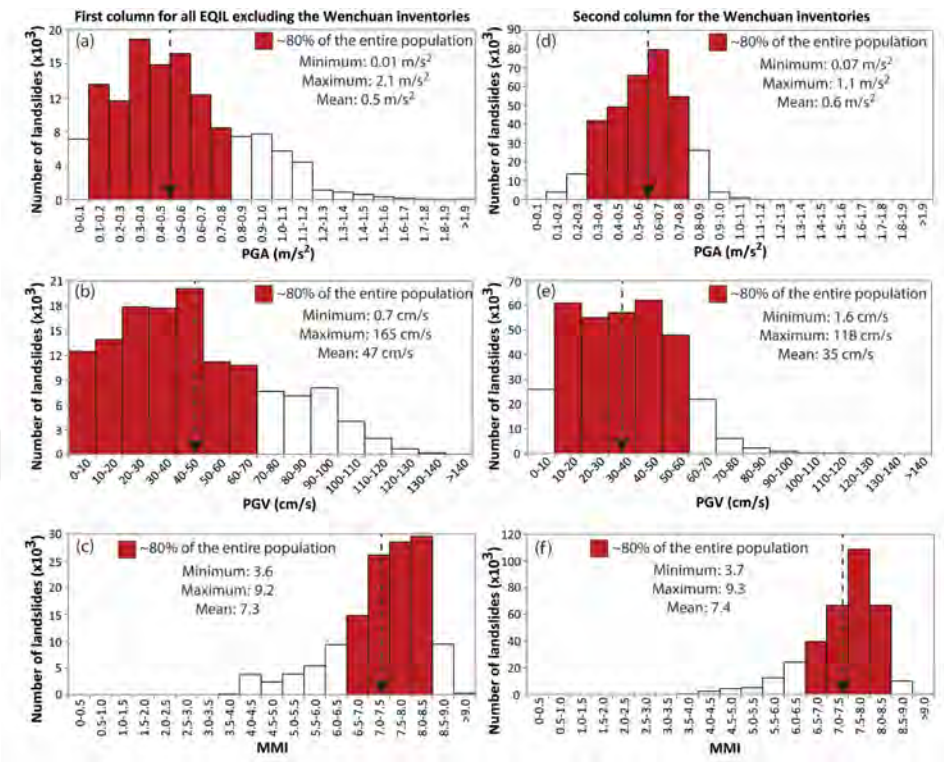

Figure 2.6. Frequency values of earthquake-induced landslides in intervals of (a) PGA, (b) PGV and (c) MMI for all EQIL excluding the Wenchuan inventories (in first column) and for the Wenchuan inventories separately (d-f) (in second column). The arrows point out the mean values.

Contrary to what was found for the topographic parameters, the distributions and mean values for the seismic parameters are quite similar for the Wenchuan inventories and all others. For the inventories excluding Wenchuan, the mean PGA, PGV and MMI values are 0.5 m/s2 (Figure 2.6a), 47 cm/s (Figure 2.6b) and 7.3 (Figure 2.6c), and those for the three Wenchuan inventories are 0.6 m/s2 (Figure 2.6d), 35 cm/s (Figure 2.6e) and 7.4 (Figure 2.6f). For the entire database excluding the Wenchuan event, approximately 80% of the population of EQIL are observed in the interval for PGA of 0.1-0.8 m/s2 (Figure 2.6a), for PGV of 0-70 cm/s (Figure 2.6b), and for MMI between 6.5 and 7.0 (Figure 2.6c).

We also analyzed the landslide-size distributions for the collected polygon-based landslide inventories in our database. Multiple studies have shown that the frequency-area distribution (FAD) of medium and large landslides follows a power-law (e.g. Guzzetti *et al.*, 2002; Malamud *et al.*, 2004) with a characteristic power-law exponent. For most landslide inventories, noncumulative power-law exponents occur in the range of 1.4–3.4, with a central tendency of 2.3–2.5 (Stark and Guzzetti, 2009a; Van Den Eeckhaut *et al.*, 2007). We calculated the power-law exponents for 43 inventories in our database based on the method proposed by Clauset *et al.* (2009), and analyzed the number of inventories for the obtained power-law exponent intervals (Figure 2.7a). The results showed that the mean

exponent value is 2.5, consistent with findings cited above. Due to the high population of medium-sized landslides, the two polygon-based Wenchuan inventories (Li *et al.*, 2014a; Xu *et al.*, 2014b) yield the highest power-law exponent values, which are 3.1 and 3.2. This could be caused by a large number of amalgamated smaller landslides that increase the frequency of medium-sized landslides. We also visually analyzed the range of landslide sizes in the EQIL inventories by combining all landslide polygon areas from the inventories (separating the Wenchuan inventories from the others) and plotting the FADs (Figure 2.7b). Similar to the FADs of the individual EQIL inventories, FADs of the combined inventories follow the power-law distribution, with power-law exponent of 3.3 for the Wenchuan inventories and 2.3 for the combination of all other inventories, which included 43 inventories provided by different groups using different mapping techniques (Figure 2.7b). Mapped landslides range from a few square meters to a few million square meters in area. The smaller landslides constitute the majority of the database. For the Wenchuan inventories, 80% of all landslides are smaller than 8000 m^2, whereas, for the other inventories, 80% of the landslides are smaller than 4000 m^2. The roll-over point (most commonly mapped landslide size) is about 1000 m^2 for the Wenchuan inventories, but only around 100 m^2 for the combined FAD of the other inventories. Also, the roll-over in the Wenchuan inventories is relatively sharper in comparison with the combined FAD of the other inventories. These differences are possibly caused by the mapping procedure of landslides; so many landslides were triggered by Wenchuan earthquake, that it was not practical to map the small ones completely.

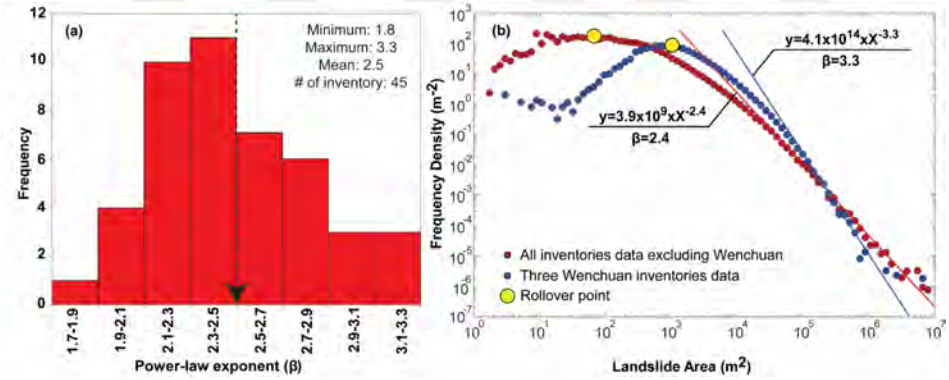

Figure 2.7. (a) Frequencies for estimated power-law exponents for the EQIL inventories and (b) the frequency-density distributions for the landslides gathered from all inventories excluding the Wenchuan event (red) and the landslides gathered from the two Wenchuan inventories (blue). The arrow points out the mean value.

2.4. Evaluation of EQIL inventories

A limited number of digital EQIL inventories are available worldwide, and the available ones differ greatly in quality, completeness, and representation. Therefore, establishing guidelines and adequate metadata for future inventories is essential (Wasowski *et al.*, 2011).

Several studies analyzed the quality and completeness of landslide inventories using a number of criteria (Gorum, 2013; Harp *et al.*, 2011; Keefer, 2002; Wasowski *et al.*, 2011). Harp *et al.* (2011) defined three basic criteria for evaluating inventories: (1) coverage of the entire area affected by landslides, (2) inclusion of all landslides down to a small enough scale, and (3) depiction of landslides as polygons rather than points. They listed 10 inventories that satisfied these criteria and thus can be considered comprehensive: 1976 Guatemala (M=7.5) (Harp *et al.*, 1981), 1978 Izu Oshima KinKai (M=6.6) (Suziki, 1979), 1980 Mammoth Lakes (M=6.5) (Harp *et al.*, 1984), 1983 Coalinga (M=6.3) (Harp and Keefer, 1990), 1993 Hakkaido Nansei-oki (M=7.8) (Tanaka, 1994), 1994 Northridge (M=6.7) (Harp and Jibson, 1995), 1995 Hyogoken Nanbu (M=6.9) (Nishida *et al.*, 1996), 1999 Chi-Chi (M=7.7) (Liao and Lee, 2000), 2004 Mid Niigata (M=6.6) and 2008 (GSI, 2005; Sekiguchi and Sato, 2006; Yagi *et al.*, 2007), and 2008 Iwate-Miyagi-Nairiku (M=6.9) (Yagi *et al.*, 2009) earthquakes.

We have only eight of these inventories (Guatemala, Izu Oshima KinKai, Mammoth Lakes, Coalinga, Northridge, Chi-Chi, Mid Niigata and Iwate-Miyagi-Nairiku) reported by Harp *et al.* (2011). Therefore, the majority of the EQIL inventories do not meet these criteria. For a robust statistical analysis, however, we need to maximize the number of inventories used. This creates a trade-off between quality and completeness. The 2007 Niigata Chuetsu-Oki (Japan) event is a good example to illustrate this. Three inventories are available for this event. The first inventory (Collins *et al.*, 2012) used a combination of field observations and analysis of oblique aerial photos for a relatively small area. During the detailed field investigation, pre-earthquake landslides were eliminated, and 70 EQIL were mapped as point data. The second study (Kokusai Kogyo, 2007) was carried out using only 1/6,000 aerial photo interpretation covering about 400 km^2 in area and resulted in 312 landslides mapped as polygons. In the third inventory (Sato *et al.*, 2008), 1/10,000 aerial photos covering about 260 km^2 in area were used for image interpretation followed by field verification, which resulted in 172 landslides mapped. These three inventories were prepared following partly the same method but yielded quite different inventory maps, both in representation and in the number of landslides mapped.

A much more striking example is the 2008 Wenchuan (China) EQIL inventories. Xu *et al.* (2014b) compared four inventory maps that they classified as nearly complete and reported significant differences in the number of landslides mapped. In those studies, about 196,000, 59,000, 60,000 and 11,300 landslides were mapped by Xu *et al.* (2014b), Dai *et al.* (2011), Gorum *et al.* (2011), and Huang and Li (2009), respectively. The number of landslides in two inventories called “nearly complete” prepared for the same event differ by a factor of about 17. As a consequence, although all inventories contain valuable information, the use of these in our analysis would yield contrasting results. Therefore, we need a methodology to evaluate the comprehensiveness of inventories to provide a basis for selecting which inventories to include in a given analysis. By combining the evaluation of quality, completeness, and representation, we can picture the comprehensiveness of any inventory.

The quality of any EQIL inventory can be defined based on its accuracy, which is the geographical and thematic correctness of the information shown on the map (Guzzetti *et al.*, 2012).

To evaluate the quality of EQIL inventory, ideally we could address the following questions:

i) Were the landslides mapped at the right location?

ii) Were the landslides mapped using a comprehensive mapping methodology?

iii) Were the landslides mapped by experienced people?

iv) Were the landslides types classified with a consistent classification method (e.g., Keefer, 1984)?

v) Were the results of individual landslide mappers crosschecked by others?

vi) How much total time did producer(s) spend on the landslide inventory map?

vii) Were contiguous landslides mapped separately or as a single landslide?

viii) How long after the earthquake was the inventory completed?

ix) Were problematic areas field checked after creating the inventory?

x) Was the boundary of mapped area indicated?

Completeness measures the extent to which an EQIL inventory includes all co-seismic landslides for a specific earthquake (Guzzetti *et al.*, 2012). To evaluate the completeness of EQIL inventory, we need to address the following questions:

i) Were the landslides mapped for the entire landslide-affected area or only for a part of the area?

ii) Was a minimum size threshold used for mapping landslides?

iii) Were pre- and post-earthquake landslides removed from the inventory?

Evaluating an EQIL inventory based on these criteria is complicated because many of them, especially the quality evaluation criteria, cannot be evaluated. For example, evaluating the landslide interpretation skills of the mapper, the detail of the mapping, and whether coalescing landslides are mapped separately or as a single polygon are difficult to evaluate without going back and examining the original imagery. Therefore, any evaluation regarding the quality and completeness of EQIL inventories has some limitations.

Quality and completeness of an inventory are two different terms that do not have to be met for the same inventory. For instance, a high-quality EQIL inventory can be incomplete if the inventory is provided partially, or a complete inventory can be low quality if landslides are not located, differentiated or classified appropriately. Beyond that, to evaluate the comprehensiveness of the inventory, there is another component: representation.

The methods of evaluating how well an inventory represents reality will be different depending on the representation type. For a point-based inventory, under ideal conditions, the point should be assigned to a consistent and clearly defined part of the landslide, ideally the scarp. Furthermore, we would expect to have the type and size of landslides in the attribute table. For a polygon-based inventory, we would expect to have an inventory with different landslide types, and differentiated source and depositional areas.

We have developed an evaluation methodology to provide a basis for selecting which inventories to include in a given analysis. To accomplish this task, we have defined a mixed set of criteria that we can evaluate without having detailed metadata of each inventory. We have used eight criteria (Table 2.3) that are partly derived from earlier studies (Gorum *et al.*, 2011; Harp *et al.*, 2011; Xu, 2014). The criteria defined for the evaluation of EQIL inventories are described in the following sections.

Table 2.3. Evaluation scheme for EQIL inventories, using two sets of criteria, with score.

Category		Criteria	Execution performance	Score
(A)	(B)			
Essential criteria	Essential criteria	i) Was the study area analyzed systematically by visual interpretation?	0-100%	0-1
		ii) Was the boundary of the mapped area indicated?	No/Yes	0/1
		iii) Were the pre- and post-earthquake landslides eliminated from the inventory?	0-100%	0-1
		iv) Was the mapping resolution of inventory enough to differentiate the individual landslides? (L=Linear resolution of roll-over point)	L>25m : <0.5 25m≥L>5m : ≥0.5 5m≥L : 1	0/1
Preferred criteria		v) Were the landslides mapped as polygons?	No/Yes	0/1
		vi) Did landslide polygons differentiate source and depositional areas?	No/Yes	0/1
	Preferred criteria	vii) Were the landslides field checked in problematic areas?	0-100%	0-1
		viii) Were the landslides classified according to type?	No/Yes	0/1

2.4.1. Evaluation Criteria

The methodology used for generating an EQIL inventory is very important for the overall evaluation of the inventory. Guzzetti *et al.* (2012) categorized the different methods used to prepare landslide inventories into four groups: (a) (semi-) automated satellite image classification; (b) observations based on aerial reconnaissance (helicopter flights, fixed-wing aircraft or UAVs (Unmanned Aerial Vehicles); (c) field survey, and (d) visual image interpretation (using satellite images or aerial photography).

If pre- and post-earthquake images are utilized, (semi-) automated image classification techniques can be the most effective approach, especially because they provide rapid results (e.g. Lacroix *et al.*, 2013; Martha *et al.*, 2010). However, these methods are still not capable of identifying coalescing landslides or landslides that are mostly vegetated, and they cannot classify landslides by type. Moreover, automated techniques are prone to

errors due to misidentification of features such as bare-earth slopes, recent fills, rock quarries, road cuts, and other excavations as landslides.

As another alternative method, aerial reconnaissance, either by fixed-wing aircraft, helicopter, or UAV, might provide detailed information for specific areas but cannot cover the entire affected area. Field mapping of landslides (Brunsden, 1985) allows characterization of landslide features such as type, depth, source, and depositional area, which might not be obtainable by any other methodology. Nevertheless, mapping landslides in the field is hampered by difficulties of landslide detection because it is not straightforward to identify the boundary of landslides, especially if they are large (Guzzetti *et al.*, 2012). Moreover, this method is limited by the time and resources available and the accessibility of the area.

Utilization of the multiple approaches to get the most information possible within monetary and time constraints could be the idealized method for EQIL mapping. On the other hand, if you evaluate the methods individually, of all available methods, visual image interpretation leads to the best results, because expert interpreters can omit non-landslide features and can systematically scan the whole affected area as long as cloud-free imagery is available. If high-resolution imagery is available, landslides can be classified by type, and source and depositional areas can be identified. Visual image interpretation can be carried out for the entire landslide-affected area, or for specific sample areas to support and validate other methods such as (semi) automatic image classification.

To analyze the conditions that cause landslide initiation, both the presence and absence of landslides is important information that should be obtained from the inventories. Harp *et al.* (2011) stress the importance of indicating the boundaries of the mapped landslide area. Due to limitations in the available images, resources, time, and cloud cover, mapping of the whole region affected by landslides might not be possible, but as long as the boundary of the mapped area is defined, it can still be valuable information. If the inventories do not indicate the mapping boundaries, but the extent of the utilized satellite imagery or flight lines of aerial surveys are indicated, such boundaries can still be defined. Based on this approach, the availability of a mapping boundary can be evaluated.

Removing landslides that occurred before and after the earthquake is essential to provide an accurate inventory of triggered features. For example, the 2015 Gorkha earthquake in Nepal occurred in a mountainous area that is highly susceptible to rainfall-induced landslides; thus, if the pre-earthquake landslides are not eliminated from the inventory, many landslides not caused by this earthquake could be erroneously related to the seismic triggering event. Therefore, the imagery must be acquired as soon as possible after the earthquake to capture the initial aspects of the landslides and the terrain (Harp *et al.*, 2011). Several approaches can be used to remove pre-earthquake landslides from the inventory, including through information gathered from local people (e.g. Chakraborty *et al.*, 2011), field observations (e.g. Harp and Jibson, 1995; Harp and Keefer, 1990), or the use of pre- and post-event imagery (e.g. Barlow *et al.*, 2014; Papathanassiou *et al.*, 2013; Xu *et al.*, 2014b). The last method is considered the best option.

Harp *et al.* (2011) stated that an ideal inventory should include all detectable landslides down to sizes of 1–5 m in length. However, it is difficult to determine the completeness of the mapping of such small features. The minimum landslide size observed in an inventory

is generally not representative of the resolution of inventories because such small landslides might be mapped only for a limited part of inventories where the imagery is of the highest quality.

Malamud *et al.* (2004) suggest a functional definition of completeness that requires a landslide inventory to include a substantial fraction of all landslides at all scales. In this definition, the roll-over point refers to the most commonly occurring landslide size in the inventory. Parker *et al.* (2015) take the position of roll-over as the minimum size where landslide mapping is complete. Based on this approach, we evaluated the roll-over points of the inventories. If the linear resolution of the roll-over point is less than 5 m, we assumed that the inventory satisfies the ideal conditions in terms of mapping resolution, and if it is higher than 25 m, we assumed that it is far from the ideal conditions. A caveat is that the roll-over position may also be controlled by the mechanical properties of the substrate (Frattini and Crosta, 2013; Stark and Guzzetti, 2009a) and therefore some inventories may not be "incomplete" but only occur in place where the mechanics do not allow small landslides (<5 m) very often.

Since, the roll-over point is not only related to the resolution of utilized imagery but also the mapping technique, this evaluation is not enough to be sure whether the mapped landslides are well delineated or not. Furthermore, except for the producer of the inventory, it is difficult for anyone to evaluate how successfully the individual landslides were mapped. There is a methodology (Marc and Hovius, 2015) proposed for the automatic detection of amalgamated polygons and it works based on geometric and topographic considerations. In this EQIL inventory database, we have five inventories that were corrected based on the referring method by Marc and Hovius (2015): 2007 Aysen Fjord (Gorum *et al.*, 2014), 1999 Chi-chi (Liao and Lee, 2000), 1976 Guatemala (Harp *et al.*, 1981), 1994 Northridge (Harp and Jibson, 1995), and 2008 Wenchuan (Dai *et al.*, 2011) EQIL inventories. However, the methodology provides only a partial correction for amalgamated landslides. Along the same slope, multiple landslides can be triggered and amalgamated. For such cases, the suggested methodology is not capable of detecting amalgamation. Therefore, through the aforementioned mapping resolution evaluation, we can only reach a conclusion about whether the completely mapped minimum landslide size of inventory is enough to differentiate the individual landslides. Beyond this evaluation, any user who works on mobilized landslide masses or frequency-area statistics of landslides should give special attention to amalgamated landslides.

Having landslides mapped as polygons rather than points is important to evaluate the overall area of landslides related to a given earthquake, and to estimate the mobilized total volume of material using empirical relations relating landslide area and volume (e.g. Klar *et al.*, 2011; Larsen *et al.*, 2010). Moreover, the source and depositional areas of landslides can be represented only with a polygon-based inventory. Therefore, it is preferred to delineate landslides as polygons (Harp *et al.*, 2011).

While it is preferable to delineate landslides as polygons, it is even better to separate landslide source and depositional areas into separate polygons (Gorum *et al.*, 2013); landslides mapped this way provide a basic demarcation of landslide processes, and only the conditions in the source area are relevant for the analysis of causal factors. For example, in terms of slope steepness at the landslide source we typically find much steeper slopes than in the depositional area. Also, it is important to separate source and

depositional areas in order to calculate the run-out distance and the total mobilized mass volume triggered by an earthquake. The lack of differentiation of source and depositional parts of landslides is one of the most significant sources of uncertainty in all landslide frequency-size related discussions. Despite the importance of this information, there are only two EQIL inventories (the 2004 Mid-Niigata by GSI of Japan, 2004 and the 2015 Gorkha by Roback *et al.*, 2017) in our database that separated source and deposition areas. On the other hand, estimating source areas from polygon inventories is possible; Jibson *et al.* (2000) mapped landslides as single polygons and then used the upper half of those polygons as the assumed source area.

Field surveying is not generally the optimal method to produce a landslide inventory map because it is time consuming and often impossible to cover the entire affected area. However, it is still necessary for validating any inventory map prepared using other techniques (Guzzetti *et al.*, 2012). With the advances in remote sensing techniques (related to very high-resolution images and UAVs), the emphasis on field surveys has decreased. Field surveying for validation is suggested only for a limited part of the inventory area; generally less than 15% (Galli *et al.*, 2008), or for verifying specific problematic areas that are difficult to identify from satellite imagery (Guzzetti *et al.*, 2012).

Keefer (1984) evaluated EQIL by considering the type of material, landslide movement, degree of internal disruption of the landslide mass, and geologic environment, and classified them into three main types of landslides. Different landslide types have different combinations of causal factors (Crosta *et al.*, 2012). Nevertheless, few EQIL inventories include landslide types (e.g. 1989 Loma Prieta (M=6.9) by Keefer, 2000; 1997 Umbria-Marche (M=6.0) and 2009 Abruzzo by Guzzetti *et al.*, 2009; 2011 Lorca (M=5.1) by Alfaro *et al.*, 2012; 2011 Eastern Honshu (M=9.1) by Wartman *et al.*, 2013).

In addition to the details of EQIL inventories, Table 4 also includes the relative quality grading of each ShakeMap as developed by Wald *et al.* (2008). This grading scale allows users to evaluate the relative uncertainty level of each ShakeMap for post-earthquake or historical earthquake ShakeMap analyses (Wald *et al.*, 2008) . In this grading system, meant primarily for the quick evaluation of near-real-time maps, uncertainty levels of ShakeMaps are presented by letters from "A" to "F", based on high- to poor-quality constraints, respectively. Lower grades are typically assigned to larger (M>6) events for which there are few stations and the fault rupture area is not available. Higher grades are typically given to ShakeMaps with numerous seismic stations and/or intensity observations, and for which the fault dimensions are constrained. For landslide analyses, those ShakeMaps with higher grades can thus be considered more reliable than those with lower grades. However, often the data constraints used to compute these grades are from reported or assigned intensities, and the summary grades do not necessarily address whether or not there were seismic recordings in the areas where landslides occurred. Thus, in principle, since each ShakeMap has spatially varying uncertainty estimates, site-specific uncertainty values should be used to consider the reliability of shaking at landslide sites.

2.4.2. Evaluating EQIL inventories using the criteria

Making an overall evaluation of the inventories using a single score ignores the fact that each of the inventories was created for a different purpose. Furthermore, the available information about inventories is not enough to make an accurate quality or completeness evaluation. Therefore, instead of such an evaluation, we separated the proposed criteria into two groups of essential and preferred criteria (Table 2.3). The essential criteria can be considered as the minimum criteria for any application of the EQIL inventory to work. The preferred criteria can be considered as the criteria we prefer for most EQIL-related applications, but they are not as significant as the essential criteria.

The content of the essential and preferred criteria can show variety based on the scope of the study. For instance, in landslide susceptibility and hazard studies, the mapping unit doesn't have to be represented by a polygon. Similarly, differentiations between the source and depositional areas or landslide types are not necessarily available for every landslide susceptibility or hazard study. In this case, the mentioned criteria can be considered as preferred criteria instead of essential. Likewise, for landslide risk assessments, if authors do not consider the runout behavior of landslides, they do not really need the landslide polygons or source versus depositional area to be differentiated. However, this information might also be required for specific hazard analyses that focus on particular landslide size range or landslide type. On the other hand, if authors focus on landform evaluation caused by EQIL, the mobilized landslide mass volume/area would be important, and in that case source and depositional areas of landslide polygons would be essential. Therefore, we considered several purposes of landslide-inventory applications (Guzzetti *et al.*, 2012), and defined two categories for EQIL inventory-related applications: (1) inventories to make a landslide susceptibility or hazard assessment, or to investigate the distribution, types, and patterns of landslides in relation to morphological and geological characteristics, and (2) inventories to study evolution of landscapes dominated by mass-wasting processes (landslide dynamic and erosion studies). For each category, we defined sets of different essential and preferred criteria (Table 2.3). The user can check these essential criteria to complete an overall evaluation of which inventories are appropriate for their application of the data. Also, they can take a particular set of criteria into account for a specific application and evaluate the available inventories.

Table 2.4 presents the results of applying the criteria described above to each of the EQIL inventories in the database. Each EQIL inventory is evaluated with a score between 0 and 1 for each criterion, some of which are binary (Table 2.3). If the criterion is fully satisfied then the score is one, if the criterion is fully ignored it is zero. Intermediate values between zero and one indicate that the criterion is partially satisfied. To make an overall evaluation on each criterion, if the score is equal or greater than 0.5 for a criterion we assume that the criterion is satisfied.

Some inventories lacked the information needed to determine the score of the individual criteria. If an analyzed criterion is not addressed in the referred study, we assumed that it was not satisfied. For instance, in some cases the specific attribute information, which was mentioned in the referred paper, did not exist in the available digital inventory. In these cases, we evaluated the inventory based on the available data. The evaluation results for

the individual criteria for all EQIL inventories in the database are given in Table 2.4, and scores are given in Table S2.2 in the Appendix.

It is important to note that some EQIL inventories in the database represent landslides triggered by an earthquake sequence rather than a main shock. For example, the 1993 Finisterre Mountains (Papua New Guinea) landslide inventory contains 5000 landslides that were triggered by two earthquakes having magnitudes of Mw 6.7 and 6.9 (Meunier *et al.*, 2008); the inventory does not distinguish which landslides were triggered by which earthquake. Such inventories are indicated in Table 2.1 with an asterisk.

Table 2.4. Summary chart for the evaluation of EQIL inventories and uncertainty of ShakeMaps for the corresponding events.

ID	Inventories	Criteria								Quality of Shakemap (Grade)
		(i)	(ii)	(iii)	(iv)	(v)	(vi)	(vii)	(viii)	
1	San Fernando	✓						✓		A
2	Guatemala	✓	✓	✓	✓	✓		✓		B
3	Friuli	✓	✓			✓			✓	A
4	Izu Oshima Kinkai	✓	✓	✓	✓	✓	✓	✓		C
5	Mount Diablo							✓		A
6	Mammoth Lakes	✓	✓	✓		✓		✓		A
7	Coalinga	✓	✓	✓	✓	✓		✓		A
8	San Salvador	✓		✓				✓		C
9a	Loma Prieta	✓	✓					✓		A
9b	Loma Prieta	✓	✓		✓	✓		✓		
10	Limon	✓	✓	✓		✓				B
11	Finisterre	✓	✓	✓		✓				N/A
12	Northridge	✓	✓	✓	✓	✓		✓		A
13	Hyogo-ken Nanbu	✓	✓	✓	✓	✓		✓		A
14a	Umbria-Marche	✓	✓	✓				✓	✓	A
14b	Umbria-Marche	✓	✓			✓		✓	✓	
15	Jueili	✓	✓	✓		✓				C
16	Chi-chi	✓		✓	✓	✓		✓		A
17	Santa Tecla									B
18	Santa Tecla									A
19	Avaj		✓					✓		A
20	Denali	✓	✓	✓		✓				B
21	Lefkada	✓	✓			✓		✓		A
22a	Mid-Niigata	✓	✓	✓	✓	✓	✓	✓		A
22b	Mid-Niigata	✓	✓	✓	✓	✓	✓	✓	✓	
22c	Mid-Niigata	✓	✓	✓	✓	✓	✓	✓	✓	
23a	Kashmir	✓	✓	✓	✓	✓		✓		A
23b	Kashmir	✓	✓			✓		✓		
23c	Kashmir	✓	✓			✓		✓		

Table 2.4. (Continued)

ID	Inventories	Criteria								Quality of Shakemap (Grade)
		(i)	(ii)	(iii)	(iv)	(v)	(vi)	(vii)	(viii)	
24	Kiholo Bay	✓	✓		✓	✓				A
25a	Aysen Fjord	✓	✓	✓		✓		✓	✓	N/A
25b	Aysen Fjord	✓	✓	✓		✓				
26a	N. Chuetsu-Oki	✓	✓		✓	✓				A
26b	N. Chuetsu-Oki	✓	✓					✓		
27	Pisco	✓	✓	✓				✓		A
28a	Wenchuan	✓	✓					✓		A
28b	Wenchuan	✓	✓			✓		✓		
28c	Wenchuan	✓	✓	✓				✓		
28d	Wenchuan	✓	✓	✓		✓		✓		
28e	Wenchuan	✓	✓	✓		✓				
28f	Wenchuan	✓	✓	✓	✓	✓		✓		
29	Iwate–Miyagi N.	✓	✓	✓	✓	✓		✓	✓	A
30a	L'Aquila/Abruzzo	✓						✓		A
30b	L'Aquila/Abruzzo	✓	✓	✓				✓	✓	
31	Sumatra	✓						✓		C
32a	Haiti	✓	✓	✓	✓	✓				A
32b	Haiti	✓	✓	✓	✓	✓		✓		
33	Sierra Cucapah	✓	✓	✓	✓	✓				A
34	Yushu	✓	✓	✓	✓	✓		✓		C
35	Eastern Honshu	✓	✓	✓	✓	✓		✓	✓	A
36	Lorca	✓						✓	✓	A
37	Sikkim							✓	✓	N/A
38a	Lushan	✓	✓		✓	✓		✓		C
38b	Lushan	✓	✓	✓	✓	✓				
39	Minxian-Zhan.	✓	✓	✓	✓	✓				C
40	Cook Straight	✓						✓		A
41	Lake Grassmere	✓						✓		C
42	Eketahuna	✓						✓		A
43	Ludian	✓	✓	✓	✓	✓				C
44	Wilberforce	✓						✓		C
45a	Gorkha	✓	✓	✓				✓		C
45b	Gorkha	✓	✓	✓		✓		✓		
45c	Gorkha	✓	✓	✓	✓	✓				
45d	Gorkha	✓	✓	✓	✓	✓	✓	✓		
46a	Kumamoto	✓	✓		✓	✓				A
46b	Kumamoto	✓	✓		✓	✓				

2.5. Discussion

We compiled information on 363 earthquakes that triggered landslides; this includes 46 events for which 66 digital inventories were generated, 89 events for which some landslide characteristics were reported, and 230 events for which triggered landslides are known. We contacted individual researchers and organizations and asked them to share their data with us to compile this database.

Many additional inventories have been compiled that were not included in this analysis either because we could not contact the authors, or we did not get their permission to use their inventory. Other inventories may also exist that are not published in international literature or are in non-English language journals or gray-literature reports. In the future, we anticipate that the number of digital EQIL inventories will increase substantially, paralleling advances in remote-sensing data and techniques, particularly the use of semi-automated image classification from high-resolution satellite images and the use of UAVs. However, guidelines are needed for the generation of EQIL inventories that take into account the quality, completeness and representation criteria outlined in this study. Therefore, further studies are necessary in order to prepare such guidelines, and to bring together scientists to share their inventories in a common platform. When inventories are generated according to such guidelines, the criteria for evaluating their quality, completeness and representation might also differ from the ones we proposed here for existing inventories. A recommended standard practice could include the following:

i) Generate inventories through semi-automatic image classification.

ii) Use pre- and post-earthquake images to isolate landslides triggered by the earthquake.

iii) Perform a quality check through visual image interpretation and field checking.

iv) Map landslides as polygons and separate the source and depositional areas.

v) Classify landslides according to type and style of movement.

The scoring system we suggest can be helpful in evaluating the suitability of EQIL inventories for a variety of applications. However, its utility is limited by the lack of knowledge regarding the analyzed EQIL inventories. The scoring system does not evaluate whether landslides are mapped correctly, how well the inventory is registered to a given coordinate system, or whether landslides are correctly classified. These are important aspects of a quality assessment but are much more difficult to evaluate without access to independent data. One solution is to make the satellite or aerial imagery used to generate the landslide inventory available so that others can examine the quality of the mapping. Developing a metadata description procedure for EQIL inventories that takes into account such criteria will also provide all users with a uniform way to evaluate the inventories.

The current paucity of publicly available EQIL data limits the range of scientific questions that can be addressed and impedes improvements in hazard assessments. One way to remove barriers to progress is to make the data easier for the community to access by collecting and share digital EQIL inventories through a centralized clearinghouse. To

address this need, we have created a ScienceBase Community titled “An Open Repository of Earthquake-triggered Ground Failure Inventories” dedicated to making EQIL and liquefaction inventories openly available to the community (Schmitt *et al.*, in press). ScienceBase (www.sciencebase.gov) is a collaborative scientific data and information management platform developed by the USGS. Community pages are designated project spaces that can be expanded over time to include more datasets.

Our aim is to enable the contribution and sharing of published EQIL inventories and accompanying methodological details based on the guidelines and criteria presented in Section 2.4. The EQIL community and the general public will then have access to the inventories in the system, and they can be used for research and other applications. Researchers that generate EQIL maps will be able to submit their inventories for inclusion as they become available. By centralizing data access and making methodological details available, we anticipate that the platform will lead towards the development of inventory mapping best practices and will ease visualization and analysis of the data with reference to other geospatial data such as climate, lithology, and topography. It would also provide a means to meet data availability requirements imposed by funding agencies and publishers. In the future, the existing ScienceBase Community could be used as the data source for the development of interactive tools, for example, presenting summary statistics and visualizations of landslide size, number, geographic extent, and earthquake parameters of one or many inventories. Qualitative and quantitative improvement of the data contained in the clearinghouse will also enable the development and delivery of near-real-time estimates of EQIL impacts driven by near real-time earthquake products such as the USGS ShakeMap, PAGER, and ShakeCast. Such estimates, as proposed by Nowicki *et al.* (2014), would provide situational awareness to government agencies, aid agencies, the media, and the general public. Next steps toward such a system require expanded data sharing and metadata documentation.

3. An updated method for estimating landslide-event magnitude[3]

3.1. Introduction

A number of interrelated factors such as topography, lithology, groundwater conditions, and ground shaking, play a role in the triggering of earthquake-induced landslides (EQIL) (Gorum *et al.*, 2011). Specific combinations of these causal factors might result in different landslide distributions for any particular earthquake. The total area of landslides (the sum of polygon areas) triggered by the 2015 Gorkha earthquake, for example, is around 90 km^2 (Roback *et al.*, 2017), which is significantly less than what we observe in the 2008 Wenchuan earthquake (~1160 km^2) (Xu *et al.*, 2014b). This reveals that the magnitude of these landslide-events should be noticeably different from each other, although both occurred in similar geomorphic (Kargel *et al.*, 2016) and seismotectonic settings and had comparable earthquake magnitudes (Wilkinson *et al.*, 2015). This implies that defining the causal factors that control the characteristics of each event is not simple or straightforward. This complexity makes it difficult to develop a globally applicable model for the prediction of EQIL (e.g. Kritikos *et al.*, 2015; Nowicki *et al.*, 2014). A landslide-event magnitude scale can improve our understanding of the relation between landslide causes and impacts because it simplifies a complex phenomenon into a single standard value that can be compared between triggering events.

Defining a magnitude scale for landslide events that relates to a physically measurable quantity is not straightforward. For instance, in seismology, the moment magnitude of an earthquake can be measured using seismic recordings but relates to a physical property of the source, the earthquake's moment (Shearer, 2009). A measure of energy released during landsliding is more difficult to obtain (Guzzetti *et al.*, 2005) because determining the total potential energy change would require mapping the starting and ending location and mass of each landslide's source material. The study of Keefer (1984) was one of the pioneer attempts to define a magnitude scale for EQIL. He used the number of landslides to define landslide-event magnitudes: an event triggering 10^2-10^3 landslides is classified as a two; 10^3 - 10^4 landslides is classified as a three, etc. Following Keefer (1984)'s method, Malamud *et al.* (2004) established a more comprehensive method by using the statistics of the landslide sizes. They considered the total landslide area predicted from a modelled probability distribution of landslide areas as a proxy for landslide-event magnitude (mLS).

[3] This chapter is based on the following paper: Tanyas, H., Allstadt, K.E., van Westen, C.J., 2018. An updated method for estimating landslide-event magnitude. Earth Surface Processes and Landforms, 43: 1836-1847. DOI: 10.1002/esp.4359

The statistics of landslide sizes can be analyzed using cumulative or the non-cumulative size distributions. These distributions can usually be represented by frequency-area-distribution (FAD) curves that are plotted for the landslide-area bins versus the corresponding non-cumulative frequency-density values.

Numerous authors have observed that the FAD of medium and large landslides exhibit power-law scaling (Dai and Lee, 2001; Fujii, 1969; Guthrie and Evans, 2004; Guzzetti *et al.*, 2002; Hovius *et al.*, 1997; Hovius *et al.*, 2000; Malamud *et al.*, 2004; Ohmori, 1988; Pelletier *et al.*, 1997; Stark and Hovius, 2001; Van Den Eeckhaut *et al.*, 2007). Though some hypotheses have been proposed (e.g. Guthrie *et al.*, 2008; Pelletier *et al.*, 1997; Van Den Eeckhaut *et al.*, 2007), the physical explanation(s) that dictates the power-law or deviations from it is not well understood but is beyond the scope of this study.

According to this concept, two features control the shape of the FAD: a power-law distribution for medium to large landslides, and a divergence from the power-law toward high frequencies with a rollover point where frequencies decrease for smaller landslides (Figure 3.1). This point, at which the FAD diverges from the power-law, is defined as the cutoff point (Stark and Hovius, 2001), whereas, the slope of the power-law distribution is defined using a power-law exponent (scaling parameter, β) (Figure 3.1).

The power-law distribution can be captured in both cumulative and non-cumulative FADs, and the power-law exponent for a non-cumulative FAD (β) can be transferred to its cumulative equivalent, α, using the relation α=β-1 (Guzzetti *et al.*, 2002). On the other hand, the rollover point is not visible in the cumulative FAD plots, and so most landslide size-distribution studies use non-cumulative FAD curves (e.g. Guzzetti *et al.*, 2002; Malamud *et al.*, 2004; Van Den Eeckhaut *et al.*, 2007).

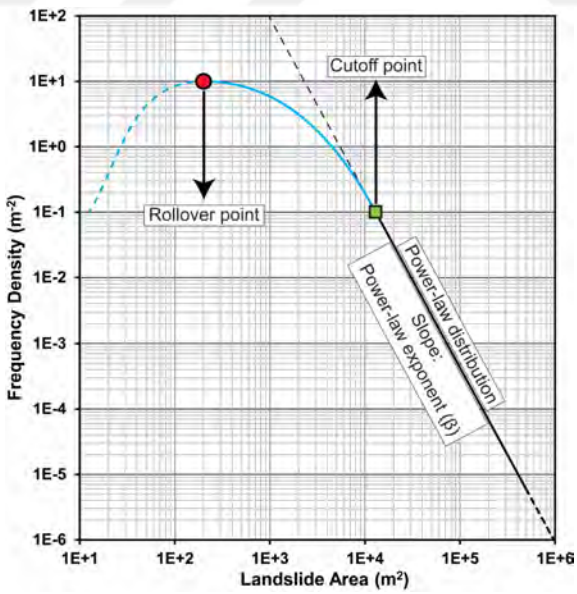

Figure 3.1. Schematic of the main components of the non-cumulative FAD plot of a landslide-event inventory.

Mainly two approaches are used to model the FAD of terrestrial landslides (Hurst *et al.*, 2013). The first method (Stark and Hovius, 2001) uses two scaling regimes in the FAD of landslides: negative power-law decay for large landslides and positive power-law for small landslides. To model the entire distribution without ignoring the part of the landslide data that does not fit a simple power-law, they proposed using the double-Pareto distribution, which follows a power-law at both tails. This model quantifies the undersampling of smaller landslides and improves estimation of the power-law scaling of larger landslides, under the assumption that undersampling is the cause of power-law divergence. However, although the double-Pareto model describes the majority of the data well, Guthrie and Evans (2004) argue that the same model fits less well at the tails of the distribution.

The second method (Malamud *et al.*, 2004) models the entire FAD of landslides, including the rollover, using a three-parameter inverse-gamma distribution (Equation 3.1).

$$p(A_L;\rho,a,s) = \frac{1}{a\Gamma(\rho)}\left[\frac{a}{A_L-s}\right]^{\rho+1} exp\left[-\frac{a}{A_L-s}\right] \qquad \text{(Equation 3.1)}$$

where ρ is the parameter primarily controlling power-law decay for medium and large values, $\Gamma(\rho)$ is the gamma function of ρ, A_L is landslide area (m^2), a is the location of the maximum of the probability distribution (m^2), which refers to rollover point, s is the exponential decay for small landslide areas (m^2), and $-(\rho+1)$ is the power-law exponent.

For most landslide inventories, non-cumulative power-law exponents fall in the range of 1.4–3.4, with a central tendency of 2.3–2.5 (Stark and Guzzetti, 2009a; Van Den Eeckhaut *et al.*, 2007). Malamud *et al.* (2004) also indicated that a power-law exponent of 2.4 provided the best fit to the data they examined.

Malamud *et al.* (2004) defined landslide-event magnitude based on the common logarithm of the total number of landslides (N_{LT}) associated with the event (Equation 3.2). They investigated three well-documented landslide inventories and defined empirical curves by fitting inverse gamma distributions to the data. They proposed that empirical curves of f(A_L) for various mLS can be obtained by multiplying the probability distribution given in Equation 3.1 by NLT (Equation 3.2).

$$mLS = logN_{LT} \qquad \text{(Equation 3.2)}$$

$$f(A_L) = N_{LT}p(A_L) \qquad \text{(Equation 3.3)}$$

The authors proposed that these empirically obtained curves are valid for the frequency-size distribution of any landslide inventory. Accordingly, they argued that the FAD of any complete inventory should be consistent with the form of these empirical curves, and for any landslide-event inventory, mLS can be defined based on a visual comparison between the empirical curves and the FAD of the medium and large landslides. Based on this theory, they also established the following relations between (1) earthquake magnitude (M) and landslide-event magnitude (Equation 3.4), and (2) landslide-event magnitude and total landslide area (A_T in km^2) (Equation 3.5).

$$mLS = 1.29M - 5.65 \qquad \text{(Equation 3.4)}$$

$$A_T = 3.07x10^{-3}x10^{mLS} \qquad \text{(Equation 3.5)}$$

The mLS estimates of Malamud *et al.* (2004) contain two main sources of uncertainty. First, they based their model on a limited dataset of three inventories, and thus were missing examples of the variety of FAD forms possibly leading to an oversimplified model. The FADs of landslide-event inventories do not always conform to the inverse-gamma distribution shape of their proposed empirical curves. Second, Malamud *et al.* (2004) proposed a fixed power-law exponent. If the power-law exponent of the investigated inventory shows a considerable difference from the modeled power-law exponent of 2.4, then the computation of mLS is highly subjective, particularly when selected using visual comparison, as they propose.

Our study aims to improve the methodology of Malamud *et al.* (2004) to estimate the landslide-event magnitude more accurately and consistently by diminishing some of the uncertainties and allowing for variations in the power-law exponent. To accomplish this, we analyze a much larger dataset of 45 earthquake-induced landslide (EQIL) inventories from around the globe (Table 3.1). We focus on the segment of the FAD that does follow a power-law for consistency with the approach of Malamud *et al.* (2004). We exclude the FAD of small landslides where we observe various rollover patterns. We propose a new method to define the magnitude of landslide events with its uncertainty. We find a relation between mLS and total landslide area and validate our model using the estimates total landslide areas. Then we evaluate and compare our methodology and that of Malamud *et al.* (2004) using the estimated and mapped total landslide areas.

3.2. Input data

We use an EQIL inventory database (Tanyaş *et al.*, 2017) (Chapter 2), which contains 66 digital EQIL inventory maps from around the world for earthquakes that occurred between 1976 and 2016. Multiple inventories exist for some earthquakes, in most cases independently derived. From that database, we use the 45 inventories for which landslide area information is available (Table 3.1). Each inventory has a different level of quality, completeness, and in some of them, landslides can be attributed to more than one earthquake (Tanyaş *et al.*, 2017) (Chapter 2).

Harp *et al.* (2011) defined three basic criteria for evaluating inventories: (1) coverage of the entire area affected by landslides, (2) inclusion of all landslides down to a small enough and defined size, and (3) depiction of landslides as polygons rather than points. Harp *et al.* (2011) described inventories as comprehensive if they satisfy these conditions.

The EQIL inventory database includes eight of the EQIL inventories considered comprehensive by Harp *et al.* (2011): 1976 Guatemala (Harp *et al.*, 1981), 1978 Izu Oshima KinKai (GSI, 1979), 1980 Mammoth Lakes (Harp *et al.*, 1984), 1983 Coalinga (Harp and Keefer, 1990), 1994 Northridge (Harp and Jibson, 1995, 1996), 1999 Chi-Chi (Liao and Lee, 2000), 2004 Mid Niigata and 2008 (GSI, 2005), and 2008 Iwate-Miyagi-Nairiku (Yagi *et al.*, 2009). Additionally, the database includes the 2010 Haiti inventory of Harp *et al.* (2016), which is considered a comprehensive inventory where landslides were mapped in a very detailed manner (Harp *et al.*, 2011; Tanyaş *et al.*, 2017) for the entire affected area. In this research, we refer to these inventories as high-detail inventories and the rest, which do not meet the three main criteria, are described as partial inventories.

Since the majority of inventories are not complete, one primary objective is to be able to define landslide-event magnitude even for inventories for a subset of the affected area. Therefore, we also include five such inventories: the 1989 Loma Prieta inventory (McCrink, 2001), the 2006 Kiholo Bay inventory (Harp *et al.*, 2014), the 2008 Wenchuan epicentral inventory (Tang *et al.*, 2016), the 2013 Lushan inventory (Li *et al.*, 2013), and the 2015 Gorkha inventory.

Three inventories identified landslide types. Lateral spreads that were differentiated in the Eastern Honshu inventory (Wartman *et al.*, 2013) were eliminated because they represent a distinct mechanism related to liquefaction. Similarly, in the Mid-Niigata inventories (Sekiguchi and Sato, 2006; Yagi *et al.*, 2007) debris flows were excluded because their larger depositional area can affect the landslide FAD.

3.3. Method

In this section we present a stepwise description of our proposed methodology after providing brief background information on the parameters we used.

The power-law distribution includes three terms:

$$p(X) = cX^{-\beta} \quad \text{(Equation 3.6)}$$

where X is observed value (in this case, landslide areas organized in bins), c is a normalization constant, and β is the power-law exponent. The normalization constant, c, depends on the power-law exponent and a cutoff point based on the definition given by Clauset *et al.* (2009). We define the normalization constant using two terms to explicitly refer the total number of landslides (N_{LT}) within the formulation:

$$c = c'N_{LT} \qquad \text{(Equation 3.7)}$$

$$N_{LT} = 10^{mLS} \qquad \text{(Equation 3.8)}$$

where c' is a constant obtained by dividing the normalization constant by the total number of landslides, and mLS is landslide-event magnitude scale. We use constant c' to integrate mLS into the equation.

Combining Equations (3.7) and (3.8) with Equation (3.6) produces the power-law and mLS equations:

$$p(X) = c'10^{mLS}X^{-\beta} \qquad \text{(Equation 3.9)}$$

$$mLS = log_{10}\left(\frac{p(X)}{c'X^{-\beta}}\right) \qquad \text{(Equation 3.10)}$$

where $p(X)$ refers to the frequency density of landslides and mLS can be computed using any X and $p(X)$ pair that lies on the line of best fit.

Table 3.1. Power-law exponents, cutoff values, landslide-event magnitudes (mLS) for the EQIL inventories in the database.

ID	Location	Date	p-value	Cutoff points (m2)	β	$m\ L\ S$ (±1σ)	Total number of landslides	Total landslide area from inventory (km^2)	Estimated total landslide area (±1σ) (km^2)	Reference study
1	Guatemala*	1976-02-04	0.67	$19135\pm7\times10^{1}$	2.21±0.14	4.79±0.08	6224	60.8	63.8±8.7	Harp et al., 1981
2	Friuli (Italy)	1976-05-06	0.45	$1466\pm1\times10^{1}$	2.20±0.09	2.91±0.57	1007	1.1	2.3±4.7	Govi, 1977
3	Izu Oshima Kinkai (Japan)*	1978-01-14	0.89	$1508\pm2\times10^{2}$	2.61±0.11	2.63±0.13	659	1.5	1.4±0.4	GSI of Japan, 1978
4	Mammoth Lakes (USA)*	1980-05-25	0**	$6784\pm2\times10^{3}$	2.29±0.09	4.37±0.09	4027	33.8	30.3±5.0	Harp et al., 1984
5	Coalinga (USA)*	1983-05-02	0.31	$1831\pm3\times10^{2}$	2.64±0.06	3.15±0.08	3980	4.7	3.5±0.5	Harp and Keefer, 1990
6	Loma Prieta, California (US)	1989-10-18	0.55	$3642\pm5\times10^{2}$	2.93±0.28	1.75±0.25	138	0.4	0.3±0.2	McCrink, 2001
7	Limon (Costa Rica)	1991-04-22	0.92	$9171\pm1\times10^{3}$	3.30±0.18	3.43±0.11	1643	8.2	5.8±1.2	Marc et al., 2016
8	Finisterre Mt./ (Papua N. G.)	1993-10-13	0.96	$34585\pm9\times10^{3}$	2.40±0.18	4.91±0.08	4790	69.0	78.8±12.8	Meunier et al., 2008
9	Northridge (USA)*	1994-01-17	0.88	$9189\pm1\times10^{3}$	2.62±0.11	4.05±0.07	11111	23.8	17.2±2.2	Harp and Jibson, 1995, 1996
10	Hyogo-ken Nanbu (Japan)	1995-01-16	0.11	$102\pm2\times10^{0}$	2.17±0.02	2.38±0.03	2353	0.5	0.9±0.1	Uchida et al., 2004
11	Umbria-Marche (Italy)	1997-09-26	0.55	$10412\pm3\times10^{1}$	2.85±0.37	3.14±0.20	210	1.9	3.5±1.4	Marzorati et al., 2002
12	Jueili (Taiwan)	1998-07-17	0.99	$10920\pm3\times10^{1}$	3.21±0.60	3.32±0.29	847	4.8	4.8±3.1	Huang and Lee, 1999
13	Chi-chi (Taiwan)*	1999-09-20	0.99	$26259\pm7\times10^{3}$	2.29±0.09	5.11±0.06	9272	127.5	113.0±11.8	Liao and Lee, 2000
14	Denali Alaska	2002-11-03	0.96	$24153\pm7\times10^{3}$	2.11±0.06	4.94±0.09	1579	121.2	82.7±11.4	Gorum et al., 2014
15	Lefkada (Greece)	2003-08-14	0.83	$19164\pm8\times10^{1}$	2.77±0.46	3.52±0.23	274	2.9	6.8±3.4	Papathanassiou et al., 2013
16a	Mid-Niigata (Japan)*[1]	2004-10-23	0.11	$520\pm2\times10^{2}$	2.31±0.21	3.91±0.77	10516	10.7	13.4±26.8	GSI of Japan, 2005
16b	Mid-Niigata (Japan)*[1]		0.96	$1683\pm4\times10^{2}$	2.32±0.05	3.85±0.06	4615	11.9	12.1±1.4	Sekiguchi and Sato, 2006
16c	Mid-Niigata (Japan)*[1]		0.25	$1157\pm2\times10^{1}$	2.48±0.04	3.11±0.04	3922	3.8	3.3±0.2	Yagi et al., 2007
17a	Kashmir (India-Pakistan)	2005-10-08	0.58	$6573\pm1\times10^{3}$	2.39±0.12	3.89±0.11	2424	10.4	13.0±2.6	Sato et al., 2007
17b	Kashmir (India-Pakistan)		0.76	$44139\pm5\times10^{1}$	2.39±0.07	4.85±0.06	1461	49.9	71.0±9.6	Basharat et al., 2014
17c	Kashmir (India-Pakistan)		0.62	$57717\pm9\times10^{1}$	3.67±0.09	5.42±0.06	2930	109.4	195.1±22.1	Basharat et al., 2016
18	Kiholo Bay (Hawaii)	2006-10-15	0.94	$17203\pm6\times10^{1}$	2.45±0.46	3.38±0.18	383	2.8	5.3±2.1	Harp et al., 2014
19a	Aysen Fjord (Chile)	2007-04-21	0.57	$19166\pm3\times10^{1}$	2.07±0.10	4.28±0.09	540	17.3	25.9±4.9	Sepúlveda et al., 2010
19b	Aysen Fjord (Chile)		0.01**	$5312\pm3\times10^{1}$	1.82±0.18	4.11±0.41	517	13.2	19.1±32.5	Gorum et al., 2014

Table 3.1. (Continued)

ID	Location	Date	p-value	Cutoff points (m2)	β	$m\ LS$ (±1σ)	Total number of landslides	Total landslide area from inventory (km^2)	Estimated total landslide area (±1σ) (km^2)	Reference study
20	Niigata Chuetsu-Oki (Japan)	2007-07-16	0.80	$828\pm3\times10^2$	2.80±0.28	1.69±0.41	312	0.4	0.3±0.2	Kokusai Kogyo, 2007
21	Pisco / (Peru)	2007-08-15	0.93	$4100\pm1\times10^2$	2.63±0.23	2.70±0.20	271	1.07	1.6±0.7	Lacroix et al., 2013
22a	Wenchuan (China)	2008-05-12	0.12	$97846\pm1\times10^4$	2.77±0.10	6.27±0.06	59108	812.2	871.2±92.9	Dai et al., 2011
22b	Wenchuan (China)		1.00	$143664\pm6\times10^3$	3.09±0.10	6.15±0.06	197481	1159.9	710.6±101.3	Xu et al., 2014b
22c	Wenchuan (China)		0**	$78826\pm5\times10^3$	3.23±0.05	6.00±0.05	69605	580.3	542.3±60.1	Li et al., 2014
22d	Wenchuan (China)		1.00	$39169\pm4\times10^3$	2.72±0.12	4.89±0.05	6727	54.6	76.5±8.0	Tang et al., 2016
23	Iwate-Miyagi Nairiku* (Japan)	2008-06-13	0.96	$5653\pm2\times10^3$	2.39±0.22	3.85±0.15	4211	12.5	12.1±3.7	Yagi et al., 2009
24a	Haiti	2010-01-12	0.99	$6330\pm1\times10^3$	2.71±0.25	3.53±0.15	4490	8.0	6.9±2.4	Gorum et al., 2013
24b	Haiti*		0**	$2674\pm5\times10^2$	2.26±0.07	4.23±0.07	23567	24.9	23.6±3.4	Harp et al., 2016
25	Sierra Cucapah (Mexico)	2010-04-04	0.13	$1457\pm1\times10^2$	2.61±0.12	2.29±0.12	453	0.7	0.8±0.2	Barlow et al., 2014
26	Yushu (China)	2010-04-13	0.01**	$581\pm6\times10^2$	2.26±0.33	2.76±0.52	2036	1.2	1.8±3.2	Xu et al., 2013
27	Eastern Honshu (Japan)[2]	2011-03-11	0.87	$1916\pm6\times10^2$	2.90±0.29	2.14±0.25	3475	1.6	0.6±0.3	Wartman et al., 2013
28a	Lushan (China)	2013-04-20	0.67	$5726\pm1\times10^3$	2.63±0.20	3.43±0.13	1289	5.2	5.8±1.6	Li et al., 2013
28b	Lushan (China)		0.94	$5359\pm1\times10^3$	2.93±0.21	3.56±0.14	15546	18.5	7.2±2.1	Xu et al., 2015
29	Minxian-Zhangxian (China)	2013-07-21	0.78	$228\pm6\times10^2$	2.27±0.11	2.41±0.16	2330	0.8	1.0±0.3	Xu et al., 2014a
30	Ludian (China)	2014-08-03	0.99	$9234\pm2\times10^3$	2.46±0.18	3.63±0.10	1024	5.2	8.2±1.7	Ying-ying et al., 2015
31a	Gorkha (Nepal)	2015-04-25	0.68	$5210\pm1\times10^3$	2.40±0.08	4.09±0.08	2654	15.6	18.6±2.6	Zhang et al., 2016
31b	Gorkha (Nepal)		0.95	$8461\pm1\times10^3$	2.04±0.09	4.10±0.08	2513	14.2	18.8±3.0	See supplementary material
31c	Gorkha (Nepal)		0**	$1344\pm1\times10^3$	2.49±0.11	4.91±0.06	24795	11.7	78.8±9.4	Roback et al., 2017
32a	Kumamoto (Japan)	2016-04-15	0.79	$6249\pm2\times10^3$	2.44±0.29	3.12±0.20	336	1.8	3.3±1.5	DSPR-KU, 2016
32b	Kumamoto (Japan)		0.56	$2362\pm1\times10^3$	2.02±0.14	3.69±0.18	2742	7.7	9.1±2.9	NIED, 2016

**High-detail inventories; **The inventories that do not meet the criteria for a power-law based on the KS test; [1]Debris flows were excluded; [2]Lateral spreads were excluded.*

3.3.1. Step 1: Test the validity of the power-law distribution

To test the validity of power-law fitting for the EQIL datasets, we used the method of Clauset *et al.* (2009), which consists of a goodness-of-fit test to measure the distance between analyzed data and synthetic data sets from a true power-law distribution. To quantify the distance between the two distributions, they used the Kolmogorov–Smirnov (KS) statistic and generated a p-value that indicates the plausibility of the hypothesis. A p-value close to one indicates a good fit to the power law distribution, whereas p-value equal or less than 0.1 might indicate that the power law is not a plausible fit to the data. For each inventory, we calculated p-values that indicate the plausibility of power-law hypothesis using KS statistics (Clauset *et al.*, 2009).

3.3.2. Step 2: Obtain the cutoff point and power-law exponent

For each inventory, we found the power-law exponent (β) and the best-fitting constant (c') of the power-law and assess the corresponding mLS value. To do so, we first identified the cutoff point for fitting and β based on the method of Clauset *et al.* (2009), which has been applied elsewhere to landslide frequency-area statistics (e.g. Bennett *et al.*, 2012; Hurst *et al.*, 2013; Li *et al.*, 2014b; Parker *et al.*, 2015; Urgeles and Camerlenghi, 2013). This approach estimates possible β values for each possible cutoff values using maximum-likelihood fitting methods with goodness-of-fit tests based on the Kolmogorov-Smirnov (KS) statistic and likelihood ratios. It operates directly on the landslide areas, and provides the cutoff and the β values. By operating directly on the landslide areas without binning eliminates additional uncertainty introduced by the binning methodology is excluded from the result. Additionally, β was calculated rigorously by considering only the part of the FAD where the power-law is valid (where $X > Xmin$, and $Xmin$ is the cutoff point). We also quantified the uncertainties in estimated cutoff and β values following the method of Clauset *et al.* (2009) that use a nonparametric bootstrap algorithm (Efron and Tibshirani, 1994).

Figure 3.2a shows an example of the visualization of estimated parameters for the 2008 Wenchuan inventory (Xu *et al.*, 2014b). In the plot, instead of bins, all data are used to generate a cumulative density distribution.

3.3.3. Step 3: Calculate the normalization constant

After obtaining the cutoff value and β for each inventory, we identified the normalization constant, c (Equation 3.6). To obtain c, we found where the power-law fit line coincides with the $p(X_{cutoff})$ value of the smallest empirical value in the interval for the power-law fitting regime where $X > Xmin$ (Figure 3.2b):

$$p(X_{cutoff}) = c(cutoff)^{-\beta} \qquad \text{(Equation 3.11)}$$

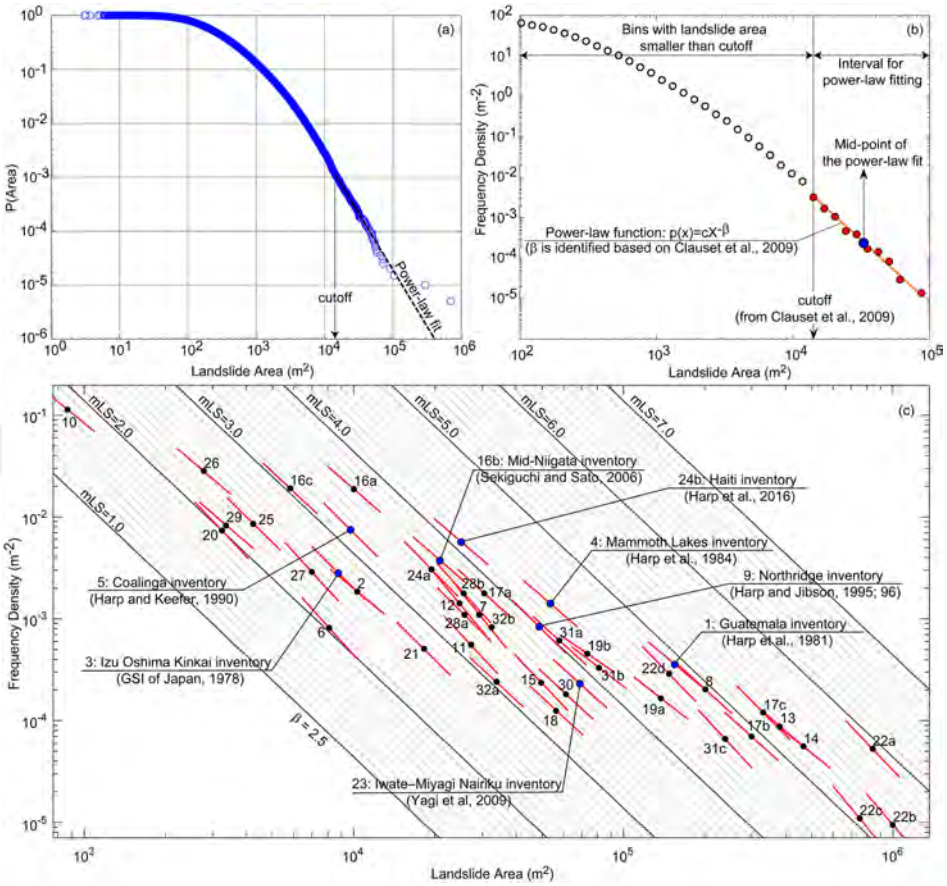

Figure 3.2. (a) Visualization of cumulative density functions P(Area) and their maximum likelihood power-law fit, (b) identification procedure of the best power-law fit and its midpoint, and (c) distribution of the midpoints of power-law fits overlain by empirical power-law fits constructed with β=2.5 where high-detail inventories are labeled. The event-specific power-law exponents (slopes) are indicated by red lines (Inventory IDs listed in Table 3.1).

3.3.4. Step 4: Plot the power-law fit with empirical lines to estimate mLS

The next step was to determine the mLS using the located power-law fit, similar to the approach of Malamud *et al.* (2004) (Figure 3.2c). We used the event-specific β values and de-trend the empirical power-law fits for each landslide-event inventory by rotating the empirical lines around the midpoint of a reference inventory until the slope matches the β value of the event. The midpoint of an inventory was selected as a point that is in between the cutoff and the largest landslide size on a logarithmic scale. We used this point as a tuning parameter. Around this point, we build empirical lines that, in contrast to Malamud *et al.* (2004), are represented by power-law distributions without a rollover. We calculated c' (Equation 3.7) for the midpoint of the reference inventory. Consequently, using the same

c' value, we read the corresponding mLS values (Figure 3.2c) for each inventory. At this point, the power-law for the specific inventory will line up with the rotated empirical curves, and any point along the fit line can be used to determine the mLS (Equation 3.10).

In choosing the reference inventory, we consider three criteria. First, the set reference point should have a central position to minimize the uncertainty caused by this selection itself. Because reorientation of all power-law fits around a central point causes less drastic deviations from the magnitude scale of Malamud *et al.* (2004) and its relation to the total number of landslides than using, for example, a point close to the edge of the midpoints' distribution. Second, to check that our estimated mLS values preserve the relation between mLS and the total number of landslides defined in Equation (3.8), we tested the most complete inventories available (labeled "high-detail inventories" in Table 1) and excluded those triggered by more than one earthquake. Third, the reference inventory should meet the criteria for a power-law based on the KS test. This means that the p-value of the reference inventory should be larger than 0.1. As a result, we defined the mLS of the three high-detail inventories (Figure 3.2c) (1983 Coalinga (Harp and Keefer, 1990), 1994 Northridge (Harp and Jibson, 1995, 1996), and 2008 Iwate-Miyagi-Nairiku (Yagi *et al.*, 2009) based on the logarithm of the total number of landslides associated with the event (Equation 3.8). Then we recalculated the mLS values for all other inventories with reference to each alternative reference point.

Therefore, for any inventory having an event-specific β, the procedure for determining mLS is as follows: (1) fix the midpoint of reference inventory; (2) calculate the constant c' by plotting the power-law fit as described earlier; and (3) calculate the mLS for the investigated inventory by using the obtained c' in Equation (3.10) with p(X) and X taken at the midpoint location.

For comparison, we also computed mLS values using the method of Malamud *et al.* (2004) that does not allow for event-specific β adjustments. We assigned an average β for the empirical power-law fits, which is the average β value obtained from the 45 inventories considered in this study (Table 1). By plotting the midpoints of the inventories on the empirical lines based on an average β value, we calculated c' (Equation 3.7) for the midpoint of the Northridge inventory (Equation 3.2) to provide a similar landslide-event magnitude scale with Malamud *et al.* (2004). Consequently, using the c' value obtained for the midpoint of Northridge inventory, we read the corresponding mLS values (Figure 3.2c) for each inventory.

3.3.5. Step 5: Identify the best approach of mLS *estimation*

We found the relation between landslide-event magnitudes and total landslide areas obtained from inventories for each alternative described in Step 4. Using the obtained relations, we estimated the total landslide areas for all inventories. We then compared the estimated areas to the total landslide areas of the inventories for each approach to identify the best method.

We also estimated the total landslide areas using the method described by Malamud *et al.* (2004) (Equation 3.5) using mLS values calculated based on the best alternative we obtained.

3.3.6. Step 6: Assess the uncertainty

We used the selected alternative and calculated mLS values for various β and cutoff couples located inside the obtained uncertainty limits to assess the uncertainty in mLS. To accomplish this task, for each inventory, we examined set of beta and cutoff values within the uncertainty limits and generated random β and cutoff values from the normal distribution with mean and standard deviation of examined data. We calculated mLS values for all pairs of these β and cutoff values to estimate the uncertainty in mLS.

3.4. Results

We plotted the FADs of all available EQIL inventories (Figure 3.3). Using the methods of Clauset *et al.* (2009) described earlier, we checked the validity of the power-law fit. We found that six out of the 45 inventories have p-values lower than 0.1. This finding show that for landslide size distribution in general, the power-law fit is a plausible hypothesis.

Figure 3.3 shows that the cutoff points are not consistent from inventory to inventory and the data distributions for small landslides are highly variable and do not follow a positive power-law scaling. However, the divergence from a power-law for small landslide sizes is beyond the scope of this study. In this study, we focus on the medium and large landslides, where we observe the power-law behavior for most of the inventories.

Power-law exponents and cutoff values with their uncertainties for all the available EQIL inventories are reported in Table 3.1. As described above, we estimated the total landslide area for all inventories and compared them with the original values (Table 3.1) gathered from the inventories (Figure 3.4). The results show that the use of the midpoint of the Northridge inventory (Harp and Jibson, 1995, 1996) as a reference point gives better total landslide area estimates than other alternatives in terms of both root mean squared error (RMSE) and mean absolute error (MAE). Using the midpoint of the Northridge inventory as the reference point to de-trend the empirical power-law fits allows us to estimate the total landslide area more successfully than the previously published methods. The estimates based on the method described by Malamud *et al.* (2004) yield much larger RMSEs and MAEs for fixed (RMSE=280 km^2 & MAE=650 km^2) and event-specific β (RMSE=2,400 km^2 & MAE=725 km^2) (Figure 3.4).

In Figure 3.5a, we present the relation between the landslide-event magnitude values and the total landslide areas for our preferred method (using the midpoint of Northridge inventory as reference point) (RMSE=77 km^2 and MAE=25 km^2). In Figure 3.5b, we compare the residuals of the estimated total landslide areas. The results show that the residuals increase as the total landslide areas of inventories increase. To estimate the variations in mLS calculated using different midpoints, we compared the differences between mLS values obtained by our method and other methods presented above. We examined the range of variation for five mLS intervals as presented in Figure 3.6. Result shows that the mean variations are 0.30, 0.33, 0.20, 0.36, and 0.63 for mLS intervals of 2-3, 3-4, 4-5, 5-6, and 6-7, respectively. For mLS values larger than 6, we have a larger variation compared to other intervals, because they have larger total areas so they actually can vary by larger amounts because they have larger total areas so they can vary by larger amounts.

As described above, we also assessed the uncertainty in our mLS estimations for each inventory (Table 3.1).

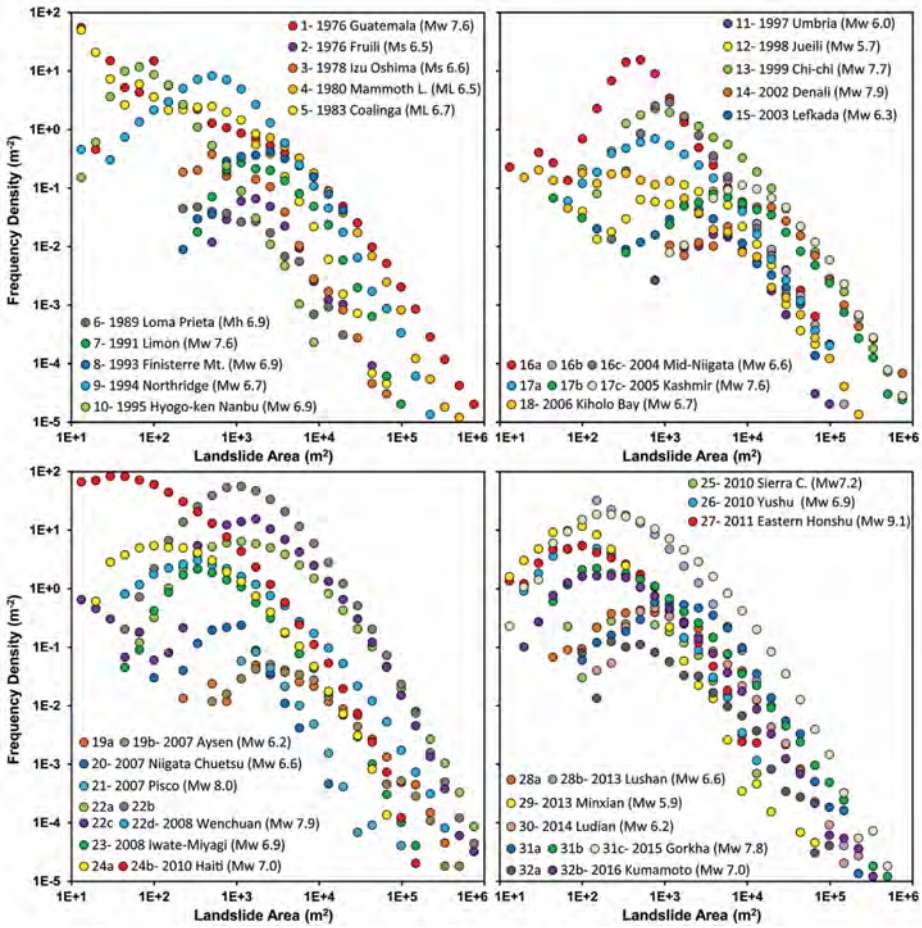

Figure 3.3. Frequency-area distributions for all inventories listed in Table 3.1 (Inventory IDs listed in Table 3.1).

3.5. Discussion

This study derives an objective landslide-event magnitude scale for EQIL inventories that is comparable to previously published scales. Both the method of Malamud *et al.* (2004) and the method presented in this study have uncertainties and limitations.

In addition to our preferred method, data-related factors such as lack of differentiation between landslide source and deposit areas (Frattini and Crosta, 2013) or the amalgamation of coalescing or adjacent landslides (Marc and Hovius, 2015) can cause a variation in the shape of FAD. These factors may also cause a suboptimal fit of a power-law to the data, as we found for six of the 45 inventories.

To test this argument, we analyzed the 2015 Gorkha (Roback *et al.*, 2017) inventory where the authors mapped almost all of the source areas separately, in addition to polygons they delineated for both source and depositional areas.

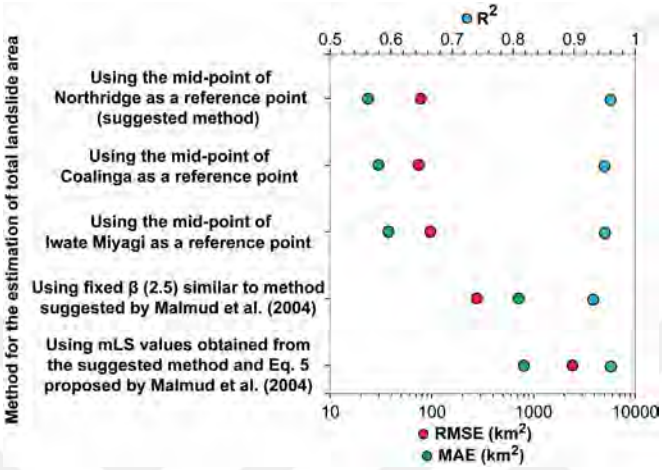

Figure 3.4. R^2, RMSE, and MAE values calculated for all inventories listed in Table 3.1 using alternative methods (alternative reference points) to estimate the total landslide area.

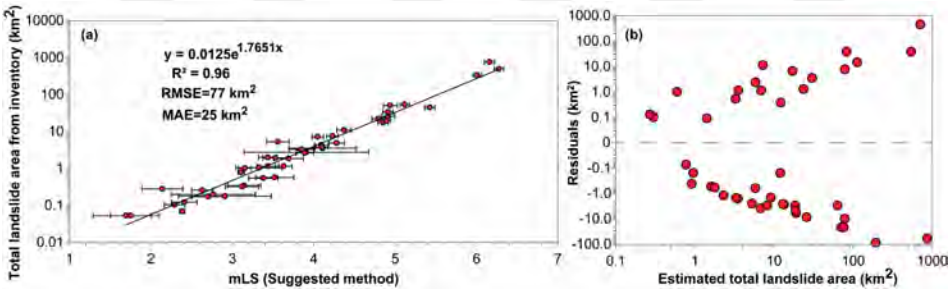

Figure 3.5. (a) Relation between the landslide-event magnitudes using ±1σ error bars and total landslide area for our preferred method (using the midpoint of the Northridge inventory as a reference point), and (b) residuals of the estimated total landslide areas.

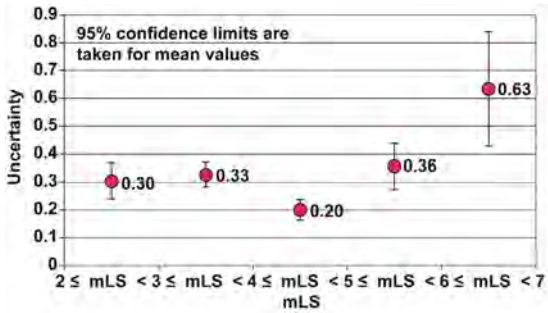

Figure 3.6. Variations in mLS calculated using different reference points.

We calculated p-values for both versions of the Gorkha inventory. As we presented in Table 3.1, the p-value is zero for the inventory including both sources and deposits of landslides, whereas p-value is 0.9 using only the source areas of the landslides.Therefore, the six inventories for which a power-law is not valid can be associated with landslide mapping techniques and uncertainties related to data quality. However, this is an extensive subject and uncertainties related to data quality are beyond the scope of this study. Instead, we focus on discussing the difficulty in characterizing the landslide FAD from the methodological perspective.

First of all, we show in Figure 3.2 that the shape of the FAD does not always follow the form proposed by Malamud *et al.* (2004). The authors utilized the inverse gamma function to model the probability density distribution of landslide areas. For comparison, we modeled the probability density distribution of inventories from the 1994 Northridge and the 2008 Wenchuan events (Figure 3.7). As expected, the probability density distribution of the Northridge inventory (p-value=0.7) (Harp and Jibson, 1995, 1996) follows the pattern of the modeled inverse gamma function proposed by Malamud *et al.* (2004) well (Figure 3.7a), because it was one of the three inventories used to develop their model. However, the same inverse gamma fitting does not work well for the 2008 Wenchuan inventory (p-value=1.0) of Xu *et al.* (2014b) (Figure 3.7b): the modeled distribution overpredicts at large landslide areas and underpredicts at small areas. Thus, the estimated β would not be representative for this inventory.

Secondly, the fitting of a landslide-event inventory to a power-law distribution and the power-law exponent (β) can be highly uncertain based on commonly used methods, such as least-squares fitting (Clauset *et al.*, 2009). Different cutoff estimations can produce different β values. Thus, ensuring reproducibility requires the cutoff value to be defined via numerical approaches such as those proposed by Clauset *et al.* (2009) rather than using visual observations.

Objectively estimating the β value and its uncertainties can allow us to define landslide-event magnitude based on empirical curves. In the method proposed by Malamud *et al.* (2004), the mLS is identified through visual comparison, which is not robust or reproducible. Moreover, using the same starting power-law fits for all inventories is problematic because the power-law exponents of inventories can vary from 1.4 to 3.4 (Stark and Guzzetti, 2009a; Van Den Eeckhaut *et al.*, 2007) and the identified mLS can vary depending on the exact location of the midpoint along the power-law fit.

Fixing β to an average value would cause large uncertainty in the estimated mLS if the β of the empirical power-law fits differ significantly from the event-specific β. One of the most striking examples is the 2008 Wenchuan (Figure 3.8) inventory by Xu *et al.* (2014b) in which β is 3.09 and mLS ranges between 5 and 6, and no single value can be assigned visually because the average β is 2.50 (Figure 3.8a). This observation not only emphasizes the importance of the power-law fit but also shows the requirement of our proposed method.

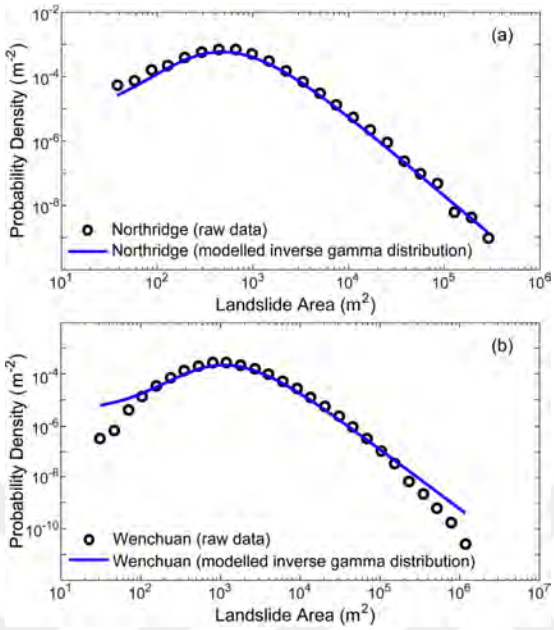

Figure 3.7. Raw and modeled probability density distribution for (a) Northridge, and (b) Wenchuan EQIL inventories.

For the Wenchuan event the mLS is calculated as 6.15 by using the suggested method (Figure 3.8b). Were the slope (β) not allowed to vary and we instead took the mLS value where the midpoint of the Wenchuan inventory lies (Figure 3.8a), the estimated mLS would be 5.33. That corresponds (using Equation 3.2) to an estimated total of 400,000 landslides, less than a quarter of the total landslides of the more robust estimate of mLS =6.15. In both approaches, the empirical lines passing through the midpoint of the Northridge inventory with different β values, have the same mLS value (mLS =4.05) because the midpoint of the Northridge inventory is the reference point whereas the Wenchuan inventory takes different mLS values for the average and the event-specific β values.

Note that the total number of landslides estimated based on Equation 3.2 is substantially more than those in the Wenchuan inventory. However, the total number of landslides is a subjective term due to several factors such as mapping methodology, amalgamation of coalescing of landslides, and the quality and resolution of interpreted imagery. Therefore, we use it here to emphasize the relative difference between different estimations.

Both Keefer (1984) and Malamud *et al.* (2004) proposed a relation between total landslide area and the magnitude of the triggering earthquake. We compared our proposed mLS values (Figure 3.9) to those predicted by Malamud *et al.* (2004) based on the earthquake magnitude (Equation 3.4). Results for the entire database show poor relation. Using only high-detail EQIL inventories provides better fit, but the relation remains relatively poor, which emphasizes that earthquake magnitude alone is not a sufficient proxy for the magnitude of EQIL inventories. This is to be expected because ground motions depend on earthquake characteristics other than just magnitude (e.g., depth, mechanism, distance, site conditions).

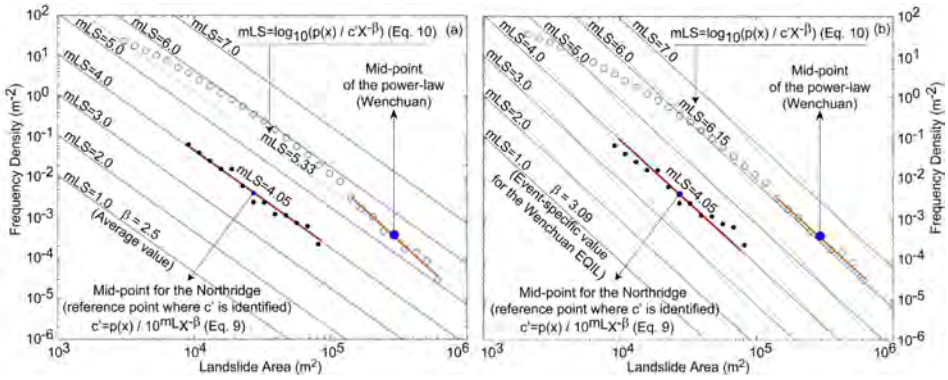

Figure 3.8. Illustration of the process of estimating mLS using the FAD of the 1994 Northridge (Harp and Jibson, 1995, 1996) and the 2008 Wenchuan (Xu et al., 2014b) EQIL inventories based on (a) a fixed β, and (b) proposed method where the empirical curves are rotated to the event-specific β for Wenchuan.

Topographic, geologic, and tectonic factors also control the landslide distribution during an earthquake. Thus, landslide-event magnitude is a more reasonable proxy than earthquake magnitude to characterize seismically triggered landslide numbers and areas. Our proposed method appears is an objective way of estimating mLS with its uncertainty level. The next step would be relating landslide magnitude to characteristics of the earthquake and the affected area.

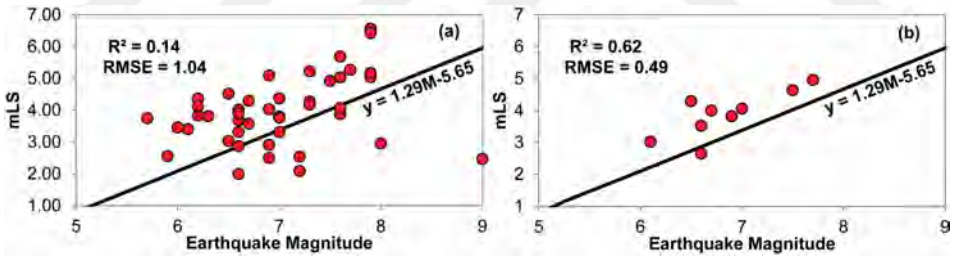

Figure 3.9. Data distribution between earthquake magnitude and mLS for (a) the entire EQIL database and (b) high-detail EQIL inventories. Black line shows proposed relation of Malamud et al. (2004).

3.6. Conclusions

In this study, we analyzed the FAD of 45 EQIL inventories and observed a power-law for medium and larger landslides. We showed that the observed power-law shapes and exponents vary significantly and therefore, one universal size model is not capable of modelling the FAD of all different landslide inventories. We have proposed an objective and automated methodology to estimate landslide-event magnitudes. We provide the codes for the methodology at https://github.com/usgs/mLS. Although the methodology was derived using EQIL inventories, it can be also applied to landslide events caused by other triggering events such as rainfall. The proposed methodology aims to diminish the uncertainty derived from the subjectivity of visually based methods. We have identified a

representative β for each specific landslide inventory in the definition of the empirical curves required for determining the landslide-event magnitude instead of using a fixed average β. We checked the validity of the proposed methodology by using the total landslide areas obtained from inventories. The analysis shows that we have improved the method of Malamud *et al.* (2004) in terms of total landslide area estimation. Therefore, we believe that the proposed mLS method can accurately estimate landslide-event magnitudes. The accurate and consistent estimation of mLS can help improve our ability to estimate total landslide area for the complete version of an inventory and even for inventories where only the larger landslides are mapped, since smaller landslides are excluded from the fitting procedure. Despite the uncertainties, the obtained mLS values also can help us understand the contributions of various explanatory variables such as the characteristics of the earthquake and the affected area. The relation between these characteristics and mLS needs to be explored with further studies. This could lead to methods for near real-time estimation of landslide-event magnitude and thus the total triggered landslide area.

4. Factors controlling landslide frequency-area distributions[4]

4.1. Introduction

The statistical properties of landslide inventories are commonly described using frequency-area-distribution (FAD) curves, which plot landslide areas versus the corresponding cumulative or non-cumulative landslide frequencies. Observations show that a power-law seems to be valid for medium and large landslides (e.g., tens to millions of square meters), and also for rock-fall distributions across the range of rock-fall sizes (e.g., Malamud *et al.*, 2004).

The slope of the power-law is defined using a power-law exponent (scaling parameter, β) (Fig. 4.1). The power law tail, where we calculate β, is arguably the most important part of the FAD because it gives insight in characteristics of landslide size distribution and contains the greatest volume of material (e.g., Bennett *et al.*, 2012). For example, Hovius *et al.* (1997) used β to quantify total denudation caused by landsliding. Power-law fit and the identified β value also are used as a tool for quantitative analysis of landslide hazard (Guzzetti *et al.*, 2005). However, the β value of a given FAD is sensitive to minor differences in the method used to estimate β (e.g., Bennett *et al.*, 2012; Tanyaş *et al.*, 2018). Additionally, other factors such as mapping techniques and expertise of mappers can cause uncertainty in FAD and β, which has not been analyzed in detail.

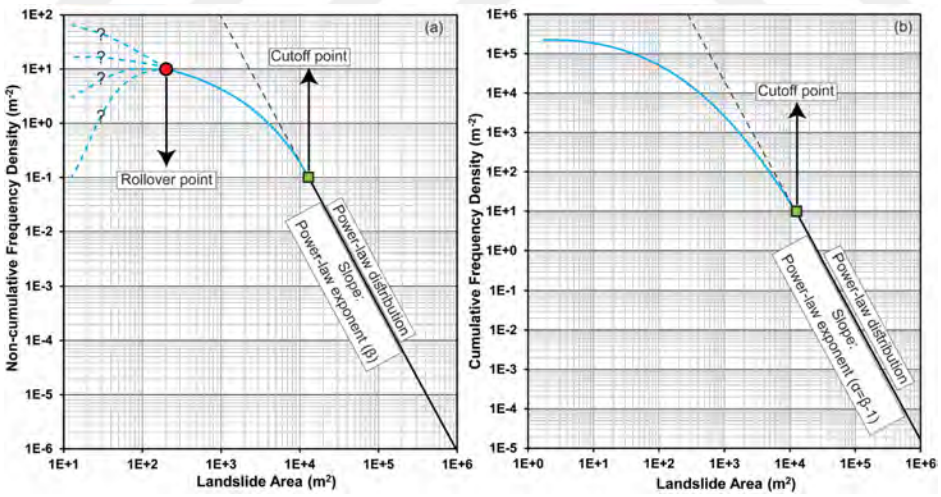

Figure 4.1. Schematic of the main components of a (a) non-cumulative, and (b) cumulative FAD of a landslide-event inventory.

[4] This chapter is based on the following paper: Tanyas, H., Allstadt, K.E., van Westen, C.J., and Jibson R.W. Factors controlling landslide frequency-area distributions, Earth Surface Processes and Landforms, under review, 2018.

For most landslide inventories, the frequencies of small landslides generally diverge from the power-law (Guzzetti *et al.*, 2002; Malamud *et al.*, 2004; Stark and Hovius, 2001; Van Den Eeckhaut *et al.*, 2007). The point where divergence begins is defined as the cutoff point (Stark and Hovius, 2001) which is visible in both the cumulative and non-cumulative FADs (Fig. 4.1). For non-cumulative landslide FADs, the peak point of the curve after which the frequency-density value begins to decrease for smaller landslides following a positive power-law decay is commonly referred to as the rollover point (e.g., Van Den Eeckhaut *et al.*, 2007) (Fig. 4.1a). Some studies refer to the cutoff point as the rollover point (e.g., Parker *et al.*, 2015), but in this study, we refer to the divergence point as the cutoff point and the peak point of the non-cumulative probability distribution curve as the rollover point.

The cause of the divergence is a controversial issue and five hypotheses for this divergence have been proposed. The focus of this issue is the cutoff point rather than the rollover point (Fig. 4.1) because that is where the divergence from the negative power-law decay is first observed.

The first hypothesis (Hypotesis-1) is that the power-law divergence is an artifact of undersampling small slides (e.g., Brardinoni and Church, 2004; Hungr *et al.*, 1999; Stark and Hovius, 2001) caused by inadequate resolution of the imagery used to create the landslide inventory.

Three other hypotheses that argue that the divergence from the power-law is real and can be attributed to physical explanations. Hypothesis-2 suggests that rollover is caused by the transition between the factors controlling slope-failure mechanisms of large, deep landslides versus small, shallow landslides (Katz and Aharonov, 2006). Guzzetti *et al.* (2002) argued that large, deep landslides are primarily controlled by friction, whereas small, shallow landslides are controlled more by cohesion. Stark and Guzzetti (2009b) and Frattini and Crosta (2013) used the mechanical properties of the substrate to propose an explanation for the power-law divergence. Stark and Guzzetti (2009b) claimed that the scaling of small, shallow failures is the result of the low cohesion of soil and regolith, whereas the power-law distribution observed for larger landslides is controlled by the greater cohesion of bedrock. Similarly, Bennett *et al.* (2012) show with empirical data that the power-law divergence and power-law distribution represent two separate types of slope failure. Type-1 refers to the numerous small, shallow slides within the top loose weathered layer of slopes where the depth and thus the size of the distribution is limited by the depth of the weathered layer. The depth of this layer limits the volume of landsliding and causes the rollover. Type-2 slides are less common, deeper and larger rock slides and falls where the depth is controlled by fractures within the bedrock. These failures have a wide range of depths and make up the power-law tail.

Li *et al.* (2014b) expanded on this idea in a three-dimensional perspective and proposed that the power-law divergence is linked to the volume-to-surface-area ratio of landslides. Decreasing this ratio causes an increase in resistance force without significantly changing the driving force. Because this ratio is lower for small, shallow landslides their number is expected to be fewer.

Hypothesis-3 is based on the geomorphology of an area and claims that the distribution of soil moisture over the landscape controls the size distribution and FADs of landslides

(Pelletier *et al.*, 1997). To model the FAD of landslides, Pelletier *et al.* (1997) examined the FADs of two historical and one EQIL-event inventory and conducted a slope-stability analysis using soil moisture as a controlling factor. They defined the domains where shear stress is greater than a threshold value and showed that FADs of these domains give similar power-law with FADs of landslides. According to this hypothesis, the landslide areas could be associated with areas of simultaneously high levels of soil moisture and steep slopes. Whereas this might be the case for medium and large landslides, the terrain surface is not dissected on a scale that would control smaller landslides, and so fewer landslides in this size range are expected. Therefore, the effect of the smooth topography at small scales causes rollover in the FAD of landslides.

Hypothesis-4 posits that the power-law divergence results from physiographic limitations (Guthrie *et al.*, Guthrie and Evans, 2004; 2008). This argument suggests that middle and upper slopes are most susceptible to landslide initiation because of steepness, and the mobilized material moves downslope and amalgamates into larger landslides. Small landslides occur where long runout is improbable because of the physiography of the slope; such areas are less common in most landscapes. Thus, this argument interprets the power-law divergence as a consequence of slope-length constraint on the downslope propagation of long-runout landslides.

Hypothesis-5 suggests that a lack of temporal mapping resolution causes rollover observed in rock-falls (Williams *et al.*, 2018). Barlow *et al.* (2012) showed the effect of temporal resolution of mapping on FADs of rock-falls. They compared inventories having temporal resolutions of 1 and 19 months stated that courser temporal resolution causes an increase in the superimposition of rock-fall events. Williams *et al.* (2018) went one step further by monitoring rock-falls on a slope (length~180m and hight~60m) at approximately 1-hour intervals. They showed that increasing temporal resolution captures many smaller failures and significantly changes the FAD. Williams *et al.* (2018) also showed that this high-temporal-resolution monitoring increased the power-law exponent to 2.27 (1 hour) from 1.78 (30 days). Additionally, they reported that the low-temporal-resolution inventory (30 days) had a rollover, whereas the inventory created from near-continuous slope monitoring did not.

There is currently no consensus on the reason why landslides show fractal size distributions and the FAD diverges from fractal scaling for small landslide areas. The arguments about whether the rollover is real or is an artifact can be traced back to the very definition of a landslide. The definition of what constitutes a single occurrence of a landslide can be complex and a matter of debate; this differs significantly from other phenomena that have a power-law relation, such as earthquakes. Earthquakes are recorded by seismometers and, except for events closely spaced in time, each distinct fault rupture can be assessed and quantified separately from others. In this context, divergence from the power-law decay is attributed to the loss of perceptibility of smaller events (Davison and Scholz, 1985). When quantifying landslides, on the other hand, the number of landslides cannot be objectively identified because of both amalgamation of coalescing or adjacent landslides and the subjectivity of mapping procedures.

Several factors cause the amalgamation of landslides in inventory maps. Delineating landslide polygons is subjective and depends on the methodology followed, the skill of the interpreters, and the time invested in the inventory (Soeters and van Westen, 1996).

Adjacent landslides commonly are delineated as a single polygon if their runouts or scars overlap and differentiation is difficult (e.g., Harp and Jibson, 1995, 1996). Poor image resolution or contrast between affected and unaffected areas might be another reason for amalgamation (Marc and Hovius, 2015). Lack of temporal resolution also can cause amalgamation of landslides.

Marc and Hovius (2015) propose a method for automatic detection and separation of amalgamated polygons. The algorithm redefines landslide polygons according to geometric and topographic considerations. For example, if a landslide polygon crosses a ridge, the algorithm splits this polygon into two along the ridge line. The methodology provides only a partial correction for amalgamated landslides, however. Along the same slope, multiple adjacent landslides can be triggered and amalgamated. For such cases, the suggested methodology is not capable of detecting amalgamation.

Li *et al.* (2014a) manually differentiate the amalgamated landslides provided by an automated landslide-detection algorithm (Parker *et al.*, 2011) for the 2008 Wenchuan EQIL. They show that amalgamated landslides can strongly bias both total number of landslides and individual landslide areas. As a result, this also significantly affects the FAD of landslides and the estimated landslide volume, which is highly sensitive to the changes both in the number of landslides and the area of each individual landslide (e.g., Li *et al.*, 2014a).

No clear physical process explains why landslide distributions should follow a power-law across the entire size distribution (Hergarten, 2003). Yet considering the literature showing that the power-law seems to be valid for medium and large landslides, it is logical to hypothesize that in the absence of artifacts, the scaling might also continue to smaller landslide sizes. If it does not, then a physical explanation should reveal something about the fundamentals of landslide processes. Whether the cutoff and rollovers are artifacts or if they reflect an actual change in the physical process for smaller slides is unclear. A consistent explanation for the observed variability in FAD patterns can help us isolate the physically based factors that yield a fundamental understanding of the landslide process. Explaining this issue also provide valuable information to understand the factors controlling the FAD of landslides and β as well.

This study aims to better understand the factors controlling the FADs of landslides, particularly why the FAD cutoffs and rollovers are present even in inventories that are considered complete. We do so by analyzing 45 digital EQIL inventories triggered by 32 earthquakes. This contrasts with the aforementioned studies that base their proposed explanations only on one or a few inventories. We analyze the different proposed rollover explanations using examples from these data and show that though each could contribute in some way, none of them by itself is adequate to cover the whole phenomenon. We elaborate on the argument that lack of temporal resolution in mapping of landslides causes superimposition and coalescence of features because the landslide events that happened at different times are formed on top of each other and afterwards look like a single event (Barlow *et al.*, 2012; Williams *et al.*, 2018). We suggest an alternative conceptual model to the existing hypotheses. Our model arguing that the divergence from the power-law and rollover are caused by lack of temporal resolution with which to capture the smallest of landslides.

4.2. Input data

Earlier studies for explaining the rollover use a variety of historical landslide inventories that are not limited to those related to earthquakes (e.g., Guzzetti *et al.*, 2002; Malamud *et al.*, 2004). We use an EQIL inventory database (Schmitt *et al.*, 2017a) that was collected by Tanyaş *et al.* (2017) (Chapter 2).

This database contains 64 digital EQIL inventory maps from around the world covering the period from 1971 to 2016. However, they have differing levels of quality and completeness because each inventory was created for a different purpose based on different expertise and materials. For example, the 2015 Gorkha EQIL inventory of Tanyaş *et al.* (2018) was created soon after the earthquake to understand the general spatial size-distribution characteristics of the triggered landslides; therefore, the inventory is preliminary and includes only a small part of the landslide-affected area with a high amount of amalgamation. On the other hand, Harp *et al.* (2016) published the 2010 Haiti inventory about six years after the event. This inventory covers the entire area affected by landslides down to the smallest resolvable landslide sizes and is far more detailed and comprehensive.

The 45 EQIL inventories from 32 earthquakes used in this study are described in Table 4.1. Except for the 2008 Wenchuan inventory of Li *et al.* (2014a) and the 2007 Pisco inventory of Lacroix *et al.* (2013), where landslides were mapped from satellite imagery using an automated algorithm and manual delineation, all other inventories were created primarily based on systematic visual interpretation of satellite images and/or aerial photography (Tanyaş *et al.*, 2017) (Chapter 2).

Tanyaş *et al.* (2018) numerically assessed the validity of power-law distribution for these earthquake-induced landslide inventories. They used the method of Clauset *et al.* (2009) and generated p-values based on the KS test. A p-value close to one indicates a good fit to the power law distribution, whereas p-value equal or less than 0.1 might indicate that the power law is not a plausible fit to the data. They showed that 39 of the 45 inventories have p-values larger than 0.1 and thus the power-law fit is a plausible hypothesis for landslide inventories in general.

Table 4.1. EQIL inventories used in this study. Cutoff and p-values were determined using the methodology of Clauset et al. (2009).

ID	Location	Date / Time	p-value	β	Approximate rollover point (m^2)	Cutoff points (m^2)	Reference study
1	Guatemala	1976-02-04 / 09:01:43 UTC	0.67	2.21±0.14		$19135±7×10^3$	Harp et al., 1981
2	Friuli (Italy)	1976-05-06 / 20:00:11 UTC	0.45	2.20±0.09	2050±211	$1466±1×10^3$	Govi, 1977
3	Izu Oshima Kinkai (Japan)	1978-01-14 / 03:24:39 UTC	0.89	2.61±0.11	537±83	$1508±2×10^2$	Suziki, 1979
4	Mammoth Lakes (USA)	1980-05-25 / 19:44:50 UTC	0*	2.29±0.09	2696±467	$6784±2×10^3$	Harp et al., 1984
5	Coalinga (USA)	1983-05-02 / 23:42:37 UTC	0.31	2.64±0.06		$1831±3×10^2$	Harp and Keefer, 1990
6	Loma Prieta, California (US)	1989-10-18 / 00:04:15 UTC	0.55	2.93±0.28		$3642±5×10^2$	McCrink, 2001
7	Limon (Costa Rica)	1991-04-22 / 21:56:51 UTC	0.92	3.30±0.18	1231±189	$9171±1×10^3$	Marc et al., 2016
8	Finisterre Mt./ (Papua N. G.)	1993-10-13 / 02:06:00 UTC	0.96	2.40±0.18	2351±354	$34585±9×10^3$	Meunier et al., 2008
9	Northridge (USA)	1994-01-17 / 12:30:55 UTC	0.88	2.62±0.11	617±74	$9189±1×10^3$	Harp and Jibson, 1995, 1996
10	Hyogo-ken Nanbu (Japan)	1995-01-16 / 20:46:52 UTC	0.11	2.17±0.02	66±8	$102±2×10^0$	Uchida et al., 2004
11	Umbria-Marche (Italy)	1997-09-26 / 09:40:26 UTC	0.55	2.85±0.37	4461±461	$10412±3×10^3$	Marzorati et al., 2002
12	Jueili (Taiwan)	1998-07-17 / 04:51:14 UTC	0.99	3.21±0.60	2168±378	$10920±3×10^3$	Huang and Lee, 1999
13	Chi-chi (Taiwan)	1999-09-20 / 17:47:18 UTC	0.99	2.29±0.09	881±138	$26259±7×10^3$	Liao and Lee, 2000
14	Denali Alaska	2002-11-03 / 22:12:41 UTC	0.96	2.11±0.06	16144±1997	$24153±7×10^3$	Gorum et al., 2014
15	Lefkada Ionian Islands (Greece)	2003-08-14 / 05:14:54 UTC	0.83	2.77±0.46	1984±219	$19164±8×10^3$	Papathanassiou et al., 2013
16a	Mid-Niigata (Japan)	2004-10-23 / 08:56:00 UTC	0.11	2.31±0.21	508±87	$520±2×10^2$	GSI, 2005
16b	Mid-Niigata (Japan)	2004-10-23 / 08:56:00 UTC	0.96	2.32±0.05	1198±207	$1683±4×10^2$	Sekiguchi and Sato, 2006
16c	Mid-Niigata (Japan)	2004-10-23 / 08:56:00 UTC	0.25	2.48±0.04	617±74	$1157±2×10^1$	Yagi et al., 2007
17a	Kashmir (India-Pakistan)	2005-10-08 / 03:50:40 UTC	0.58	2.39±0.12	804±152	$6573±1×10^3$	Sato et al., 2007
17b	Kashmir (India-Pakistan)	2005-10-08 / 03:50:40 UTC	0.76	2.39±0.07	4166±547	$44139±5×10^3$	Basharat et al., 2014
17c	Kashmir (India-Pakistan)	2005-10-08 / 03:50:40 UTC	0.62	3.67±0.09	8767±1450	$57717±9×10^3$	Basharat et al., 2016
18	Kiholo Bay (Hawaii)	2006-10-15 / 17:07:49 UTC	0.94	2.45±0.46		$17203±6×10^3$	Harp et al., 2014
19a	Aysen Fjord (Chile)	2007-04-21 / 17:53:46 UTC	0.57	2.07±0.10	2115±527	$19166±3×10^3$	Sepúlveda et al., 2010
19b	Aysen Fjord (Chile)	2007-04-21 / 17:53:46 UTC	0.01*	1.82±0.18	2578±512	$5312±3×10^3$	Gorum et al., 2014

Table 4.2. (Continued)

ID	Location	Date / Time	p-value	β	Approximate rollover point (m^2)	Cutoff points (m^2)	Reference study
20	Niigata Chuetsu-Oki (Japan)	2007-07-16 / 01:13:22 UTC	0.80	2.80±0.28	1009±109	$828±3×10^2$	Kokusai Kogyo, 2007
21	Pisco (Peru)	2007-08-15 / 23:40:57 UTC	0.93	2.63±0.23	2080±332	$4100±1×10^3$	Lacroix et al., 2013
22a	Wenchuan (China)	2008-05-12 / 06:28:01 UTC	0.12	2.77±0.10	1110±190	$97846±1×10^4$	Dai et al., 2011
22b	Wenchuan (China)	2008-05-12 / 06:28:01 UTC	1.00	3.09±0.10	1110±190	143664±6×10	Xu et al., 2014b
22c	Wenchuan (China)	2008-05-12 / 06:28:01 UTC	0*	3.23±0.05	1661±211	$78826±5×10^3$	Li et al., 2014a
22d	Wenchuan (China)	2008-05-12 / 06:28:01 UTC	1.00	2.72±0.12	357±67	$39169±4×10^3$	Tang et al., 2016
23	Iwate–Miyagi Nairiku (Japan)	2008-06-13 / 23:43:45 UTC	0.96	2.39±0.22	384±60	$5653±2×10^3$	Yagi et al., 2009
24a	Haiti	2010-01-12 / 21:53:10 UTC	0.99	2.71±0.25	122±16	$6330±1×10^3$	Gorum et al., 2013
24b	Haiti	2010-01-12 / 21:53:10 UTC	0*	2.26±0.07	39±8	$2674±5×10^2$	Harp et al., 2016
25	Sierra Cucapah (Mexico)	2010-04-04 / 22:40:42 UTC	0.13	2.61±0.12	496±113	$1457±1×10^2$	Barlow et al., 2014
26	Yushu (China)	2010-04-13 / 23:49:38 UTC	0.01*	2.26±0.33	106±15	$581±6×10^2$	Xu et al., 2013
27	Eastern Honshu (Japan)	2011-03-11 / 05:46:24 UTC	0.87	2.90±0.29	97±18	$1916±6×10^2$	Wartman et al., 2013
28a	Lushan (China)	2013-04-20 / 00:02:47 UTC	0.67	2.63±0.20	496±97	$5726±1×10^3$	Li et al., 2013
28b	Lushan (China)	2013-04-20 / 00:02:47 UTC	0.94	2.93±0.21		$5359±1×10^3$	Xu et al., 2015
29	Minxian-Zhangxian (China)	2013-07-21 / 23:45:56 UTC	0.78	2.27±0.11	106±15	$228±6×10^2$	Xu et al., 2014a
30	Ludian (China)	2014-08-03 / 08:30:13 UTC	0.99	2.46±0.18	761±139	$9234±2×10^3$	Ying-ying et al., 2015
31a	Gorkha (Nepal)	2015-05-12 / 07:05:19 UTC	0.68	2.40±0.08	1397±193	$5210±1×10^3$	Zhang et al., 2016
31b	Gorkha (Nepal)	2015-05-12 / 07:05:19 UTC	0.95	2.04±0.09	135±17	$8461±1×10^3$	Tanyas et al., 2018
31c	Gorkha (Nepal)	2015-05-12 / 07:05:19 UTC	0*	2.49±0.11	211±38	$1344±1×10^3$	Roback et al., 2017
32a	Kumamoto (Japan)	2016-04-15 / 16:25:06 UTC	0.79	2.44±0.29	377±114	$6249±2×10^3$	DSPR-KU, 2016
32b	Kumamoto (Japan)	2016-04-15 / 16:25:06 UTC	0.56	2.02±0.14	192±25	$2362±1×10^3$	NIED, 2016

4.3. Analysis

4.3.1. FADs of EQIL inventories

We calculate the cutoff and p-values using the method described by Clauset *et al.* (2009) (Table 4.1) and plotted the landslide FADs from the inventories analyzed (Fig. 4.2). We identify the landslide size bin where the corresponding FAD begins to roll over. We consider them approximate rollover points (Table 4.1) because the locations of rollover points differ slightly based on the binning methodology. We identify rollover points using ten different bin sizes to quantify the variation in rollover point. As a result, we define average rollover values with 95% confidence intervals. Empirical curves from Malamud *et al.* (2004) also are shown for comparison. Results show that power-law scaling at medium to large landslide areas exists for 39 inventories having p-value larger than 0.1 (Table 4.1), whereas all of them diverge from power-law scaling for smaller areas (Fig. 4.2). The FADs for medium to large landslides of many of the inventories match the shape, though not necessarily the slope of the modeled rollover of Malamud *et al.* (2004). Most of the FADs plot below the theoretical curves, which (Malamud *et al.*, 2004) interprets as an indicator of incompleteness. Some inconsistencies are difficult to explain. For example, the FADs of some inventories extend beyond the empirical curves at small landslide areas (Fig. 4.2(g)-(h)). In these inventories, the rollover point is not located where predicted by the empirical curves. In fact, for a significant number of EQIL inventories, the form and position of the rollover do not follow the modeled empirical distribution curves. Furthermore, we observe FADs without an obvious rollover for some inventories such as the Guatemala (Harp *et al.*, 1981), Coalinga (Harp and Keefer, 1990), Loma Prieta (McCrink, 2001), Kiholo Bay (Harp *et al.*, 2014) and Lushan (Xu *et al.*, 2015) inventories (Fig. 4.2h). This implies that existing rollover explanations need to be re-evaluated.

4.3.2. Rollover and cutoff sizes

We plot the rollover points of all EQIL inventories in the same graph for comparison (Fig. 4.3a). This plot shows that the 2010 Haiti inventory of Harp *et al.* (2016), which also is well documented and one of the most complete inventories in this EQIL inventory database (Tanyaş *et al.*, 2018), gives the smallest rollover size (~40 m^2) with the highest frequency density value (y-axis in a FAD graph). At the other end of the spectrum, the 2002 Denali inventory of Gorum *et al.* (2014) has the largest rollover size (~16,000 m^2). Gorum *et al.* (2014) noted that many small landslides might not have been mapped in this inventory because of low-resolution satellite imagery. However, the meaning of this large rollover size should not entirely be associated with the poor resolution of the interpreted imagery; many other studies use imagery of similarly low resolution (Fig. 4.3b). Also, it could reflect real differences in the distribution. For example, Jibson *et al.* (2004) stated that compared to comparable or lower magnitudes earthquakes, the Denali earthquake had significantly lower concentrations of rock-falls and rock slides and proposed that this was because the earthquake was deficient in high-frequency energy and attendant high-amplitude accelerations. This argument requires a comprehensive analysis considering the dominant frequencies of earthquakes that is beyond the scope of this study.

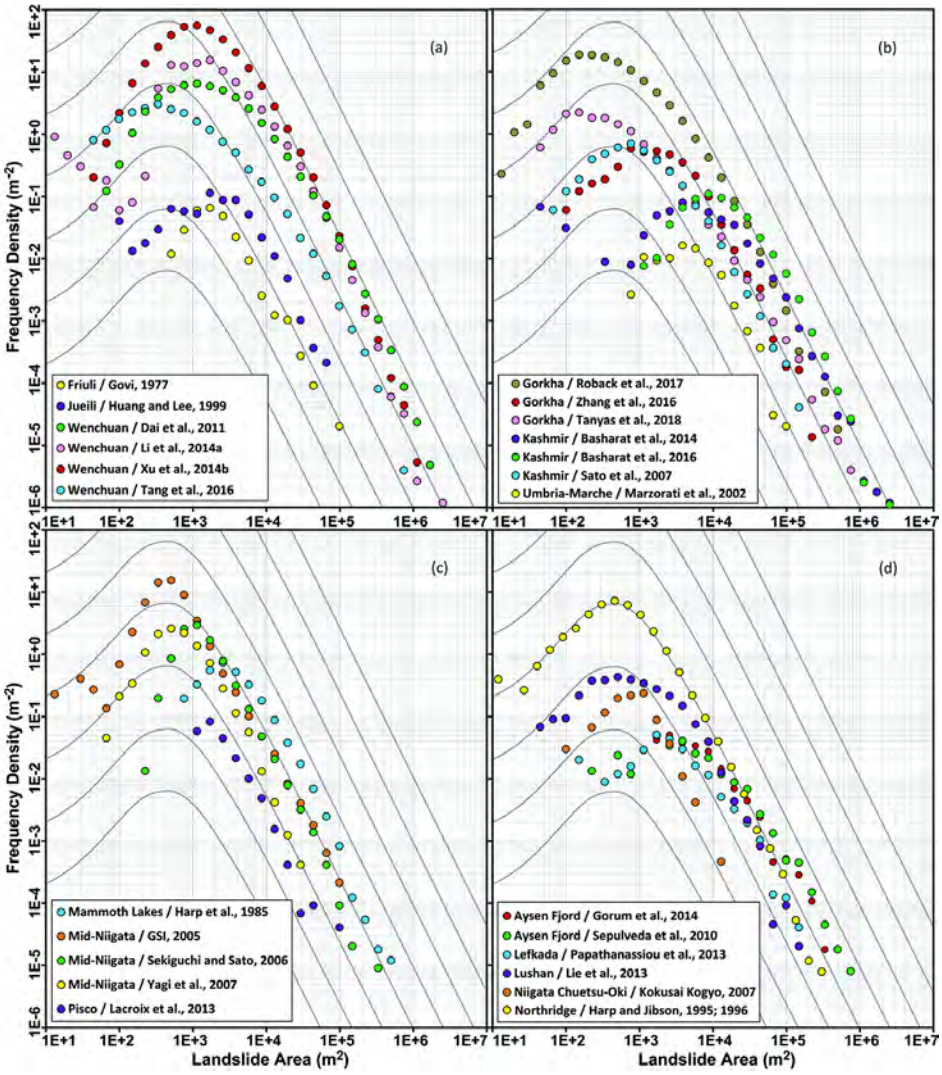

Figure 4.2. FADs of the landslide inventories used in this study, grouped by FAD shape similarity from (a) to (h), overlain on the empirical curves of Malamud et al. (2004) which are shown in black.

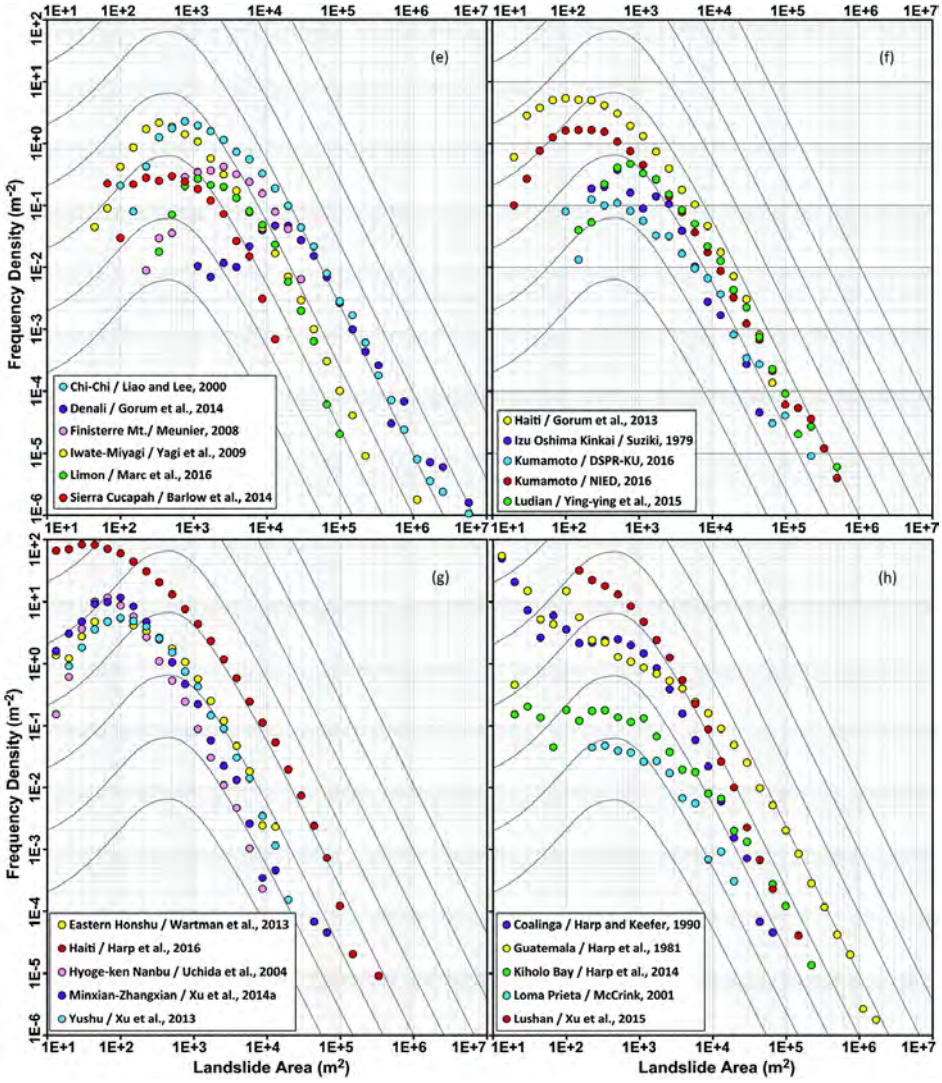

Figure 4.2. (Continued)

We compare the rollover sizes with the cutoff values (R^2=0.333 and RMSE=0.486) (Fig. 4.4a). Although the results show no one-to-one relation between rollover and cutoff values, the increasing cutoff values correlate generally with increasing rollover values. Also, we plot both the rollover and cutoff values in relation to imagery resolution (Fig. 4.4b & 4.4c). The lack of systematic patterns show that high resolution imagery is not required to have a small rollover or cutoff value and vice versa. However, the results do reveal that only the smallest rollovers occur with the highest resolution imagery. This implies that spatial resolution partly controls the rollover point but that other factors also contribute to the divergence from a power-law.

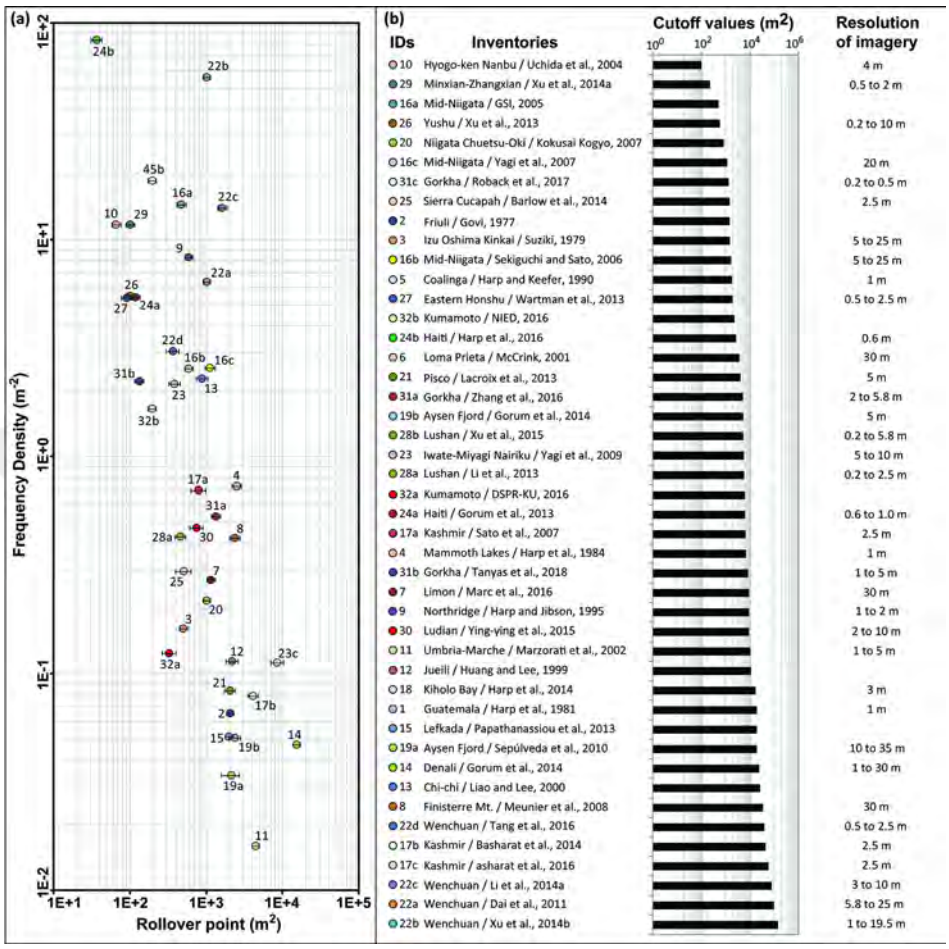

Figure 4.3. Graphs showing the (a) distribution of rollover points, and (b) the inventories with the scale/resolution of used imageries sorted in descending order according to their cutoff values.

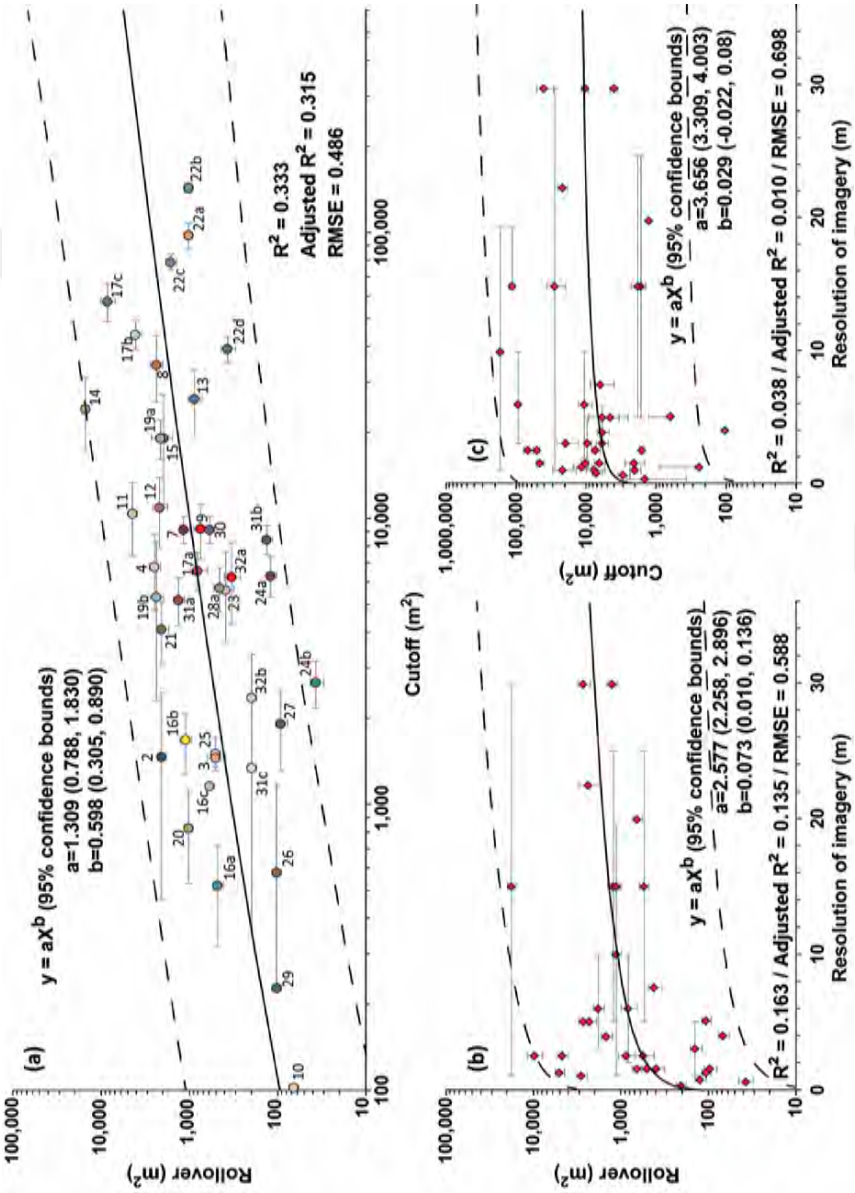

Figure 4.4. Graphs showing the relation between (a) the cutoff and the rollover points, and (b) the rollover and (c) the cutoff values in relation to the resolution of used imagery during the mapping of landslides. 95% confidence intervals for the true responses are indicated by dashed lines.

4.3.3. Proposed hypotheses

Here, we analyze the different proposed rollover hypotheses using examples from the data presented above.

Hypothesis-1 argues that the divergence/rollover is an artifact based on limitations in mapping small landslides. But most event inventories that claim to be complete, which means they include virtually all landslides triggered by the corresponding event down to a well-defined size, also have a rollover (Guzzetti *et al.*, 2002; Malamud *et al.*, 2004). If the divergence were purely a mapping artifact, a very large number of small landslides should be observable following earthquakes, but field investigations and published comprehensive landslide inventories show this not to be the case (Malamud *et al.*, 2004).

To demonstrate this contrast between the theoretical expectation and the field data, we analyze the FAD from the Northridge inventory (Harp and Jibson, 1995, 1996), which used high-altitude analog aerial photography and thus might have inadequate resolution to detect very small landslides. Figure 4.5 shows the Northridge data diverging from the power-law fit around landslide areas of 9,000 m^2. However, Harp and Jibson (1995, 1996) estimated that they missed no more than about 20% of landslides greater than 5 m in maximum dimension and no more than 50% of those smaller than 5 m. They also estimated that they mapped more than 90% of the area covered by landslides, which suggests that most of the landslides larger than 5 m across (≈25 m^2) were mapped in the Northridge inventory.

This resolution estimate differs significantly from the cutoff value. If, in fact, Harp and Jibson (1995, 1996) could not map the small landslides as completely as they thought because of inadequate image resolution, then the FAD for a theoretically complete version of the inventory should follow a power-law also for small landslides. To test this argument, we construct a power-law curve for the Northridge inventory (Fig. 4.5). Based on this theoretical distribution, we calculate the number of landslides for each bin from 25 m^2 to the cutoff point (≈9,000 m^2). For each bin, we also estimate the number of landslides that theoretically should exist and calculate the difference between these values and the number of landslides in the same bins for the actual inventory. The results indicate that more than eight million more landslides would have been triggered than were mapped in the existing Northridge inventory of Harp and Jibson (1995, 1996). Even if landslides smaller than 1,000 m^2 are eliminated, more than 20,000 landslides would be missing from the inventory, which is double the entire number of landslides in the inventory. Also, we estimate the number of theoretically missing landslides for other inventories (Fig. 4.6) using the same method. We tentatively select the lower landslide bin of 25 m^2 for these estimations. Results show that the number of theoretically missing landslides ranges between 3×10^3 and 4×10^{10}, which indicates a dramatic, implausible contradiction between the hypothesis and the data. Thus, it appears that mapping resolution alone is inadequate to explain the power-law divergence.

Hypothesis-2 argues that a change in the underlying failure process from small, shallow failures located in soil and regolith to large, deep bedrock slides causes rollover due to the transition from shear resistance controlled by cohesion to friction. However, we do not know the underground conditions in each landslide-affected area, which would be necessary to evaluate this argument. On the other hand, Larsen *et al.* (2010) assume that

landslides that are smaller than about 100,000 m^2 are generally a combination of both bedrock and soil failures; larger landslides are assumed to be entirely in bedrock. But this does not provide a consistent definition for shallow and deep landslides because Larsen *et al.* (2010) also show that, for example, small landslides (~10 m^2) can involve bedrock at a depth ranging from 0.1 to 10 m. Therefore, landslide size is not a reliable measure to estimate the underlying material.

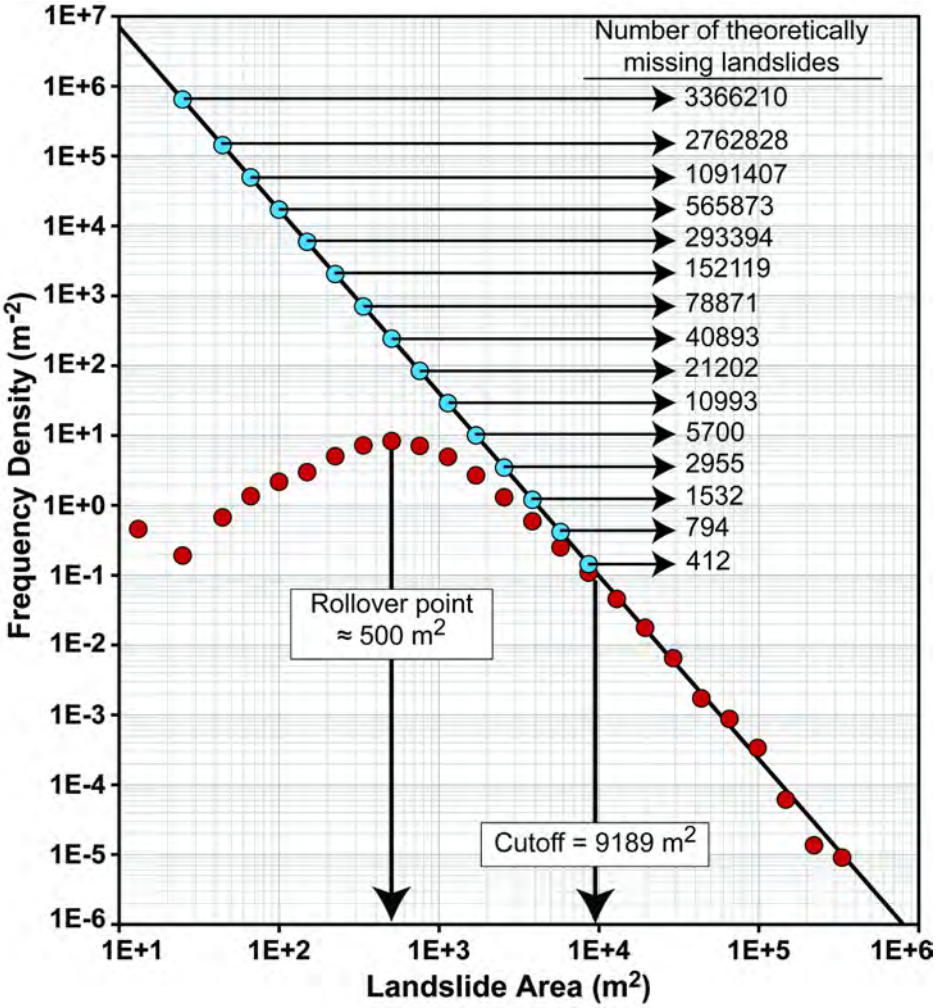

Figure 4.5. Non-cumulative FAD and its power-law fit for the landslide inventory of the 1994 Northridge earthquake (Harp and Jibson, 1995, 1996). The differences between the number of landslides based on the inventory and the power-law fit are indicated. Power-law exponents (-2.62) and cutoff values (9189 m^2) were estimated using the methodology presented by Clauset et al. (2009).

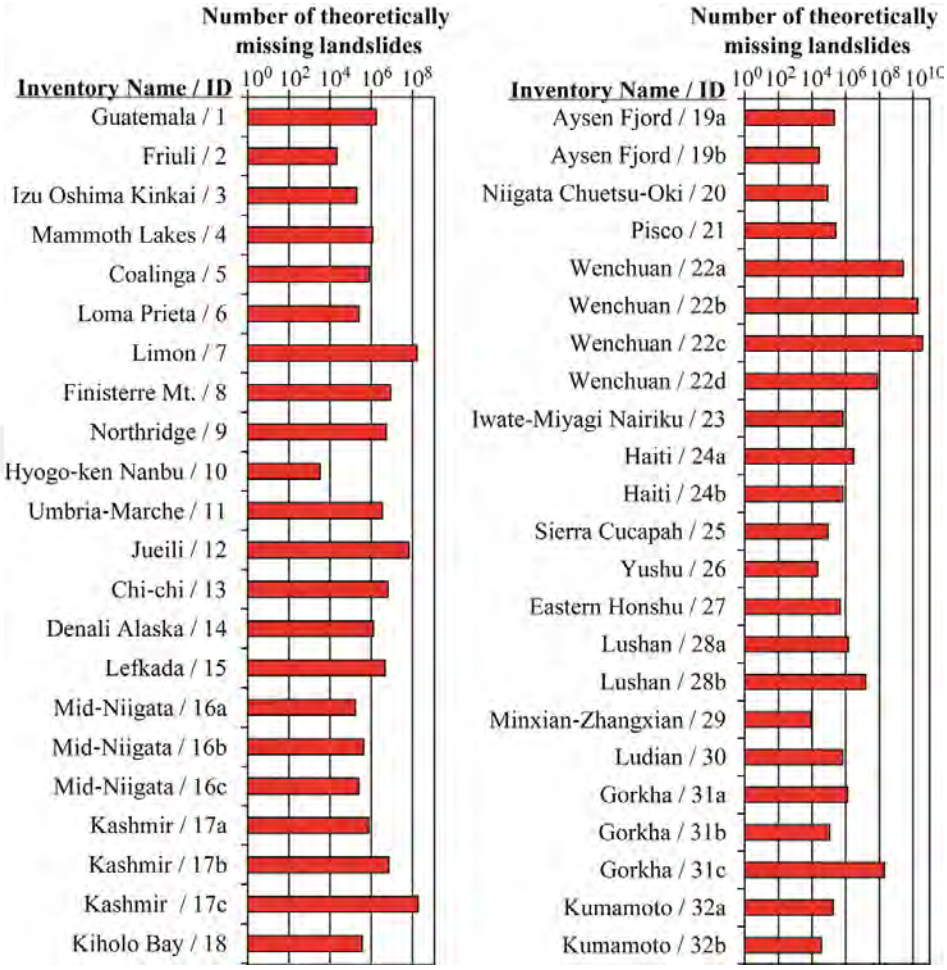

Figure 4.6. Estimated number for theoretically missing landslides in each inventory (Inventory IDs listed in Table 4.1).

Figure 4.3 shows variety in cutoff values from around 102 to 105 m^2. For example, in the 2008 Wenchuan inventory (Xu *et al.*, 2014b) the observed cutoff value is around 144,000 m^2 (Table 4.1), which corresponds roughly to a landslide width of about 400 m. Hypothesis-2 would suggest landslides 144,000 m^2 as the cutoff for small, shallow landslides located within the top soil layer of the hillslope lacking cohesion compared to deeper bedrock. Published studies from Wenchuan, however indicate that rock slides and rock avalanches are moderately common in the Wenchuan inventory, whereas soil slides are much less numerous (Gorum *et al.*, 2011). Xu *et al.* (2014b) state that only 2% of the area affected by landslides is located within unconsolidated deposits. However, landslides smaller than 144,000 m^2 constitute about 50% of total area affected by landslides. This implies that there were many bedrock slides smaller than the observed cutoff value

(<144,000 m^2). Figure 4.3 also shows 15 inventories having cutoff values larger than 104 m^2. As discussed above, classifying such landslides as small soil failures is problematic.

An example from the other end of the spectrum is the Hyogo-ken Nanbu inventory (Uchida *et al.*, 2004), where the cutoff point is 102 m^2 (Table 4.1). Fukuoka *et al.* (1997) report that many shallow debris slides and soil slides were triggered by this earthquake. Similarly, Gerolymos (2008) state that most landslides originated within un-saturated soil. That is why, in this case, the question is why a divergence from the power-law up to the size of 100 m^2 is not observed. Therefore, although Hypothesis-2 does probably account for some of the small-landslide divergence, this explanation appears unable to consistently explain the power-law divergence for each inventory (Table 4.1).

Hypothesis-3 argues that the distribution of soil moisture associated with river networks controls the geometry of landslides. This argument might not apply to earthquake-induced landslides, however, where slides tend to be triggered preferentially in upslope areas rather than along stream networks and are strongly influenced by topographic amplification (Guzzetti *et al.*, 2002). Shallow landslides in upslope areas, which account for a large proportion of all earthquake-triggered landslides (Keefer, 1984) are unlikely to be affected by soil-moisture conditions related to river drainages far downslope. Also, the landslide-affected area of some inventories (e.g., Harp and Jibson, 1995, 1996) was arid, yet extensive seismically induced landsliding still occurred.

To more thoroughly examine Hypothesis-3, we analyze the EQIL inventory database. In each inventory, we calculate the drainage density of the study area, which is the sum of the channel lengths per unit area (Carlston, 1963). To do that, we first derive the river channel network using the r.stream.extract module (Peter, 1994) of GRASS GIS (Neteler and Mitasova, 2013) and then calculate drainage density per square kilometer. We use the Shuttle Radar Topography Mission (SRTM) ~30-m-resolution digital elevation model (NASA Jet Propulsion Laboratory (JPL), 2013) in the analyses. We also use GRASS GIS (Neteler and Mitasova, 2013) r.geomorphon code developed by Jasiewicz and Stepinski (2013) to identify 10 landform classes (flat, summit, ridge, shoulder, spur, slope, hollow, footslope, valley and depression). This algorithm calculates landforms and associated geometry using pattern recognition. The algorithm self-adapts to identify the most suitable spatial scale at each location and check the visibility of the neighborhood to assign one of the terrestrial forms. We mask flat regions and exclude them for the estimation of drainage densities because the river channel network algorithm gives errors in flat regions. We compare the drainage densities to both rollover and cutoff values (Fig. 4.7) and see no relation between either of them. These findings are not sufficient to reject the possible contribution of this approach to the divergence from power-law, but they imply that other process(es) contribute to the divergence.

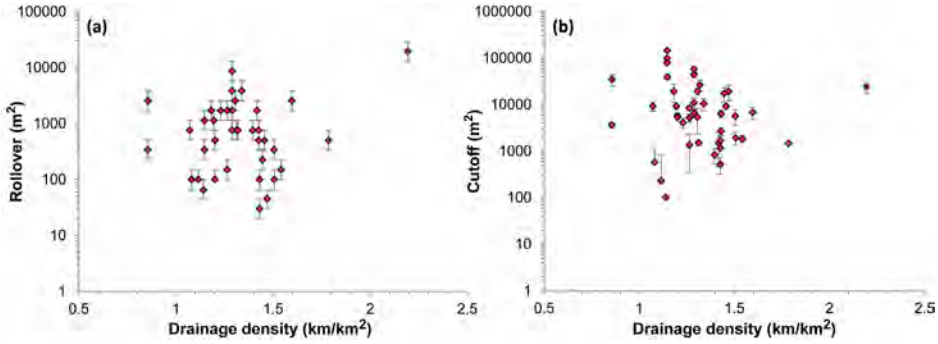

Figure 4.7. Graphs showing the relation between (a) the rollover and (b) the cutoff values in relation to drainage density of landslide effected areas in each inventory.

Hypothesis-4 associates the lack of small landslides with physiographic limitations (slope length) and considers runout zones as an integral part of landslides. However, as described above, landslide deposits (runouts) bias the FAD of landslides, and an ideal inventory would omit runout and only use the source area to define the size of the landslide. Hypothesis-4 suggests that most regions have more areas where large landslides can occur than where small landslides can occur. According to this hypothesis, the upper parts of slopes should be dominated by medium and large landslides, whereas the small landslides should be observed at the lower parts of slopes or on shorter slopes. To test this hypothesis, we analyze the 2015 Gorkha (Roback *et al.*, 2017) inventory where the authors mapped almost all of the source areas separately. We check the size distribution of landslides for lower, middle and upper parts of slopes. To do so, we use the various landforms that we derive above for the entire landslide-affected area of the Gorkha earthquake. We then categorize the obtained landform classes based on their relative position along a slope. We group the summit, ridge, and shoulder landform classes as observable landforms occurring in the upper slope; we associate slope, spur, and hollow with middle slopes. The other landforms, including flat, footslope, and valley, are associated with lower slopes. We calculate zonal statistics for all landslide source polygons and identify the dominant landform category for each landslide. We use the landform class with the most area inside the landslide polygon to identify the dominant landform category. Finally, we check the landslide size distributions for each of the slope segments (Fig. 4.8). Results show quite similar size distributions in different slope segments. Landslides of all sizes occur in each part of the slope. Therefore, the suggested physiographic argument does not seem to explain why the FAD diverges from the negative power-law-distribution.

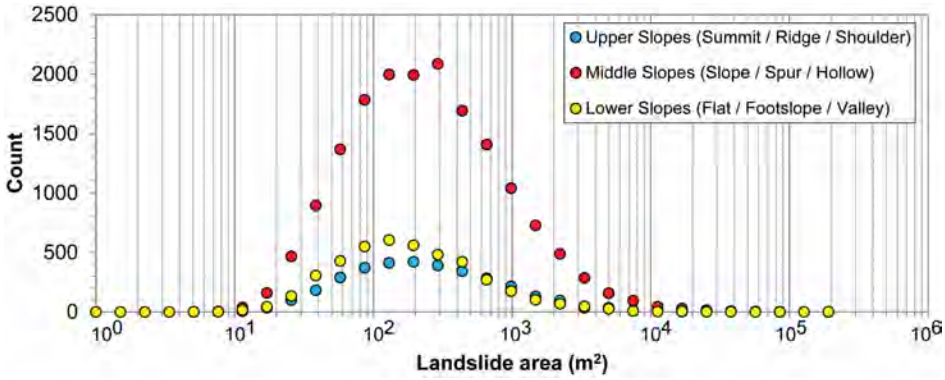

Figure 4.8. Landslide size distributions for different segments of a hillslope differentiated based on various landform groups.

Hypothesis-5 associates the divergence from a power-law with a lack of temporal resolution. However, there is only one case study supporting this argument by monitoring rock-falls on a slope. Validity of this hypothesis for other types of landslide-events has not been checked so far. Therefore, further analyses in other cases and developing a conceptual understanding on this hypothesis are required.

In addition to the above-mentioned hypotheses aiming to explain the divergence from a power-law, there are some factors controlling FADs of landslides. These factors are analyzed in the following section.

4.3.4. Amalgamation due to lack of spatial resolution and mapping preferences

Landslide inventories are created for different purposes and thus both the spatial resolution of examined images and the time invested in making an inventory vary. Figure 4.9 shows an example of amalgamation for the 2015 Gorkha earthquake. The number and boundaries of landslides in this area cannot be determined in a strictly objective way (Fig. 4.9a). Different mapping preferences produce different landslide sizes and numbers (Fig. 4.9b-d). In Figure 4.9b-d, we map this area using progressively more detailed approaches, and the result is landslide counts that vary by almost a factor of three. But all three inventories would be considered valid. Figure 4.9b does not differentiate coalescing landslides; the resulting inventory (Set-1) contains 88 landslides. Figure 4.9c differentiates some of the coalesced landslides that show clear color differences; the resulting landslide Set-2 contains 184 mapped landslides. Figure 4.9d differentiates landslides as much as possible based on both color and textural differences; the result is 253 mapped landslides (Set-3). The shows that when higher resolution images are available, more detailed mapping is possible, and even more landslides can be differentiated.

The same area also was mapped by different authors; the resulting landslide numbers are 19 (Kargel *et al.*, 2016), 32 (Zhang *et al.*, 2016), 40 (Tanyaş *et al.*, 2018), 42 (Gnyawali and Adhikari, 2017), and 151 (Roback *et al.*, 2017).

This example shows that the number of landslides mapped in the same area by different people differed by almost an order of magnitude, and our application of different mapping approaches yielded a difference of a factor of three. Different mapping methods do not significantly affect the total landslide area, but they have an important effect on the landslide FAD. Figure 4.10 shows the FADs of the landslide sets created in this example. From Set-1 to Set-3 the sizes of the biggest landslides decrease, and the rollover points shift toward smaller landslide sizes because the number of small landslides increases. Similarly, because we divide the amalgamated landslides into smaller ones from Set-1 to Set-3, the ratio of small to large landslides increases, and therefore the corresponding power-law exponents also increase.

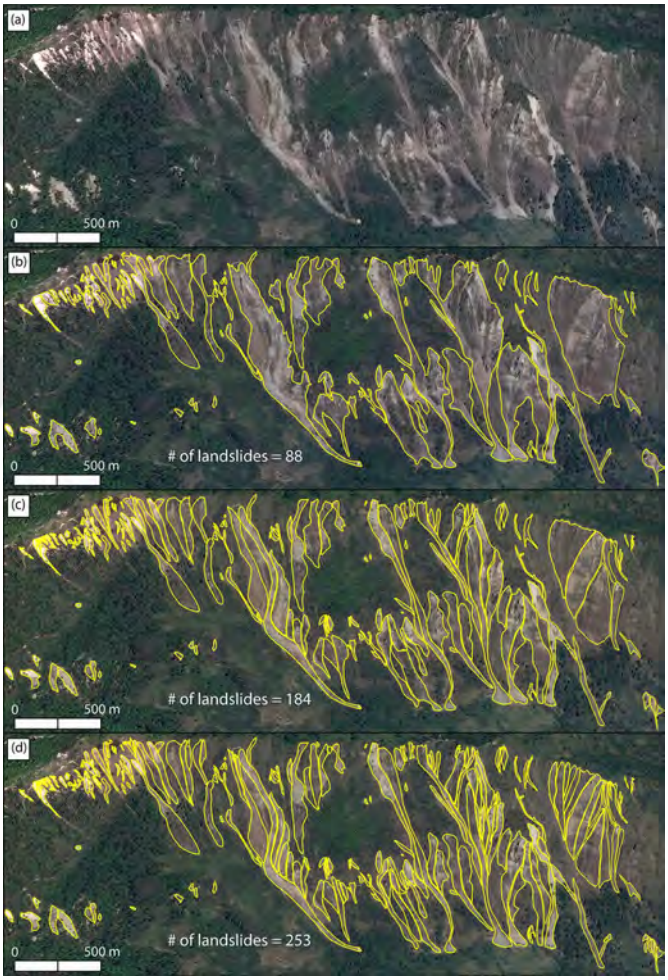

Figure 4.9. An example of an EQIL site near the town of Gumda (28.199°lat, 84.853°lon) from the 2015 Gorkha earthquake: (a)source photograph showing landslides, (b) landslide delineation using maximum amalgamation, (c) landslide delineation using moderate amalgamation, and (d) detailed landslide delineation separating landslides to the maximum extent possible (minimal amalgamation).

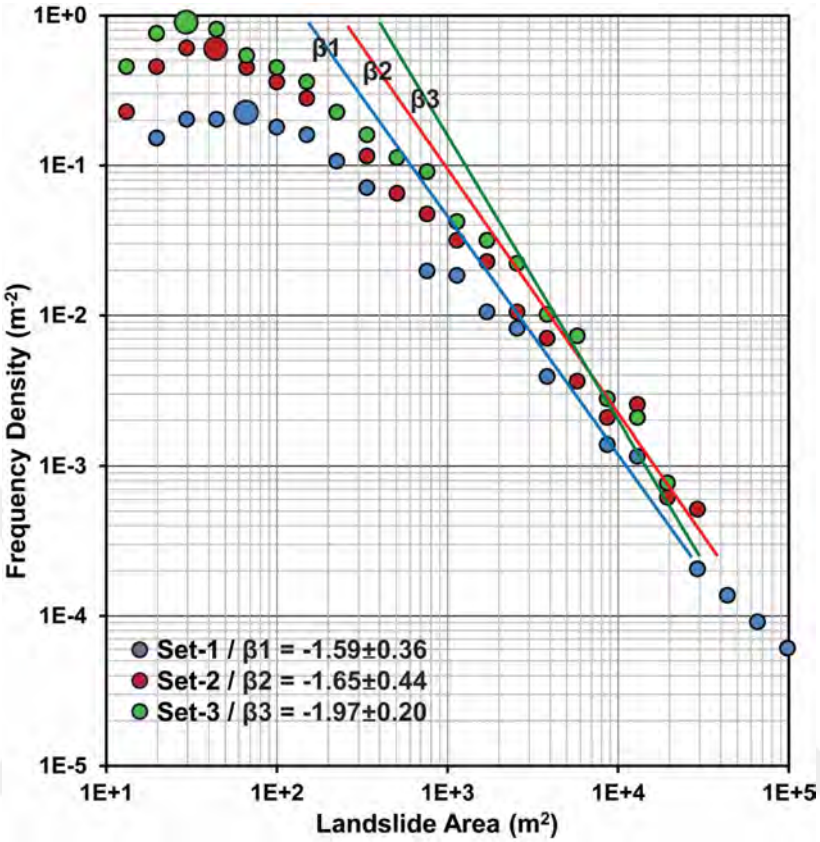

Figure 4.10. FADs and their corresponding power-law fit of different landslide sets presented in Figure 4.9. Larger dots indicate rollover points.

4.3.5. Subjectivity of mapping procedure

To demonstrate the effect of subjectivity of mapping procedures on the resulting FAD, we examine earthquakes for which multiple inventories were produced and compare their FADs. To provide comparable FADs from each earthquake, we trim the inventories to the same extent as the smallest one. As result, we examine landslides from different inventories mapped for the same areal extent. We plot the FADs using the landslides mapped for those areal extents and compare the resulting total number of landslides, total landslide areas (sums of polygon areas), power-law exponents, and rollover sizes. Figure 4.11 shows two examples of the explained comparison of the inventories provided for the 2010 Haiti and 2005 Kashmir earthquakes; figure 4.12 shows the differences between total number of landslides, total landslide areas, power-law exponents, and rollover sizes for all cases. For the same areal extent, the 2010 Haiti inventory of Harp *et al.* (2016) includes 16,379 more landslides than the inventory provided by Gorum *et al.* (2013). This is the largest difference observed in terms of the total number of landslides (Fig. 4.12). For the same areal extent, the difference in the total mapped landslide area in these inventories is 16.9 km^2. We also calculate the total landslide area of completely overlapping polygons of different inventories. The total landslide area mapped by Gorum

et al. (2013) is 5.9 km^2, but 20% of those landslides do not overlap with the polygons delineated by Harp *et al.* (2016). Thus, in total, Harp *et al.* (2016) mapped about 18 km^2 of coseismic landslides that Gorum *et al.* (2013) did not. This means that in this case amalgamation is not the main reason for the significant difference between these two inventories. The inventories were produced using similar visual image-interpretation approaches using detailed images (with a spatial resolution of 0.6-1 m), although Harp *et al.* (2016) did the mapping more carefully over a much longer time period than did Gorum *et al.* (2013).

The difference between the FADs of the Haiti inventories (Fig. 4.11c) implies that a similar number of medium and large landslides (>103 km^2) were mapped in both studies, but Harp *et al.* (2016) mapped a large number of small landslides (<103 km^2) not mapped by Gorum *et al.* (2013). The FAD of the Harp *et al.* (2016) inventory has a smaller rollover point (~30 m^2) and larger power-law exponent (β=2.89) than the Gorum *et al.* (2013) inventory (~100 m^2 and β=2.09). These results are consistent with Figure 4.10, but in this case the differences cannot be attributed to amalgamation of coalescing or adjacent landslides but the subjectivity of the mapping procedures.

We also analyzed three inventories from the 2005 Kashmir earthquake (Fig. 4.11b and 11d). The 2005 Kashmir inventories yield the largest difference in total landslide area mapped for the same areal extent (Fig. 4.11d). The total landslide area mapped by Basharat *et al.* (2016) is 33.6 km^2 (420%) larger than the area mapped by Sato *et al.* (2007). The total landslide area mapped by Sato *et al.* (2007) is 8.0 km^2, and only 45% of this landslide area overlaps with the polygons delineated by Basharat *et al.* (2016). However, Sato *et al.* (2007) mapped 127 more landslides than did Basharat *et al.* (2016). These two Kashmir inventories used the similar mapping method and the same satellite imagery (SPOT 5). These two inventories are quite different although they are from the same event, have the same areal extent, and used the same mapping method. Their FADs also are quite different, and the rollover point is much smaller in the Sato *et al.* (2007) inventory (~760 m^2) as compared to the Basharat *et al.* (2016) inventory (~8650 m^2). In contrast, however, the Basharat *et al.* (2016) inventory has a higher power-law exponent (β=3.01) than the Sato *et al.* (2007) inventory (β=2.37).

Figure 4.11 shows that mapping preferences could cause a large difference in FADs of landslides and related factors such as β. The largest difference between power-law exponents in the examined cases is the Haiti example with 0.80 (Fig. 4.12). Considering the power-law exponent of the Haiti inventory of Gorum *et al.* (2013) (β=2.09±0.80), the difference is 38% of the calculated value. This shows that the uncertainty in β values caused by mapping preferences can be as much as 38%. Korup *et al.* (2012) state that minute numerical errors in model parameters of FADs can cause uncertainty greater than a factor of two in erosion or mobilization rates. Thus, we can expect a large uncertainty, for example, in denudation rate (e.g., Hovius *et al.*, 1997) because of this variance in β.

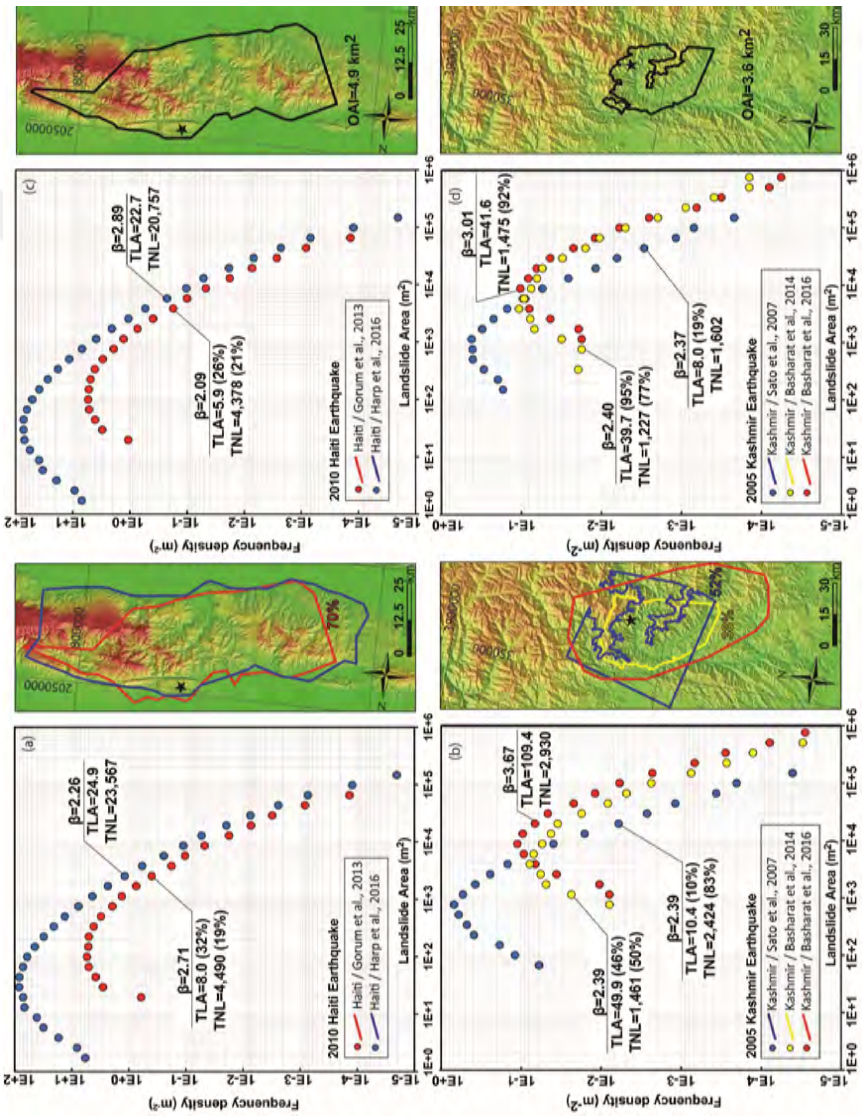

Figure 4.11. FADs of inventories produced for (a) & (b) the same earthquakes with the extent of the corresponding inventories' mapped areas, and (c) & (d) the trimmed versions of them for the common areas. TLA: Total landslide area (km²), TNL: Total number of landslides, OAI: Overlapping areas of inventories.

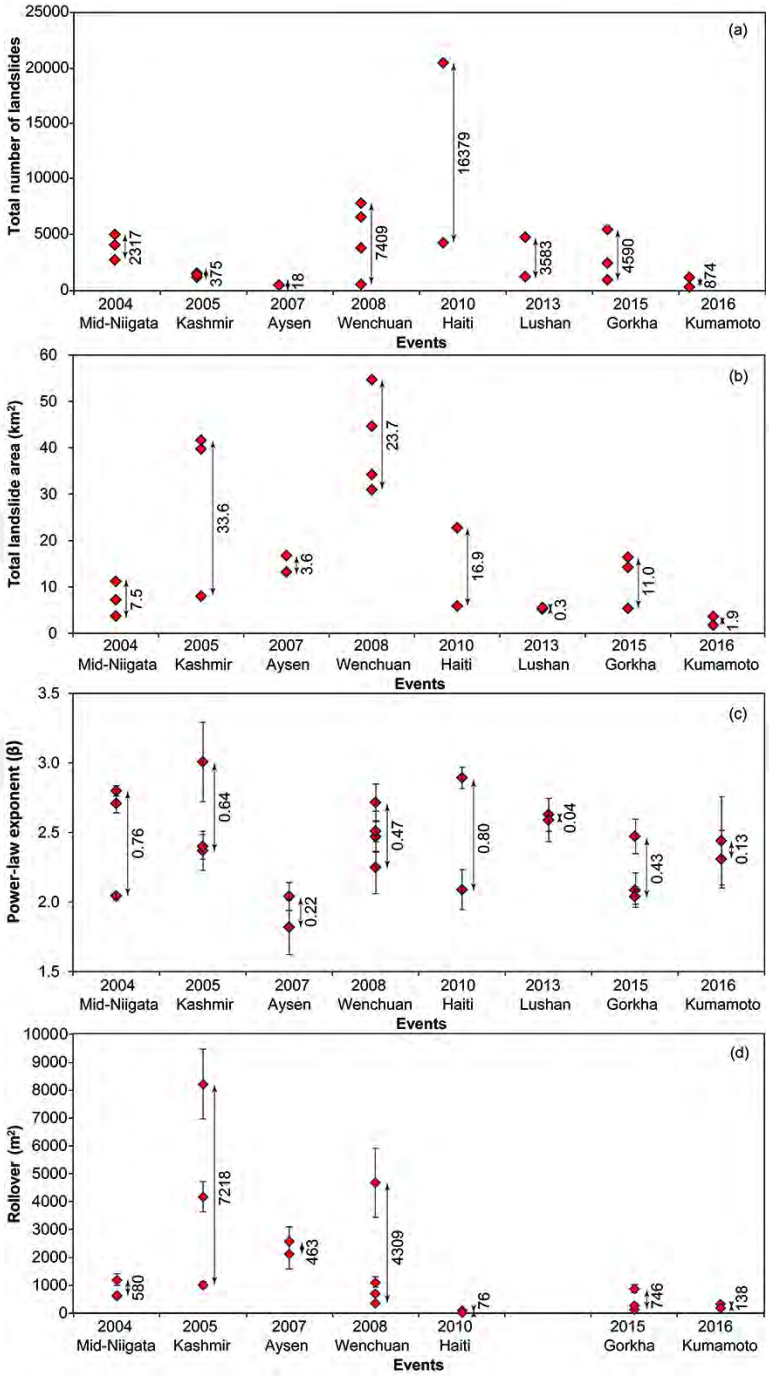

Figure 4.12. Variability in (a) total number of landslides, (b) total landslide area (c) β, and (d) rollover sizes for the events having multiple inventories. To plot this figure, we trimmed the inventories to the same extent as the smallest one.

Several studies have explored the relation between variations in β with regional differences in structural geology, morphology, hydrology and climate (e.g. Bennett *et al.*, 2012; Chen, 2009; Densmore *et al.*, 1998; Dussauge-Peisser *et al.*, 2002; Hergarten, 2012; Li *et al.*, 2011; Sugai *et al.*, 1995). However, the analyses presented above reveal that the uncertainties are likely too high to discriminate physical regional differences. This is because regardless of these factors and despite the similarities in terms of overall mapping methodology and images used, differences in mapping skills, mapping criteria, thresholds of minimum landslides that are mapped, and the time dedicated to mapping might result in very different inventories. As a result, FADs of landslides and related factors such as β are exposed to an intrinsic noise caused by the subjectivity of the mapping procedure. Unfortunately, quantifying the quality of the inventories directly from FADs is impossible without re-mapping the landslides from the original imagery from which the inventories were made. Thus, further standardization of landslide mapping procedures and proper metadata of landslide inventories that explain the mapping procedure and time investments are the only ways to minimize this noise and potentially, one day, be able to resolve the signal of regional differences.

4.3.6. Effect of distinguishing between landslide sources and deposits on FAD shape

Some inventories distinguish landslide sources from deposits, at least for larger landslides. The FADs and rollover points in such inventories differ somewhat from those of inventories where landslides are mapped as a single polygon without differentiating erosion and accumulation areas. In the 2004 Mid-Niigata (GSI, 2005) inventory, large and small landslides are defined separately, and for the large landslides the sources and deposits were mapped separately. For the 2004 Mid-Niigata (GSI, 2005) and the 2015 Gorkha inventories (Roback *et al.*, 2017), we divide the landslides into two sets. In Set-1 the sources and deposits of landslides are considered together; in Set-2 the deposits of large landslides are ignored, and we only consider the source areas (Fig. 4.13).

The exclusion of landslide deposits in Set-2 decreases the size of individual landslides and shifts the position of the entire FAD toward smaller sizes. The rollover points also shift from 3850 m^2 to 1700 m^2 (Fig. 4.13a) and from 210 m^2 to 30 m^2 (Fig. 4.13b) in the Mid-Niigata and the Gorkha inventories, respectively.

Figure 4.13 shows significant differences between FADs from source-only inventories and those constructed using entire landslide polygons. However, a rollover in the FAD is present even when landslide deposits are excluded.

We also numerically check the validity of a power-law fit for both versions of the Mid-Niigata and the Gorkha inventories. Results show that in both cases size distributions of landslide source areas have significantly larger p-values (better fits) than size distributions considering sources and deposits of landslides together (Fig. 4.13). In the Mid-Niigata case, both versions of the inventory have p-values larger than 0.1, whereas the p-value of Set-1 for the 2015 Gorkha earthquake is zero. This shows that the Roback *et al.* (2017) Gorkha inventory that includes deposits does not fit a power-law. However, for the same inventory, the exclusion of landslide deposits yields a good power-law fit with a p-value of 1. These findings show that differentiation of source and deposit areas strongly affects the resultant FAD.

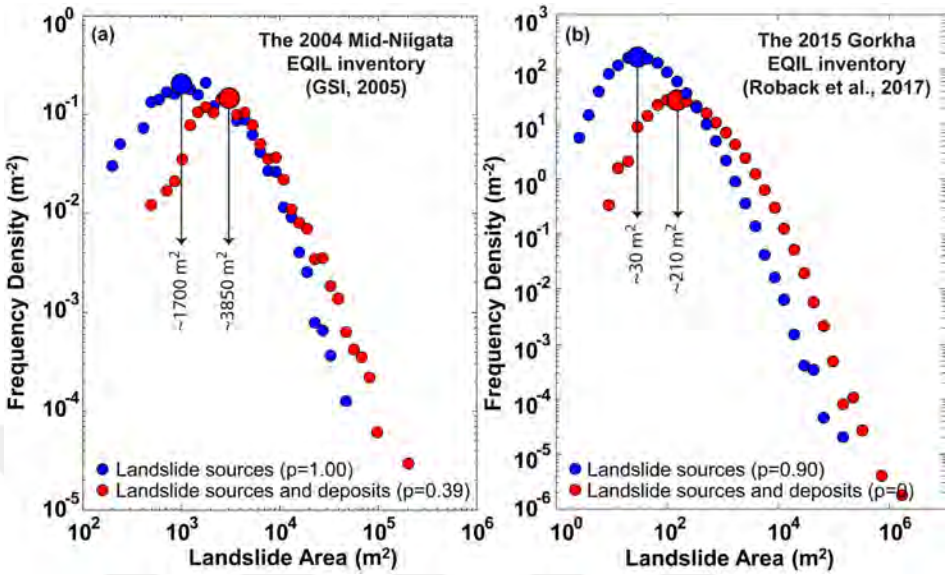

Figure 4.63. FADs for different subsets of (a) the 2004 Mid-Niigata (GSI, 2005), and (b) the Gorkha (Roback et al., 2017) EQIL inventories. Larger dots indicate rollover points.

4.4. Discussion

Several hypotheses have been proposed for the causes of the deviation from a power-law relation for smaller landslides. Our findings show that each hypothesis helps us to grasp a part of the phenomenon but no single existing explanation accounts for the deviation and rollover in all cases, and different factors contribute to explain the causes of the rollover in different cases. Especially, lack of spatial image resolution and details of the underlying failure process as proposed in previously published studies clearly contribute to the divergence from the power-law. Additionally, lack of temporal resolution also is a considerable factor because identifying each individual landslide event that actually occurred is impeded by lack of temporal resolution. We approach this issue within the context of successive slope failure, as described below.

4.4.1. A proposed explanation for the divergence from the power-law: Successive slope failure

A single mapped landslide polygon can be the result of successive episodes of movement and enlargement. Frattini and Crosta (2013) referred to this issue and stated that even for accurate inventories of single events, many smaller landslides can be undetectable because of reworking during the event by larger coalescent landslides. For example, earthquake shaking can cause part of a slope to collapse, which creates a scarp and a runout zone. The scarp itself can be unstable and further fail and expand afterward; this produces an additional landslide above the first one, but this subsequent landslide will be mapped as part of the original failure. This process can occur in succession during a later part of the shaking of the mainshock or as a result of aftershocks, subsequent rainfall, or progressive failure owing to weakened soil material and changes in the slope stress field.

Thus, what we observe as a single landslide polygon is a snapshot of the geometry of an accumulation of successive sliding events at the time the imagery was collected; the slope will continue to evolve indefinitely as it adapts to the new conditions (Fig. 4.14). Therefore, the inverse-cascade model, which is the qualitative explanation provided for the fractal distribution of landslides (Malamud and Turcotte, 2006), should be valid for the formation of mapped individual landslides. As we described above, the inverse-cascade model suggests that slope instability begins in a location and spreads to surrounding metastable areas. The landslide population formed as a result of this process has a fractal size distribution. As the inverse-cascade model is applied to slopes shaken by earthquakes, we call this sliding process successive slope failure.

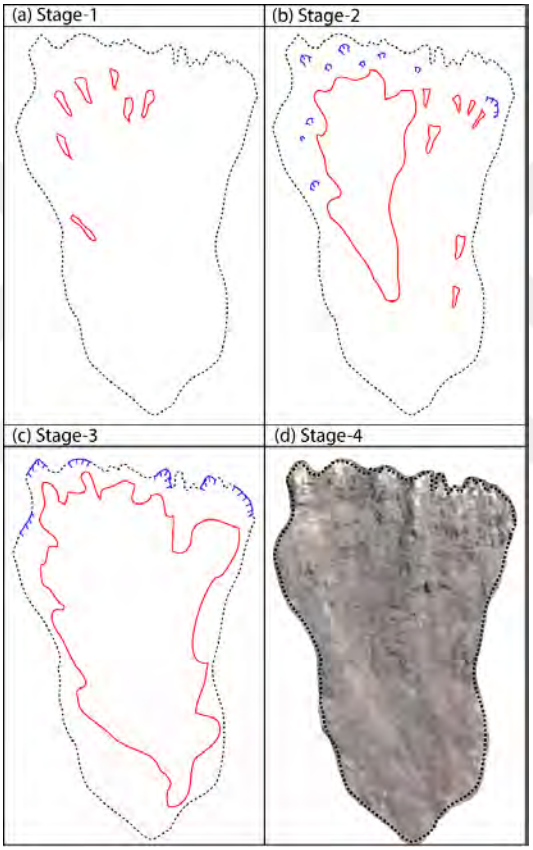

Figure 4.14. Schematic drawing showing different hypothetical stages of the landslide initiation process: (a) small slides are triggered making a initiating larger landslide that will be formed in the next stage; (b) a larger slide is triggered, and it decreases the stability of entire slope; tension cracks and some other new small slides form; (c) slides of various sizes are triggered; they coalesce and form a larger body, but the overall slope remains unstable; and (d) many other slides are triggered, which cover the previously triggered landslides; they form an even larger final landslide geometry, until the slope reaches a stable state. Dashed black lines represent the final landslide geometry; red lines show newly triggered landslides in each stage; and blue lines show tension cracks.

Successive slope failure encompasses processes such as progressive and retrogressive failures, which are specific mechanisms that can contribute to successive slope failure. Progressive slope failure is a common mode of failure that occurs in cohesive materials such as clays (Bjerrum, 1967). In progressive slope failure, after the initiation of the first landslide, the scarp is in a metastable condition, and a second slide begins to mobilize from the scarp area sometime after the initial slide (Bjerrum, 1967). This can continue to cascade upslope through the progressive propagation of a shear surface along which shear strength is reduced from peak to residual values. This occurs because shear strength is not constant along a potential failure surface in cohesive materials; the strength changes from peak to residual (Bjerrum, 1967). Thus, spatial and temporal strength heterogeneities are the cause of progressive failures. Successive slope failure applies more generally than progressive failure because successive slope failure occurs in different types of soil and rock. For example, Terzaghi (1962) described rock masses generally as media having discontinuous joints differing in persistence. Intact rock bridges occur between these discontinuous joints. Failures begin with the failure of an individual rock bridge and keep occurring successively as the shear strength of each individual bridge is exceeded. Eberhardt *et al.* (2004) modeled the rock-mass strength degradation in natural rock slopes based on the conceptual framework of Terzaghi (1962). They show that stresses ahead of the shear plane increase and subsequent intact rock bridges fail in a consecutive manner until the surface of failure extends to the point where kinematic release becomes possible.

Successive slope failure also can occur as a result of retrogressive failure, which refers to a specific failure geometry wherein a failure zone migrates upslope (Cruden and Varnes, 1996). However, successive slope failure is much more general than retrogressive failure; it can involve destabilization of slopes laterally, upslope, downslope, or by several mechanisms and geometries. It is simply the process of an initial slope failure destabilizing surrounding areas.

Successive slope failure might not apply to landslides in massive rocks where failure commonly is controlled by discontinuities such as faults, fractures, shear zones, bedding planes and joints (Hoek and Brown, 1997). Such discontinuities isolate the landslide mass from the rest of the slope. Therefore, for rock-falls, having a frequency-size distribution without rollover is understandable in some cases (e.g., Malamud *et al.*, 2004). Even in this situation, however, landslide margins are likely to produce smaller, continuing failures as the disturbed topography seeks equilibrium. For example, Williams *et al.* (2018) showed a rollover in frequency-size distribution of rock-falls if mapping is conducted using a low temporal resolution.

4.4.2. The interpretation of the proposed explanation

The successive-slope-failure hypothesis, which extends the argument raised for rock-falls in Hypothesis-5 (Barlow *et al.*, 2012; Williams *et al.*, 2018) provides a conceptual model to explain the power-law divergence. Figure 4.15 schematically presents this hypothesis in terms of FAD; landslide numbers observed at different size bins are shown. Figure 4.15a shows a theoretical FAD assuming that all EQIL triggered during the event are detected and that landslide FADs across all size ranges follow a pure power-law behavior. However, in practice, larger landslides are mapped because many smaller ones that occur at the

initiation of sliding are incorporated into larger ones or are mapped together into amalgamated polygons (Fig. 4.15b). Additionally, some of the smaller landslides are superimposed by larger ones. Therefore, some landslides could not be mapped into their correct size bins, and they are transferred into a larger landslide bin. This causes identification of more large landslides because the smaller slides merge into larger ones. This also causes identification of fewer total landslides, particularly in the smaller size range, than theoretically expected based on the power-law distribution assumption; this, in turn, causes the divergence from the power-law distribution (Fig. 4.15c). Without conducting a continuous monitoring, capturing the effect of this misclassification on small landslide bins is not possible. Thus, the misclassification of landslide size bins might or might not cause a distinctive decrease in small landslide bins. If it is distinctive, a rollover and positive power-law decay for smaller landslide sizes emerges (Fig. 4.15c). This is observed in most of the inventories presented in this study (Fig. 4.2). If the effect of unmapped small landslides is less distinct, landslide FADs still diverge from a power-law distribution but do not show a rollover point. Figure 4.2h shows such an unusual trend in the FADs for the Coalinga (Harp and Keefer, 1990), Guatemala (Harp *et al.*, 1981), and Lushan (Xu *et al.*, 2015) inventories. This likely reflects the complicated interplays between mapping methodology, landslide amalgamation, and the successive-landslide-formation process on the final FAD.

This explanation implies that neither divergence from the negative power-law distribution of medium and large landslides nor a positive power-law distribution for landslides smaller than the rollover point are attributable to the incompleteness of an inventory: both of these characteristics can occur in complete landslide inventories. In our proposed explanation, some of the small landslides that could not be mapped in the correct size bins are included in the larger bins; therefore, an inventory with a rollover can be relatively complete in terms of total mobilized landslide area.

Our proposed explanation suggests that neither the rollover nor cutoff points indicate the exact lower landslide size at which the inventory can be assumed to be complete (e.g., Parker *et al.*, 2015; Van Den Eeckhaut *et al.*, 2007). Because we generally do not know the minimum landslide size where mapping is nearly complete, the rollover point can be used as an upper-bound estimate of that value.

The proposed explanation also suggests that mapping many medium and large landslides should inevitability cause misclassification of a relatively large number of small landslides, and this leads to a shift in both rollover and cutoff values towards larger sizes (see Figure 4.15). To test this argument, we arbitrarily select three landslide sizes of 1,000 m^2, 2,500 m^2, and 5,000 m^2 as the thresholds between small and medium landslides, and we correlate both the rollover and cutoff points with the percentages of landslides having areas greater than 1,000 m^2, 2,500 m^2, and 5,000 m^2 (Fig. 4.16). The results confirm our argument and show that in an inventory that includes a relatively large number of large landslides both the rollover and cutoff values shift toward larger sizes compared to inventories having relatively few large landslides. This finding provides evidence to support our hypothesis about the cause of FAD rollover.

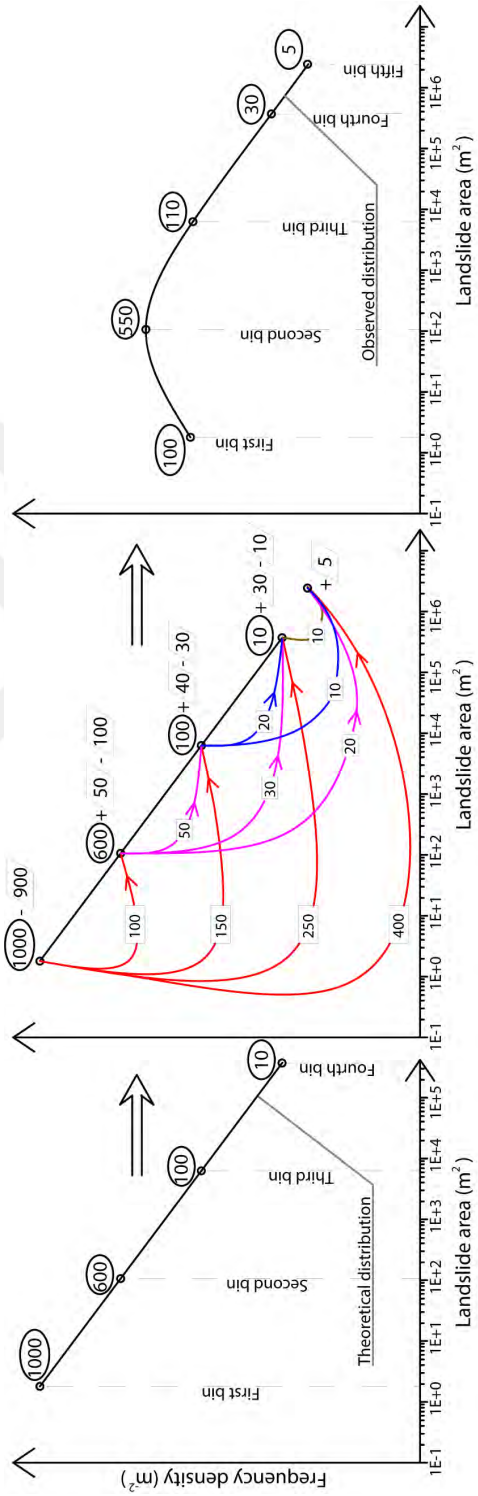

Figure 4.15. Schematic drawing showing the number of landslides of different sizes in different theoretical situations. (a) Theoretical FAD of landslides if all individual landslides were mapped perfectly; (b) Smaller landslides are amalgamated or mapped inside larger ones. For example, 900 small landslides in the first bin are merged into larger ones; 100 landslides into the second bin; 150 into the third bin; etc. (c) The resulting observed FAD with rollover. The numbers shown in ovals and parallelograms indicate the initial/final and transferred number of landslides, respectively. The numbers of landslides transferred from smaller bins to larger ones are not equal to each other because multiple small landslides merged together and formed fewer larger landslides. The given landslide numbers are partially arbitrary; both the numbers of landslides in each bin and the numbers of landslides transferred from smaller bins to larger ones have a decreasing trend from small to larger landslide sizes.

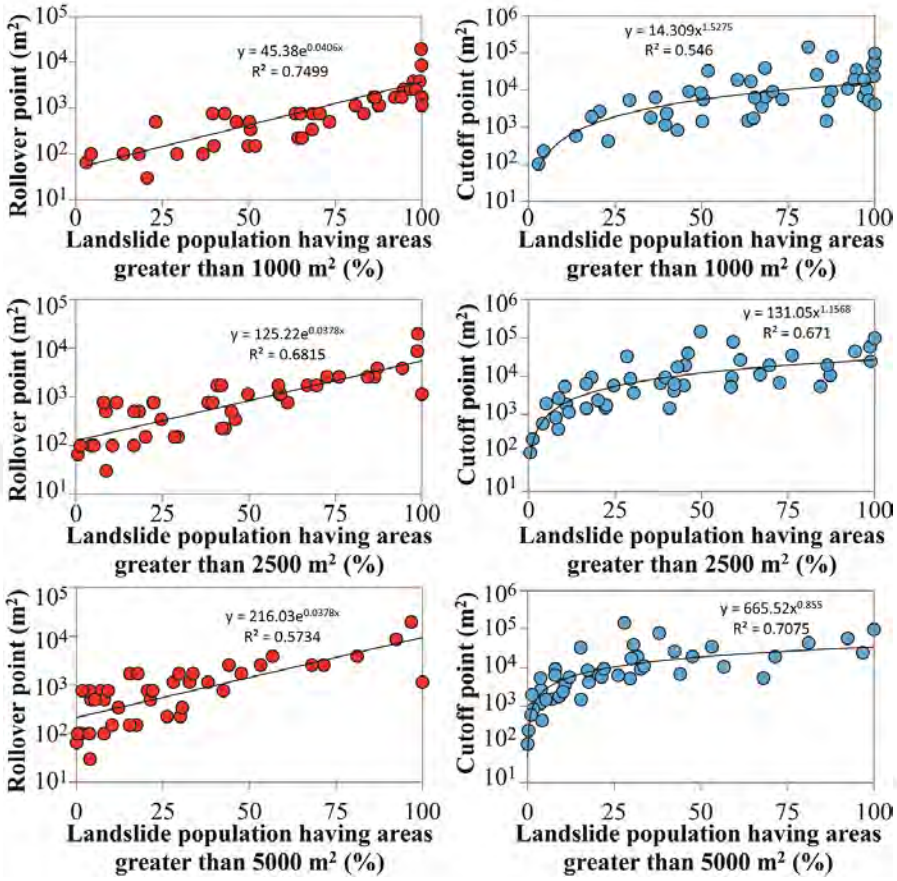

Figure 4.16. Relation between the percentage of landslide population having areas larger than 1,000 m^2, 2,500 m^2, and 5,000 m^2 and the location of the rollover and cutoff points.

Additionally, as presented above, the findings of Barlow *et al.* (2012) and Williams *et al.* (2018) derived for rock-falls also support our conceptual model to explain the power-law divergence. However, this conceptual model still needs to be proven by high temporal resolution slope monitoring.

4.5. Conclusions

This study examines the factors controlling the FADs of landslide inventories and provides an alternative explanation for the deviation from power-law scaling observed in the FADs by analyzing 45 EQIL inventories. All existing rollover explanations described above provide a partial understanding of why landslide FADs do not follow the power-law theory for small landslides. Although not all explanations contribute to each case, each inventory probably involves some combination of the proposed explanations.

We propose an additional explanation: successive slope failure, in which smaller slides sequentially destabilize surrounding slopes and merge to form larger slides that are detectable after the earthquake.

Studies by Barlow *et al.* (2012) and Williams *et al.* (2018) demonstrate the importance of temporal resolution on rock-fall FADs and provide observational support for our hypothesis. We use this argument and present a theoretical background with all findings obtained from 45 EQIL inventories showing that the actual number of coalesced landslides within each landslide polygon is unknown because we lack the necessary time resolution of observations used for mapping. This means that low time resolution, a mapping artifact, is one of the reasons for the divergence from the power-law. Therefore, the divergence from a power-law does not necessarily imply incompleteness of an inventory.

Additionally, we show that mapping methodology, amalgamation of coalescing landslides due to the quality and resolution of the imagery, the level of expertise of mappers, and undifferentiated landslide source and deposit areas causes intrinsic noise in landslide FADs. These factors contribute in various combinations to determine the FAD shape, which is defined by the power-law exponent, cutoff point, and rollover. That is why the shape of a FAD, and thus β, can vary significantly because of the complicated interplay between the given factors. The uncertainty in β values caused by these factors can be as much as 38% (e.g., $\beta=2.09\pm0.80$ in Haiti inventory of Gorum *et al.* (2013)). A 38% uncertainty can cause substantial errors in prediction of erosion rates (e.g., Korup *et al.*, 2012) and landslide hazard assesments (e.g., Guzzetti *et al.*, 2005) because of the resulting divergence in both landslide-event magnitude and probabilities of landslide size.

Based on these findings, our analyses lead to four main conclusions. First, the rollover point generally is at a larger landslide area than the lower limit of completely mapped landslide size of the inventory. Second, various mapping techniques can yield different total numbers of landslides, and thus the number of landslides is a subjective measure. Third, the FAD-based completeness evaluation of Malamud *et al.* (2004) needs to be revised. Finally, inventories that depict landslide source areas separately from depositional areas yield more physically meaningful FADs for EQIL inventories.

The highlighted uncertainty in FADs of landslides implies that the power-law derived from a low-quality inventory does not describe landslides very well. This shows the need for a standard mapping methodology to be able to obtain more consistent and quantitative information about landslides from FAD comparisons. Working with compatible inventories can help in modeling FADs of EQIL inventories more accurately. Such a FAD model also can help better quantify landslide event inventories and provide a reasonable basis to evaluate the completeness of inventories. Reliable FADs of EQIL also can help improve our knowledge regarding landscape evolution processes.

5. Rapid prediction of magnitude-scale of landslide events triggered by an earthquake[5]

5.1. Introduction

An earthquake-induced landslide-event refers to landslides triggered by a particular earthquake. Such landslides are one of the most destructive secondary hazards associated with earthquakes in mountainous environments (e.g., Jibson *et al.*, 2000). Therefore, the estimation of earthquake-induced landslide hazard is an important risk mitigation component in seismically active mountainous areas (Wasowski *et al.*, 2011).

EQIL inventories are the primary data source to extend our knowledge of the relationship between earthquakes and the landslides they can trigger (e.g., Tanyaş *et al.*, 2017). Using an EQIL inventory, we can assess the distribution of landslides and better evaluate the total earthquake impacts considering this secondary seismic hazard (e.g., Robinson *et al.*, 2017).

The impact of EQIL-events can be quantified using landslide inventories (e.g., Malamud *et al.*, 2004). Keefer (1984) used the number of triggered landslides (N_{LT}) to define an EQIL-event magnitude scale (mLS), which quantifies the severity of the event, and it is defined as follows:

$$mLS = logN_{LT} \qquad \text{(Equation 5.1)}$$

According to the method proposed by Keefer (1984), the magnitude scale of an EQIL-event triggering 10^2 - 10^3 landslides is classified as ”class 2”; 10^3 - 10^4 landslides is classified as ”class 3”, etc. This is an important concept because we could better evaluate the relation between landslide causes and impacts as a quantitative approach simplifies a complex phenomenon into a single, or a few, standard values (i.e., landslide-event magnitudes) which can be compared between triggering events (Tanyaş *et al.*, 2018) (Chapter 3).

Malamud *et al.* (2004) used Keefer (1984)’s method to define mLS ($Eq.5.1$) and improved this method using the size statistics of the landslides associated with various triggers such as an earthquake, a rapid snowmelt or a large storm. Malamud *et al.* (2004) established that the frequency-area distribution of landslides follows an inverse power-law for medium-

[5] This chapter is based on the following paper: Tanyas, H., van Westen, C.J., Persello, C., and Alvioli M. Rapid prediction of magnitude-scale of landslide events triggered by an earthquake, Landslides, under review, 2018.

to large-sized landslides, while the distribution shows a rollover at smaller landslide sizes. They modelled the frequency-area distribution of three well-documented event inventories and defined empirical curves to identify mLS. Many studies make use of the empirical distribution of landslide sizes, independently on the trigger of the landslide event (Malamud *et al.*, 2004). For example, Guzzetti *et al.* (2005) extracted the probability of landslide size from frequency-size statistics of landslides and used this information for quantitative analysis of landslide hazard. The power-law region of the distribution can also be reproduced by different physically-based models (Alvioli *et al.*, 2014; Alvioli *et al.*, 2018b; Hergarten, 2012).

A magnitude scale for the landslide-events can be defined by identifying the power-law fits for medium and large landslides. Thus, the examined landslide inventory may be partial (i.e., some small landslides may be missing), but the assigned mLS is equivalent to the one associated to complete landslide-event based on a frequency-area distribution, obtained by properly rescaling a frequency density curve to the measured distribution in the power-law region as in Malamud et el., (2004). Malamud *et al.* (2004) also proposed a method to estimate the total landslide area (A_T), maximum landslide area (A_{Lmax}) and volume triggered (V_{LT}) by one event (e.g., earthquake, rainstorm) in relation with mLS ($Eq. 5.2 - Eq. 5.4$), defined as follows:

$$A_T = 3.07x10^{-3}x10^{mLS} \quad \text{(Equation 5.2)}$$

$$A_{Lmax} = 1.10x10^{-3}xN_{LT}^{0.714} \quad \text{(Equation 5.3)}$$

$$V_{LT} = 7.30x10^{-6}xN_{LT}^{1.1222} \quad \text{(Equation 5.4)}$$

Regarding the estimation of mLS, Tanyaş *et al.* (2018) (Chapter 3) introduced an updated method that better fits the observations. They determined a slope (power-law exponent) of the power-law fit for each specific landslide inventory and used this value instead of the average value (2.4) used by Malamud *et al.* (2004) to define the empirical frequency-area distribution curves. To construct the empirical curves, Tanyaş *et al.* (2018) rotated the power-law fits around a reference point identified considering the most reliable EQIL inventories. They then determined the mLS using the constructed empirical frequency-area distribution curves. They also checked the variation in mLS in their proposed method based on different reference points and identified 95% confidence limits for various mLS intervals (Table 5.1). The mLS values determined by Tanyaş *et al.* (2018) are presented in Table 5.2.

Table 5.1. Variation in mLS (Tanyaş et al., 2018) (Chapter 3).

	mLS				
	2≤mLS<3	3≤mLS<4	4≤mLS<5	5≤mLS<6	6≤mLS<7
Variation	±0.30	±0.33	±0.20	±0.36	±0.63

Tanyaş *et al.* (2018) also proposed an updated equation to estimate total landslide area (A_T) triggered by an earthquake in relation with mLS (Equation 5.5):

$$A_T = 0.0125e^{(1.7651*mLS)} \quad \text{(Equation 5.5)}$$

However, calculation of mLS requires a landslide inventory which is not available for most of the landslide triggering earthquakes. The preparation of a landslide inventory is a tedious process (e.g., Wasowski *et al.*, 2011), despite advances in mapping techniques, and it may take months to complete when based on visual image interpretation, or weeks when based on (semi-) automated image classification (Martha *et al.*, 2010). In any case, the time required to create an EQIL inventory is too long to provide information for rapid emergency response phase after an earthquake (Robinson *et al.*, 2017).

To capture the effect of an EQIL-event without having an inventory, some statistical relations were proposed, using a global dataset, between earthquake magnitude and the area affected by landslides or the maximum landslide distance, either from the epicenter or the rupture zone (Keefer, 1984; Rodriguez *et al.*, 1999). However, Jibson and Harp (2012) found that the proposed landslide distance buffers differ between plate-boundary earthquakes and intraplate earthquakes, where seismic-wave attenuation is generally much lower and thus the proposed relation could not be used for accurate estimation of any of these landslide distance limits.

Marc *et al.* (2016) proposed an expression to estimate the total volume and area of EQIL. Their expression is based on seismogenic characteristics (e.g., seismic moment and asperity depth), landscape steepness, and material sensitivity (rock strength and pore pressure). However, the required inputs such as the parameters describing rock strength, earthquake asperity depth, and ground motion attenuation are often not precisely known (Li *et al.*, 2017).

Given these circumstances, rapid prediction of mLS of EQIL-events could provide us valuable information not only for studies regarding landscape evolution (e.g., Malamud *et al.*, 2004) and hazard assessments (Guzzetti *et al.*, 2005) but also for applications in emergency response. We could evaluate the severity of an EQIL-event in near-real time, providing a rapid prediction of mLS.

In this study, we use 23 EQIL inventories and their mLS values calculated by Tanyaş *et al.* (2018). We propose a method to predict mLS that can lead to estimates of the total triggered landslide area, total landslide volume and frequency-area distribution of landslides. We construct a stepwise linear regression model using both seismogenic and morphologic predictors. We predict the mLS of EQIL-events and validate our method using the leave-one-out technique.

5.2. Materials

5.2.1. Available data

An EQIL inventory database including 66 digital EQIL inventories from around the world was presented by Tanyaş *et al.* (2017) and detailed information regarding their mapping methodologies was given. From this database, Tanyaş *et al.* (2018) examined the inventories for which landslide area information is available and calculated the mLS values for 45 EQIL inventories from 32 earthquakes (Fig. 5.1). We examined those 45 EQIL inventories which were analyzed by Tanyaş *et al.* (2018) in terms of their mLS values and excluded some of them following the inventory selection criteria presented below. The list of EQIL inventories, their main characteristics and references were presented in Table 5.2.

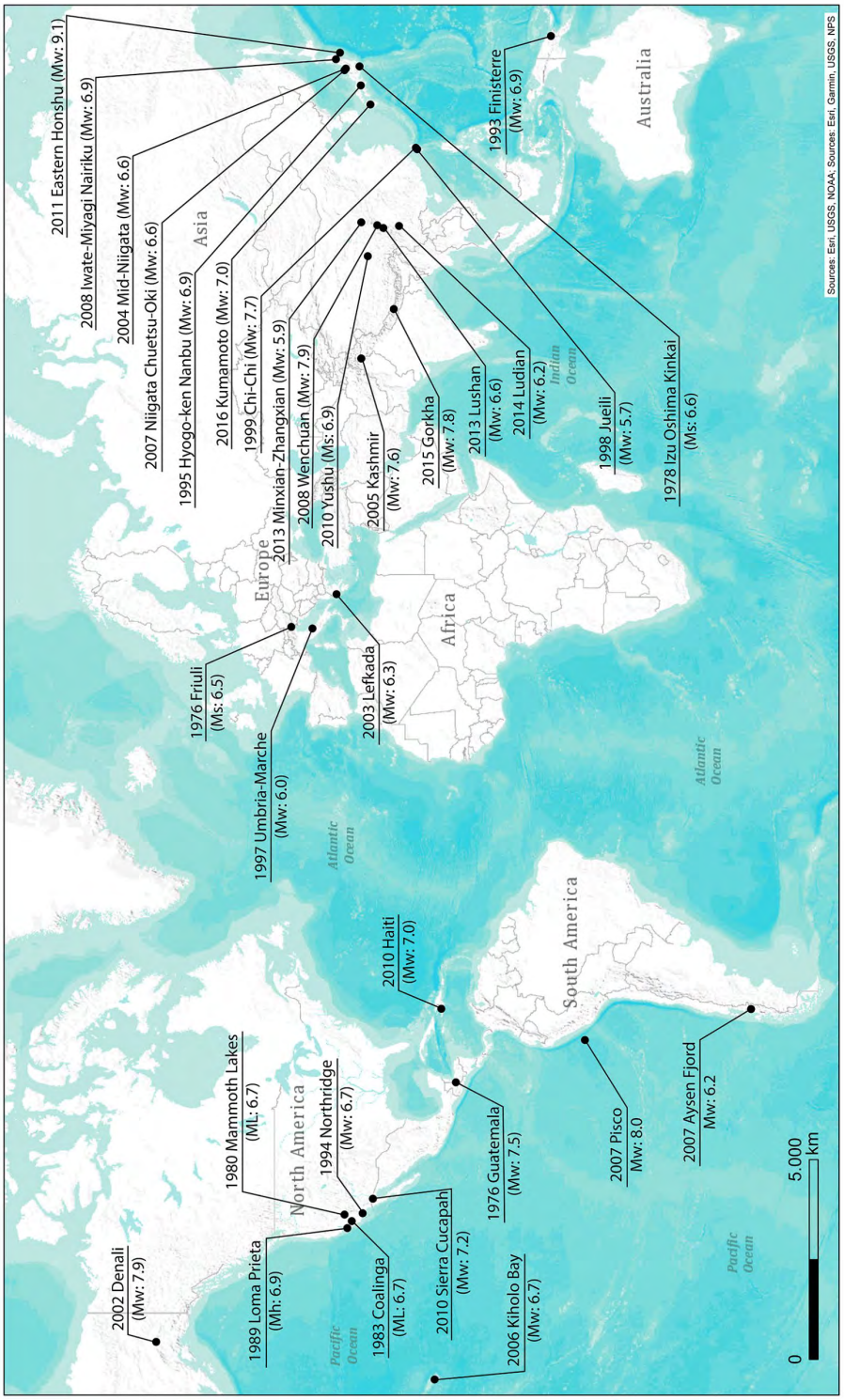

Figure 5.1. Distribution of examined earthquakes with a landslide inventory listed in Table 5.2.

Table 5.2. Examined EQIL inventories.

ID	Location	Date	Earthquake magnitude	$m\ L\ S$ ($\pm 1\sigma$)	Total number of landslides	Total landslide area from inventory (km^2)	Quality of Shakemap (Grade)	Fault type	Score**	Reference study	Included inventories	Reasoning
1	Guatemala	1976-02-04	7.5 (Mw)	4.79±0.08	6224	60.8	A	S	3.5	Harp et al., 1981	✓	
2	Friuli (Italy)	1976-05-06	6.5 (Ms)	2.91±0.57	1007	1.1	A	T	2.4	Govi, 1977	✓	
3	Izu Oshima Kinkai (Japan)	1978-01-14	6.6 (Ms)	2.63±0.13	659	1.5	C	S	3.5	Suziki, 1979	✓	
4	Mammoth Lakes (USA)	1980-05-25	6.1 (ML)	4.37±0.09	4027	33.8	A	NDC	2.9	Harp et al., 1984		Triggered by several earthquakes
5	Coalinga (USA)	1983-05-02	6.7 (ML)	3.15±0.08	3980	4.7	A	T	3.3	Harp and Keefer, 1990	✓	
6	Loma Prieta, California (US)	1989-10-18	6.9 (Mh)	1.75±0.25	138	0.4	A	T	2.2	McCrink, 2001		Partial inventory
7	Limon (Costa Rica)	1991-04-22	7.6 (Mw)	3.43±0.11	1643	8.2	B	T	2.9	Marc et al., 2016	✓	
8	Finisterre Mt./ (Papua N.G.)	1993-10-13	6.9 (Mw)	4.91±0.08	4790	69.0	D	T	2.9	Meunier et al., 2008		Triggered by several earthquakes
9	Northridge (USA)	1994-01-17	6.7 (Mw)	4.05±0.07	11111	23.8	A	T	3.1	Harp and Jibson, 1995, 1996	✓	
10	Hyogo-ken Nanbu (Japan)	1995-01-16	6.9 (Mw)	2.38±0.03	2353	0.5	A	S	3.9	Uchida et al., 2004	✓	
11	Umbria-Marche (Italy)	1997-09-26	6.0 (Mw)	3.14±0.20	210	1.9	A	N	2.3	Marzorati et al., 2002		Triggered by several earthquakes
12	Jueili (Taiwan)	1998-07-17	5.7 (Mw)	3.32±0.29	847	4.8	N/A	T	3.2	Huang and Lee, 1999		No ShakeMap
13	Chi-chi (Taiwan)	1999-09-20	7.7 (Mw)	5.11±0.06	9272	127.5	A	T	2.5	Liao and Lee, 2000	✓	
14	Denali Alaska	2002-11-03	7.9 (Mw)	4.94±0.09	1579	121.2	B	S	2.5	Gorum et al., 2014	✓	
15	Lefkada (Greece)	2003-08-14	6.3 (Mw)	3.52±0.23	274	2.9	A	S	2.4	Papathanassiou et al., 2013	✓	
16a	Mid-Niigata (Japan)	2004-10-23	6.6 (Mw)	3.91±0.77	10516	10.7	A	T	3.4	GSI of Japan, 2005		Triggered by several earthquakes
16b	Mid-Niigata (Japan)		6.6 (Mw)	3.85±0.06	4615	11.9	A	T	3.5	Sekiguchi and Sato, 2006		Triggered by several earthquakes
16c	Mid-Niigata (Japan)		6.6 (Mw)	3.11±0.04	3922	3.8	A	T	3.5	Yagi et al., 2007		Triggered by several earthquakes
17a	Kashmir (India-Pakistan)	2005-10-08	7.6 (Mw)	3.89±0.11	2424	10.4	A	T	3.5	Sato et al., 2007		Inventory 17c has a larger
17b	Kashmir (India-Pakistan)		7.6 (Mw)	4.85±0.06	1461	49.9	A	T	2.3	Basharat et al., 2014		Inventory 17c has a larger
17c	Kashmir (India-Pakistan)		7.6 (Mw)	5.42±0.06	2930	109.4	A	T	2.2	Basharat et al., 2016	✓	
18	Kiholo Bay (Hawaii)	2006-10-15	6.7 (Mw)	3.38±0.18	383	2.8	A	N	2.8	Harp et al., 2014		Partial inventory
19a	Aysen Fjord (Chile)	2007-04-21	6.2 (Mw)	4.28±0.09	540	17.3	N/A	S	2.4	Sepúlveda et al., 2010		No ShakeMap
19b	Aysen Fjord (Chile)		6.2 (Mw)	4.11±0.41	517	13.2	N/A	S	3.4	Gorum et al., 2014		No ShakeMap

Table 5.2. (Continued)

ID	Location	Date	Earthquake magnitude	$m\ L\ S$ (±1σ)	Total number of landslides	Total landslide area from inventory (km²)	Quality of Shakemap (Grade)	Fault type	Score**	Reference study	Included inventories	Reasoning
20	Niigata Chuetsu-Oki (Japan)	2007-07-16	6.6 (Mw)	1.69±0.41	312	0.4	A	T	2.5	Kokusai Kogyo, 2007		Including pre-earthquake landslides
21	Pisco / (Peru)	2007-08-15	8.0 (Mw)	2.70±0.20	271	1.07	A	T	3.4	Lacroix et al., 2013	✓	
22a	Wenchuan (China)	2008-05-12	7.9 (Mw)	6.27±0.06	59108	812.2	A	T	2.4	Dai et al., 2011		Inventory 22b has a larger coverage
22b	Wenchuan (China)		7.9 (Mw)	6.15±0.06	197481	1159.9	A	T	3.4	Xu et al., 2014b	✓	
22c	Wenchuan (China)		7.9 (Mw)	6.00±0.05	69605	580.3	A	T	3.0	Li et al., 2014		Inventory 22b has a larger coverage
22d	Wenchuan (China)		7.9 (Mw)	4.89±0.05	6727	54.6	A	T	3.7	Tang et al., 2016		Inventory 22b has a larger coverage
23	Iwate-Miyagi Nairiku (Japan)	2008-06-13	6.9 (Mw)	3.85±0.15	4211	12.5	A	T	3.7	Yagi et al., 2009	✓	
24a	Haiti	2010-01-12	7.0 (Mw)	3.53±0.15	4490	8.0	A	S	3.9	Gorum et al., 2013		Inventory 24b has a larger coverage
24b	Haiti		7.0 (Mw)	4.23±0.07	23567	24.9	A	S	3.8	Harp et al., 2016	✓	
25	Sierra Cucapah (Mexico)	2010-04-04	7.2 (Mw)	2.29±0.12	453	0.7	A	S	3.6	Barlow et al., 2014	✓	
26	Yushu (China)	2010-04-13	6.9 (Mw)	2.76±0.52	2036	1.2	C	S	3.9	Xu et al., 2013	✓	
27	Eastern Honshu (Japan)	2011-03-11	9.1 (Mw)	2.14±0.25	3475	1.6	A	T	3.5	Wartman et al., 2013	✓	
28a	Lushan (China)	2013-04-20	6.6 (Mw)	3.43±0.13	1289	5.2	C	T	2.6	Li et al., 2013		Inventory 28b has a larger coverage
28b	Lushan (China)		6.6 (Mw)	3.56±0.14	15546	18.5	C	T	3.9	Xu et al., 2015	✓	
29	Minxian-Zhangxian (China)	2013-07-21	5.9 (Mw)	2.41±0.16	2330	0.8	C	T	3.9	Xu et al., 2014a	✓	
30	Ludian (China)	2014-08-03	6.2 (Mw)	3.63±0.10	1024	5.2	C	S	3.5	Ying-ying et al., 2015	✓	
31a	Gorkha (Nepal)	2015-04-25	7.8 (Mw)	4.09±0.08	2654	15.6	C	T	3.4	Zhang et al., 2016		Inventory 31c has a larger coverage
31b	Gorkha (Nepal)		7.8 (Mw)	4.10±0.08	2513	14.2	C	T	3.8	Tanyas et al., 2018		Inventory 31c has a larger coverage
31c	Gorkha (Nepal)		7.8 (Mw)	4.91±0.06	24795	11.7	C	T	3.8	Roback et al., 2017	✓	
32a	Kumamoto (Japan)	2016-04-15	7.0 (Mw)	3.12±0.20	336	1.8	A	S	3.6	DSPR-KU, 2016		Inventory 32b has a larger coverage
32b	Kumamoto (Japan)		7.0 (Mw)	3.69±0.18	2742	7.7	A	S	3.8	NIED, 2016	✓	

We used both seismogenic and morphologic independent variables in a linear regression analysis. As seismogenic variables, we collected earthquake magnitudes and the estimated values of peak ground acceleration (PGA), peak ground velocity (PGV) and Modified Mercalli Intensity (MMI) from the U.S. Geological Survey (USGS) ShakeMap system (Allen *et al.*, 2008; Garcia *et al.*, 2012). The ShakeMap system provides the deterministic estimates of ground motion parameters in near real-time. Additionally, we used Global Centroid-Moment Tensor (CMT) half-duration (the duration of the rupture process) (Dziewonski *et al.*, 1981; Ekström *et al.*, 2012) as another seismogenic variable.

We used The Shuttle Radar Topography Mission digital elevation model (about 30 meters resolution) (NASA Jet Propulsion Laboratory, JPL, 2013) to create morphologic variables.

5.2.2. Selection of inventories

Each of the available EQIL inventories has a varying level of quality and completeness, which are difficult to assess both quantitatively and qualitatively due to lack of metadata regarding mapping preferences and the subjectivity of mapping procedure. We checked the mapping techniques of selected landslide inventories to get a general idea about the quality of mapping. In each inventory, the landslide-affected area was analyzed systematically by visual interpretation of satellite images and/or aerial photography. In addition, Tanyaş *et al.* (2017) (Chapter 2) introduced an evaluation system to help users assess the suitability of the available inventories for different types of studies. They listed four essential criteria to check whether the inventory suitable for a landslide susceptibility or hazard assessment, or to investigate the distribution, types, and patterns of landslides in relation to morphological and geological characteristics (Table 5.3). Based on this approach, Tanyaş *et al.* (2017) assigned scores to each inventory. We indicated those scores in Table 5.2 to have a general idea about the quality of mapping in the examined inventories. Scores show that each inventory meets at least half of the criteria and we assumed that their quality is high enough to be used in this study.

Table 5.3. Evaluation scheme for EQIL inventories (Tanyaş et al., 2017) (Chapter 2).

Essential Criteria		Execution performance	Score
i)	Was the study area analyzed systematically by visual interpretation?	0-100%	0-1
ii)	Was the boundary of the mapped area indicated?	No/Yes	0/1
iii)	Were the pre- and post-earthquake landslides eliminated from the inventory?	0-100%	0-1
iv)	Was the mapping resolution of inventory enough to differentiate the individual landslides? (L=Linear resolution of roll-over point)	L>25m : <0.5 25m≥L>5m : ≥0.5 5m≥L : 1	0/1

Considering the some other available information about inventories provided by Tanyaş *et al.* (2017), we discarded several of them to increase the reliability of the applied method. The list of selected EQIL inventories and the exclusion criteria are presented in Table 5.2.

We excluded partial EQIL inventories for which we know that only part of the landslide-affected area was mapped. for example, the 1989 Loma Prieta EQIL inventory is such a partial inventory that McCrink (2001) only mapped part of triggered landslides to test a dynamic slope stability method. Similarly, part of landslide-affected area associated with the 2006 Kiholo Bay earthquake was mapped in detailed by Harp *et al.* (2014) to check if the landslide-distribution pattern is predictable using high-resolution ground-motion simulation model. EQIL inventories that can be attributed to more than one earthquake were also excluded, such as the 1980 Mammoth Lakes (Harp *et al.*, 1984), the 1993 Finisterre (Meunier *et al.*, 2008), the 1997 Umbria-Marche (Marzorati *et al.*, 2002), and the 2004 Mid-Niigata (Geospatial Information Authority of Japan, 2005; Sekiguchi and Sato, 2006; Yagi *et al.*, 2007). In each of these inventories, the earthquake associated with the triggered landslides is not clear, and thus this can cause a problem in the representation of seismogenic variables regarding these inventories. Also, we excluded the 2007 Niigata Chuetsu-Oki inventory (Kokusai Kogyo, 2007) because pre-earthquake landslides were not eliminated in this inventory (Collins *et al.*, 2012). If we have more than one inventory for the same earthquake, we only included the one that has the largest number of landslides and covers the largest area (Table 5.2). We also excluded the earthquakes without ShakeMap, such as the 1998 Jueili and 2007 Aysen Fjord earthquakes. For the rest of inventories, we checked the uncertainties of ShakeMaps. The relative uncertainty level of each ShakeMap is described by a quality grading developed by Wald *et al.* (2008). The grades of the selected ShakeMaps (Table 5.2) show that none of them belongs to the poorest grades, which are D and F.

5.3. Methods

Delineation of the geographical boundary of a landslide event is usually no trivial task. For example, in the case of inventories prepared by field campaigns, a crucial step is to determine the area that was actually surveyed by the researchers (Bornaetxea *et al.*, 2018; Guzzetti *et al.*, 2012). Inventories prepared by visual interpretation of aerial or satellite imagery (Alvioli *et al.*, 2018c; Casagli *et al.*, 2017; Guzzetti *et al.*, 2012), as is the case for many of the inventories considered in this work, should indicate the boundary of the available images, or the actual area mapped. However, in many cases this information is not available.

The peak ground acceleration (PGA) contours, which show a correlation with landslide density (e.g. Meunier *et al.*, 2007), was used to identify the landslide-affected area. Wilson and Keefer (1985) are the first who proposed a minimum threshold of 0.05g to such a boundary. They used the data gathered by Keefer (1984) regarding the 40 EQIL inventories. However, EQIL inventory maps were only available for a few of the 40 reported earthquakes (Tanyaş *et al.*, 2017) (Chapter 2), and the general relations and conclusions reported were pieced together from various resources, listed in Keefer and Tannaci (1981). Similar minimum PGA thresholds that covers all triggered landslides were also reported for individual EQIL inventories as 0.01g for the 1980 Irpinia earthquake (Del Gaudio and Wasowski, 2004) and 0.02-0.04g for the Mineral, Virginia earthquake (Jibson and Harp, 2012). Recently, Jibson and Harp (2016) analyzed six EQIL events and explored the absolute minimum PGA value considering the very smallest failures (<1 m^3) triggered by the corresponding earthquakes. They examined four of those inventories by field studies

and showed that PGA contour covering all landslides ranges from 0.02g to 0.08g. They investigated two other inventories using aerial-photographic interpretations and pointed out the PGA range of 0.05-0.11g as an absolute outermost limit of triggered landslides.

Jibson and Harp (2016) also stated that the proposed outermost limits of triggered landslides can only be valid where susceptible slopes are extensive. Yet the actual area that is affected by landslides depends on the local topographic, lithologic, climatic and land cover conditions, which are different for each earthquake-affected area, and the interaction between these features and ground shaking causes the specific landslide distribution pattern. Thus, for some of the inventories such a common PGA limit could be larger or smaller than the real landslide-affected area. In this study, we also assumed that the susceptible slopes are extensive in our examined sites to estimate the boundary of a landslide-affected area.

Note that in the case of EQIL, there can be a significant difference between the area that includes the entire landslide population, and one that includes the vast majority (e.g. 90%) of them. Hancox *et al.* (2002) use the term “main area affected by landslides”. Despite the lack of explanation regarding the parameter in the referred paper, we adapted that term here, modifying it slightly to the main landslide-affected area, and defined it to include the area containing 90% of the mapped landslides. To define the term main landslide-affected area, we examined the inventories and we systematically calculated the percentage of the total number of landslides contained within various PGA contours. We began examining from the highest to lowest PGA contours provided by the USGS ShakeMap system and keep examining till we find the PGA contour covering 90% of the mapped landslides. All other analyses were conducted for the identified main landslide-affected areas.

Eliminating the flat regions as non-susceptible zones to landsliding is a generally accepted approach in landslide modelling studies (e.g. Kritikos *et al.*, 2015). Thus, we defined those regions and subtracted them from the main landslide-affected areas. To identify the flat areas, we used the GRASS GIS module r.geomorphon by Jasiewicz and Stepinski (2013) to extract the “flat” landform class, and an algorithm that gets rid of the sparse pixel result developed by Alvioli *et al.* (2018a). The algorithm starts from the pixels classified as “flat” by r.geomorphons, and shrinks the borders of the flat raster map by a few pixels and then grows it again; the procedure is repeated until sparse pixels disappear

In our regression model, we did not use the variables such as lithology, landcover or climate that we could not evaluate their contribution to landsliding. For example, we did not include lithologic units because without knowing their geotechnical properties, the description of a lithologic unit is not enough to evaluate its role in landslide initiation process. Instead, we used morphologic variables which were used in statistical landslide probability assessments (e.g., Budimir *et al.*, 2015; Reichenbach *et al.*, 2018). For example, Budimir *et al.* (2015) examined EQIL causal factors in their review papers. They investigated nine studies and presented the percentages at which covariates were found to be significant. Budimir *et al.* (2015) stated that in all those studies slope was found as a significant variable. On the other hand, distance to streams was found significant in at least 20% of those studies, while profile curvature, topographic wetness index (TWI) and surface roughness were found significant in at least 10% of those studies. Tanyaş *et al.* (2017) analyzed about 554,000 landslide initiation points from 46 EQIL-events and examined the frequency values of earthquake-induced landslides in intervals of slope,

surface roughness, local relief and distance to streams. They stated that the highest landslide frequencies are concentrated in particular intervals for all of these parameters. This implies that these variables may be good candidates to check their significance in our regression analysis as well.

Slope is a factor controlling the normal and shear stresses, which take a role in slope stability. Local relief is the maximum difference in height in a local neighborhood of each pixel and can be related to slope instability caused by tectonic uplift. It partially correlates with slope. Both slope and local relief are related to the magnitude of static stress loading in hillslopes (Parker *et al.*, 2015). TWI (Moore *et al.*, 1991) is a proxy for potential soil wetness used to estimate the spatial variability of wetness within a landscape (e.g., Nowicki Jessee *et al.*, 2018). It can take a role in slope stability by changing the pore water pressure. We used vector ruggedness measure (VRM) to consider surface roughness. It quantifies local variation in terrain more independently of slope than other methods such as land surface ruggedness index or terrain ruggedness index (Sappington *et al.*, 2007). Tanyaş *et al.* (2017) (Chapter 2) showed that the majority of EQIL are initiated at low VRM values, and the number of observed EQIL decreases while VRM increases. Distance to stream is proxy related to fluvial undercutting (e.g., Kritikos *et al.*, 2015) that cause high rates of shear stress as a result of loss of lateral support (Korup, 2004). Tanyaş *et al.* (2017) showed that the majority of EQIL are initiated close to river channels and the frequency of observed landslides gradually decrease while going far away from channels. Profile curvature is a measure describing the concavity/convexity of slope along the vertical direction. Having a concave surface can increase slope instability by increasing the subsurface drainage that can cause high water pressure (e.g., Pierson, 1980).

To create our morphologic variables used as covariates in our regression model, we worked with a few of the modules of GRASS GIS (Neteler and Mitasova, 2013) and SAGA GIS (Conrad *et al.*, 2015). In total, we derived six DEM derivatives (Table 5.4) using the module given within parentheses; slope (r.slope.aspect) (Hofierka *et al.*, 2009), topographic wetness index (r.topidx) (Cho, 2000), vector ruggedness measure (r.vector.ruggedness) (Sappington *et al.*, 2007), distance to stream (r.watershed and r.grow) (Ehlschlaeger, 1989), local relief (r.geomorphon) (Jasiewicz and Stepinski, 2013) and profile curvatures (r.param.scale) (Wood, 1996).

We also tested five seismogenic variables (PGA, PGV, MMI, earthquake magnitude and half duration) in linear regression analysis (Table 5.4). MMI is a scale classifying the shaking strength observed at a site while PGV and PGA refer to the highest speed of shaking and the largest increase in velocity respectively, experienced by a particle on the ground during an earthquake (Bormann *et al.*, 2013). If the variables such as fault-rupture mechanism and fault geometry are known, they are also taken into account, and a ShakeMap is created accordingly (e.g., Wald, 2013). Therefore, we can assume that fault-rupture mechanism and fault geometry is represented by the resultant ground motion parameters provided by ShakeMap. One of these ground motion parameters is used in almost all statistical based EQIL prediction models (e.g., Nowicki Jessee *et al.*, 2018; Nowicki *et al.*, 2014; Robinson *et al.*, 2017). PGA, PGV and MMI are collinear variables and thus we considered three of them to identify the most significant ground motion parameter for this study. The other two seismogenic variables, earthquake magnitude and

half duration are proxies for energy released by rupturing and duration of rupturing, respectively.

Apart from two independent variables (earthquake magnitude and half-duration) which do not have any variation within a landslide-affected area, we calculated both mean value and its standard deviation for each independent variable to represent the characteristics of main landslide-affected areas.

Table 5.4. List of independent variables

Class	Independent variables (mean & maximum)	Source / GIS module	Reference
Seismogenic	PGA	USGS ShakeMap	(Garcia *et al.*, 2012)
Seismogenic	PGV	USGS ShakeMap	(Garcia *et al.*, 2012)
Seismogenic	MMI	USGS ShakeMap	(Garcia *et al.*, 2012)
Seismogenic	Earthquake Magnitude	USGS ShakeMap	(Garcia *et al.*, 2012)
Seismogenic	Half-duration	Global CMT	(Dziewonski *et al.*, 1981; Ekström *et al.*, 2012)
Morphologic	Slope	r.slope.aspect (GRASS GIS)	(Hofierka *et al.*, 2009)
Morphologic	Topographic Wetness Index (TWI)	r.topidx (GRASS GIS)	(Cho, 2000)
Morphologic	Vector Ruggedness Measure (VRM)	r.vector.ruggedness (GRASS GIS)	(Sappington *et al.*, 2007)
Morphologic	Distance to Stream	r.watershed & r.grow (GRASS GIS)	(Ehlschlaeger, 1989)
Morphologic	Local Relief	r.geomorphon* (GRASS GIS)	(Jasiewicz and Stepinski, 2013)
Morphologic	Profile Curvature	r.param.scale (GRASS GIS)	(Wood, 1996)

*Search radius was taken as 90 m in the calculation of local relief.

We evaluated the significance level of each variable used in the linear regression model based on p-values. We selected a significance level of 5%, which refers to a p-value of 0.05 as a confidence level, below which the relation between the examined independent and dependent variables were considered significant (Moore *et al.*, 2012). To decide on the best predictor subset, we run the stepwise linear regression algorithm provided by Matlab (Version R2017b). We applied a forward feature selection method which searches for covariates to add to the model based on p-value. The algorithm tests the model with and without a potential covariate at each step considering p-value. The algorithm tests not only the individual terms but also their interactions (e.g., multiplication of variables). If any of the available covariates in the model has a p-value less than 0.05, the one with the smallest p-value is added into a model and this procedure is repeated till the significant

covariates are included into the model. This procedure provided us the set of covariates giving the best model performance. We then checked the collinearity between those variables using the variance inflation factor (VIF) (Chatterjee and Hadi, 2015); a VIF larger than 10 is assumed as an indication of a collinearity.

Because we have limited observations, to validate our model, we used the leave-one-out methodology and predicted mLS values for each earthquake using the described stepwise linear regression algorithm. Considering p-values, we selected the best predictor subset and the corresponding best model.

5.4. Results

To define the term main landslide-affected area, we compared the differences in PGA values covering the various landslide populations. For example for the Haiti inventory (Harp *et al.*, 2016), PGA contours of 0.23g, 0.36g, 0.41g, and 0.48g contain 100%, 90%, 80%, and 70% of the entire mapped landslide population, respectively. We calculated these values for all inventories. Table 5.5 shows the PGA values and the percentage of the total number of landslides falling within these limiting PGA contours for each inventory. Table 5.5 shows that except for the 2007 Pisco, Peru earthquake (Mw 8.0), the 0.12g is the minimum PGA contour covering at least 90% of the mapped landslides in each inventory. The 2007 Pisco earthquake is an offshore event where significant part of the area covered by large peak ground acceleration (PGA) locates at sea. Therefore, for this earthquake the 0.12g PGA contour covers about 80% of the mapped landslides (Table 5.5). Given these observations, we took the 0.12g PGA contour as an estimate for the boundary of main landslide-affected area. This PGA value is slightly larger than the PGA range (0.05-0.11g) indicated in the literature (e.g., Jibson and Harp, 2016) as the outmost limit of EQIL, and thus consistent with the literature.

We calculated our predictors for the area bounded by the 0.12g PGA contour in each landslide-affected area. The stepwise regression algorithm identified five predictors as the best subset explaining our dependent variable: earthquake magnitude, profile curvature (mean), profile curvature (std), TWI (mean), and earthquake magnitude x TWI (mean) (Table 5.6). The regression model run using these predictors show that each predictor has a p-value less than 0.05 and thus, they all have high a significance in our model. We checked the collinearity between predictors using VIF. We excluded our interaction term (Earthquake Magnitude x TWI (mean)) from the collinearity evaluation (Friedrich, 1982). The results show that VIF values for all other variables are less than two and thus, the collinearity is not an issue for the selected variables. Among the selected variables, earthquake magnitude (EqM), profile curvature (mean) and TWI (mean) have explicit physical meaning in our regression equation in addition to their statistical significance. On the other hand, profile curvature (std) and the interaction term (EqM x TWI (mean)) have only statistical significance.

Table 5.5. PGA contours and percentages of their landslide coverage for each inventory. The grey colored PGA values are the ones that are higher than PGA 0.12g.

ID	Inventories	PGA (g) contour covering the specified percentage of total landslide population					
		100%	**90%**	**80%**	**70%**	**60%**	**50%**
1	Guatemala / Harp *et al.*, 1981	0.08	0.14	0.17	0.33	0.38	0.43
2	Friuli / Govi, 1977	0.21	0.38	0.43	0.46	0.48	0.51
3	Izu Oshima Kinkai / Suziki, 1979	0.12	0.2	0.24	0.26	0.28	0.36
4	Coalinga / Harp and Keefer, 1990	0.10	0.14	0.18	0.22	0.26	0.33
5	Limon / Marc *et al.*, 2016	0.30	0.33	0.35	0.36	0.38	0.41
6	Northridge / Harp and Jibson, 1995; 1996	0.13	0.27	0.30	0.34	0.38	0.41
7	Hyogo-ken Nanbu / Uchida *et al.*, 2004	0.57	0.71	0.74	0.76	0.76	0.76
8	Chi-chi / Liao and Lee, 2000	0.05	0.32	0.41	0.51	0.56	0.60
9	Denali / Gorum *et al.*, 2014	0.17	0.27	0.32	0.35	0.36	0.37
10	Lefkada / Papathanassiou *et al.*, 2013	0.40	0.55	0.62	0.64	0.68	0.68
11	Kashmir / Basharat *et al.*, 2014	0.44	0.71	0.86	0.94	1.07	1.16
12	Pisco / Lacroix *et al.*, 2013	0.04	0.08	0.13	0.14	0.15	0.15
13	Wenchuan / Xu *et al.*, 2014b	0.08	0.33	0.41	0.48	0.53	0.58
14	Iwate-Miyagi Nairiku / Yagi *et al.*, 2009	0.25	0.37	0.40	0.47	0.70	0.95
15	Haiti / Harp *et al.*, 2016	0.23	0.36	0.41	0.48	0.52	0.57
16	Sierra Cucapah / Barlow *et al.*, 2014	0.31	0.56	0.59	0.64	0.65	0.67
17	Yushu / Xu *et al.*, 2013	0.09	0.12	0.14	0.21	0.31	0.35
18	Eastern Honshu / Wartman *et al.*, 2013	0.16	0.28	0.36	0.38	0.4	0.44
19	Lushan / Xu *et al.*, 2015	0.07	0.17	0.23	0.29	0.32	0.35
20	Minxian / Xu *et al.*, 2014a	0.09	0.12	0.13	0.15	0.16	0.17
21	Ludian / Ying-ying *et al.*, 2015	0.12	0.14	0.16	0.17	0.18	0.19
22	Gorkha / Roback *et al.*, 2017	0.08	0.24	0.25	0.26	0.27	0.27
23	Kumamoto / NIED, 2016	0.23	0.42	0.45	0.48	0.52	0.54

Table 5.6. Results of the model developed using the selected five covariates.

Coefficients	Estimate	Standard Error	p-Value
(Intercept)	-262.639279	40.820191	0.000006
Earthquake Magnitude (EqM)	40.371160	5.787513	0.000002
Profile curvature (mean)	9160.059501	3235.300450	0.011520
Profile curvature (std)	-204.932535	70.415537	0.009747
TWI (mean)	40.098121	6.146669	0.000005
EqM x TWI (mean)	-6.039333	0.869701	0.000002

We presented the adjusted R^2, root-mean-square error (RMSE) and mean absolute error (MAE) values for the best fit line (Fig. 5.2). The adjusted R^2 value shows that the model explains 86% of the variability of the response data around its mean. On the other hand, the average magnitude of the error is 0.39 (RMSE) and the absolute differences between predicted and calculated mLS value is 0.30 (MAE).

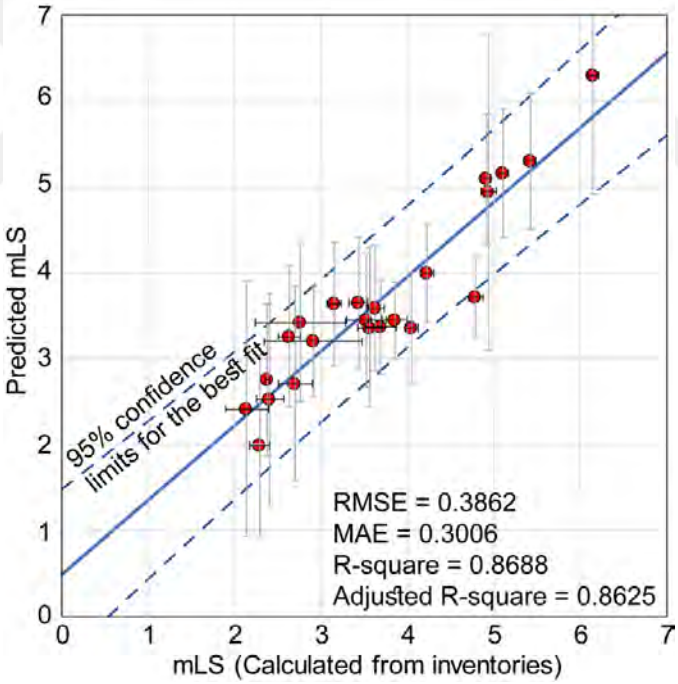

Figure 5.2. Graph showing the model result. The confidence intervals which are shown by vertical error bars are calculated for each prediction separately. Uncertainties in calculated mLS values are given by using ±1σ error bars. Calculated mLS values are obtained from Tanyaş et al. (2018) (Chapter 3).

To validate this model, for each predictor subset, we followed the leave-one-out technique and predicted the entire mLS array. Results show that adjusted R^2 is 0.79, RMSE is 0.50 and MAE is 0.40 (Fig. 5.3a). The residuals show a random distribution around a constant value without a distinct pattern and the average residual value is 0.0004 (Fig. 5.3b). This supports our assumption that a linear dependence exists between mLS and the variables. The average uncertainty for the calculated mLS values, which were shown by horizontal error bars in Fig. 5.3a and vertical error bars in Fig. 5.3b, is 0.15. In a few cases (e.g., EQIL Inventory ID of 2, 10, 12, 20 and 21), the residuals are lower than uncertainties in calculated mLS values. These are the cases that our predictions are considerably successful. In all cases, our predictions stay within the 95% confidence limits for the best fit line passing from origin (Fig. 5.3a).

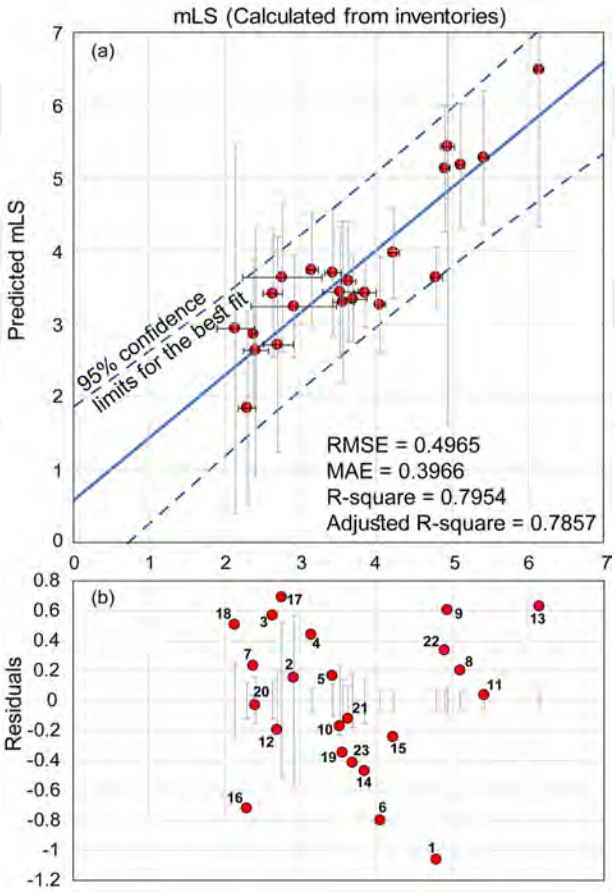

Figure 5.3. Graphs showing the results of validation using the leave-one-out methodology: (a) the distribution of calculated versus predicted mLS values and the best fit line passing from the origin; and (b) the residuals for predicted mLS values. The confidence intervals which are shown by vertical error bars are calculated for each prediction separately in (a). The uncertainties in calculated mLS values (±1σ) are given by horizontal error bars in (a) and vertical error bars in (b). Calculated mLS values are obtained from Tanyaş et al. (2018) (Chapter 3). The number in the lower graph refer to the EQIL Inventory IDs listed in Table 5.5.

We can predict mLS and other measures that we can estimate using mLS, soon after an earthquake, in four-steps (Fig. 5.4): (i) the PGA map of an investigated earthquake is obtained from USGS ShakeMap system and the SRTM DEM is obtained for the areas bounded by minimum PGA value of 0.12g; (ii) the independent variables listed in Table 5.6 are collected/derived for non-flat areas; (iii) the proposed regression equation is run using the coefficients listed in Table 5.6 and mLS is predicted for the examined earthquake; and (iv) the maximum landslide area ($Eq. 5.3$), total landslide volume ($Eq. 5.4$) and total landslide area ($Eq. 5.5$) are estimated using existing methodologies (Malamud *et al.*, 2004; Tanyaş *et al.*, 2018). Further, the variation ranges for the estimated mLS are calculated using the confidence intervals given in Table 5.1. Frequency-size distribution of the examined landslide-event can be estimated using the empirical curves proposed by Malamud *et al.* (2004).

We used the 2004 Mid-Niigata earthquake as an example to show the application of the proposed method (Fig. 5.5), which presented in Figure 5.4. We have three inventories (Geospatial Information Authority of Japan, 2005; Sekiguchi and Sato, 2006; Yagi *et al.*, 2007) regarding this earthquake but all of them includes landslides triggered by a sequence of earthquakes rather than a single mainshock. Therefore, we discarded these inventories in the modelling stage (See Table 5.2) because they may include more landslides and thus the predicted mLS using a single earthquake may be lower than the calculated mLS.

The predicted mLS (3.07 ± 0.33), total landslide area (A_T) [2.82 km^2 (-1.24, +2.12)] and maximum landslide area (A_{Lmax}) [0.16 km^2 (-0.07, +0.11)] are close to the values calculated from the 2004 Mid-Niigata inventory map created by Yagi *et al.* (2007) (mLS=3.11 ± 0.04; A_T=3.80 km^2 and A_{Lmax}=0.17 km^2). On the other hand, our predictions are lower than the values calculated from three of the inventories (See Table 5.2) as we expected.

As a result, following our proposed methodology, we simulated a prediction in absence of a landslide-event inventory. First, we predicted the landslide-event magnitude scale which gives us a preliminary idea about the severity of investigated landslide-event in terms of total landslide area. Second, we estimated the total landslide volume which is a valuable information regarding landslide evolution processes. Third, we estimated the frequency-size distribution of landslides which can be useful for quantitative analysis of landslide hazard.

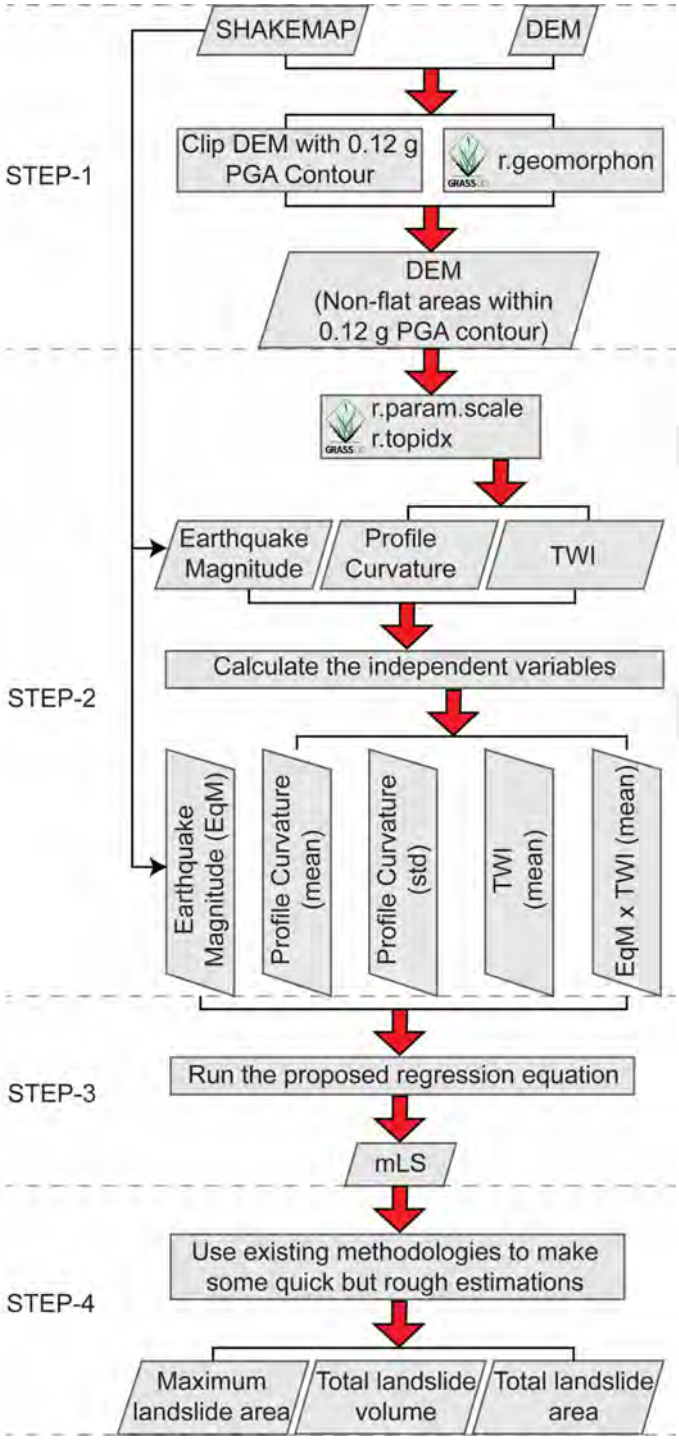

Figure 5.4. Flowchart for the proposed method.

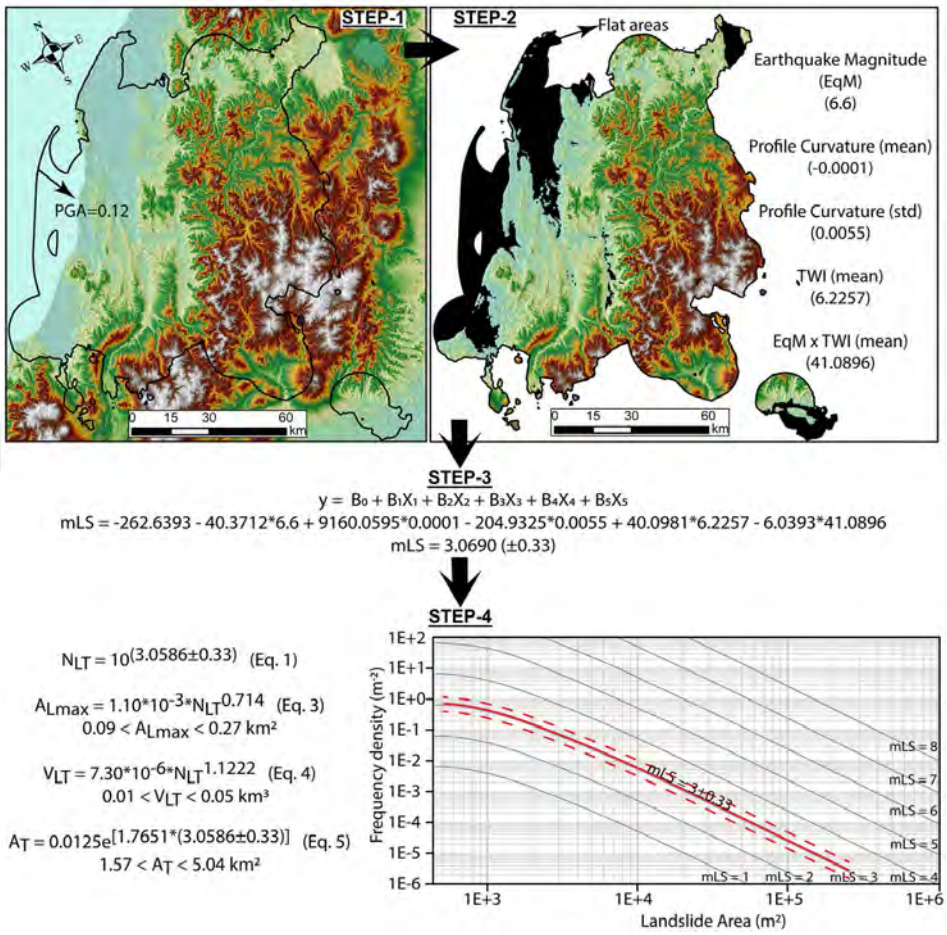

Figure 5.5. Schematic drawing which shows the four-step followed to apply the proposed methodology to predict mLS and related parameters for the 2004 Mid-Niigata earthquake. N_{LT}: The number of triggered landslides; A_{Lmax}: Maximum landslide area; V_{LT}: Total landslide volume; A_T: Total landslide area.

5.5. Discussion and Conclusions

We analyzed 23 EQIL inventories to develop an approach to predict the landslide-event magnitude scale in near real-time. We restricted our analyses within non-flat regions located within the main landslide-affected areas, which were identified using the PGA contour containing 90% of the landslides and largest PGA values. For each of the main landslide-affected areas, we calculated mean values of three seismogenic and six morphologic independent variables and their standard deviations (Table 5.4). Additionally, we gathered earthquake magnitude and half-duration for each earthquake and examined 20 variables in total. We assumed a linear dependence for mLS over the variables and identified five variables as the best subset of the independent parameters using a stepwise linear regression algorithm. Using the selected subset of variables, we identified the

coefficients of the regression model and validated this model using the leave-one out approach, since we have limited observations.

Validation results show that our proposed approach provides a nice prediction (Adjusted R^2 = 0.79, RMSE = 0.50 & MAE=0.40) for mLS. We can make a prediction for an earthquake in near-real time, as the required predictors can be derived rapidly after an earthquake. The most relevant advantage of our method is that we use both static and dynamic parameters, which are publicly available. The static predictors are DEM derivatives and thus they can be easily derived for any location on the globe. Earthquake magnitude and ShakeMap data can be obtained using USGS ShakeMap system in near-real time.

The proposed method has some limitations. Results showed that our approach gives poor prediction results in a few cases (Fig. 5.3). There can be five reasons for that. First, offshore events may not be well characterized using the proposed approach. In offshore earthquakes, most of the areas bounded by 0.12g PGA contour are not located on land, and thus our morphological predictors may not represent the landslide-affected area well. Figure 5.3 shows that for two offshore earthquakes we have residuals, which are larger than MAE (0.40). The 1978 Izu Oshima Kinkai (3) and the 2010 Eastern Honshu (18) earthquakes give residual values of 0.57 and 0.50, respectively. Second, the quality of the ShakeMap may also affect our model performance since we identify the main landslide-affected area using the PGA values from the raster files provided by USGS ShakeMap system. The relatively poor quality of ShakeMap regarding the 2010 Yushu earthquake may be the reason for having a larger residual (0.69) than the average value for this earthquake. Third, the inventories used for the calculation of mLS values may be partial or may contain landslides which were not triggered by the specific earthquake. If these landslides are medium or large in size, this may affect the calculated mLS value. On the other hand, mapping of landslide is a subjective procedure (e.g., Tanyaş *et al.*, 2017); each landslide inventory can be exposed to various level of amalgamation and the delineated landslide polygons may show minor/major differences comparing to the actual landslide boundaries based on the quality of an inventory. However, evaluating the quality and completeness of the inventories is not possible without examining the landslides from the original imagery from which the inventories were made, which is very time consuming. This implies an uncertainty in mLS that we could not assess quantitively. Further studies need to assess this uncertainty. Fourth, the simplicity of the proposed method may be the main reason for poor prediction in some cases. We used earthquake magnitude (EqM), profile curvature (mean & standard deviation), topographic wetness index (TWI) (mean), and EqM x TWI (mean) (Table 5.6) to derive our regression equation. Mean values and their standard deviations we used for these variables may not represent the landslide-affected areas in a few cases, affecting the prediction performance. Moreover, we could not consider some variables that take a role in landslide initiation process and thus the resultant landslide-event magnitude. For example, the geotechnical features that control the shear strength parameters of slope material are not available globally. We have global lithologic map (e.g., Hartmann and Moosdorf, 2012) but evaluating the strength parameters of a slope material solely based on their lithologic definitions is not a reliable method. Similarly, we could not account for the effect of previous earthquakes (Parker *et al.*, 2015), or previously occurred landslides (Samia *et al.*, 2017) because we do not have globally available dataset to quantify the effect of such variables. Last but not least,

working with limited number of inventories is a considerable drawback of this study. Although, we worked with the largest EQIL dataset (Tanyaş *et al.*, 2017) (Chapter 2), the number of selected inventories is still limited to take into account some seismogenic or environmental characteristics of the examined landslide-events. With a larger EQIL inventory database, landslide-events can be categorized based on some common features and different regression coefficients can be provided for each of those categories. For example, offshore earthquakes can be analyzed separately to address the possible drawback mentioned above. Similarly, categorizing the earthquakes having different faulting mechanism would be possible with a larger database. Although the ground motion estimates provided by a ShakeMap take into account the characteristics of faulting mechanism such as fault type and geometry (e.g., Wald, 2013), categorization of inventories considering these features may help us to improve our mLS predictions. However, now we have 10 landslide-events associated with strike-slip faulting and 13 events with thrust faulting, while no EQIL inventory associated with normal faulting (Table 5.2). Therefore, we did not make such a categorization because we would have either category with no observation or a category with 10 observations, which would give us statistically less reliable outputs.

Rapid prediction of mLS can improve our ability to estimate the intensity of landslide-events within a day after an earthquake and, thus, it can provide useful information in the emergency response phase. As presented in Figure 5.5, using the predicted mLS we can also estimate maximum landslide area, total landslide area and volume, which can help us better understand the balance between crustal advection and seismically induced mass wasting and thus the landscape evolution process (e.g., Hovius *et al.*, 2011). We can also estimate the frequency-size distribution of landslide-event using the empirical curves of Malamud *et al.* (2004). Tanyaş *et al.* (2018) emphasized the variation in the slope of frequency-size distribution curves and argue that modelling the frequency-size distribution of landslides may not be accurate using an average slope as Malamud *et al.* (2004) did. However, in the absence of landslide-event inventory, to provide estimates regarding the size distribution of landslides the empirical curves of Malamud *et al.* (2004) can be still useful. Our method needs further calibration using a larger dataset to be sure about its validity globally. With a larger EQIL database, this model can be improved addressing some of the drawbacks mentioned above and predict mLS with smaller uncertainties.

6. A global slope unit-based method for the near real-time prediction of earthquake-induced landslides[6]

6.1. Introduction

Earthquakes can severely impact society in both underdeveloped and developed countries (Linnerooth-Bayer and Amendola, 2000). In underdeveloped countries, exposure and vulnerability to earthquakes have increased (Bhattarai and Conway, 2010) because of unplanned settlements and uncontrolled urban sprawl. Ground shaking itself causes around 60% of all economic losses and deaths induced by earthquakes, while the remaining 40% are due to secondary effects such as tsunamis, liquefaction, fires, and landslides (Daniell *et al.*, 2017). Earthquake-induced landslides (EQIL) are one of the most damaging secondary hazards associated with earthquakes (Jibson *et al.*, 2000). Therefore the estimation of earthquake-induced landslide hazard is an important risk mitigation component in seismically active mountainous areas (Wasowski *et al.*, 2011).

In the last decades, a variety of statistical, heuristic or physically-based modeling methods have been applied for landslide susceptibility assessment also over large areas (Allstadt *et al.*, 2017; Reichenbach *et al.*, 2018), although the inclusion of proper seismic indicators is still a challenge, due to the large number of possible earthquake scenarios and associated landslide effects (e.g., Budimir *et al.*, 2014; Nowicki *et al.*, 2014). Several global approaches to predict EQIL exist. Nadim *et al.* (2006) were one of the first to generate a global earthquake-induced landslide susceptibility map based on heuristic methods with global datasets of climate, lithology, earthquake activity and topography.

In addition to pre-earthquake hazard assessment, another important component is to evaluate the expected landslide distribution or density immediately after an earthquake has occurred, before landslides can be mapped using satellite images, in order to support relief operations. Godt *et al.* (2008b) developed a model with a spatial resolution of 1 km to examine the probable spatial extent of EQIL, based on three EQIL inventories. They introduced a hybrid model with a combination of a simplified Newmark approach and a heuristic model. Nowicki *et al.* (2014) developed a statistical model with a spatial resolution of 1 km based on logistic regression using five EQIL inventories to estimate the probability of landslide occurrence in a given area. This model was later improved using grids of 250 m and 23 EQIL inventories from a variety of tectonic and geomorphic settings by Nowicki Jessee *et al.* (2018). The U.S. Geological Survey (USGS) is currently running these three models in parallel in testing mode to improve them with additional data acquisition (Allstadt *et al.*, 2017). Also, statistical models have been proposed for global post-earthquake

[6] This chapter is based on the following paper: Tanyas, H., Rossi, M., Alvioli, M., van Westen, C.J., and Marchesini, I. A global slope unit-based method for the near real-time prediction of earthquake-induced landslides. Geomorphology, accepted, 2018.

application. Kritikos *et al.* (2015) used fuzzy logic to estimate the probability of landslide occurrence associated with earthquakes, based on three EQIL inventories with a spatial resolution of 60 m. Parker *et al.* (2017) examined nine EQIL inventories and proposed a logistic regression model to express the spatial probability (with 30 meters spatial resolution) of EQIL considering the effect of missing small landslides. Robinson *et al.* (2017) suggested using fuzzy logic to predict landslide point density using a training set which is created by mapping part of EQIL soon after an earthquake.

There are three main challenges in near real-time estimation of EQIL distribution: (i) reliable ground motion parameters, (ii) missing causal factors, and (iii) a limited number of EQIL inventories. The most important is related to the relatively poor quality and/or spatial resolution of ground motion parameters derived from ShakeMap (Allen *et al.*, 2008; Garcia *et al.*, 2012). ShakeMap is a system (Allen *et al.*, 2008; Garcia *et al.*, 2012) developed by the U.S. Geological Survey (USGS) to provide the deterministic estimates of ground motion parameters after an earthquake. The spatial resolution of ShakeMap grid is 1 km, which does not account for topographic amplification of seismic energy, one of the key factors to control landsliding (Meunier *et al.*, 2007). Also, the quality of ShakeMap data might be low for some earthquakes where information on the rupturing event is poor (Wald *et al.*, 2008). Additional requirements for real-time EQIL distribution modeling are knowledge of the rock mass strength (Hoek and Brown, 1980), the effect of previous earthquakes (Parker, 2013), and previously occurred landslides (Samia *et al.*, 2017). However, it is difficult to take these causal factors fully into account in a globally applicable approach, due to the lack of global geotechnical data and sufficiently complete landslide inventories. A Global Landslide Catalog (GLC) was developed by Kirschbaum *et al.* (2010) with the goal of identifying rainfall-triggered landslide events around the world, regardless of size, impacts or location. A similar attempt for EQIL inventories was reported by Tanyaş *et al.* (2017) (Chapter 2). However, these landslide databases are far from complete. This is related to another problem in real time modeling of EQIL distribution, which is the lack of sufficient digital EQIL inventories to generate relevant statistical models for different tectonic and physiographic settings. Additionally, the existing EQIL inventories differ substantially in terms of quality and completeness (Tanyaş *et al.*, 2018) (Chapter 3). Each inventory was created for a different purpose based on different expertise and materials. Thus, some of the inventories are not complete; includes only a small part of the landslide-affected area.

One of the common features of existing global approaches is that they use pixels as mapping units. A mapping unit should be a portion of the land surface having different ground conditions from the adjacent units across definable boundaries (Hansen, 1984b). The selection of proper mapping units is crucial because it determines how thematic and landslide data are sampled to prepare the training and prediction subsets for statistical susceptibility modeling (Rossi and Reichenbach, 2016). A meaningful mapping unit should maximize internal homogeneity and between-units heterogeneity of a defined domain (Guzzetti *et al.*, 1999). In a pixel-based analysis, the study area is divided into regular squares regardless of the internal homogeneity of mapping units, and the defined grids usually do not represent a physical property of the terrain (Schlögel *et al.*, 2018). Slope Units (SUs) are used to overcome this significant drawback of pixel-based analyses. SUs divide the terrain into mapping units with similar hydrological and geomorphological

conditions, and they are shaped by similar processes occurring in the natural landscape under the same geo-environmental conditions. Therefore, SU is considered a well-suited terrain subdivision for landslide susceptibility modeling and zonation (e.g., Carrara, 1988; Guzzetti *et al.*, 1999; Guzzetti *et al.*, 2006).

Another issue that has not been addressed in existing models is the sampling balance between inventories used in modeling. Including a different number of observations from different inventories may result in a training set with lack of representativeness due to the dominance of an inventory with larger observation points. For example, Allstadt *et al.* (2018) evaluated the results of three global statistical approaches (Godt *et al.*, 2008b; Nowicki Jessee *et al.*, 2018; Nowicki *et al.*, 2014) for landslides triggered by the 2016 Kaikōura, New Zealand earthquake and stated that all models overpredict hazard. Allstadt *et al.* (2018) noted that this could be attributed to the effect of large landslide population of the 2008 Wenchuan, China earthquake that was used in all models for training and/or validation.

For a given earthquake, two different training and modeling strategies can be followed. The first strategy is to develop a single model and apply it to any future earthquake to estimate EQIL probabilities. In this case, the model is trained for the optimum number of inventories and validated using the rest of the inventories. This is the method commonly applied in similar modeling studies (e.g., Kritikos *et al.*, 2015; Nowicki *et al.*, 2014). However, this may not be realistic as earthquakes may occur in different climatic, geologic and topographic conditions and trigger landslides with different spatial distributions. Thus, this alternative does not consider the similarities and differences between training and validation areas, and thus the representativeness of training set either. The representativeness of training sets is an important factor that significantly affects the quality of landslide susceptibility assessment (e.g., Kalantar *et al.*, 2018). Carrara *et al.* (2008) noted that a reliable training set should be selected from areas with similar local conditions (e.g., geological units, structures, land-use, rainfall distribution) that can differ even between neighboring areas. For a near real-time globally applicable model, such an optimal selection for a training set that would be representative of all the possible settings, may not be possible due to the limited number of EQIL inventories. Unless a future earthquake hits an area in which an inventory already exists, we need to train our model using inventories from “similar” historical events around the globe. Robinson *et al.* (2017) stated that the models developed for rapid assessment of EQIL suffer from inadequate training data that are not representative of the site of prediction. They suggest using only a part of landslides mapped in first few hours or days immediately after an earthquake as the training set. However, mapping part of triggered landslides is still a time-consuming process and thus this approach is not suitable for near real-time predictions. The second possible strategy is identifying EQIL zones based on causal factors and group the inventories accordingly. In this case, the statistical model is trained and validated for each zone, and when an earthquake occurs, one can apply the model specifically trained within similar training areas (EQIL zones). For example, Petschko *et al.* (2014) defined 16 different domains based on lithological classes in a regional scale susceptibility assessment for an area in Austria. A similar worldwide categorization of predictive models for possible EQIL zones, along with a large number of EQIL inventories, may improve the prediction of EQIL distribution, yet we may not have enough data to develop reliable EQIL zones.

Two questions need to be addressed to choose the best alternative: (i) How can we define an optimum training set? (ii) How can we categorize the EQIL inventories?

This study addresses the drawbacks and issues listed above and aims at developing an improved model for near real-time estimation of the probability of EQIL occurrence. To accomplish this task, we examined a set of 64 EQIL inventories, subdivided our study areas using SUs and carried out susceptibility analyses based on logistic regression.

6.2. Materials

We used an on-line EQIL inventory database (Schmitt *et al.*, 2017a), which was collected and presented by Tanyaş *et al.* (2017) (Chapter 2). It contains 64 digital EQIL inventories for 46 earthquakes with varying levels of quality and completeness (Table 6.1). In only a few of those inventories, the types of landslides were identified (Tanyaş *et al.*, 2017). The 2011 Eastern Honshu, Japan inventory (Wartman *et al.*, 2013) is the only one having records for lateral spreads, which is a type of landslide generally occurs as a result of soil liquefaction in saturated sands, gravel, silt, or occasionally triggered by seismically-induced disturbance in sensitive clays (Keefer, 2002). Because the lateral spreads have a completely different triggering mechanism than other types of landslides and we do not have enough data to train a predictive model for this type of landsliding, we excluded the lateral spreads from the inventory of Wartman *et al.* (2013). We assumed that the inventories do not include lateral spreads but various types of landslides such as coherent and disrupted slides and falls (Keefer, 1984).

To derive morphometric variables, we used the Shuttle Radar Topography Mission (SRTM) digital elevation model (with 30 meters resolution) (NASA Jet Propulsion Laboratory (JPL), 2013). We used the deterministic estimates of ground motion parameters (GMP) released by the U.S. Geological Survey (USGS) ShakeMap system (Allen *et al.*, 2008; Garcia *et al.*, 2012) to characterize the different EQIL. We used the global product of Sayre *et al.* (2014) to consider various lithologic and climatic conditions observed on landslide-affected areas examined in this study. This product has 250 m spatial resolution.

6.3. Method

We presented the framework of our methodology in five steps, which are illustrated in Fig. 6.1 and read as follows:

Step 1: We considered a subset of the EQIL inventories presented by Tanyaş *et al.* (2017), (Chapter 2) discarding the ones we believe are not sufficiently reliable for numerical modeling. We then created SU maps for the selected inventories using the algorithm developed by Alvioli *et al.* (2016).

Step 2: We selected independent parameters that will be used in both logistic regression analysis and k-means clustering (Jain, 2010), to categorize the inventories. We considered sampling balance between different inventories while we decide on independent parameters.

Step 3: We defined the necessary features of a training set needed to run a global analysis. We considered the optimum size and representativeness of a training set, in conjunction with the best set of independent parameters. This also allowed to identify the inventories causing low model performance.

Step 4: We categorized the inventories using the selected independent parameters.

Step 5: We developed three models trained by (i) all inventory (Version 1 in Fig. 6.1), (ii) all inventories except the ones with low model performance (Version 2), (iii) groups of inventories emerging from clustering (Version 3). We examined the performance of our models using the leave-one-out technique.

Step 6: We tested the proposed global analysis using four earthquakes with a few landslides were reported.

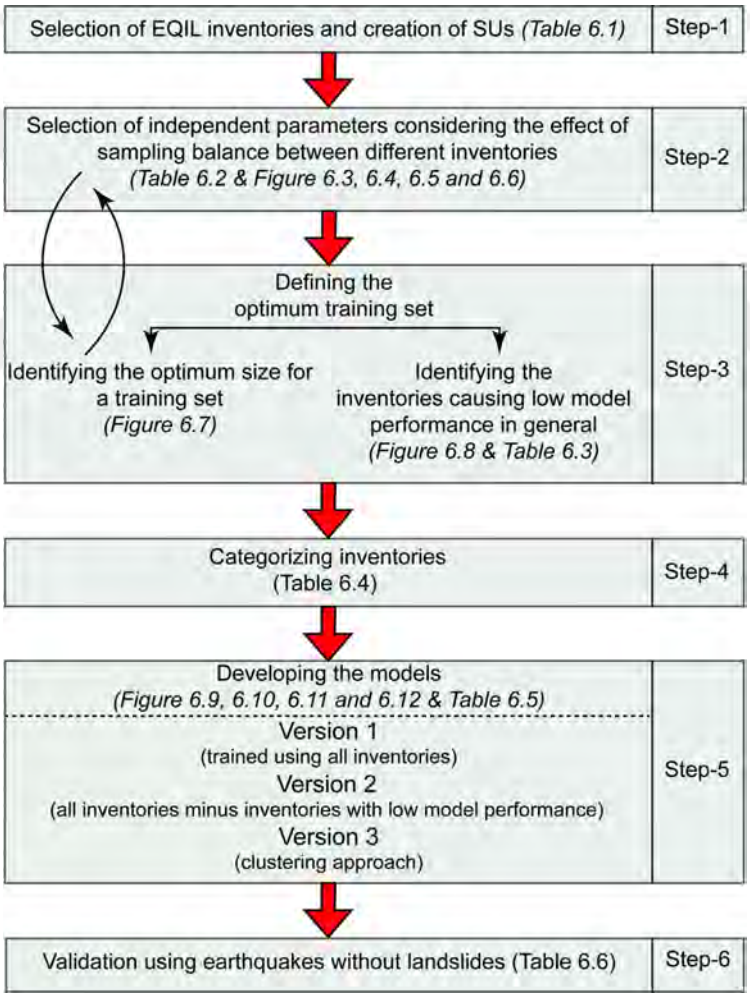

Figure 6.1. Workflow of the method proposed in this work for a global approach to predict earthquake-induced landslide events.

6.3.1. Selection of earthquake-induced landslide inventories and events

Harp *et al.* (2011) defined three basic criteria for evaluating the quality of landslides inventories related to (i) the coverage of the entire area affected by landslides, (ii) the inclusion of all landslides down to a size of 1 - 5 m in length, and (iii) the depiction of landslides as polygons rather than points. In our database, we have seven of the high-quality inventories listed by (Harp *et al.*, 2011): 1976 Guatemala (Harp *et al.*, 1981), 1978 Izu Oshima KinKai (Suziki, 1979), 1980 Mammoth Lakes (Harp *et al.*, 1984), 1983 Coalinga (Harp and Keefer, 1990), 1994 Northridge (Harp and Jibson, 1995, 1996), 1999 Chi-Chi (Liao and Lee, 2000), and 2008 Iwate-Miyagi-Nairiku (Yagi *et al.*, 2009).

We did not consider in the analysis those EQIL inventories in the database that did not have the adequate quality (Table 6.1). We excluded those inventories that contained landslides from several subsequent events, instead of a single earthquake. We also discarded EQIL inventories for which from the authors or the literature report that the landslide-affected area was not systematically surveyed (Bornaetxea *et al.*, 2018), for the resulting inventories are probably not complete. The term completeness refers to whether an EQIL inventory includes all landslides above a specified size triggered by a specific earthquake (Guzzetti *et al.*, 2012). Here we refer to completeness of the inventory within a given boundary, which may be cover only a part of the landslide-affected area. We do not discard inventories obtained systematic survey of a subset of the landslide-affected area, such as the 1989 Loma Prieta (McCrink, 2001), the 2006 Kiholo Bay (Harp *et al.*, 2014) and the 2015 Gorkha (Tanyaş *et al.*, 2018) (Chapter 3) inventories. If we have more than one inventory for the same earthquake, we only included the one that has the largest number of landslides and covers a wider area.

We also evaluated the uncertainty level of ShakeMaps to select the inventories. The relative uncertainty level of each ShakeMap is described by a quality grading developed by Wald *et al.* (2008). In this grading system, meant primarily for the quick evaluation of near real-time maps, uncertainty levels of ShakeMaps are presented by letters from "A" to "F", based on high- to poor-quality constraints, respectively. According to this grading system, we discarded the earthquakes which had a poor grade (grade ≤ D). The list of EQIL inventories, their main characteristics and references, and the exclusion criteria are presented in Table 6.1.

In addition to EQIL inventories, for validation of the proposed model, we considered four earthquakes for which only a few landslides were reported in the media, but no inventory is available. To identify such earthquakes, we examined the earthquake catalog of the countries that EQIL are being monitored well by their national survey institutions. Tanyaş *et al.* (2017) (Chapter 2) sorted the countries based the number of EQIL reported earthquakes. Their study shows that the US EQIL inventories are generated for most of the earthquakes that trigger landslides, followed by Japan and Taiwan. Therefore, we focused on these countries.

We identified the first two earthquakes from Japan; the 2011 eastern Honshu (Mw=6.0) and 2013 Hokkaido (Obihiro) (Mw=6.9) earthquakes. ShakeMaps of these earthquakes show that both of the earthquakes affected mountainous regions with strong intensity (Fig.

6.2). Based on the records of the Japan Meteorological Agency (http://www.jma.go.jp/jma) no landslides were reported for both earthquakes. The third earthquake is the 2014 Napa (6.0) earthquake in the US. Collins (2014) conducted a reconnaissance survey in the earthquake-affected area, and although he did not map the entire areas systematically, he mapped 11 landslides on steep slopes and reported an overall lack of landslides in the entire area. The fourth earthquake is the 2016 Yujing (Mw=6.4) earthquake in Taiwan, where the epicenter was located in a mountainous area where some landslides were triggered by the 1999 Chi-chi earthquake. We checked the imagery provided by Google Earth for the earthquake-affected area and did not observe any landslide triggered by the event, nor did we find any reported landslide in the media regarding this event.

6.3.2. Slope Units

We delineated SUs for study areas, which are systematically surveyed landslide-affected areas. SUs can be delineated manually using topographic maps of adequate scale and quality (Carrara, 1988), but that would be a time-consuming and error-prone process (Alvioli *et al.*, 2016). In this study, we used the r.slopeunits software module (Alvioli *et al.*, 2016) for the automatic delineation of SUs. The module is integrated into GRASS GIS (Neteler and Mitasova, 2013), and automates the delineation of SUs, given a DEM and a set of user-defined input parameters.

The software uses an iterative and adaptive algorithm that divides the study area into large sub-catchments, which are in turn divided into half-basins, and eventually into SUs based on hydrological and geomorphological conditions. As a result of this adaptive approach, the obtained SUs map contains polygons of varying sizes and shapes. The output of the software can be tuned by optimized a few input parameters (Alvioli *et al.*, 2016; Alvioli *et al.*, 2018c; Schlögel *et al.*, 2018). Moreover, the software contains an option to impose a threshold size below which SUs would be merged with the adjacent polygons facing, on average, the same direction.

We optimized the average SU size considering the spatial resolution of selected independent variables. All such predictors have a 30-meter resolution as they are all derived from the SRTM DEM, whereas the ground motion parameters have a significantly lower resolution. As the grid size for ShakeMap is around 1 km, we used a comparable size threshold of 1 km^2 for minimum SU area, below which SUs merging procedure is enabled. The use of larger SUs gives the advantage that the analysis is less sensitive to EQIL inventories with lower quality. The quality of an inventory is determined by the geographical and thematic correctness of the information (Guzzetti *et al.*, 2012). In pixel-based susceptibility assessments, low-quality inventories may have a misleading effect on susceptibility assessments, if the pixel size is relatively small (resolution ≤90 meters), because of a wrong landslide location. If we work with polygon-based landslide inventory and raster data with small pixel sizes, the sampling of landslide pixels may be a crucial strategy in terms of model result (Rossi and Reichenbach, 2016). Sampling landslide pixels from the centroid of the landslide polygon or only the scarp area would result in different sets of independent variables in the susceptibility analyses. Therefore, working with geomorphological SUs that have similar aspect mitigates the drawbacks of pixel-based analyses.

Table 6.1. EQIL inventories we used in this study

ID	Location	Date	Magnitude	Number of landslides	E. Surveyed Area (km²)	Quality of ShakeMap (Grade)	Reference study	Included inventories	Reasoning
1	San Fernando, Cal. (USA)	1971-02-09	6.6 (Mw)	391	320	A	Morton, 1971		Triggered by several earthquakes
2	Guatemala	1976-02-04	7.5 (Mw)	6224	5870	B	Harp et al., 1981	✓	
3	Friuli (Italy)	1976-05-06	6.5 (Ms)	1007	533	A	Govi, 1977	✓	
4	Izu Oshima Kinkai (Japan)	1978-01-14	6.6 (Ms)	659	1170	C	Suziki, 1979	✓	
5	Mount Diablo, Cal. (USA)	1980-01-24	5.8 (Mw)	105	-	A	Wilson et al., 1985		Not systematically surveyed
6	Mammoth Lakes, Calif. (USA)	1980-05-25	6.5 (ML)	4027	2323	A	Harp et al., 1984		Triggered by several earthquakes
7	Coalinga, California (USA)	1983-05-02	6.7 (ML)	3980	2139	A	Harp and Keefer, 1990	✓	
8	San Salvador (El Salvador)	1986-10-10	5.7 (Mw)	268	-	C	Rymer, 1987		Not systematically surveyed
9a	Loma Prieta, California (USA)	1989-10-18	6.9 (Mh)	1775	-	A	Keefer and Manson, 1998		Not systematically surveyed
9b	Loma Prieta, California (USA)	1989-10-18	6.9 (Mh)	138	2200	A	McCrink, 2001	✓	
10	Limon (Costa Rica)	1991-04-22	7.6 (Mw)	1643	2032	B	Marc et al., 2016	✓	
11	Finisterre Mt./ (Papua N. G.)	1993-10-13	6.9 (Mw)	4790	4744	D	Meunier et al., 2008		Triggered by several earthquakes
12	Northridge, California (USA)	1994-01-17	6.7 (Mw)	11111	4522	A	Harp and Jibson, 1995	✓	
13	Hyogo-ken Nanbu (Japan)	1995-01-16	6.9 (Mw)	2353	176	A	Uchida et al., 2004	✓	
14a	Umbria-Marche (Italy)	1997-09-26	6.0 (Mw)	233	679	A	Esposito et al., 2000;Antonini et al., 2002		Triggered by several earthquakes
14b	Umbria-Marche (Italy)	1997-09-26	6.0 (Mw)	210	264	A	Marzorati et al., 2002		Triggered by several earthquakes
15	Jueili (Taiwan)	1998-07-17	5.7 (Mw)	847	744	D	Huang and Lee, 1999		Poor quality of ShakeMap
16	Chi-chi (Taiwan)	1999-09-20	7.7 (Mw)	9272	36039	A	Liao and Lee, 2000	✓	
17	Santa Tecla (El Salvador)	2001-01-13	7.7 (Mw)	139	-	B	Ministerio de Medio Ambiente y Recursos Nat., El Salvador, 2001		Not systematically surveyed
18	Santa Tecla (El Salvador)	2001-02-13	6.6 (Mw)	62	-	A			Not systematically surveyed
19	Avaj (Iran)	2002-06-22	6.5 (Mw)	50	-	A	Mahdavifar et al., 2006		Not systematically surveyed
20	Denali Alaska (USA)	2002-11-03	7.9 (Mw)	1579	7748	B	Gorum et al., 2014	✓	

Table 6.1. (Continued)

ID	Location	Date	Magnitude	Number of landslides	E. Surveyed Area (km²)	Quality of ShakeMap (Grade)	Reference study	Included inventories	Reasoning
21	Lefkada Ionian Islands (Greece)	2003-08-14	6.3 (Mw)	274	172	A	Papathanassiou et al., 2013	✓	
22a	Mid-Niigata (Japan)	2004-10-23	6.6 (Mw)	10516	1075	A	GSI of Japan, 2005		Triggered by several earthquakes
22b	Mid-Niigata (Japan)	2004-10-23	6.6 (Mw)	4615	252	A	Sekiguchi and Sato, 2006		Triggered by several earthquakes
22c	Mid-Niigata (Japan)	2004-10-23	6.6 (Mw)	3922	252	A	Yagi et al., 2007		Triggered by several earthquakes
23a	Kashmir (India-Pakistan)	2005-10-08	7.6 (Mw)	2424	2234	A	Sato et al., 2007		Inventory 23c has larger coverage
23b	Kashmir (India-Pakistan)	2005-10-08	7.6 (Mw)	1461	1227	A	Basharat et al., 2014		Inventory 23c has larger coverage
23c	Kashmir (India-Pakistan)	2005-10-08	7.6 (Mw)	2930	5402	A	Basharat et al., 2016	✓	
24	Kiholo Bay (Hawaii)	2006-10-15	6.7 (Mw)	383	171	A	Harp et al., 2014	✓	
25a	Aysen Fjord (Chile)	2007-04-21	6.2 (Mw)	540	1444	N/A	Sepúlveda et al., 2010		No ShakeMap
25b	Aysen Fjord (Chile)	2007-04-21	6.2 (Mw)	517	1515	N/A	Gorum et al., 2014		No ShakeMap
26a	Niigata Chuetsu-Oki (Japan)	2007-07-16	6.6 (Mw)	312	396	A	Kokusai Kogyo, 2007		Including pre-earthquake landslides
26b	Niigata Chuetsu-Oki (Japan)	2007-07-16	6.6 (Mw)	70	–	A	Collins et al., 2012		Not systematically surveyed
27	Pisco / (Peru)	2007-08-15	8.0 (Mw)	271	24259	A	Lacroix et al., 2013	✓	
28a	Wenchuan (China)	2008-05-12	7.9 (Mw)	13114	24188	A	Qi et al., 2010		Inventory 28d has larger coverage
28b	Wenchuan (China)	2008-05-12	7.9 (Mw)	59108	47484	A	Dai et al., 2011		Inventory 28d has larger coverage
28c	Wenchuan (China)	2008-05-12	7.9 (Mw)	60109	29472	A	Gorum et al., 2011		Inventory 28d has larger coverage
28d	Wenchuan (China)	2008-05-12	7.9 (Mw)	19748	75424	A	Xu et al., 2014b	✓	
28e	Wenchuan (China)	2008-05-12	7.9 (Mw)	69605	37523	A	Li et al., 2014		Inventory 28d has larger coverage
28f	Wenchuan (China)	2008-05-12	7.9 (Mw)	6727	177	A	Tang et al., 2016		Inventory 28d has larger coverage
29	Iwate–Miyagi Nairiku (Japan)	2008-06-13	6.9 (Mw)	4211	595	A	Yagi et al., 2009	✓	
30a	L'Aquila/Abruzzo (Italy)	2009-04-06	6.3 (Mw)	570	1137	A	Guzzetti et al., 2009		Triggered by several earthquakes
30b	L'Aquila/Abruzzo (Italy)	2009-04-06	6.3 (Mw)	89	–	A	Piacentini et al. 2013		Triggered by several earthquakes

Table 6.1. (Continued)

ID	Location	Date	Magnitude	Number of landslides	E. Surveyed Area (km^2)	Quality of ShakeMap (Grade)	Reference study	Included inventories	Reasoning
31	Sumatra (Indonesia)	2009-09-30	7.6 (Mw)	87	-	C	Umar et al., 2014		Not systematically surveyed
32a	Haiti	2010-01-12	7.0 (Mw)	4490	2350	A	Gorum et al., 2013		Inventory 32b has larger coverage
32b	Haiti	2010-01-12	7.0 (Mw)	23567	3866	A	Harp et al., 2016	✓	
33	Sierra Cucapah (Mexico)	2010-04-04	7.2 (Mw)	453	1520	A	Barlow et al., 2014	✓	
34	Yushu (China)	2010-04-13	6.9 (Mw)	2036	1234	C	Xu et al., 2013	✓	
35	Eastern Honshu (Japan)	2011-03-11	9.1 (Mw)	3475	21447	A	Wartman et al., 2013	✓	
36	Lorca (Spain)	2011-05-11	5.1 (Mw)	270	-	A	Alfaro et al., 2012		Not systematically surveyed
37	Sikkim (India)	2011-09-18	6.9 (Mw)	164	-	N/A	Chakraborty et al., 2011		No ShakeMap
38a	Lushan (China)	2013-04-20	6.6 (Mw)	1289	945	C	Li et al., 2013		Inventory 38b has larger coverage
38b	Lushan (China)	2013-04-20	6.6 (Mw)	15546	5351	C	Xu et al., 2015	✓	
39	Minxian-Zhangxian (China)	2013-07-21	5.9 (Mw)	2330	357	C	Xu et al., 2014a	✓	
40	Cook Straight (New Zealand)	2013-07-21	6.5 (Mw)	35	-	A	Van Dissen et al., 2013		Not systematically surveyed
41	Lake Grassmere (New Zealand)	2013-08-16	6.5 (Mw)	501	-	C	Van Dissen et al., 2013		Not systematically surveyed
42	Eketahuna (New Zealand)	2014-01-20	6.1 (Mw)	176	-	A	Rosser et al., 2014		Not systematically surveyed
43	Ludian (China)	2014-08-03	6.2 (Mw)	1024	291	C	Ying-ying et al., 2015	✓	
44	Wilberforce (New Zealand)	2015-01-05	5.6 (Mw)	265	-	C	GNS Science, 2015		Not systematically surveyed
45a	Gorkha (Nepal)	2015-04-25	7.8 (Mw)	4312	28130	C	Kargel et al., 2016		Inventory 45d has larger coverage
45b	Gorkha (Nepal)	2015-04-25	7.8 (Mw)	2654	17194	C	Zhang et al., 2016		Inventory 45d has larger coverage
45c	Gorkha (Nepal)	2015-04-25	7.8 (Mw)	2513	1197	C	Tanyas et al., 2018		Inventory 45d has larger coverage
45d	Gorkha (Nepal)	2015-04-25	7.8 (Mw)	24903	28344	C	Roback et al., 2017	✓	
46a	Kumamoto (Japan)	2016-04-15	7.0 (Mw)	336	457	A	DSPR-KU, 2016		Inventory 46b has larger coverage
46b	Kumamoto (Japan)	2016-04-15	7.0 (Mw)	2742	5851	A	NIED, 2016	✓	

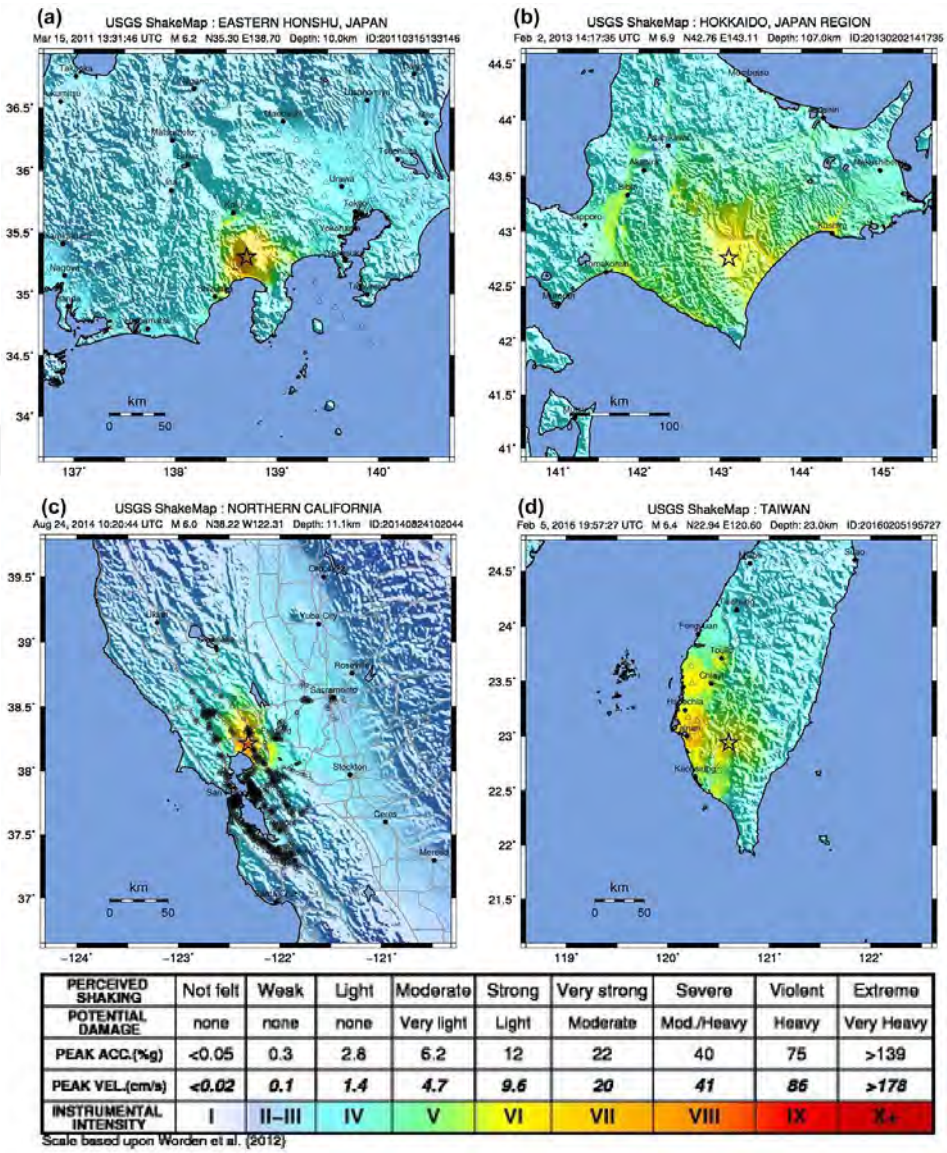

Figure 6.2. The ShakeMaps (Allen et al., 2008; Garcia et al., 2012) regarding (a) 2011 eastern Honshu, (b) 2013 Hokkaido, (c) 2014 Napa, and (d) 2016 Yujing earthquakes.

Although it is difficult to analyze the completeness of the EQIL inventories, due to lack of validation data, we examined the EQIL systematically by visual interpretation (Tanyaş *et al.*, 2017). Therefore, we assumed that non-landslide observations are equally reliable as landslide observations within the landslide-examined area. We limited our study areas to the reported landslide-examined areas. These areas refer to the explicitly surveyed area, which was called the effective surveyed areas (ESAs) (Bornaetxea *et al.*, 2018). When ESA was not indicated in the corresponding paper/report, we delineated a convex-hull

polygon encompassing all the mapped landslides and used this as an estimation of the ESA (Table 6.1).

To eliminate the flat regions as non-susceptible zones to landsliding (e.g., Kritikos *et al.*, 2015), we used the GRASS GIS (Neteler and Mitasova, 2013) r.geomorphon module developed by Jasiewicz and Stepinski (2013). This algorithm calculates various landform classes and associated geometry using machine vision approach. The flat regions identified by the algorithm, after additional supervised processing, were masked and excluded from the susceptibility assessments.

6.3.3. Statistical Approach

Several statistical methods such as logistic regression, weight of evidence, likelihood ratio, and neural network among the others can be applied for landslide susceptibility assessments (e.g., Guzzetti *et al.*, 2006). Among them, logistic regression is the most commonly preferred and recommended method (Brenning, 2005; Budimir *et al.*, 2015). It provides a relative estimate of landslide spatial occurrence based on local terrain conditions. The dependent variable of the logistic regression model is categorical (presence or absence), whereas the independent variables can be categorical, numerical or both (e.g., Atkinson and Massari, 1998). The logistic retrogression is expressed by the following equation:

$$logit(y) = \beta_0 + \beta_1 X_1 + \beta_2 X_2 + \cdots + \beta_i X_i + e$$

where y is the dependent variable, X_i is the i-th independent variable, β_0 is the constant, β_i is the i-th regression coefficient and e is the error. The relative probability of landslide occurrence is;

$$p = \frac{exp^{(\beta_0 + \beta_1 X_1 + \beta_2 X_2 + \cdots + \beta_i X_i)}}{1 + exp^{(\beta_0 + \beta_1 X_1 + \beta_2 X_2 + \cdots + \beta_i X_i)}}$$

In this study, we used the LAND-slide Susceptibility Evaluation (LAND-SE) software (Rossi and Reichenbach, 2016) that performs susceptibility modeling and zonation using logistic regression, quantifies the model performances, and the associated uncertainty.

We evaluated our model results using the receiver operating characteristics (ROC) curve, which is a technique for visualizing, organizing and selecting classifiers based on their performance (Fawcett, 2006). To assess the overall performance of a model, we check the variation in AUC value (varying between 0.5 for a random classification model and 1 for a perfect model), which is a metric referring to the area under the ROC Curve. Also, we use the confusion matrix containing the percentages of the four possible outcomes of a model: True Positive (TP), True Negative (TN), False Positive (FP) and False Negative (FN) (Fawcett, 2006). In the evaluation of susceptibility models, TP rate (TPR) is also called sensitivity, refers to the proportion of unstable mapping units (SUs with landslides) correctly classified by the model and is calculated as TPR=TP/(TP+FN). TN rate (TNR) is also called specificity, refers to the proportion of stable SUs (without landslides) correctly classified by the model and is calculated as TNR=TN/(TN+FP). We also consider the total percentage of TP and TN, referred in the literature as overall accuracy ACC = (TP+TN)/(TP+TN+FP+FN), as an additional metric of the model performance.

6.3.4. Dependent and independent variables

In our case, the dependent variable stores the information regarding the landslide occurrence within a SU. To define our dependent variable, we overlaid the landslides with SUs, and considered the presence of one or more landslides in the SU to characterize it as unstable, and stable otherwise.

Independent variables refer to factors controlling landslide occurrence. A number of interrelated factors such as topography, lithology, groundwater conditions, and ground shaking, play a role in the triggering of EQIL (Gorum *et al.*, 2011). To select the independent variables, we mainly considered two features of the data; (i) internal consistency, and (ii) interpretability. By consistency, we refer to data having the same origin and resolution. In this regard, we used global scale products, which provide the required information consistently anywhere in the world. Interpretability refers to the possibility of understanding the physical meaning of the examined predictor in terms of landsliding. For example, global scale geologic maps are available in the literature. However, in a global scale study, ranking geologic units from the most landslide prone to less prone is not feasible, because it is not their geological definitions that make those units landslide prone, but their lithological features. Units having the same geological definition may have considerably different landslide susceptibility because of their geotechnical characteristics. Similarly, the given definitions for land cover and climate zones is not sufficient to rank them based on susceptibility to sliding. Therefore, we did not consider the factors like geology, land cover or climate.

We categorized the independent variables as dynamic and static variables (Table 6.2). With the term dynamic, we referred to landslide triggering factors which are completely different in each EQIL-event (i.e., ground shaking parameters). Conversely, with the term static we referred to the variables that we assume as nearly constant through time (e.g., morphological variables).

The dynamic variables are immediately available after a new earthquake occurrence and then possibly used in our model for the forecast of EQIL in an operative phase. In the analysis, we used the estimated ground motion parameters of peak ground velocity (PGV), peak ground acceleration (PGA) and the Modified Mercalli Intensity (MMI) at the location of each landslide from the U.S. Geological Survey (USGS) ShakeMap Atlas 2.0 (Garcia *et al.*, 2012). MMI is a scale classifying the shaking strength observed at a site while PGV and PGA refer to the highest speed of shaking and the largest increase in velocity respectively, experienced by a particle on the ground during an earthquake (Bormann *et al.*, 2013). In order to explain the distribution of EQIL, the role of some earthquake-related factors such as fault-rupture mechanism and fault geometry (e.g., Gorum and Carranza, 2015; Gorum *et al.*, 2013; Tatard and Grasso, 2013) are also introduced in the literature. If these variables are known, they are taken into account, and a ShakeMap is created accordingly (e.g., Wald, 2013). Therefore, to avoid duplicated variables we only used ShakeMap products.

For static variables, we derived different morphometric variables from the SRTM DEM using the modules available in GRASS GIS (Neteler and Mitasova, 2013). The predictors, the GRASS modules used to derive them, and the relative references are listed in Table 6.2.

Each delineated SU was characterized by descriptive statistics of the predictors (mean values and standard deviations) (e.g., Rossi *et al.*, 2010) to create the dataset for the susceptibility assessment. The selection of those independent factors that control the characteristics of each EQIL-event was done considering the significance of each independent variable when modeling susceptibility using single EQIL inventory and their combination. We evaluated the significance level of each variable based on p-values (e.g., Chang *et al.*, 2008). We selected a p-value of 0.05 as a confidence level, below which the relation between the examined independent and dependent variables (R Core Team, 2017) was considered significant.

6.3.5. Categorization of the EQIL inventories

To categorize the earthquake-affected areas, and thus the inventories, we used one of the most widely used clustering algorithms, k-means (Jain, 2010). This method identifies a partition of the data, into a predefined number of clusters, such that the squared error between the mean of a cluster and the points in the cluster is minimized. The average values of selected independent variables derived using SUs were used as inputs of clustering. In modelling stage, we derived the average values for the ESAs, whereas in the near real-time application of the method, ESAs can be defined using PGA contours. Jibson and Harp (2016) stated that PGA range of 0.05-0.11g as an absolute outermost limit of triggered landslides.

Table 6.2. List of independent variables

Class	Independent variables	GRASS GIS module	Reference
Dynamic	PGA	-	(Garcia *et al.*, 2012)
Dynamic	PGV	-	(Garcia *et al.*, 2012)
Dynamic	MMI	-	(Garcia *et al.*, 2012)
Static	Slope	r.slope.aspect	(Hofierka *et al.*, 2009)
Static	Topographic Wetness Index (TWI)	r.topidx	(Cho, 2000)
Static	Vector Ruggedness Measure (VRM)	r.vector.ruggedness	(Sappington *et al.*, 2007)
Static	Distance to stream	r.watershed & r.grow	(Ehlschlaeger, 1989)
Static	Local relief	r.geomorphon	(Jasiewicz and Stepinski, 2013)
Static	Landform classes	r.geomorphon	(Jasiewicz and Stepinski, 2013)
Static	Plan Curvature	r.param.scale	(Wood, 1996)
Static	Profile Curvature	r.param.scale	(Wood, 1996)

We used the R (R Core Team, 2017) package “clusterboot” developed by Hennig (2007) for both clustering and evaluating the stability of the clusters. Hennig (2007) uses the Jaccard coefficient, a measure of similarity between clusters, as a cluster-wise measure of cluster stability. We assessed the distribution of the Jaccard coefficient using a

bootstrap approach for every single cluster as compared to the most similar cluster in the bootstrapped data sets. This clustering algorithm could identify not only the clusters in the data but also some important, meaningful patterns. The Jaccard coefficient ranges between 0 to 1 with higher values indicating greater similarity of grouping. A Jaccard coefficient between 0.6 and 0.75 indicates that there is a pattern, between 0.75 and 0.85 a valid cluster, and above 0.85 a 'highly stable" cluster, whereas a Jaccard coefficient less than or equal to 0.5 refers to a dissolved (unstable) cluster (Hsu, 2015).

6.4. Analyses

6.4.1. Selection of independent parameters

To evaluate the significance of variables for each EQIL inventory separately, we ran a susceptibility model 20 times, using different training and validation sets for each run. The datasets were selected with a random procedure to have an equal number of stable and unstable SUs. Then, without disturbing this ratio, we sampled 75% of SUs as training set and the other 25% as a validation set. We calculated p-values for all independent variables regarding these 20 runs (Fig. 6.3a). By counting the cases in which independent variables indicate high significance, we evaluated the overall significance of each variable (Fig. 6.3b).

We also evaluated the significance of variables using a dataset combined from all inventories. To guarantee the same representativeness, we randomly selected an equal number of SUs for each inventory. In total, the combined inventories had 150,000 SUs with 22,000 presence and 128,000 absence conditions. Each landslide-affected area differs from others in terms of its size, and thus we observe different numbers of SUs in each inventory (Fig. 6.4). The number of SUs with landslides varies largely and ranges from 27 in the 1989 Loma Prieta inventory (McCrink, 2001) to 9011 in the 2008 Wenchuan inventory (Xu *et al.*, 2014b). To create the final combined dataset, we selected a threshold of 100 SUs with landslides and sampled from each inventory accordingly. Four inventories did not have enough unstable SUs to fulfill this requirement, hence for these, we sampled all the unstable SUs (< 100) and an equal number of stable SUs. For the remaining inventories, we sampled 100 unstable and 100 stable SUs. We used this combined, balanced dataset to examine the variation of the significance of the independent variables and ran our susceptibility models 20 times. The observed variation of the p-values for each variable is shown in Fig. 6.5.

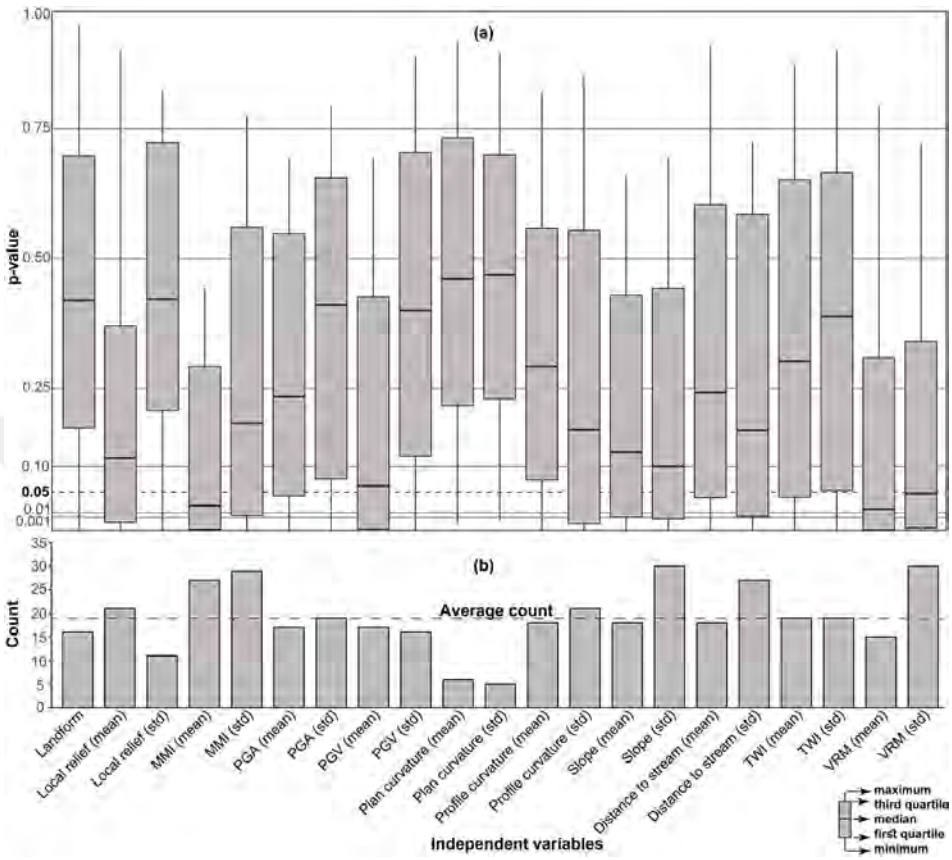

Figure 6.3. A summary graph regarding the selection of independent variables including (a) boxplots showing the distributions of p-values for each variable and (b) count of the times each variable had a p-value less than 0.05 in the susceptibility assessments (x20 runs per inventory).

Results indicate that the significance of the variables from the analysis of individual inventories (Fig. 6.3) are not always consistent with the results from the combined dataset (Fig. 6.5). The standard deviation of vector ruggedness measure (VRM), which quantifies terrain ruggedness by measuring the dispersion of vectors orthogonal to the terrain surface (Sappington *et al.*, 2007), is one of the most frequently observed variables in the inventory-based significance assessment (Fig. 6.3). However, in the combined dataset, the median p-value we obtained for this variable is 0.17, and thus VRM (std) does not a have a high significance in the combined model. On the other hand, in general, the variables with high significance from the combined dataset also have high significance based on inventory-based analyses. Therefore, we selected the following variables having high significance (median p-value < 0.05) in the susceptibility based on combined dataset: local relief (mean), local relief (std), MMI (mean), MMI (std), profile curvature (std), slope (mean), slope (std), distance to stream (mean), distance to stream (std), and VRM (std). We checked the pairwise collinearity among the selected set of variables (Belsley and Kuh,

1980), and figure 6.6 shows the results of the analysis. We discarded the following variable with values in the correlation matrix larger than 0.7: (i) local relief (std) being correlated with to local relief (mean) and slope (std), (ii) distance to stream (mean) being correlated with local relief (mean) and distance to stream (std), and (iii) VRM (std) being correlated with slope (mean) and slope (std). As a result, we identified seven independent variables for modeling; local relief (mean), profile curvature (std), slope (mean), slope (std), distance to stream (std), MMI (mean), and MMI (std). The physical meanings of these variables are described in the following. Slope and its standard deviation are notoriously related to the occurrence of landslides. Local relief is the maximum difference in height in a local neighborhood of each pixel and can be related to slope instability caused by tectonic uplift. It partially correlates with slope. The large standard deviation of profile curvature can be interpreted as a slope surface that has, for example, upwardly both concave and convex features. Standard deviation of stream distance is directly related to drainage density and one can expect low-density regions to be associated with large standard deviations of distance to streams, and vice-versa. This quantity can be correlated with lithological and climatic characteristics of the territory. Finally, the mean value of MMI as the triggering variable representing the severity of ground shaking contributes to the sliding forces. A large standard deviation in MMI for a given slope unit may be associated with dramatic variation in morphology or lithologic units. The actual relevance of each variable, in conjunction with the others, is given by the significance within the specific statistical model, provided by p-values.

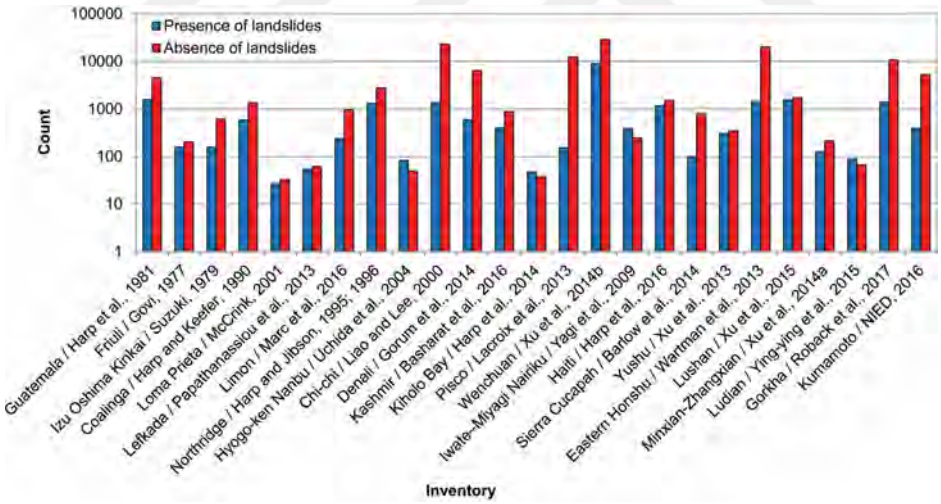

Figure 6.4. Number of SUs with presence and absence of landslides in each inventory.

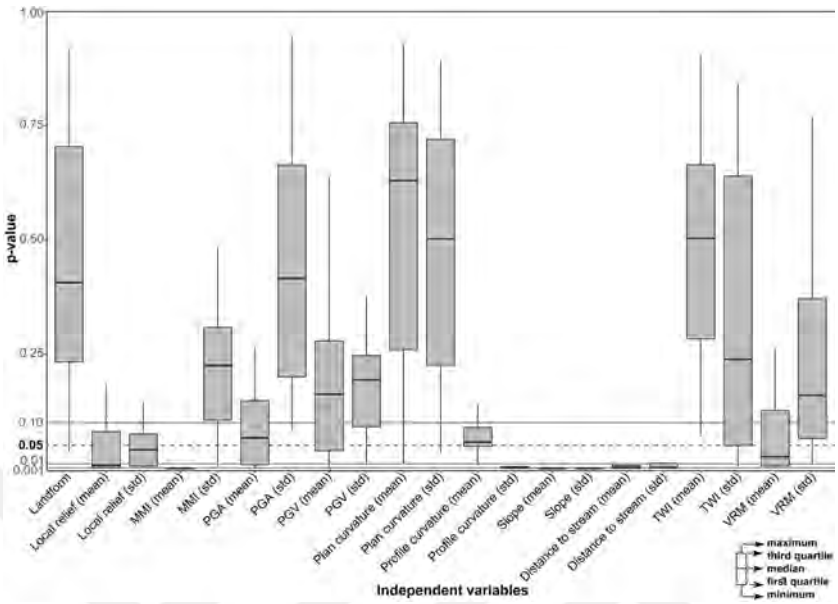

Figure 6.5. Boxplots of p-values for each variable of the combined data set obtained after 20 susceptibility computations.

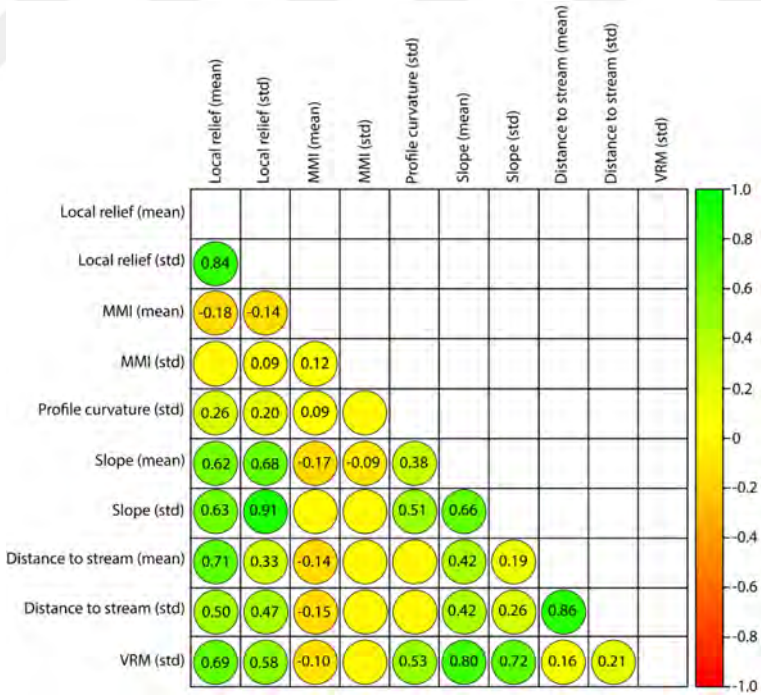

Figure 6.6. Diagram showing the correlation matrix of examined variables.

6.4.2. Defining the Optimum Training Set

We identified the optimum training set considering its size and representativeness, by testing different models. We used the high-quality inventories listed by Harp *et al.* (2011) for the validation of the models. To create the training dataset, we randomly selected an increasing number of EQIL. We then examined the susceptibility model validation performances (for the different validation inventories), analyzing the variation of AUC values and their uncertainty obtained for five different training sets. The same five sets were prepared and evaluated using a different number of inventories (Fig. 6.7). The results of this analysis show that the AUC values do not steadily increase when the training sets include more inventories, but they stabilized after a certain number. Additionally, AUC (Area Under ROC Curve) values show similar variation (overlapping bars) up to 12 inventories. For example, in Figure 6.7e, the AUC values for a model trained by randomly selected eight inventories changes between ~0.6 to ~0.7, overlapping to the variation bars obtained considering a lower number of inventories. However, we do not observe such a variation considering at least 12 inventories. On the other hand, Figure 6.7g shows that the uncertainty of the model decreases following the increase in the size of the training set. The uncertainty values stabilize to a value close to 0.05 when at least eight inventories are used. We use this to justify the creation of training sets using at least eight inventories (corresponding to ~800 presence and ~800 absence SUs) and where is possible with at least 12 inventories, to develop a stable model with low uncertainty.

In addition, the analysis in Fig. 6.7 shows that the EQIL inventories may not always be accurate enough to predict all the EQIL validation inventories. For example, Figure 6.7b shows that we could not improve the AUCs of the model although we tried various combinations of training sets. Another aspect resulting from the analysis is that the AUC seems not to be completely controlled by the size of the training set but also by its representativeness. For example, Figure 6.7d shows that the AUC value is 0.86 (but with large variation) for a model trained by a single randomly selected inventory, whereas the average AUC value is around 0.78 for the models trained by at least 12 inventories. This may indicate that it would be better selecting specific EQIL inventories, in place of a combination of them, as training dataset to generate susceptibility models applicable to earthquake occurring in similar EQIL zones.

To examine this in more detail, we selected the 1978 Izu Oshima KinKai (Suziki, 1979) inventory (Fig. 6.7d) as a validation set, and trained separate models using each of the other inventories (Fig. 6.8). We also trained a model by selecting part of the SUs belonging to the Izu Oshima Kinkai inventory. We used this last as a reference to select the models that even if trained with other inventories are able to perform better.

Results show that the accuracy (ACC) is around 80% when we trained the model using the Chi-chi, Denali, Gorkha, Kashmir, Kiholobay, Lefkada, Loma Prieta, or Yushu inventories. On the other hand, training a model with some other inventories such as Coalinga, Hyoge-ken Nanbu, Kumamoto, Ludian, Lushan, or Minxian-Zhangxian causes a much lower model performance. For example, ACC is 21% when the model is trained with the Hyoge-ken Nanbu inventory.

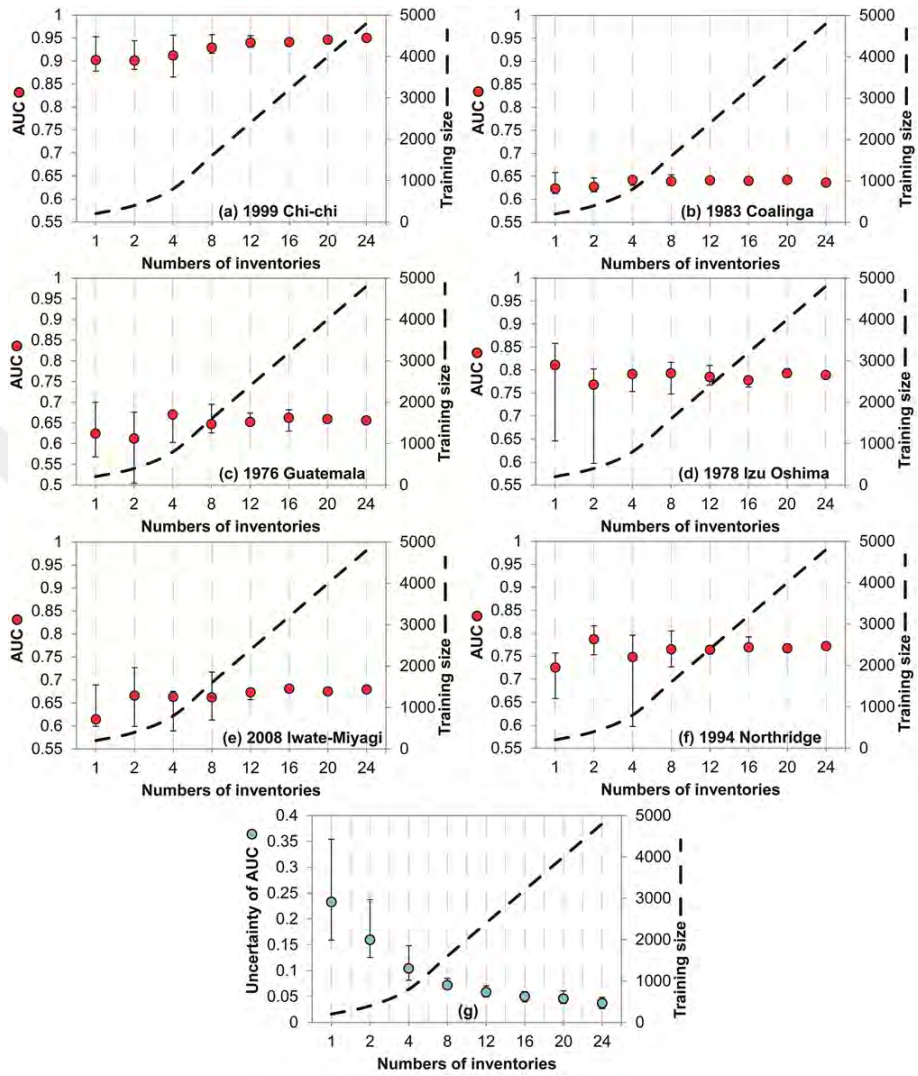

Figure 6.7. Graphs showing the variations in AUC for models based on a varying number of inventories and with changing validation inventories: (a) 1999 Chi-chi (Liao and Lee, 2000), (b) 1983 Coalinga (Harp and Keefer, 1990), (c) 1976 Guatemala (Harp et al., 1981), (d) 1978 Izu Oshima KinKai (Suziki, 1979), (e) 2008 Iwate-Miyagi-Nairiku (Yagi et al., 2009), (f) 1994 Northridge (Harp and Jibson, 1995, 1996) inventories. AUC is shown as dots, and vertical lines show the data range of AUC based on five replicas. In (g) the uncertainty of AUC is shown in relation to the size of the training set.

To assess the sensitivity of the model performance for various combinations of training inventories we used again the Izu Oshima Kinkai as a validation inventory. First, we combined the eight inventories listed above that gave the highest model performance (selected group 1). Second, we randomly selected one of the inventories used in selected group1 and replaced it with the badly predicting Hyoge-ken Nanbu inventory (selected

group 2). Third, we selected the Chi-chi inventory, which gives a high model performance and combined with seven inventories that give a low model performance (selected group 3). Lastly, we combined all inventories excluding the Izu Ohima Kinkai inventory itself and trained a model (selected group 4). Figure 6.8 shows that the model accuracy decreases from 83% to 58%, from selected group 1 to selected group 3. In addition, ACC is 70% for the model combining all the inventories, which is also much lower than the value of the model using the most representative inventories in selected group 1. These findings reveal that excluding irrelevant inventories from the training set helps us to improve the model performance.

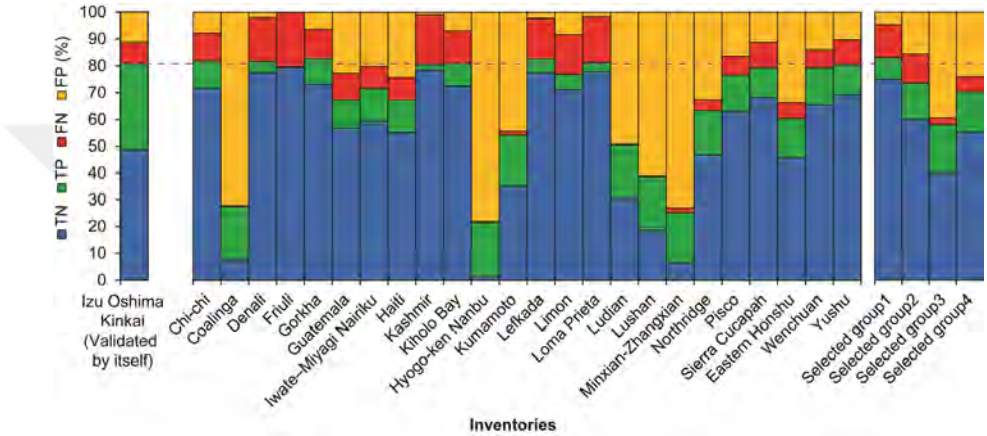

Figure 6.8. Results of models validated by the 1978 Izu Oshima KinKai inventory (Suziki, 1979) and trained by various inventories or inventory sets. TN: True Negative; TP: True Positive; FN: False Negative; FP: False Positive. The accuracy (ACC) of the models represented graphically by the sum of the two lower bars is compared with the accuracy obtained training the model in the validation area (dashed reference line). See text for explanation of the selected groups 1 to 4 on the right-hand side.

To additionally examine this issue, we conducted analyses similar to that made for the Izu Oshima Kinkai inventory, for all the inventories. The validation performance results in terms of ACC are shown in the matrix in Table 6.3.

Table 6.3 reveals that models trained by single specific inventories give a low performance in most of the cases. To identify them, we calculated the averages of accuracy of the models trained by each inventory (right column in Table 6.3). We defined a given inventory as not suitable for training if the resulting model on average is not capable of estimating at least half of presence and absence SUs correctly. As can be seen in Table 6.3, this was the case for five inventories: 1983 Coalinga (Harp and Keefer, 1990), 1995 Hyogo-ken Nanbu (Uchida *et al.*, 2004), 2014 Ludian (Ying-ying *et al.*, 2015), 2013 Lushan (Xu *et al.*, 2015), and 2013 Minxian-Zhangxian (Xu *et al.*, 2014a) inventories.

We explain such low performances of models trained by certain inventories for two reasons: (i) the factors controlling landslide initiation may be different for the inventories used for training and validation, or (ii) the inventory used to train the model may have low quality. Low quality refers to lack of geographical and thematic correctness of the information shown on the map (Guzzetti *et al.*, 2012).

Table 6.3. Table showing the validation accuracy (ACC) of models trained and validated by different inventories. Accuracy values from 0 to 50 were highlighted in red, from 51 to 75 in orange, and from 76 to 100 in green.

Model trained by \ Model validated by	Chi-chi	Coalinga	Denali	Friuli	Gorkha	Guatemala	Izu Oshima Kinkai	Iwate–Miyagi Nairiku	Haiti	Kashmir	Kiholo Bay	Hyogo-ken Nanbu	Kumamoto	Lefkada	Limon	Loma Prieta	Ludian	Lushan	Minxian-Zhangxian	Northridge	Pisco	Sierra Cucapah	Eastern Honshu	Wenchuan	Yushu	**Average**
Chi-chi	91	70	79	56	82	72	82	56	63	43	69	71	92	69	57	52	53	54	51	73	99	73	93	85	58	**69**
Coalinga*	55	64	9	45	29	38	28	63	47	33	53	65	39	25	22	21	63	62	55	50	70	34	28	51	51	**43**
Denali	95	44	72	65	89	74	82	40	56	67	64	54	93	62	77	51	44	53	45	68	99	86	93	79	55	**68**
Friuli	95	45	91	67	89	74	80	60	57	72	53	44	93	61	80	45	60	44	65	63	65	89	93	80	57	**69**
Gorkha	87	70	91	61	80	73	83	50	62	46	62	64	93	64	61	48	45	56	50	61	98	80	92	85	55	**68**
Guatemala	83	70	8	58	75	68	67	66	59	48	64	81	81	54	52	48	43	57	61	72	91	61	78	76	55	**63**
Izu Oshima Kinkai	63	70	36	44	55	60	68	59	53	36	59	62	84	51	33	52	64	66	63	72	87	32	81	71	61	**59**
Iwate–Miyagi Nairiku	76	71	40	55	79	65	72	72	59	37	62	80	82	54	54	52	61	57	61	74	89	66	79	70	54	**65**
Haiti	75	70	44	58	60	69	67	61	63	41	59	72	86	64	46	47	50	62	59	73	85	67	87	76	59	**64**
Kashmir	95	70	92	65	89	74	80	39	58	75	52	47	92	61	79	42	38	43	44	68	99	84	93	81	46	**68**
Kiholo Bay	90	71	65	46	86	71	81	63	59	48	79	65	83	74	63	55	35	54	42	73	98	53	86	81	57	**67**
Hyogo-ken Nanbu*	36	48	87	57	20	38	21	67	53	36	62	68	25	53	33	53	46	45	37	44	13	56	34	25	53	**43**
Kumamoto	60	70	18	47	45	52	54	68	51	34	59	75	68	51	27	41	60	66	54	68	78	47	70	69	56	**55**
Lefkada	90	42	88	48	86	74	83	43	60	58	66	56	90	85	73	50	44	53	36	71	99	68	92	83	58	**67**
Limon	70	68	85	63	57	68	77	40	57	52	71	45	89	59	76	45	60	57	40	64	68	89	88	46	55	**63**
Loma Prieta	90	65	24	55	88	72	81	44	57	59	48	39	88	51	73	62	46	52	44	69	99	71	91	84	53	**64**
Ludian*	43	48	21	32	37	36	51	62	44	30	28	34	29	40	21	41	61	68	61	44	61	11	9	66	50	**40**
Lushan*	49	58	63	44	36	40	39	61	45	28	54	24	43	34	20	31	65	71	55	45	66	16	21	68	50	**44**
Minxian-Zhangxian*	17	36	20	43	19	28	25	60	44	31	54	15	14	20	20	15	60	58	67	36	27	11	13	56	48	**32**
Northridge	79	72	17	47	68	57	63	63	54	34	59	70	77	53	31	65	42	60	61	70	97	47	73	80	57	**59**
Pisco	73	69	86	58	54	70	77	51	62	44	62	72	89	63	53	57	62	65	58	71	78	77	89	68	60	**66**
Sierra Cucapah	90	70	56	61	64	73	79	48	63	53	68	59	88	67	64	52	60	63	63	70	86	80	85	80	58	**67**
Eastern Honshu	58	71	8	46	50	52	60	67	54	33	59	70	63	47	24	64	60	63	63	68	69	40	57	70	60	**55**
Wenchuan	76	70	66	54	63	67	79	60	59	39	62	75	90	65	42	52	57	64	63	75	94	68	90	82	57	**66**
Yushu	72	70	61	44	58	65	80	56	59	39	58	65	84	55	38	48	63	64	62	69	87	69	85	73	63	**63**

If this is the case the training inventories spatially do not represent the EQIL causal factors properly, and thus give a low model performance. In any case, excluding these inventories from a training set helps to improve the model performance.

6.4.3. Categorization

For the EQIL inventory dataset, k-means algorithm identified five clusters with a Jaccard coefficient higher than 0.5 (Table 6.2). However, Cluster-5 was constituted by a single inventory, which is the 2006 Kiholo Bay inventory of Harp *et al.* (2014). Thus, we repeated the clustering for four clusters, and we had at least four inventories for each cluster (Table 6.4). This decreased the Jaccard coefficients for Cluster-1 and Cluster-4 to 0.5, which is the limit of unstable clusters.

In addition to the summary statistics we used to define these clusters, we examined some of the characteristics of the analyzed landslide-affected areas (e.g., faulting mechanism, lithologic units, climatic conditions) to evaluate the success of our clustering (Table 6.4). Similar characteristics observed in the inventories categorized under the same cluster can be interpreted as a sign for a tailored categorization. For example, under the most stable cluster (Cluster-3) (Table 6.4), we have the 2008 Wenchuan (Mw 7.9) and 2015 Gorkha (Mw 7.8) earthquakes, occurred in similar geomorphic (Kargel *et al.*, 2016) and seismotectonic settings (Wilkinson *et al.*, 2015). The 2005 Kashmir earthquake (Mw 7.6) is another continental thrust earthquake similar to the Wenchuan and Gorkha earthquakes and categorized under Cluster-3. On the other hand, in both the Wenchuan and Lushan earthquakes, the landslide-affected areas are exposed to similar climatic conditions; warm temperature climate with dry winter and hot summer while in Kashmir tundra and snow climate, fully humid conditions are observed (Kottek *et al.*, 2006). The 2013 Lushan (Mw 6.6) earthquake that also categorized under Cluster-3 occurred in similar tectonic, topographic and geologic conditions with the 2008 Wenchuan earthquake (Zhou *et al.*, 2016). On the other hand, the 2014 Ludian earthquake (Mw 6.2), occurred about 300 km south of the epicentral area of the 2008 Wenchuan earthquake, is also categorized under Cluster-3. However, the 2014 Ludian earthquake occurred on a strike-slip fault that is a different faulting mechanism than the formers. Another inventory categorized under Cluster-3 is the 2006 Kiholo Bay, Hawaii earthquake (Mw 6.7) occurred in a completely different tectonic setting as a result of normal faulting. We can list similar common features for the inventories categorized under other clusters. This shows that considering our knowledge regarding the characteristics of landslide-affected areas, we can partly validate the meaning of these clusters.

To get the lowest uncertainty, for each cluster we perform the susceptibility analysis, selecting for each inventory the maximum number of unstable SUs as possible (i.e., we did not use the same number of SUs for each inventory in the cluster). For example, in Cluster-1, we have four inventories (Table 6.4): Denali (7019 SUs, of which 592 with landslides), Friuli (362/158 with landslides), Lefkada (116/54), and Limon (1206/239). To obtain at least 1600 SUs (800 presence and 800 absence SUs) for the training set, we sampled 478 SUs for Denali, 316 for Friuli, 108 for Lefkada and 478 for the Limon inventory with an equal proportion of stable and unstable SUs (Table 6.4).

Table 6.4. EQIL inventories with some of their characteristics, clusters with the relative Jaccard coefficient and the number of SUs selected for the modeling for each cluster

Inventory	Dominant faulting mechanism	Dominant lithologic unit(s)	Dominant climatic condition(s)	Cluster ID (Five classes)	Jaccard coefficient	Cluster ID (Four classes)	Jaccard coefficient	Number of SUs	
Denali	Strike-slip	Mixed Sedimentary Rocks	Very Cold Moist / Wet					478	
Friuli	Thrust	Carbonate Sedimentary Rocks	Cool / Cold Vey Wet					316	
Lefkada	Strike-slip	Carbonate Sedimentary Rocks	Warm Wet	1	0.59	1	0.50	108	1686
Limon	Thrust	Carbonate Sedimentary Rocks and Intermediate Volcanics	Hot / Warm Very Wet					478	
Chi-chi	Thrust	Siliciclastic Sedimentary Rocks	Warm Very Wet					306	
Coalinga	Thrust	Siliciclastic Sedimentary Rocks	Warm Semi-Dry						
Guatemala	Strike-slip	Acidic and Basic Volcanics	Hot / Warm Wet					306	
Haiti	Strike-slip	Mixed Sedimentary Rocks and Basic Volcanics	Hot / Very Hot Wet					306	
Iwate–Miyagi	Thrust	Pyroclastics, Basic and Acidic Volcanics	Cool Very Wet					306	
Izu Oshima Kinkai	Strike-slip	Basic Volcanics and Mixed Sedimentary Rocks	Warm Very Wet	2	0.68	2	0.67	306	2196
Loma Prieta	Thrust	Siliciclastic Sedimentary Rocks	Warm Wet / Moist					54	
Minxian-Zhangxian	Thrust	Siliciclastic and Mixed Sedimentary Rocks	Cool Wet / Moist						
Northridge	Thrust	Siliciclastic Sedimentary Rocks	Warm Semi-Dry					306	
Pisco	Thrust	Acidic Plutonics, Intermediate Volcanics and Carbonate Sedimentary Rocks	Warm Dry / Cool Semi-Dry					306	
Gorkha	Thrust	Metamorphics	Warm Very Wet					804	
Kashmir	Thrust	Siliciclastic Sedimentary Rocks	Cold / Cool / Warm / Hot Wet					804	
Ludian	Strike-slip	Mixed Sedimentary Rocks	Warm Wet / Moist						
Lushan	Thrust	Siliciclastic / Mixed / Carbonate Sedimentary Rocks and Metamorphics	Cool / Warm Wet	3	0.78	3	0.80		2488
Wenchuan	Thrust	Siliciclastic / Mixed / Carbonate Sedimentary Rocks, Metamorphics, Acidic Plutonics and Intermediate Volcanics	Cold / Cool / Warm Wet					804	
Kiholo Bay	Normal	Basic Volcanics	Hot Wet / Very Wet	5	0.50			76	
Hyogo-ken Nanbu	Strike-slip	Acidic Plutonics	Warm Very Wet						
Kumamoto	Strike-slip	Basic Volcanics and Pyroclastics	Warm Very Wet					608	
Sierra Cucapah	Strike-slip	Acidic Plutonics and Metamorphics	Warm Dry / Hot Semi-Dry	4	0.55	4	0.50	196	2020
Eastern Honshu	Thrust	Acidic Plutonics, Pyroclastics and Unconsolidated Sediments	Warm / Cool Very Wet					608	
Yushu	Strike-slip	Mixed Sedimentary Rocks and Metamorphics	Very Cold Wet / Moist and Cold Moist					608	

6.4.4. Model Results

For each inventory used for validation, we ran four models following different approaches (Fig. 6.9 and Table 6.5). First, we trained and validated a model using the same inventories (Named "By itself" in Figure 6.9). We used the result of this analysis as a term of reference for other approaches. Second, we ran a model for each inventory using leave-one-out (LOO) (Version 1) approach. Third, we excluded the five inventories with low model performance indicated earlier and ran a model for each inventory using LOO (Version 2). Lastly, we used the 4 clusters defined above and ran a model LOO within each cluster (Version 3). Also, in these runs, we excluded the five inventories with low performances.

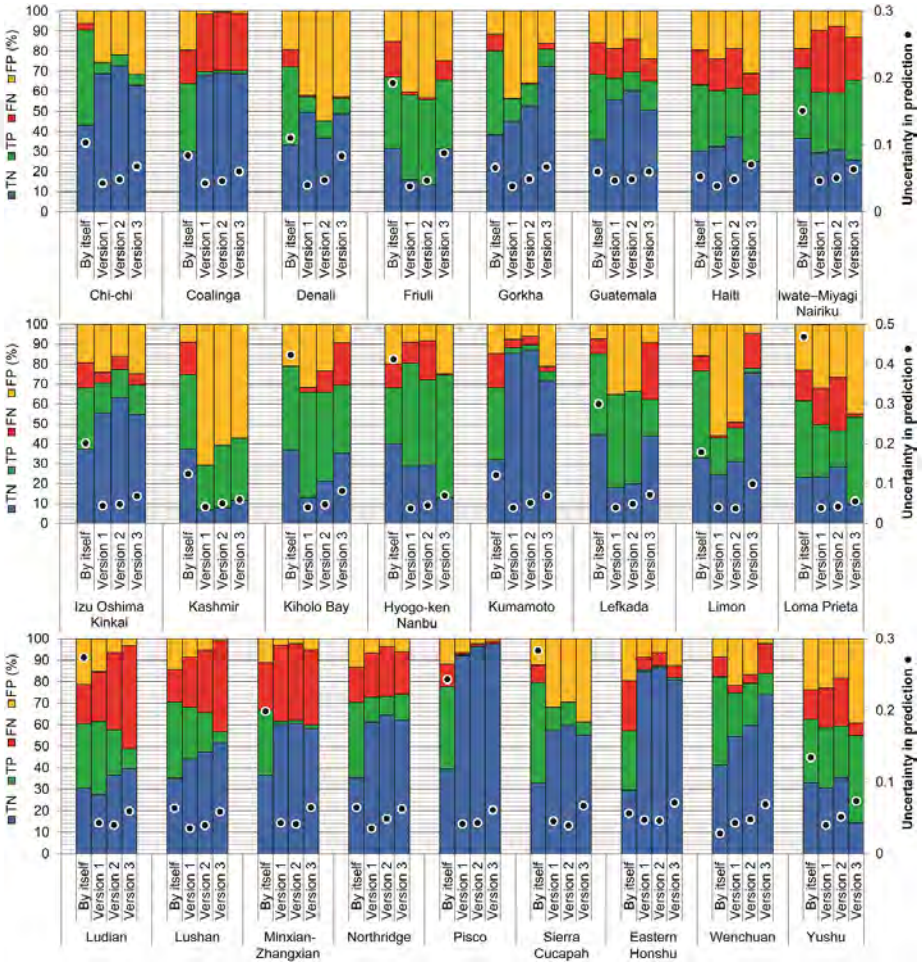

Figure 6.9. Graph showing the model performances obtained using every single inventory for validation. True Negative (TN), True Positive (TP), False Negative (FN), and False Positive (FP). The accuracy (ACC) of the models is represented graphically by the sum of the two lower bars. Dots show the uncertainty in the model prediction calculated by adopting a bootstrapping re-sampling technique (Rossi et al., 2010).

Table 6.5. Results of the covariate coefficients of the logistic regression modeling for different approaches

	Version 1		Version 2	
Coefficient	Estimate	Std. Error	Estimate	Std. Error
Intercept	-5.320238	0.303145	-6.970518	0.382131
Local relief (mean)	0.000008	0.000006	-0.000002	0.000003
MMI (mean)	0.470639	0.033963	0.613354	0.043806
MMI (std)	3.872863	0.526501	2.411564	0.580256
Profile Curvature (std)	-72.636361	18.096957	-83.335130	18.008694
Slope (mean)	0.052909	0.007717	0.061207	0.006733
Slope (std)	0.104255	0.016841	0.135553	0.018339
Distance to stream (std)	0.000365	0.000898	0.002635	0.000991

	Version 3 / Cluster1		Version 3 / Cluster2		Version 3 / Cluster3		Version 3 / Cluster4	
Coefficient	Estimate	Std. Error	Estimate	Std. Error	Estimate	Std. Error	Estimate	Std. Error
Intercept	-5.685920	1.203035	-9.825747	0.779450	-8.865352	0.954572	-7.872276	0.989411
Local relief (mean)	0.000028	0.000025	0.000058	0.000015	-0.000002	0.000005	0.000086	0.000050
MMI (mean)	0.329124	0.139046	0.957197	0.085839	0.627472	0.086758	0.712053	0.110239
MMI (std)	2.126097	1.266574	3.064755	1.147362	5.259031	1.449796	3.185642	1.086221
Profile Curvature (std)	-20.477350	24.398948	150.787097	118.238679	-323.307406	142.804829	327.010531	168.990175
Slope (mean)	0.073601	0.024969	0.015551	0.021006	0.109437	0.017495	-0.001040	0.037150
Slope (std)	0.115960	0.038856	0.245183	0.042968	0.186239	0.039213	0.162854	0.047157
Distance to stream (std)	0.000172	0.002360	-0.001316	0.001967	0.003957	0.002495	0.000034	0.001902

Results show that Version 2 brings to an overall improvement of the model performance than Version 1 (Fig. 6.10a) in 18 (72%) out of 25 cases. However, in two cases (Denali and Hyogo-ken Nanbu) we observe the opposite (Fig. 6.10a). Clustering (Version 3) significantly improved the model performance in almost half of the cases (in 11 events, 44%) (Fig. 6.10b). For example, for the 1991 Limon event, the total percentage of truly estimated landslide and non-landslide SUs is almost double (78%) by clustering (Fig. 6.9). Also, for the 2015 Gorkha event, the 2005 Kashmir, and the 2008 Wenchuan events, clustering leads to a substantial improvement of ACC (10% or more) (Fig. 6.9). On the other hand, there are 14 (56%) out of 25 cases where we observe a decrease in model performance after clustering (Fig. 6.10b). Among these are the four events that we excluded from training sets (1995 Hyogo-ken Nanbu, 2014 Ludian, 2013 Lushan, 2013 Minxian-Zhangxian) because they cause a decrease in model performance (Table 6.3). If

we ignore them, the average decrease in model performance for the remaining ten inventories is 3.7% in terms of ACC, whereas the average improvement for the other 11 was 10.0%.

In none of the clusters, we observe a common improvement that is valid for each member of a cluster. Contrary, we observe a common decrease in model performance in Cluster 4 (Fig. 6.10b).

Figure 6.11 shows an example of the results of landslide susceptibility assessment given for the Wenchuan event. The predicted probabilities (Fig. 6.11a and 6.11b) and their uncertainty map (Fig. 6.11c) are shown in the figure 6.11. Four-fold (or contingency) plot (Fig. 6.11d) and ROC plot (Fig. 6.11e) summarize graphically, the susceptibility results.

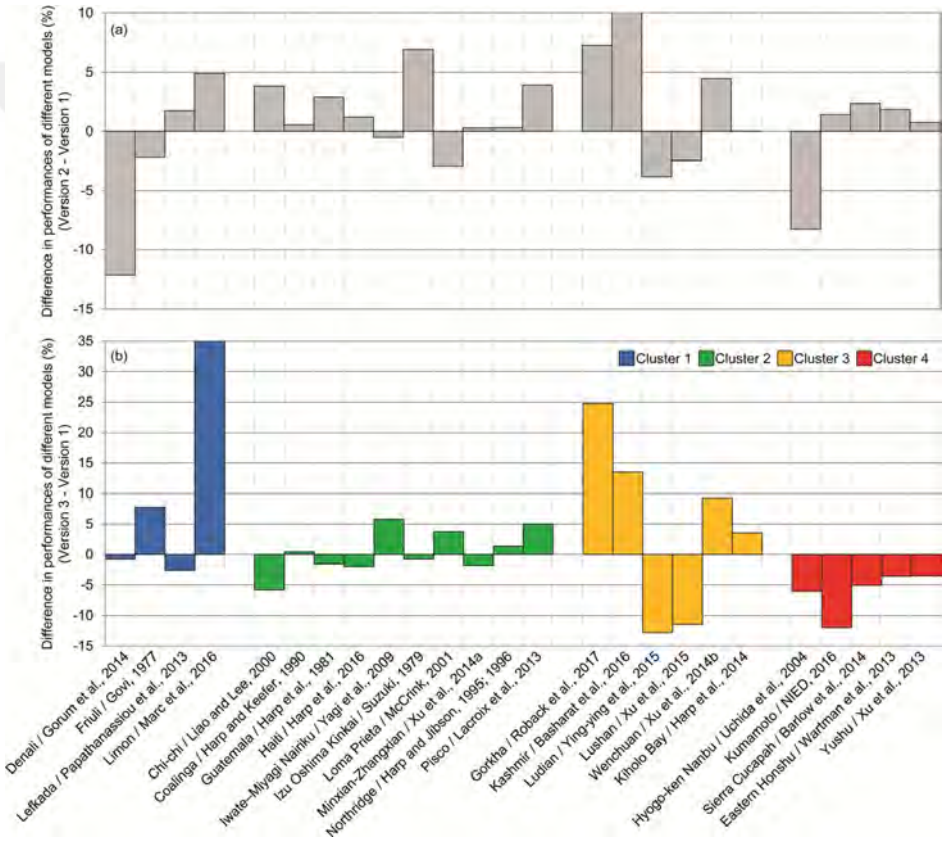

Figure 6.10. Graph showing the comparisons between the model performances based on the difference between (a) Version 2 (all inventories minus five worst ones using Leave One Out approach) and Version 1 (all inventories using Leave One Out approach), and (b) Version 3 (clustering approach) and Version 1.

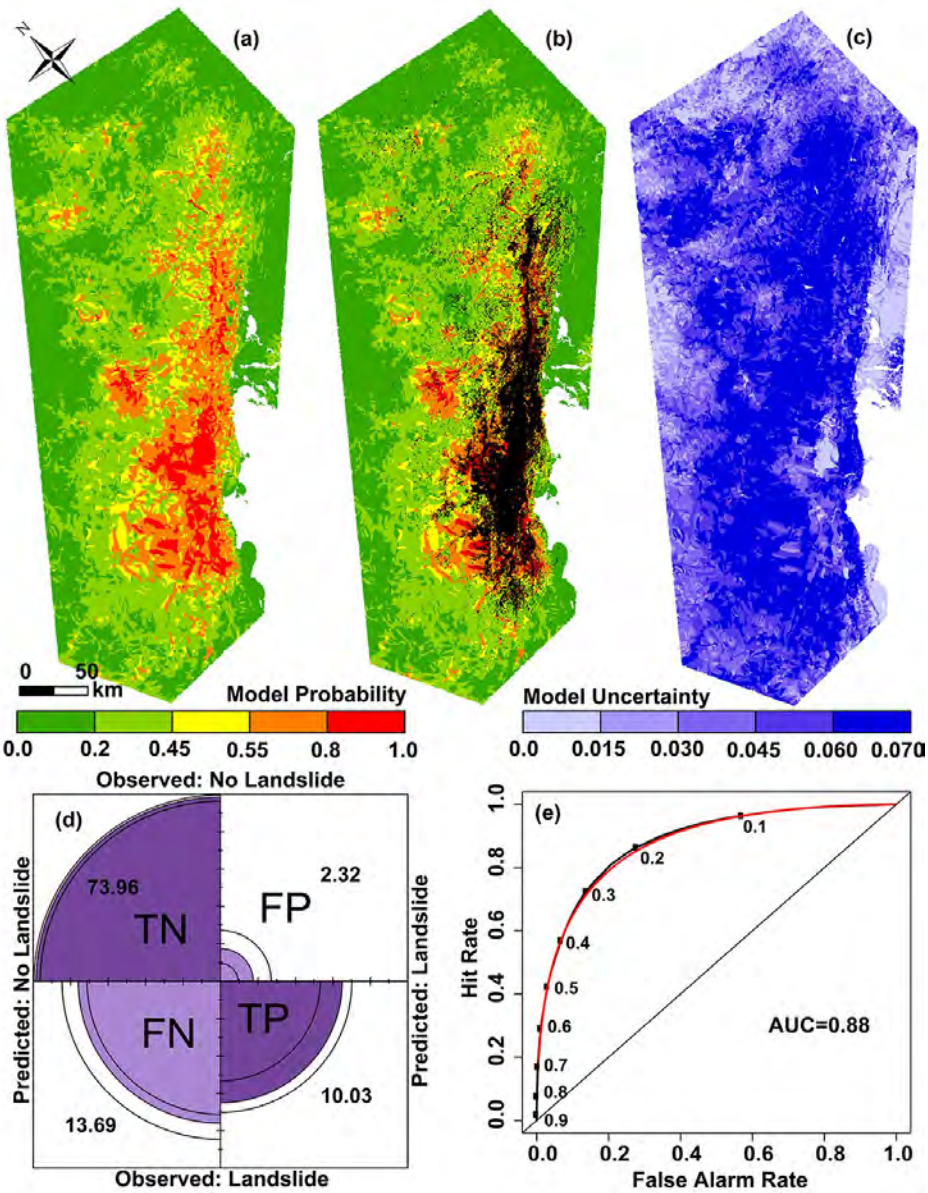

Figure 6.11. An example for the results of landslide susceptibility assessment obtained for the Wenchuan event. (a) the landslide susceptibility zonation, (b) the susceptibility zonation overlaid by the landslide inventory (with black dots referring to observed landslide occurrences), (c) model uncertainty map, (d) four-fold/contingency plots summarizing the confusion matrix values, and (e) ROC curve.

An overall evaluation of different approaches shows that we do not have a large difference in model performance (Fig. 6.12). As an average, the ACC ranges between 65% and 70%, and thus we can always estimate 65% - 70% of landslide occurrences in slope units (SUs) regardless of the approach.

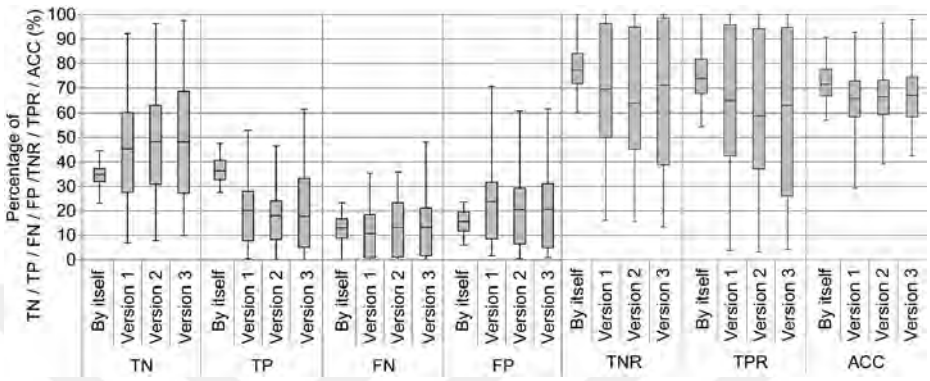

Figure 6.12. Overall results for classification performance obtained from the different versions of the statistical model.

Figure 6.12 also shows that in all cases FN (mean values vary from 10% to 13%) is less than FP (20% - 25%). FP refers to an overprediction; the SUs erroneously predicted as unstable by the model. On the other hand, FN refers to SUs erroneously predicted as stable. For the application in near real-time as basis for an emergency response, this is a major problem with FN being a good indicator of the model reliability which should produce result the smallest as possible. As an average, the specificities (TNR) of models range between 65% and 70%, while sensitivities are in between 60% and 65%.

To test this approach with earthquakes that were not used as data in the modeling training phase, we used the selected earthquakes (2011 eastern Honshu, 2013 Hokkaido, 2014 Napa, and 2016 Yujing earthquakes) for which only a few landslides were reported.

Based on the proposed method, for Napa and Yujing earthquakes we used the model Version 3 / Cluster 2, whereas for eastern Honshu and Hokkaido earthquakes we used Version 3 / Cluster 4 (Table 6.5). Results showed that our global statistical approach successfully estimated the absence of landslides in slope units for these four events. Table 6.6 shows that the proposed model identified at least 98% of the slope units as non-landslide units.

Table 6.6. Model results for non-landslide triggered earthquakes.

	TN (%)	TP (%)	FN (%)	FP (%)
Eastern Honshu	98.31	0.00	0.00	1.69
Obihiro	99.98	0.00	0.00	0.02
Napa	99.85	0.00	0.10	0.05
Yujing	98.37	0.00	0.01	1.63

6.5. Discussion

In this study, we analyzed the representativeness of earthquake-induced landslide inventories as training data for predictive near real-time models for landslide probability estimation after an earthquake. This analysis was missing in the previous global scale studies. For example, Kritikos *et al.* (2015) trained their model using only the 1994 Northridge (Harp and Jibson, 1995, 1996) and the 2008 Wenchuan (Xu *et al.*, 2014b) inventories and validated it using only the 1999 Chi-Chi (Liao and Lee, 2000) inventory. As a result, they argue that their model works successfully beyond the training environments. Table 6.3 shows that we have similar results for the same inventories. We used the 1999 Chi-Chi (Liao and Lee, 2000) inventory as a validation set and observed that the model performance, in terms of accuracy ACC was 79% when we used the 1994 Northridge inventory as training data and 76% when we used the 2008 Wenchuan inventory. However, a model trained by the Northridge inventory can give a poor model performance in other areas (see Table 6.3), for example for the Denali earthquake (where ACC was only 17%). This reveals that a model may not work properly beyond the spatial training domain, with performances depending on similarities/dissimilarities between the explanatory variables controlling the landslide occurrence, across the examined areas. Nowicki *et al.* (2014) discuss this issue as well. They tested the success of their global analysis on four different EQIL inventories and observed that their model predicts landslides more accurately when applied to the Wenchuan and Chi-Chi events, and less accurately when applied to the Northridge and Guatemala datasets. They noted that this may be caused by the particular geomorphological or climatological differences between the various events.

Given these findings, we clustered the EQIL inventory database based on topographic predictors and ground shaking parameters. Our analysis, based on Jaccard coefficients, identified one valid cluster, one pattern and two unstable clusters because we still had a limited dataset of suitable EQIL inventories. This indicates that our method can be improved with a larger EQIL database to identify additional stable clusters. Our findings show that clustering introduced a remarkable improvement in the modeling performance of some of the events. Therefore, when a new earthquake occurs, using our proposed clustering method, a set of inventories having similar characteristics (EQIL zone) with the examined area can be defined. Then the prediction model can be run using the most representative training set. To derive the required variables, we can examine the maping units located inside PGA values larger than 0.05g, as an absolute outermost limit of triggered landslides (Jibson and Harp, 2016).

The limited number of EQIL inventories is not the unique obstacle that limits the success of clustering of inventories. Both the quality and the completeness of landslide inventories is an issue that directly affects the reliability of the susceptibility analysis (e.g., Pellicani and Spilotro, 2015). Working with relatively large mapping units helped us to minimize the sensitivity of our model regarding the quality of inventories, whereas completeness is still an issue we could not address otherwise. We tested every possible combination of the available inventories by using them both as training and validation sets and identified five inventories that always caused low model performance. A defect in the completeness/representativeness of EQIL inventories may also be the reason for low

model performance, because some of the landslide free areas may actually be affected by landslides (Bornaetxea *et al.*, 2018) introducing inaccuracy in the dependent variable. If this is the case, even the evaluation of the success of our clustering may be inaccurate. For example, the Ludian and Lushan datasets are two of the inventories that resulted in a low model performance in general. They both belong to our valid cluster, Cluster 3. However, clustering caused a decrease in their model performance, while all other members of the same group gave better result after clustering (Fig. 6.10b). If we attribute this decrease to the inventories inaccuracies, we can argue that in case of having an adequate number of inventories available to define a stable group, clustering improves the performance of such a group. This argument will need to be validated by further studies.

One drawback of the method proposed in this study originates from the definition of the dependent variables. For a given SU, we considered the presence of at least one landslide is enough to identify our dependent variable as a presence for the examined SU. As a matter of fact, the number of landslides is a subjective term and may show a large variation under the control of several factors such as mapping methodology, amalgamation of coalescing landslides, and the quality and resolution of interpreted imagery (Tanyaş *et al.*, 2018) (Chapter 3). To address this issue, areal coverage of landslides for each mapping units may be considered as the dependent variable. This needs to be examined in further studies.

Another drawback of our method is represented by the dynamic predictors. The resolution of ShakeMap is rather low and does not account for topographic amplification of seismic energy, which can significantly increase amplitude of shaking at slope tops and ridges (Jafarzadeh *et al.*, 2015). Therefore, improvement in ground shaking parameters may help considerably to improve the model results.

6.6. Conclusions

This study proposes a comprehensive method for near real-time landslide probability estimation using a logistic regression model based on slope units and incorporating 25 EQIL inventories. We examine three different models that all developed using leave-one-out and trained by (i) all inventory (Version 1), (ii) all inventories minus five inventories with low model performance (Version 2), (iii) identified groups of inventories (Version 3). We show that we can correctly predict the stability condition of at least 65% of mapping units using any of these models.

Previous studies noted that the global analyses suffer from having a lack of EQIL inventories (e.g., Kritikos *et al.*, 2015) and inadequate training data that are not representative of the site of prediction (e.g., Robinson *et al.*, 2017). Given these remarks, we examine the size and representativeness of the training set for a global analysis considering the classification performance. We conclude that if the training set has adequate representativeness, we can have high performance regardless from its size, whereas if the training set has a lack of representativeness, its size does not make any difference in classification performance. An increase in the size of training set mainly helps us to have a model with lower uncertainty. These findings show us that we can follow a balanced sampling strategy between different inventories to create our training set. Therefore, to overcome the dominance of some inventories in a training set caused by

their large landslide population, we can sample an equal number of landslides from each inventory participated into a training set to increase the representativeness of a training set.

We propose to categorize the EQIL-events considering the similarity between static and dynamic causal factors to identify the most relevant training set for a given landslide-event. We categorize our inventories into four groups and develop a specific model for each of them. The findings of these models show that if we have an adequate number of inventories to identify a stable group, categorization of inventories and developing a specific model helps to increase model performance. However, our findings release that we need a larger EQIL database to create stable EQIL zones. The available EQIL database has not adequate representativeness to successfully predict EQIL distribution in every landslide-effective area. In the future, with a larger EQIL database, we can improve this global approach identifying more stable EQIL zones. We can also upgrade this model with smaller, higher detail SUs, if we have higher resolution ground shaking parameters.

We also conclude that the training set constituted by inventories with unknown quality and completeness levels may result in low model performance. Therefore, we propose to include the inventories with reliable metadata that help us to evaluate their quality and completeness levels.

The proposed categorization method and the available EQIL inventory database (Schmitt *et al.*, 2017b) can be used to improve the performance of any global statistical approach for rapid assessment of EQIL. This could provide valuable information regarding potential blockages of roads, streams and rivers, and other critical lifelines which are critical for the emergency-response phase.

7. Synthesis

7.1. Introduction

Earthquake-induced landslides (EQIL) are phenomena that have been studied by scientists for more than 200 years. The first known scientific investigation on this phenomenon was conducted in the Calabria region of Italy after the 1783 earthquake, and many more events have been studied since then (Keefer, 2002). The new developments in investigation techniques have made significant contributions to this scientific area (Wasowski *et al.*, 2011). The new findings were gathered and presented in many review publications with both worldwide (Keefer, 2002; Rodriguez *et al.*, 1999) and national scale (Hancox *et al.*, 2002; Hancox *et al.*, 1997; Papadopoulos and Plessa, 2000; Prestininzi and Romeo, 2000). As a cumulative result of these studies, the relations between distribution, type, and area coverage of landslides with a series of causal factors were tested, and presented (Keefer, 1984; Rodriguez *et al.*, 1999). However, further research showed that these relations are not always valid (e.g., Jibson and Harp, 2012) and that there are other additional important factors such as fault type, fault rupture, propagation direction of rupture or fault geometry which also play an important role in analyzing the expected coseismic landslide distribution.

In the last two decades, landslide-size statistics have also been used for both characterization and quantification of EQIL-events. Observations show that for most earthquake-triggered landslide inventories, both the area and volume distribution of medium and large landslides tend to follow a power-law which indicates fractal scaling (e.g., Malamud *et al.*, 2004). Though no clear physical explanation dictating fractal scaling exists (Hergarten, 2003), fractal scaling is seen for many natural phenomena such as earthquakes and forest fires (e.g. Hergarten, 2003; White *et al.*, 2008). This is a useful observation if it can be quantified because, for example, it allows one to learn something about the entire population of medium to large landslides by mapping only the largest (Malamud *et al.*, 2004). For example, Guzzetti *et al.* (2005) extracted the probability of landslide size from frequency-size statistics of landslides and used this information for the quantitative analysis of landslide hazard.

For most earthquake-triggered landslide inventories, the frequency-size distributions depart from the power-law for small landslides toward high frequencies with a rollover point where frequencies decrease for smaller landslides (e.g., Malamud *et al.*, 2004). The reason for divergence from the power-law is controversial. Explaining this issue can provide valuable information to better understand the factors controlling both sliding process and frequency-size distribution of landslides.

In addition to the above summarized statistical relations, modelling regarding the probability of EQIL occurrence has become a common approach in the last decade (Godt *et al.*, 2008a; Kritikos *et al.*, 2015; Nowicki Jessee *et al.*, 2018; Nowicki *et al.*, 2014; Parker *et al.*, 2017; Robinson *et al.*, 2017). However, the generation of earthquake-induced landslide susceptibility maps is complicated, as each earthquake has specific characteristics (location, depth, magnitude, fault type, etc.) and existing earthquake-induced landslide inventories only display the situation of a single EQ event out of a whole

distribution of possible future earthquakes, whereas for the other possible earthquakes no landslide inventories are generally available. As a result, most of the existing earthquake-induced landslide susceptibility methods are still rather simplified and hampered by an inadequate number of inventories to train those models.

7.2. Highlights of the Research

This research aimed to address the above listed issues. The main highlights of the research are:

- We compiled all digitally available EQIL inventories and created the largest EQIL repository available world-wide. We worked with the authors of inventories to make them publicly accessible through the U.S. Geological Survey ScienceBase platform. We examined the compiled inventories considering their quality, completeness, and representation using a set of criteria. By centralizing data access and making methodological details available, we anticipate that the platform will lead towards the development of better inventory maps, with relevant metadata. The data access will also allow better analysis of the data concerning the relation with other geospatial data such as climate, lithology, and topography.
- We analyzed the frequency-size distribution of EQIL inventories and concluded that one universal size model is not capable of modeling the FAD of all different landslide inventories because the observed power-law shapes and exponents vary significantly. We proposed an objective and automated methodology to estimate landslide-event magnitudes using the frequency-size distribution of landslides. We also proposed an equation to estimate the total landslide area in relation with landslide event magnitude scale.
- We examined the factors controlling the frequency-size distribution of EQIL including rollover and divergence from the power-law towards smaller landslide sizes. We concluded that several factors cause intrinsic noise in landslide frequency-size distributions, notable the mapping methodology, amalgamation of coalescing landslides, the quality and resolution of the imagery, the level of expertise of mappers, and the use of undifferentiated landslide source and deposit areas. We showed that lack of spatial image resolution and details of the underlying failure process as proposed in previously published studies clearly contribute to the divergence from the power-law, but no single existing explanation accounts for the deviation and rollover in all cases, and different factors contribute to explaining the causes of the rollover in different cases. We proposed an additional universally applicable explanation: successive slope failure, in which smaller slides sequentially destabilize surrounding slopes and merge to form larger slides that are detectable after the earthquake.
- We proposed a regression equation using static and dynamic predictors, which are rather general but publicly available to predict the magnitude scale of EQIL. We show that our approach successfully predicts landslide-event magnitude values and provides results along with their statistical significance and confidence levels. However, to test the validity of the approach globally, it should be calibrated using a larger and more representative dataset. A global, near real-

time assessments regarding landslide-event magnitude scale then can be achieved by retrieving the readily available ShakeMaps, along with topographic and thematic information, and applying the calibrated model.

- We developed a method to predict the probability of EQIL occurrence in near real-time. For the first time, we proposed to categorize the EQIL-events considering the similarity between static and dynamic causal factors to identify the most relevant training set for a given landslide-event. We showed that if we have an adequate number of inventories to identify a stable group, categorization of inventories and developing a specific model helps to increase model performance. We also showed that the training set constituted by inventories with unknown quality and completeness levels might result in low model performance.

7.3. Future Work

There are some limitations which are not only valid for this research but also similar EQIL modeling studies:

- Quantifying quality and completeness levels of inventories is not possible without examining the landslides from the original imagery from which the inventories were made, which is very time-consuming. However, both susceptibility and frequency-size distribution analyses are affected by these factors. To cope with this issue, a standard practice should be followed to create a landslide inventory. Guidelines should be developed for the standardized mapping of EQIL inventories, and provision of metadata. The undocumented inventories with unknown quality and completeness levels should not be used or only be used with great care if it is necessary.

- EQIL inventories are needed to train a model to predict the distribution of EQIL. However, the representativeness of the inventories is still a concern. We showed that 50% of all accessible EQIL inventories are from Asia, while only 5% are from South America. Therefore, categorizing the inventories is a solution to increase the representativeness of a training set. However, our findings indicate that we need a larger EQIL database to create stable EQIL zones. The available EQIL database still does not show adequate representativeness to successfully predict EQIL distribution in every landslide-effective area. In the future, with a larger EQIL database, the available global models should be updated using stable EQIL zones.

- Characteristics of the ground motion such as frequency content and duration have been noted as a factor that may alter the frequency-area distribution relative to other events (Jibson, 2011; Jibson *et al.*, 2004). For example, Jibson *et al.* (2004) stated that the 2002 Denali earthquake had significantly lower concentrations of small landslides (rock-falls and rock-slides) compared to the earthquake with comparable or lower magnitude earthquakes. They argued that this was because the earthquake shaking was deficient in high-frequency, high-amplitude accelerations. This hypothesis has not yet been tested or quantified to date and thus requires further analyses.

- In order to predict the probability of landslide occurrence, using both physical or statistical models, the accessibility of input layers-particularly at a global level-and their uncertainties is a continuing challenge. The uncertainty of those layers should be taken into consideration. Due to the global availability requirements, these factors cannot be very specific for certain areas, and therefore relevant factors such as structural geological setting and lithology cannot be taken into account, as these data are not globally available.
- Ground-shaking characterization is an important component of rapid-assessment studies, and ShakeMap is the most commonly used tool to derive the required parameters. However, ShakeMap does not currently directly account for topographic amplification (Sepúlveda *et al.*, 2005), duration of shaking (Jibson, 2011; Jibson *et al.*, 2004), or rupture direction (e.g., Gallen *et al.*, 2016), which are important factors in the landslide initiation process (Jibson, 2011; Jibson *et al.*, 2004). Further research needs to take these factors into account.
- Characterizing the shear strength of landslide material is a key issue (Dreyfus *et al.*, 2013) that has been difficult to address in global scale studies that aim to predict the probability of EQIL occurrence. None of the proposed methods provides a commonly accepted approach to estimate shear strengths or their relative contribution to landslide susceptibility.

Addressing each of these issues in the context of existing models is perhaps more important than developing new models, and these should be taken into consideration while developing new models.

Bibliography

Allen TI, Marano KD, Earle PS, Wald DJ. 2009. PAGER-CAT: A composite earthquake catalog for calibrating global fatality models. Seismological Research Letters **80**: 57-62

Allstadt KE, Jibson RW, Thompson EM, Massey CI, Wald DJ, Godt JW, Rengers FK. 2018. Improving Near-Real-Time Coseismic Landslide Models: Lessons Learned from the 2016 Kaikoura, New Zealand, Earthquake. Bulletin of the Seismological Society of America. DOI: https://doi.org/10.1785/0120170297

Allstadt KE, Thompson EM, Hearne M, Nowicki Jessee MA, Zhu J, Wald DJ, Tanyas H. 2017. Integrating Landslide and Liquefaction Hazard and Loss Estimates with Existing USGS Real-Time Earthquake Information Products. In *16th World Conference on Earthquake Engineering, Santiago, Chile*.

Barlow J, Barisin I, Rosser N, Petley D, Densmore A, Wright T. 2014. Seismically-induced mass movements and volumetric fluxes resulting from the 2010 Mw=7.2 earthquake in the Sierra Cucapah, Mexico. Geomorphology. DOI: https://doi.org/10.1016/j.geomorph.2014.11.012

Bennett G, Molnar P, Eisenbeiss H, McArdell B. 2012. Erosional power in the Swiss Alps: characterization of slope failure in the Illgraben. Earth Surface Processes and Landforms **37**: 1627-1640. DOI: 10.1002/esp.3263

Bird JF, Bommer JJ. 2004. Earthquake losses due to ground failure. Engineering Geology **75**: 147-179. DOI: https://doi.org/10.1016/j.enggeo.2004.05.006

Bouysse P. 2010. Geological Map of the World: Commission for the Geological Map of the World, scales: 1: 50,000,000 and 1: 25,000,000.

Brunsden D. 1985. Landslide types, mechanisms, recognition, identification. In *Landslides in the South Wales coalfield, edited by: Morgan, CS, Proceedings Symposium, April*; 1-3.

Budimir MEA, Atkinson PM, Lewis HG. 2014. Seismically induced landslide hazard and exposure modelling in Southern California based on the 1994 Northridge, California earthquake event. Landslides. DOI: 10.1007/s10346-014-0531-8

Carro M, De Amicis M, Luzi L, Marzorati S. 2003. The application of predictive modeling techniques to landslides induced by earthquakes: the case study of the 26 September 1997 Umbria–Marche earthquake (Italy). Engineering Geology **69**: 139-159. DOI: 10.1016/s0013-7952(02)00277-6

Cauzzi C, Edwards B, Fäh D, Clinton J, Wiemer S, Kästli P, Cua G, Giardini D. 2015. New predictive equations and site amplification estimates for the next-generation Swiss ShakeMaps. Geophysical Journal International **200**: 421-438. DOI: 10.1093/gji/ggu404

Cauzzi C, Fäh D, Wald DJ, Clinton J, Losey S, Wiemer S. 2018. ShakeMap-based prediction of earthquake-induced mass movements in Switzerland calibrated on historical observations. Natural Hazards **92**: 1211-1235. DOI: 10.1007/s11069-018-3248-5

Chakraborty I, Ghosh S, Bhattacharya D, Bora A. 2011. Earthquake induced landslides in the Sikkim-Darjeeling Himalayas – An aftermath of the 18th September 2011 Sikkim earthquake. 8 p. Report of Geological Survey of India. Koltaka.

Clauset A, Shalizi CR, Newman ME. 2009. Power-law distributions in empirical data. SIAM review **51**: 661-703. DOI: 10.1137/070710111

Collins BD, Kayen R, Tanaka Y. 2012. Spatial distribution of landslides triggered from the 2007 Niigata Chuetsu–Oki Japan Earthquake. Engineering Geology **127**: 14-26. DOI: 10.1016/j.enggeo.2011.12.010

Crosta G, Agliardi F, Frattini P, Sosoi R. 2012. SafeLand Deliverable 1.1: landslide triggering mechanisms in Europe - Overview and state of the art (378pp). SafeLand FP7, Deliverable 1.1. Retrieved from https://www.ngi.no/download/file/5969. 378.

Dai F, Lee C. 2001. Frequency–volume relation and prediction of rainfall-induced landslides. Engineering Geology **59**: 253-266. DOI: https://doi.org/10.1016/S0013-7952(00)00077-6

Dai F, Xu C, Yao X, Xu L, Tu X, Gong Q. 2011. Spatial distribution of landslides triggered by the 2008 Ms 8.0 Wenchuan earthquake, China. Journal of Asian Earth Sciences **40**: 883-895. DOI: 10.1016/j.jseaes.2010.04.010

Dreyfus D, Rathje EM, Jibson RW. 2013. The influence of different simplified sliding-block models and input parameters on regional predictions of seismic landslides triggered by the Northridge earthquake. Engineering Geology **163**: 41-54. DOI: https://doi.org/10.1016/j.enggeo.2013.05.015

Earle PS, Wald DJ, Jaiswal KS, Allen TI, Hearne MG, Marano KD, Hotovec AJ, Fee J. 2009. Prompt Assessment of Global Earthquakes for Response (PAGER): A System for Rapidly Determining the Impact of Earthquakes Worldwide. In *Open-File Report*.

Efron B, Tibshirani RJ. 1994. An introduction to the bootstrap, CRC press, New York. CRC press

Fan X, Juang CH, Wasowski J, Huang R, Xu Q, Scaringi G, van Westen CJ, Havenith H-B. 2018. What we have learned from the 2008 Wenchuan Earthquake and its aftermath: A decade of research and challenges. Engineering Geology **241**: 25-32. DOI: https://doi.org/10.1016/j.enggeo.2018.05.004

Fielding EJ. 1996. Tibet uplift and erosion. Tectonophysics **260**: 55-84. DOI: https://doi.org/10.1016/0040-1951(96)00076-5

Frattini P, Crosta GB. 2013. The role of material properties and landscape morphology on landslide size distributions. Earth and Planetary Science Letters **361**: 310-319. DOI: 10.1016/j.epsl.2012.10.029

Fujii Y. 1969. Frequency distribution of landslides caused by heavy rainfall. Journal Seismological Society Japan 22 **244-247**. DOI: http://doi.org/10.4294/zisin1948.22.3_244

Gallen SF, Clark MK, Godt JW. 2015. Coseismic landslides reveal near-surface rock strength in a highrelief, tectonically active setting. Geology. DOI: 10.1130/g36080.1

Gallen SF, Clark MK, Godt JW, Roback K, Niemi NA. 2016. Application and evaluation of a rapid response earthquake-triggered landslide model to the 25 April 2015 Mw 7.8 Gorkha earthquake, Nepal. Tectonophysics. DOI: https://doi.org/10.1016/j.tecto.2016.10.031

Galli M, Ardizzone F, Cardinali M, Guzzetti F, Reichenbach P. 2008. Comparing landslide inventory maps. Geomorphology **94**: 268-289. DOI: https://doi.org/10.1016/j.geomorph.2006.09.023

Garcia D, Mah R, Johnson K, Hearne M, Marano K, Lin K, Wald D, Worden C, So E. 2012. ShakeMap Atlas 2.0: an improved suite of recent historical earthquake ShakeMaps for global hazard analyses and loss model calibration. In *World Conference on Earthquake Engineering*.

Geospatial Information Authority of Japan. 2005. 1:25,000 Damage Map of the Mid Niigata Prefecture Earthquake in 2004: 3sheets.

Godt J, Sener B, Verdin K, Wald D, Earle P, Harp E, Jibson R. 2008. Rapid assessment of earthquake-induced landsliding. In *Proceedings of the First World Landslide Forum.*: United Nations University, Tokyo, Japan.

Gorum T. 2013. Towards a Better Understanding of Earthquake Triggered Landslides (Doctoral dissertation). In *ITC*. University of Twente.

Gorum T, Fan X, van Westen CJ, Huang RQ, Xu Q, Tang C, Wang G. 2011. Distribution pattern of earthquake-induced landslides triggered by the 12 May 2008 Wenchuan earthquake. Geomorphology **133**: 152-167. DOI: 10.1016/j.geomorph.2010.12.030

Gorum T, Korup O, van Westen CJ, van der Meijde M, Xu C, van der Meer FD. 2014. Why so few? Landslides triggered by the 2002 Denali earthquake, Alaska. Quaternary Science Reviews **95**: 80-94. DOI: 10.1016/j.quascirev.2014.04.032

Gorum T, van Westen CJ, Korup O, van der Meijde M, Fan X, van der Meer FD. 2013. Complex rupture mechanism and topography control symmetry of mass-wasting pattern, 2010 Haiti earthquake. Geomorphology **184**: 127-138. DOI: 10.1016/j.geomorph.2012.11.027

Guthrie R, Evans S. 2004. Magnitude and frequency of landslides triggered by a storm event, Loughborough Inlet, British Columbia. Natural Hazards and Earth System Science **4**: 475-483. DOI: 10.5194/nhess-4-475-2004

Guthrie RH, Deadman PJ, Cabrera AR, Evans SG. 2008. Exploring the magnitude–frequency distribution: a cellular automata model for landslides. Landslides **5**: 151-159. DOI: 10.1007/s10346-007-0104-1

Guzzetti F, Cardinali M, Reichenbach P, Carrara A. 2000. Comparing landslide maps: A case study in the upper Tiber River Basin, central Italy. Environmental management **25**: 247-263. DOI: 10.1007/s002679910020

Guzzetti F, Malamud BD, Turcotte DL, Reichenbach P. 2002. Power-law correlations of landslide areas in central Italy. Earth and Planetary Science Letters **195**: 169-183. DOI: 10.1016/S0012-821X(01)00589-1

Guzzetti F, Mondini AC, Cardinali M, Fiorucci F, Santangelo M, Chang K-T. 2012. Landslide inventory maps: New tools for an old problem. Earth-Science Reviews **112**: 42-66. DOI: https://doi.org/10.1016/j.earscirev.2012.02.001

Guzzetti F, Reichenbach P, Cardinali M, Galli M, Ardizzone F. 2005. Probabilistic landslide hazard assessment at the basin scale. Geomorphology **72**: 272-299. DOI: 10.1016/j.geomorph.2005.06.002

Hancox G, Perrin N, Dellow G. 2002. Recent studies of historical earthquake-induced landsliding, ground damage, and MM intensity in New Zealand. Bulletin of the New Zealand Society for Earthquake Engineering **35**: 59-95

Hansen A. 1984. Engineering geomorphology: the application of an evolutionary model of Hong Kong's terrain. Zeitschrift fur Geomorphologie, N F Supplementband **51**: 39-50

Harp EL, Hartzell SH, Jibson RW, Ramirez-Guzman L, Schmitt RG. 2014. Relation of Landslides Triggered by the Kiholo Bay Earthquake to Modeled Ground Motion. Bulletin of the Seismological Society of America **104**: 2529-2540. DOI: 10.1785/0120140047

Harp EL, Jibson RW. 1995. Inventory of landslides triggered by the 1994 Northridge, California earthquake: U.S. Geological Survey Open-File Report. 95-213.

Harp EL, Jibson RW. 1996. Landslides triggered by the 1994 Northridge, California earthquake. Bulletin of the Seismological Society of America **86**: 319-332

Harp EL, Keefer DK. 1990. Landslides triggered by the earthquake in Rymer, M.J. and Ellsworth, W.L., eds., "The Coalinga, California, Earthquake of May 2, 1983". U.S. Geological Survey Professional Paper **1487**: 335–347

Harp EL, Keefer DK, Sato HP, Yagi H. 2011. Landslide inventories: The essential part of seismic landslide hazard analyses. Engineering Geology **122**: 9-21. DOI: https://doi.org/10.1016/j.enggeo.2010.06.013

Harp EL, Tanaka K, Sarmiento J, Keefer DK. 1984. Landslides from the May 25–27, 1980, Mammoth Lakes, California, earthquake sequence. U.S. Geological Survey Miscellaneous Investigations Series Map.

Harp EL, Wilson RC, Wieczorek GF. 1981. Landslides from the February 4, 1976, Guatemala earthquake, U.S. Geological Survey Professional Paper 1204-A, 35 p, 2 plates. https://pubs.er.usgs.gov/publication/pp1204A.: Washington.

Hovius N, Stark CP, Allen PA. 1997. Sediment flux from a mountain belt derived by landslide mapping. Geology **25**: 231-234. DOI: 10.1130/0091-7613(1997)025<0231:SFFAMB>2.3

Hovius N, Stark CP, Hao-Tsu C, Jiun-Chuan L. 2000. Supply and removal of sediment in a landslide-dominated mountain belt: Central Range, Taiwan. The Journal of Geology **108**: 73-89. DOI: 10.1086/314387

Huang R, Fan X. 2013. The landslide story. Nature Geoscience **6**: 325-326. DOI: 10.1038/ngeo1806

Huang R, Li W. 2009. Analysis of the geo-hazards triggered by the 12 May 2008 Wenchuan Earthquake, China. Bulletin of Engineering Geology and the Environment **68**: 363-371. DOI: 10.1007/s10064-009-0207-0

Hurst M, Ellis M, Royse K, Lee K, Freeborough K. 2013. Controls on the magnitude-frequency scaling of an inventory of secular landslides. Earth Surface Dynamics **1**: 67. DOI: 10.5194/esurf-1-67-2013

Jibson RW. 1993. Predicting earthquake-induced landslide displacements using Newmark's sliding block analysis. Transportation research record:

Jibson RW. 2007. Regression models for estimating coseismic landslide displacement. Engineering Geology **91**: 209-218. DOI: https://doi.org/10.1016/j.enggeo.2007.01.013

Jibson RW. 2011. Methods for assessing the stability of slopes during earthquakes—A retrospective. Engineering Geology **122**: 43-50. DOI: https://doi.org/10.1016/j.enggeo.2010.09.017

Jibson RW, Harp EL. 2012. Extraordinary distance limits of landslides triggered by the 2011 Mineral, Virginia, earthquake. Bulletin of the Seismological Society of America **102**: 2368-2377. DOI: 10.1785/0120120055

Jibson RW, Harp EL. 2016. Ground motions at the outermost limits of seismically triggered landslides. Bulletin of the Seismological Society of America **106**: 708-719. DOI: 10.1785/0120150141

Jibson RW, Harp EL, Michael JA. 2000. A method for producing digital probabilistic seismic landslide hazard maps. Engineering Geology **58**: 271-289. DOI: https://doi.org/10.1016/S0013-7952(00)00039-9

Jibson RW, Harp EL, Schulz W, Keefer DK. 2004. Landslides triggered by the 2002 Denali Fault, Alaska, earthquake and the inferred nature of the strong shaking. Earthquake spectra **20**: 669-691. DOI: http://dx.doi.org/10.1193/1.1778173

Kargel JS, Leonard GJ, Shugar DH, Haritashya UK, Bevington A, Fielding EJ, Fujita K, Geertsema M, Miles ES, Steiner J, Anderson E, Bajracharya S, Bawden GW, Breashears DF, Byers A, Collins B, Dhital MR, Donnellan A, Evans TL, Geai ML, Glasscoe MT, Green D, Gurung DR, Heijenk R, Hilborn A, Hudnut K, Huyck C, Immerzeel WW, Jiang Liming, Jibson R, Kääb A, Khanal NR, Kirschbaum D, Kraaijenbrink PDA, Lamsal D, Liu Shiyin, Lv Mingyang, McKinney D, Nahirnick NK, Nan Zhuotong, Ojha S, Olsenholler J, Painter TH, Pleasants M, KC P, Yuan Q, Raup BH, Regmi D, Rounce DR, Sakai A, Shangguan Donghui, Shea

JM, Shrestha AB, Shukla A, Stumm D, van der Kooij M, Voss K, Wang Xin, Weihs B, Wolfe D, Wu Lizong, Yao Xiaojun, Yoder MR, Young N. 2016. Geomorphic and geologic controls of geohazards induced by Nepal's 2015 Gorkha earthquake. Science **351**. DOI: https://doi.org/10.1126/science.aac8353

Kaynia AM, Skurtveit E, Saygili G. 2011. Real-time mapping of earthquake-induced landslides. Bulletin of Earthquake Engineering **9**: 955-973. DOI: 10.1007/s10518-010-9234-2

Keefer DK. 1984. Landslides caused by earthquakes. Geological Society of America Bulletin **95**: 406-421. DOI: 10.1130/0016-7606(1984)95<406:LCBE>2.0.CO;2

Keefer DK. 1994. The importance of earthquake-induced landslides to long-term slope erosion and slope-failure hazards in seismically active regions. Geomorphology **10**: 265-284

Keefer DK. 2002. Investigating landslides caused by earthquakes–a historical review. Surveys in Geophysics **23**: 473-510. DOI: 10.1023/A:1021274710840

Keefer DK, Tannaci NE. 1981. Bibliography of landslides, soil liquefaction, and related ground failures in selected historic earthquakes. U. S. Geological Survey. Open-File Report, .

Kennedy IT, Petley DN, Williams R, Murray V. 2015. A systematic review of the health impacts of mass Earth movements (landslides). PLOS Currents Disasters **7**. DOI: 10.1371/currents.dis.1d49e84c8bbe678b0e70cf7fc35d0b77

Klar A, Aharonov E, Kalderon-Asael B, Katz O. 2011. Analytical and observational relations between landslide volume and surface area. Journal of Geophysical Research: Earth Surface (2003–2012) **116**. DOI: 10.1029/2009JF001604

Kokusai Kogyo. 2007. Aerial photo interpretation of earthquake damage from the 2007 Niigata Chuetsu–oki Earthquake. Kokusai Kogyo Co., Ltd: Japan.

Korup O. 2006. Effects of large deep-seated landslides on hillslope morphology, western Southern Alps, New Zealand. Journal of Geophysical Research: Earth Surface **111**: n/a-n/a. DOI: 10.1029/2004JF000242

Kritikos T, Robinson TR, Davies TR. 2015. Regional coseismic landslide hazard assessment without historical landslide inventories: A new approach. Journal of Geophysical Research: Earth Surface **120**: 711-729. DOI: 10.1002/2014JF003224

Lacroix P, Zavala B, Berthier E, Audin L. 2013. Supervised method of landslide inventory using panchromatic SPOT5 images and application to the earthquake-triggered landslides of Pisco (Peru, 2007, Mw8. 0). Remote Sensing **5**: 2590-2616. DOI: 10.3390/rs5062590

Larsen IJ, Montgomery DR, Korup O. 2010. Landslide erosion controlled by hillslope material. Nature Geoscience **3**: 247-251. DOI: 10.1038/ngeo776

Lee C-T. 2014. Statistical seismic landslide hazard analysis: An example from Taiwan. Engineering Geology **182**: 201-212. DOI: 10.1016/j.enggeo.2014.07.023

Li G, West AJ, Densmore AL, Jin Z, Parker RN, Hilton RG. 2014a. Seismic mountain building: Landslides associated with the 2008 Wenchuan earthquake in the context of a generalized model for earthquake volume balance. Geochemistry, Geophysics, Geosystems **15**: 833-844. DOI: 10.1002/2013GC005067

Li L, Lan H, Wu Y. 2014b. The volume-to-surface-area ratio constrains the rollover of the power law distribution for landslide size. The European Physical Journal Plus **129**: 1-7. DOI: 10.1140/epjp

Li W-l, Huang R-q, Xu Q, Tang C. 2013. Rapid susceptibility mapping of co-seismic landslides triggered by the 2013 Lushan Earthquake using the regression model developed for the 2008 Wenchuan Earthquake. Journal of Mountain Science **10**: 699-715. DOI: 10.1007/s11629-013-2786-2

Liao H-W, Lee C-T. 2000. Landslides triggered by the Chi-Chi earthquake. In *Proceedings of the 21st Asian conference on remote sensing*; 383-388.

Liu-Zeng J, Wen L, Oskin M, Zeng L. 2011. Focused modern denudation of the Longmen Shan margin, eastern Tibetan Plateau. Geochemistry, Geophysics, Geosystems **12**. DOI: 10.1029/2011GC003652

Malamud BD, Turcotte DL, Guzzetti F, Reichenbach P. 2004. Landslide inventories and their statistical properties. Earth Surface Processes and Landforms **29**: 687-711. DOI: 10.1002/esp.1064

Marano KD, Wald DJ, Allen TI. 2010. Global earthquake casualties due to secondary effects: a quantitative analysis for improving rapid loss analyses. Natural Hazards **52**: 319-328. DOI: 10.1007/s11069-009-9372-5

Marc O, Hovius N. 2015. Amalgamation in landslide maps: effects and automatic detection. Natural Hazards and Earth System Science **15**: 723-733. DOI: 10.5194/nhess-15-723-2015

Marc O, Hovius N, Meunier P. 2016a. The mass balance of earthquakes and earthquake sequences. Geophysical Research Letters **43**: 3708-3716. DOI: 10.1002/2016GL068333

Marc O, Hovius N, Meunier P, Gorum T, Uchida T. 2016b. A seismologically consistent expression for the total area and volume of earthquake-triggered landsliding. Journal of Geophysical Research: Earth Surface **121**: 640-663. DOI: 10.1002/2015JF00373

Marc O, Meunier P, Hovius N. 2017. Prediction of the area affected by earthquake-induced landsliding based on seismological parameters. Nat. Hazards Earth Syst. Sci. **17**: 1159-1175. DOI: 10.5194/nhess-17-1159-2017

Martha TR, Kerle N, Jetten V, van Westen CJ, Kumar KV. 2010. Characterising spectral, spatial and morphometric properties of landslides for semi-automatic detection using object-oriented methods. Geomorphology **116**: 24-36. DOI: https://doi.org/10.1016/j.geomorph.2009.10.004

Martino S, Prestininzi A, Romeo R. 2014. Earthquake-induced ground failures in Italy from a reviewed database. Natural Hazards Earth System Sciences **14**: 799-814. DOI: 10.5194/nhess-14-799-2014

Marui H, Nadim F. 2009. Landslides and Multi-Hazards. In *Landslides – Disaster Risk Reduction*, Sassa K, Canuti P (eds). Springer Berlin Heidelberg: Berlin, Heidelberg; 435-450.

Marzorati S, Luzi L, De Amicis M. 2002. Rock falls induced by earthquakes: a statistical approach. Soil Dynamics and Earthquake Engineering **22**: 565-577. DOI: 10.1016/S0267-7261(02)00036-2

McCalpin J. 1984. Preliminary age classification of landslides for inventory mapping. In *Proceedings 21st Engineering Geology and Soil Engineering Symposium, April*; 5-6.

McCrink PT. 2001. Regional Earthquake-Induced Landslide Mapping Using Newmark Displacement Criteria, Santa Cruz County, California, in H. Ferriz and Anderson, ed. Engineering Geology Practice in Northern California, Association of Engineering Geologists Special Publication 12, California Geological Survey Bulletin **210**: 77-93

Meunier P, Hovius N, Haines AJ. 2007. Regional patterns of earthquake-triggered landslides and their relation to ground motion. Geophysical Research Letters **34**:

Meunier P, Hovius N, Haines JA. 2008. Topographic site effects and the location of earthquake induced landslides. Earth and Planetary Science Letters **275**: 221-232. DOI: 10.1016/j.epsl.2008.07.020

Nadim F, Kjekstad O, Peduzzi P, Herold C, Jaedicke C. 2006. Global landslide and avalanche hotspots. Landslides **3**: 159-173. DOI: 10.1007/s10346-006-0036-1

NASA Jet Propulsion Laboratory (JPL). 2013. NASA Shuttle Radar Topography Mission United States 1 arc second. NASA EOSDIS Land Processes DAAC, USGS Earth Resources Observation and Science (EROS) Center, Sioux Falls, South Dakota (https://lpdaac.usgs.gov), accessed January 1, 2015.

Newmark NM. 1965. Effects of earthquakes on dams and embankments. Geotechnique **15**: 139-160

Nishida K, Kobashi S, Mizuyama T. 1996. Analysis of distribution of landslides caused by 1995 Hyogoken Nanbu earthquake referring to a database specialized for sediment related disasters. . Journal of Japan Society of Erosion Control Engineering 49 (1), 19–24, doi.org/10.11475/sabo1973.49.19 (in Japanese with English abstract):

Nowicki Jessee MA, Hamburger MW, Allstadt KE, Wald DJ, Robeson SM, Tanyas H, Thomas EM. in press. A Global Empirical Model for Near Real-time Assessment of Seismically Induced Landslides. Journal of Geophysical Research: Earth Surface:

Nowicki MA, Wald DJ, Hamburger MW, Hearne M, Thompson EM. 2014. Development of a globally applicable model for near real-time prediction of seismically induced landslides. Engineering Geology **173**: 54-65. DOI: https://doi.org/10.1016/j.enggeo.2014.02.002

Ohmori H. 1988. Magnitude, frequency and geomorphological significance of rocky mud flows, landcreep and the collapse of steep slopes. Zeitschrift fur Geomorphology **67**: 55-65

Papadopoulos GA, Plessa A. 2000. Magnitude–distance relations for earthquake-induced landslides in Greece. Engineering Geology **58**: 377-386. DOI: https://doi.org/10.1016/S0013-7952(00)00043-0

Papathanassiou G, Valkaniotis S, Ganas A, Pavlides S. 2013. GIS-based statistical analysis of the spatial distribution of earthquake-induced landslides in the island of Lefkada, Ionian Islands, Greece. Landslides **10**: 771-783. DOI: 10.1007/s10346-012-0357-1

Parker R, Hancox G, Petley D, Massey C, Densmore A, Rosser N. 2015. Spatial distributions of earthquake-induced landslides and hillslope preconditioning in the northwest South Island, New Zealand. Earth Surface Dynamics **3**: 501. DOI: 10.5194/esurf-3-501-2015

Parker RN. 2013. Hillslope memory and spatial and temporal distributions of earthquake-induced landslides. Durham University.

Parker RN, Densmore AL, Rosser NJ, de Michele M, Li Y, Huang R, Whadcoat S, Petley DN. 2011. Mass wasting triggered by the 2008 Wenchuan earthquake is greater than orogenic growth. Nature Geoscience **4**: 449-452. DOI: 10.1038/ngeo1154

Parker RN, Rosser NJ, Hales TC. 2017. Spatial prediction of earthquake-induced landslide probability. Nat. Hazards Earth Syst. Sci. Discuss. **2017**: 1-29. DOI: 10.5194/nhess-2017-193

Pašek J. 1975. Landslides inventory. Bulletin of the International Association of Engineering Geology - Bulletin de l'Association Internationale de Géologie de l'Ingénieur **12**: 73-74. DOI: 10.1007/bf02635432

Pelletier JD, Malamud BD, Blodgett T, Turcotte DL. 1997. Scale-invariance of soil moisture variability and its implications for the frequency-size distribution of landslides. Engineering Geology **48**: 255-268. DOI: https://doi.org/10.1016/S0013-7952(97)00041-0

Pellicani R, Spilotro G. 2015. Evaluating the quality of landslide inventory maps: comparison between archive and surveyed inventories for the Daunia region (Apulia, Southern Italy). Bulletin of Engineering Geology and the Environment **74**: 357-367

Petley D. 2012. Global patterns of loss of life from landslides. Geology **40**: 927-930. DOI: 10.1130/G33217.1

Prestininzi A, Romeo R. 2000. Earthquake-induced ground failures in Italy. Engineering Geology **58**: 387-397. DOI: https://doi.org/10.1016/S0013-7952(00)00044-2

Roback K, Clark MK, West AJ, Zekkos D, Li G, Gallen SF, Champlain D, Godt JW. 2017. Map data of landslides triggered by the 25 April 2015 Mw 7.8 Gorkha, Nepal earthquake: U.S. Geological Survey data release. DOI: https://doi.org/10.5066/F7DZ06F9

Robinson TR, Rosser NJ, Densmore AL, Williams JG, Kincey ME, Benjamin J, Bell HJA. 2017. Rapid post-earthquake modelling of coseismic landslide magnitude and distribution for emergency response decision support. Nat. Hazards Earth Syst. Sci. Discuss. **2017**: 1-29. DOI: 10.5194/nhess-2017-83

Rodriguez C, Bommer J, Chandler R. 1999. Earthquake-induced landslides: 1980–1997. Soil Dynamics and Earthquake Engineering **18**: 325-346. DOI: https://doi.org/10.1016/S0267-7261(99)00012-3

Rosser B, Dellow S, Haubrock S, Glassey P. 2017. New Zealand's National Landslide Database. Landslides. DOI: 10.1007/s10346-017-0843-6

Saade A, Abou-Jaoude G, Wartman J. 2016. Regional-scale co-seismic landslide assessment using limit equilibrium analysis. Engineering Geology **204**: 53-64. DOI: https://doi.org/10.1016/j.enggeo.2016.02.004

Sappington J, Longshore KM, Thompson DB. 2007. Quantifying landscape ruggedness for animal habitat analysis: a case study using bighorn sheep in the Mojave Desert. The Journal of wildlife management **71**: 1419-1426. DOI: 10.2193/2005-723

Sato HP, Koarai M, Une H, Iwahashi J, Miyahara B, Yamagishi H. 2008. GIS Analysis on Geomorphological Features of Slope Failures Triggered by the Niigataken Chuetsu-oki Earthquake in 2007. Journal of the Geographical Survey Institute of Japan, 114, 91-102, http://www.gsi.go.jp/common/000048571.pdf. (in Japanese):

Schlögel R, Torgoev I, De Marneffe C, Havenith HB. 2011. Evidence of a changing size–frequency distribution of landslides in the Kyrgyz Tien Shan, Central Asia. Earth Surface Processes and Landforms **36**: 1658-1669. DOI: 10.1002/esp.2184

Schmitt RG, Tanyas H, Jessee MAN, Zhu J, Biegel K, Allstadt KE, Jibson RW, Thompson EM, van Westen CJ, Sato HP, Wald DJ, Godt JW, Gorum T. in press. An Open Repository of Earthquake-triggered Ground Failure Inventories, U.S. Geological Survey data release collection, https://doi.org/10.5066/F7H70DB4.

Sekiguchi T, Sato HP. 2006. Feature and distribution of landslides induced by the Mid Niigata Prefecture Earthquake in 2004, Japan. Journal of the Japan Landslide Society **43**: 142-154

Sepúlveda SA, Murphy W, Jibson RW, Petley DN. 2005. Seismically induced rock slope failures resulting from topographic amplification of strong ground motions: The case of Pacoima Canyon, California. Engineering Geology **80**: 336-348. DOI: 10.1016/j.enggeo.2005.07.004

Shafique M, van der Meijde M, Khan MA. 2016. A review of the 2005 Kashmir earthquake-induced landslides; from a remote sensing prospective. Journal of Asian Earth Sciences **118**: 68-80. DOI: https://doi.org/10.1016/j.jseaes.2016.01.002

Shearer PM. 2009. Introduction to seismology. Cambridge University Press: Cambridge

Shieh CL, Chen YS, Tsai YJ, Wu JH. 2009. Variability in rainfall threshold for debris flow after the Chi-Chi earthquake in central Taiwan, China. International Journal of Sediment Research **24**: 177-188. DOI: http://dx.doi.org/10.1016/S1001-6279(09)60025-1

Stark CP, Guzzetti F. 2009. Landslide rupture and the probability distribution of mobilized debris volumes. Journal of Geophysical Research: Earth Surface **114**. DOI: 10.1029/2008JF001008

Stark CP, Hovius N. 2001. The characterization of landslide size distributions. Geophysical Research Letters **28**: 1091-1094. DOI: 10.1029/2000GL008527

Suziki K. 1979. On the Disaster Situation/Land Condition Map of the Izu-Oshima Kinkai Earthquake, 1978. Journal of the Japan Cartographers Association **17(2)**: 16-22. DOI: 10.11212/jjca1963.17.2_16

Tanaka K. 1994. Landslides triggered by the earthquake - case study of Okushiri Island affected by the Hokkaido Nansei Oki earthquake. In: The Japan Landslide Society Branch, ed., Landslides Triggered by the Earthquake

Tang C, Westen CJV, Tanyaş H, Jetten VG. 2016. Analyzing post-earthquake landslide activity using multi-temporal landslide inventories near the epicentral area of the 2008 Wenchuan earthquake. Natural Hazards and Earth System Sciences 16.12 (2016): 2641. DOI: 10.5194/nhess-16-2641-2016

Tanyaş H, van Westen CJ, Allstadt KE, Anna Nowicki Jessee M, Görüm T, Jibson RW, Godt JW, Sato HP, Schmitt RG, Marc O, Hovius N. 2017a. Presentation and Analysis of a Worldwide Database of Earthquake-Induced Landslide Inventories. Journal of Geophysical Research: Earth Surface **122**: 1991-2015. DOI: 10.1002/2017JF004236

Tanyaş H, van Westen CJ, Allstadt KE, M.A. JN, Gorum T, Jibson RW, Godt JW, Sato HP, Schmidt RG, Marc O, Hovius N. 2017b. Presentation and Analysis of a World-Wide Database of Earthquake-Induced Landslide Inventories. Journal of Geophysical Research: Earth Surface **122**: 1991-2015. DOI: 10.1002/2017JF004236

Terzaghi K. 1950. Mechanism of Landslides. In *Application of Geology to Engineering Practice*, Paige S (ed). Geological Society of America.

Urgeles R, Camerlenghi A. 2013. Submarine landslides of the Mediterranean Sea: Trigger mechanisms, dynamics, and frequency-magnitude distribution. Journal of Geophysical Research: Earth Surface **118**: 2600-2618. DOI: 10.1002/2013JF002720

Van Den Eeckhaut M, Poesen J, Govers G, Verstraeten G, Demoulin A. 2007. Characteristics of the size distribution of recent and historical landslides in a populated hilly region. Earth and Planetary Science Letters **256**: 588-603. DOI: 10.1016/j.epsl.2007.01.040

Wald D, Wald L, Worden B, Goltz J. 2003. ShakeMap, a tool for earthquake response. U.S. Geological Survey Fact Sheet 087-03 (2003).

Wald DJ. 2013. Adding secondary hazard and ground-truth observations to PAGER's loss modeling. In *Proceedings of the 10th International ISCRAM Conference*, Comes T, F. Fiedrich, S. Fortier, Geldermann J, T.Müller (eds): Baden-Baden, Germany.

Wald DJ, Lin K-w, Quitoriano V. 2008. Quantifying and qualifying USGS ShakeMap uncertainty, U.S. Geological Survey Open File Report 2008–1238, 26 pp.

Wald DJ, Quitoriano V, Heaton TH, Kanamori H, Scrivner CW, Worden CB. 1999. TriNet "ShakeMaps": Rapid Generation of Peak Ground Motion and Intensity Maps for Earthquakes in Southern California. Earthquake spectra **15**: 537-555. DOI: 10.1193/1.1586057

Wartman J, Dunham L, Tiwari B, Pradel D. 2013. Landslides in eastern Honshu induced by the 2011 Tohoku earthquake. Bulletin of the Seismological Society of America **103**: 1503-1521. DOI: 10.1785/0120120128

Wasowski J, Keefer DK, Lee C-T. 2011. Toward the next generation of research on earthquake-induced landslides: Current issues and future challenges. Engineering Geology **122**: 1-8. DOI: 10.1016/j.enggeo.2011.06.001

Wieczorek GF. 1984. Preparing a detailed landslide-inventory map for hazard evaluation and reduction. Bulletin of the Association of Engineering Geologists **21**: 337-342

Wieczorek GF, Wilson RC, Harp EL. 1985. Map showing slope stability during earthquakes in San Mateo County, California. In *IMAP*.

Wilkinson S, Chiaro G, Pokhrel RM, Kiyota T, Katagiri T, Sharma K, Goda K. 2015. The 2015 Gorkha Nepal earthquake: Insights from earthquake damage survey. DOI: 10.3389/fbuil.2015.00008

Wilson R, Keefer D. 1985. Predicting areal limits of earthquake-induced landsliding, in Earthquake Hazards in the Los Angeles Region—An Earth Science Perspective, J. Ziony (Editor), U.S. Geol.ogical Survey Professional Paper 1360. 317-345

Wilson RC, Keefer DK. 1983. Dynamic analysis of a slope failure from the 6 August 1979 Coyote Lake, California, earthquake. Bulletin of the Seismological Society of America **73**: 863-877

Xu C. 2014. Preparation of earthquake-triggered landslide inventory maps using remote sensing and GIS technologies: Principles and case studies. Geoscience Frontiers. DOI: 10.1016/j.gsf.2014.03.004

Xu C, Xu X, Yao X, Dai F. 2014. Three (nearly) complete inventories of landslides triggered by the May 12, 2008 Wenchuan Mw 7.9 earthquake of China and their spatial distribution statistical analysis. Landslides **11**: 441-461. DOI: 10.1007/s10346-013-0404-6

Yagi H, Sato G, Higaki D, Yamamoto M, Yamasaki T. 2009. Distribution and characteristics of landslides induced by the Iwate–Miyagi Nairiku Earthquake in 2008 in Tohoku District, Northeast Japan. Landslides **6**: 335-344. DOI: 10.1007/s10346-009-0182-3

Yagi H, Yamasaki T, Atsumi M. 2007. GIS analysis on geomorphological features and soil mechanical implication of landslides caused by 2004 Niigata Chuetsu earthquake. Journal of the Japan Landslide Society **43**: 294-306. DOI: 10.3313/jls.43.294

Summary

Earthquakes may cause severe impacts in both urban and rural areas, especially in less-developed countries, due to inadequate spatial planning and building control. In seismically active mountainous regions, the impact of seismic shaking is aggravated by secondary hazards, of which earthquake-triggered landslides are often the most damaging phenomena. Many studies confirm that earthquake losses due to landslides and related ground failures can be very high.

For reducing earthquake disaster losses in mountainous regions, it is important to predict the areas that might be affected by earthquake-induced landslides (EQIL), in order to use this in risk management. It is also very important to predict if landslides may be triggered immediately after an earthquake, in order to facilitate the rescue operations, before the landslides can be actually mapped using satellite imagery. This research focuses on the development of methods for rapid assessment of earthquake-induced landslides, based on knowledge obtained from a database of historical events.

Frequency-area distribution (FAD) of landslides can be used to derive summary statistics regarding an EQIL-event, which could help us to provide valuable information in the emergence response phase. The power-law relation for the FAD of medium and large landslides (e.g., tens to millions of square meters), which has been observed by numerous authors, provides the basis to model the size distribution of landslides and to estimate landslide-event magnitude (mLS). Using a rapid prediction of landslide-event magnitude immediately following an earthquake, we can evaluate the severity of a landslide-event in near real-time. We can estimate the total landslide area and volume based on empirical relations proposed by previous studies.

For many EQIL inventories the FAD of small landslides diverges from the power-law distribution, with a rollover point below which frequencies decrease for smaller landslides. Some studies conclude that this divergence is an artifact of unmapped small landslides due to lack of spatial or temporal resolution; others state that it is caused by the change in the underlying failure process. An explanation for this dilemma is essential both to evaluate the factors controlling FADs of landslides and also power-law scaling, which is a crucial factor regarding both landscape evolution and landslide hazard assessment.

Rapid assessment of the spatial distribution of EQIL could provide valuable information in the emergency response phase. Previous studies proposed global analyses with the aim of predicting EQIL distributions in near real-time. However, all previous studies are based on grid cells as basic mapping units, which do not reflect the physical properties of terrain units and whose size do not match the resolution of existing thematic data at a global scale. Moreover, none of the existing analyses considers sampling balance between different inventories or categorizing the inventories to construct a training set with higher statistical representativeness. Also, most of the previously proposed models are based on a limited number of historical EQIL inventories.

EQIL inventories are essential tools to extend our knowledge of the relationship between earthquakes and the landslides they can trigger. Unfortunately, such inventories are difficult to generate and therefore scarce, and the available ones differ regarding their

quality and level of completeness. Moreover, access to existing EQIL inventories is currently difficult because there was no centralized database.

To address these issues, we compiled EQIL inventories from around the globe based on an extensive literature study. The database contains information on 363 landslide-triggering earthquakes and includes 66 digital landslide inventories. To make these data openly available, we created a repository to host the digital inventories that we have permission to redistribute through the U.S. Geological Survey ScienceBase platform. The hope is that it will grow over time as more authors contribute their inventories. We analyzed the distribution of EQIL events by time period and location, more specifically breaking down the distribution by continent, country, and mountain region.

Additionally, we analyzed frequency distributions of EQIL characteristics, such as the approximate area affected by landslides, the total number of landslides, the maximum distance from fault rupture zone, and distance from epicenter when the fault plane location is unknown. For the available digital EQIL inventories, we examined the underlying characteristics of landslide size, topographic slope, roughness, local relief, distance to streams, peak ground acceleration, peak ground velocity, and Modified Mercalli Intensity. We developed an evaluation system to help users assess the suitability of the available inventories for different types of EQIL studies.

Using the compiled inventories, we analyzed the frequency-area distribution (FAD) of EQIL inventories. We developed an updated method for estimating mLS and its uncertainty that better fits the observations and is more reproducible, robust, and consistent than existing methods. We validated our model by computing mLS for all of the inventories in our dataset and compared that to the total landslide areas of the inventories. We demonstrated that our method is able to estimate the total landslide area of the events in this larger inventory dataset more successfully than the existing methods.

We proposed a method to predict landslide-event magnitude, using five predictors, both morphometric and seismogenic, which are globally and readily available. These predictors were used within a stepwise linear regression and validated using the leave-one-out technique. We demonstrated that our approach successfully predicts landslide-event magnitude values globally and provided results along with their statistical significance and confidence levels. The proposed approach can provide information globally and in near real-time, by retrieving data from the USGS ShakeMaps, along with topographic and thematic information. The results may provide valuable information regarding landscape evolution processes, landslide hazard assessments and contribute to the rapid emergency response after earthquakes in mountainous terrain.

We also examined the factors controlling the FADs of landslides and propose that the successive slope-failure process is the main reason for the underestimation of small landslides and thus the divergence from a power-law. This reveals that the divergence from the power law is not necessarily attributed to the incompleteness of an inventory. Because of the subjectivity of mapping procedures, the total number of landslides and total landslide areas in inventories differ significantly, and so do the shapes of FADs.

Finally, we developed an improved global statistical model that overcomes the drawbacks of previously developed methods to estimate the probability of the occurrence of EQIL.

We used slope units, which are terrain partitions attributed to similar hydrological and geomorphological conditions and to processes that shape natural landscapes. A set of 25 EQIL-events were selected and categorized based on the similarity between causal factors to determine the most relevant training set to predict a given landslide-event. As a result, we developed a specific model for each category. We sampled an equal number of landslide points from each inventory to overcome the dominance of some inventories with large landslide population. We used seven independent thematic variables for both categorizing the inventories and modeling, based on logistic regression. The results show that categorizing landslide-events introduces a remarkable improvement in the modeling performance of many events. The categorization of existing inventories can be applied within any statistical, global approach to earthquake-induced landslide events. The proposed categorization approach and the classification performance can be further improved with the acquisition of new inventory maps.

Appendix

Table S1.1. Summary table for the 136 EQIL inventories gathered from the previous works.*

ID for reported EQIL inventories	Location	Date	Magnitude	Depth (km)	Aproximate area affected by landslide (km^2)	Max epicentral distance (km)	Max distance from fault-rupture zone to landslides (km)	Fault type	References
1	New Madrid, Missouri (US)	02.07.1812	Ms: 7.5	-	40000	-	-	Thrust/Reverse	Quoted by Keefer, 1984
2	Marlborough (New Zealand)	10.16.1848	Mw: 7.4	12	1500	-	-	Strike-slip	Quoted by Honcox et al., 2002
3	Wairarapa (New Zealand)	01.23.1855	Mw: 8.2	33	19000	-	-	Strike-slip	Quoted by Honcox et al., 2002

Table S2.2. The results of evaluation carried out for digitally available 64 EQIL inventories (The given ID numbers are same with the ones we used in Table 2.1 in Chapter 2).*

Criteria			Execution performance	Score	Inventories						
					(1)	(2)	(3)	(4)	(5)	(6)	(7)
(A)	(B)				San Fernando	Guatemala	Friuli	Izu Oshima Kinkai	Mount Diablo	Mammoth Lakes	Coalinga
Essential criteria	Essential criteria	i)	0-100 %	0-1	0.8	1	1	1	0	1	1
		ii)	No/Yes	0/1	0	1	1	1	0	1	1
		iii)	0-100 %	0-1	0	0.5	0	1	0	0.5	0.5
		iv)	L>25m : <0.5 25m≥L>5m : ≥0.5 5m≥L : 1	0/1	0	1	0.4	0.5	0	0.4	0.8
Preferred criteria		v)	No/Yes	0/1	0	1	1	1	0	1	1
		vi)	No/Yes	0/1	0	0	0	1	0	0	0
	Preferred criteria	vii)	0-100 %	0-1	0.5	1	0	1	0	1	1
		viii)	No/Yes	0/1	0	0	1	0	1	0	0

*The entire table is presented as Supporting Information in the link provided below:

https://agupubs.onlinelibrary.wiley.com/doi/full/10.1002/2017JF004236

Biography

Hakan Tanyaş was born on the 23th of July 1983 in Ankara, Turkey. He studied in the Middle East Technical University, Turkey and received a BSc on Geological Engineering in 2007. He then began working for industry and worked as a geotechnical engineer for five years. He started a MSc program regarding a geotechnical slope stability problem in 2008 and he received his MSc degree in 2011. In 2012, he joined the remote sensing and GIS laboratory of the Middle East Technical University as a teaching and research assistant. He started a PhD program there but in 2014, he resigned from his position and began the PhD program at the University of Twente, Faculty of Geo-information Science and Earth Observation (ITC), Netherlands. During his PhD, he worked at USGS Colorado, USA, Golden office and CNR IRPI, Italy, Perugia office as a visiting scientist.

Author's publications

Peer-reviewed journal articles

1. **Tanyaş, H.,** Rossi, M., Alvioli, M., van Westen, C.J., and Marchesini, I. A global slope unit-based method for the near real-time prediction of earthquake-induced landslides. Geomorphology, accepted, 2018.

2. Nowicki Jessee, M.A., Hamburger, M.W., Allstadt, K., Wald, D.J., Robeson, S.M., **Tanyas, H**., Hearne, M., and Thompson, E.M., 2018. A Global Empirical Model for Near Real-time Assessment of Seismically Induced Landslides. Journal of Geophysical Research: Earth Surface, 123. https://doi.org/10.1029/2017JF004494

3. **Tanyaş, H**., Allstadt, K.E., van Westen, C.J., 2018. An updated method for estimating landslide-event magnitude. Earth Surface Processes and Landforms, 43: 1836-1847. DOI: 10.1002/esp.4359

4. **Tanyas, H**., van Westen, C.J., Allstadt, K.E., Jesse (Nowicki), M.A., Gorum, T., Jibson, R.W., Godt, J.W., Sato, H.P., Schmidt, R.G., Marc, O., Hovius, N., 2017. Presentation and Analysis of a World-Wide Database of Earthquake-Induced Landslide Inventories. Journal of Geophysical Research: Earth Surface 122: 1991-2015. DOI: 10.1002/2017JF004236

5. **Tanyas, H**., Dirican, M., Süzen. M.L., Turkmenoglu, A.G., Kolat, C. and Atakuman, C., 2017. Identification of Possible Source Areas of Stone Raw Materials Combining Remote Sensing and Petrography. International Journal of Remote Sensing. 38:13, 3923-3942. DOI: 10.1080/01431161.2017.1312032

6. Tang, C., Van Westen, C.J., **Tanyas, H**., and Jetten, V.G., 2016. Analysing post-earthquake landslide activity using multi-temporal landslide inventories near the epicentral area of the 2008 Wenchuan earthquake, Nat. Hazards Earth Syst. Sci., 16, 2641-2655, https://doi.org/10.5194/nhess-16-2641-2016

7. **Tanyaş, H**., Kolat, Ç., Süzen. M.L., 2014. A New Approach to Estimate Cover-Management Factor of RUSLE and Validation of RUSLE Model in the watershed of

Kartalkaya Dam. Journal of Hydrology, 528, 584-598. https://doi.org/10.1016/j.jhydrol.2015.06.048

8. **Tanyaş, H**., Ulusay, R., 2013. Assessment of structurally-controlled slope failure mechanisms and remedial design considerations at a feldspar open pit mine, Western Turkey. Engineering Geology, 155, pp. 54-68. https://doi.org/10.1016/j.enggeo.2012.12.017

Peer-reviewed reports

1. Schmitt RG, **Tanyas H**, Nowicki Jessee MA, Zhu J, Biegel KM, Allstadt KE, Jibson RW, Thompson EM, van Westen CJ, Sato HP, Wald DJ, Godt JW, Gorum T, Xu C, Rathje EM, Knudsen KL. 2017. An open repository of earthquake-triggered ground-failure inventories. In Data Series: Reston, VA; 26. https://doi.org/10.3133/ds1064

2. Allstadt, K., Thompson, E.M., Wald, D.J., Hamburger, M.W., Godt, J.W., Knudsen, K.L., Jibson, R.W., Jessee, M.A., Zhu, J., Hearne, Baise, M.L.G., **Tanyas H**., and Marano, K.D. 2016. USGS approach to real-time estimation of earthquake-triggered ground failure - Results of 2015 workshop, U.S. Geological Survey Open-File Report 2016-1044. https://doi.org/10.3133/ofr20161044

Peer-reviewed journal articles (under revision or in progress)

1. **Tanyaş, H**., Allstadt, K.E., van Westen, C.J., and Jibson R.W. Factors controlling landslide frequency-area distributions, Earth Surface Processes and Landforms, under review, 2018.

2. **Tanyas, H**., van Westen, C.J., Persello, C., and Alvioli M. Rapid prediction of magnitude-scale of landslide events triggered by an earthquake, Landslides, under review, 2018.

3. Tang, C., **Tanyas, H**., van Westen, C.J., Tang, C., Fan, X., and Jetten, V.G. Analysing post-earthquake mass movement volume dynamics with multi-source DEMs. Engineering Geology, under review, 2018.

4. Zhang, J., van Westen, C.J., **Tanyas, H**., Mavrouli, O., Ge, Y., Bajrachary, S., Gurung, D.R., Dhital, M.R., and Khanal, N.R.: How size and trigger matter: analyzing rainfall- and earthquake-triggered landslide inventories and their causal relation in the Koshi River basin, Central Himalaya, Nat. Hazards Earth Syst. Sci. Discuss., https://doi.org/10.5194/nhess-2018-109, under review, 2018.

5. Fan X., Scaringi G., West A.J., **Tanyas H**., Hovius N., van Westen C.J., Hales T.C., Korup O., Jibson R.W., Zhang L., Allstadt K.E., Evans S.G., Xu C., Li G., Pei X., Xu Q., and Huang R. Earthquake-induced chains of geo-hazards: Pattern, mechanism and impacts, Reviews of Geophysics, under review, 2018.

6. Lombardo, L., Bakka, H., **Tanyas, H**., Van Westen, C.J., Mai, P.M., and Huser R. Geostatistical modeling to capture seismic-shaking patterns from earthquake-induced landslides, Earth Surface Processes and Landforms, in progress, 2018.

ITC Dissertation List

https://www.itc.nl/Pub/research_programme/Research-review-and-output/PhD-Graduates